**YEAR END TECHNICAL REPORT**
September 29, 2022 to September 28, 2023

# Chemical Process Alternatives for Radioactive Waste

**Date submitted:**

December 8, 2023


**Principal Investigator:**

Leonel E. Lagos, Ph.D., PMP®

**Florida International University Collaborators:**

Dwayne McDaniel, Ph.D., P.E. (Project Manager)
Anthony Abrahao, M.S.
Aparna Aravelli, Ph.D.
Amer Awwad, M.S., P.E.
Mayren Echeverria Boan, Ph.D.
Mackenson Telusma, M.S.
DOE Fellows



**Submitted to:**

U.S. Department of Energy
Office of Environmental Management
Under Cooperative Agreement DE-EM0005213



FIU | Applied Research Center
FLORIDA INTERNATIONAL UNIVERSITY

Addendum:

This document represents one (1) of five (5) reports that comprise the Year End Reports for the period of September 29, 2022 to September 28, 2023 prepared by the Applied Research Center at Florida International University for the U.S. Department of Energy Office of Environmental Management (DOE-EM) under Cooperative Agreement No. DE-EM0005213.

The complete set of FIU's Year End Reports for this reporting period includes the following documents:

Project 1: Chemical Process Alternatives for Radioactive Waste
Document number: FIU-ARC-2022-800012997-04b-007

Project 2: Environmental Remediation Science and Technology
Document number: FIU-ARC-2022-800013918-04b-006

Project 3: Waste and D&D Engineering and Technology Development
Document number: FIU-ARC-2022-800013919-04b-007

Project 4: DOE-FIU Science & Technology Workforce Development Initiative
Document number: FIU-ARC-2022-800013920-04b-011

Project 5: Long-Term Stewardship of Environmental Remedies: Contaminated Soils and Water and STEM Workforce Development
Document number: FIU-ARC-2022-800013922-04b-005

Each document will be submitted to OSTI separately under the respective project title and document number as shown above. In addition, the documents are available at the DOE Research website for the Cooperative Agreement between the U.S. Department of Energy Office of Environmental Management and the Applied Research Center at Florida International University: https://doeresearch.fiu.edu

**DISCLAIMER**

This report was prepared as an account of work sponsored by an agency of the United States government. Neither the United States government nor any agency thereof, nor any of their employees, nor any of its contractors, subcontractors, nor their employees makes any warranty, express or implied, or assumes any legal liability or responsibility for the accuracy, completeness, or usefulness of any information, apparatus, product, or process disclosed, or represents that its use would not infringe upon privately owned rights. Reference herein to any specific commercial product, process, or service by trade name, trademark, manufacturer, or otherwise does not necessarily constitute or imply its endorsement, recommendation, or favoring by the United States government or any other agency thereof. The views and opinions of authors expressed herein do not necessarily state or reflect those of the United States government or any agency thereof.

# TABLE OF CONTENTS

TABLE OF CONTENTS ..... i
LIST OF FIGURES ..... iv
LIST OF TABLES ..... xiii
PROJECT 1 EXECUTIVE SUMMARY ..... 1
MAJOR TECHNICAL ACCOMPLISHMENTS ..... 6
TASK 17: ADVANCED TOPICS FOR HLW MIXING AND PROCESSES ..... 9
Subtask 17.2: Evaluation of Pipeline Flushing Requirements for HLW at Hanford and Savannah River Site ..... 9
Subtask 17.2: Introduction ..... 9
Subtask 17.2: Objectives ..... 10
Subtask 17.2: Methodology ..... 10
Subtask 17.2: Results and Discussion ..... 12
Subtask 17.2: Conclusions ..... 14
Subtask 17.2: References ..... 14
TASK 18: TECHNOLOGY DEVELOPMENT AND INSTRUMENTATION EVALUATION ..... 16
Subtask 18.3: Development of a Coating Deployment Platform for the H-Canyon Exhaust Tunnel ..... 16
Subtask 18.3: Introduction ..... 16
Subtask 18.3: Objectives ..... 17
Subtask 18.3.1: Improvement of Mobile Platform Efficiency ..... 17
Subtask 18.3.1: Methodology ..... 17
Subtask 18.3.1: Results and Discussion ..... 20
Subtask 18.3.1: Conclusions ..... 21
Subtask 18.3.1: References ..... 21
Subtask 18.3.2: Integration of the Coating Application System ..... 22
Subtask 18.3.2: Methodology ..... 22
Subtask 18.3.2: Results and Discussion ..... 23
Subtask 18.3.2: Conclusions ..... 24
Subtask 18.3.2: References ..... 24
Subtask 18.4: Long-Term Surveillance of Nuclear Facilities and Repositories using Mobile Systems ..... 24
Subtask 18.4: Introduction ..... 24
Subtask 18.4: Objectives ..... 25

Subtask 18.4: Methodology ..... 25
Subtask 18.4: Results and Discussion ..... 27
Subtask 18.4.1: Conclusions ..... 37
Subtask 18.4.1: References ..... 37
Subtask 18.5: Development of Robotic Systems for DOE Sites ..... 37
Subtask 18.5: Introduction ..... 37
Subtask 18.5: Objectives ..... 38
Subtask 18.5: Methodology ..... 38
Subtask 18.5: Results and Discussion ..... 39
Subtask 18.5: Conclusions ..... 75
Subtask 18.5: References ..... 76
TASK 19: PIPELINE INTEGRITY AND ANALYSIS ..... 77
Subtask 19.1: Pipeline Corrosion and Erosion Evaluation ..... 77
Subtask 19.1: Introduction ..... 77
Subtask 19.1: Objectives ..... 78
Subtask 19.1.1: Evaluation of SRNL Stainless Steel Coupons for Erosion Testing using DWPF Glass Frit ..... 78
Subtask 19.1.1: Methodology ..... 78
Subtask 19.1.1: Research Results and Discussion ..... 78
Subtask 19.1.1: Conclusions ..... 102
Subtask 19.1.1: References ..... 102
Subtask 19.1.2: Caustic Simulant Testing using the Bench Scale Flow Loop ..... 103
Subtask 19.1.2: Methodology ..... 103
Subtask 19.1.2: Research Results and Discussion ..... 103
Subtask 19.1.2: Conclusions ..... 114
Subtask 19.1.2: References ..... 114
Subtask 19.1.3: Automated Erosion and Corrosion Detection using fluid flow dynamics and advanced data analytics ..... 115
Subtask 19.1.3: Introduction ..... 115
Subtask 19.1.3: Methodology, Results and Discussion ..... 115
Subtask 19.1.3: Conclusions ..... 137
Subtask 19.1.3: References ..... 137
Subtask 19.2: Evaluation of Nonmetallic Components in the Waste Transfer System ..... 138

Subtask 19.2: Introduction ..... 138
Subtask 19.2: Objectives ..... 139
Subtask 19.2: Methodology, Results and Discussion ..... 139
Subtask 19.2.2: Conclusions ..... 153
Subtask 19.2.2: References ..... 153
TASK 20: Corrosion Protection and Characterization of EM Infrastructure ..... 154
Subtask 20.1: Evaluation of Coatings for the H-Canyon Exhaust Tunnel ..... 154
Subtask 20.1: Introduction ..... 154
Subtask 20.1: Objectives ..... 154
Subtask 20.1.1: Evaluation of Coatings through Accelerated Aging Tests ..... 155
Subtask 20.1.1: Methodology ..... 155
Subtask 20.1.1: Results and Discussion ..... 160
Subtask 20.1.1: Conclusions ..... 167
Subtask 20.1.1: References ..... 167
Subtask 20.1.2: Establish a Ranking of Coating Candidates from Research Findings ..... 168
Subtask 20.1.2: Methodology ..... 168
Subtask 20.1.2: Results and Discussion ..... 168
Subtask 20.1.2: Conclusions ..... 168
Subtask 20.2: Corrosion Evaluation of Steel Canisters for Hanford Integrated Disposal Facility ..... 168
Subtask 20.2: Introduction ..... 168
Subtask 20.2: Objectives ..... 169
Subtask 20.2.1: Corrosion Behavior of Canister Materials for the Steel Corrosion Study at Hanford - 304 Stainless Steel ..... 169
Subtask 20.2.1: Methodology ..... 169
Subtask 20.2.1: Results and Discussion ..... 173
Subtask 20.2.1: Conclusions ..... 179
Subtask 20.2.1: References ..... 179
CONFERENCE PARTICIPATION, PUBLICATIONS, AWARDS & ACADEMIC MILESTONES ..... 180
ACKNOWLEDGEMENTS ..... 180
APPENDIX ..... 181

# LIST OF FIGURES

Figure 1. Major components for flushing experiments. 10
Figure 2. CAD model of the updated 330-foot flush loop. 11
Figure 3. Constructed 330-foot extension used for flushing. 11
Figure 4. 20 vol.% Fully-flooded (left), Density and mass flow verses time (right), approximate FTLV. 13
Figure 5. 20 vol.% Gravity drained (left), Density and mass flow verses time (right), approximate FTLV. 13
Figure 6. Vector thrust testing setup. 18
Figure 7. Dual EDF unit equipped with vector thrust units. 18
Figure 8. Free body diagram of vector thrust unit and platform interaction. 18
Figure 9. PCB modules for motor controller, microcontroller and IMU integration. 19
Figure 10. Small-scale wall mockup. 19
Figure 11. Graph of thrust force generated at maximum thrust angle of 30 degrees. 20
Figure 12. Dual EDF platform being tested with vector thrust units. 20
Figure 13. Large wall crawler platform integrated with PCB modules. 21
Figure 14. Large 5-Fan wall crawler. 22
Figure 15. Spray enclosure pieces. 22
Figure 16. Spray mechanism installed on large EDF platform. 23
Figure 17. Testing of large EDF platform and pattern creation using aerosol spray. 23
Figure 18. Deployment of spray material on vertical surface. 24
Figure 19. Hanford's Tank Farm retrieval operations in September 2016 (left) and 2018 (right). 26
Figure 20. Mobile platform integration. 27
Figure 21. FIU's mobile ground platforms. 27
Figure 22. FIU's mobile platform original (left) and upgraded (left) embedded computer. 28
Figure 23. Ground platform lidar integration. 28
Figure 24. All-terrain ground platform donated by WRPS (left) and troubleshooting (right). 29
Figure 25. All-Terrain ground platform donated by WRPS. 29
Figure 26. Captured 3D point cloud (left) and 2D Map Generated using SLAM (right). 30
Figure 27. Legged robot autonomous mapping. 30
Figure 23. FIU’s technology delivered at WRPS’s CTF. 31
Figure 29. FIU’s technology deployed at Hanford’s CTF. 31
Figure 30. Deployment at Hanford’s CTF. 32

Figure 31. Waste segregation test bench. 32
Figure 32. Pneumatic gripper. 33
Figure 33. Pneumatic gripper controller. 33
Figure 34. QR code automated calibration. 34
Figure 35. Color masking identification technique. 34
Figure 36. Waste segregation pick-and-place demonstration. 34
Figure 37. Sample of waste images for training machine-learning prediction model. 35
Figure 38. Locate and rover behavior tree. 35
Figure 39. Object detection using FIU's machine learning segmentation model. 36
Figure 40. Waste sorting automation. 36
Figure 41. DOE, FIU, and WRPS Technology Development Collaboration Meeting at FIU. 39
Figure 42. Deployed miniature inspection rover at AP-105 tank. 40
Figure 43. FIU's miniature inspection rover deployment at AP-105 DST. 40
Figure 44. Resin-printed rover in partial assembly. 41
Figure 45. Miniature Rover resin parts before post-processing. 41
Figure 46. Press-fit insert tolerance testing on rigid resin. 42
Figure 47. Chassis CNC machining. 42
Figure 48. 3D Printed (top) and machined (bottom) chassis components. 43
Figure 49. Chassis's complaint connection. 43
Figure 50. Drivetrain gearbox upgrade. 43
Figure 51. Tether distribution board (units in mm). 44
Figure 52. Microcontroller board schematic (units in mm). 44
Figure 53. Camera board schematic (units in mm). 45
Figure 54. Motor Board (units in mm). 45
Figure 55. Miniature rover's redesigned self-regulated tether distribution board. 45
Figure 56. Miniature rover's controller board. 46
Figure 57. Miniature rover's motor board. 46
Figure 58. Improved Miniature Inspection Rover. 46
Figure 59. Control box's main circuit board. 47
Figure 60. Miniature rover control box board. 47
Figure 61. Miniature rover control box board final prototype. 47
Figure 62. Tether connection board final prototype. 47
Figure 63. Upgraded Control Box. 48

Figure 64. Grounded (left) and ungrounded (right) video feed. ..... 48
Figure 65. Rover video feedback spectrum analysis. ..... 48
Figure 66. Minitower's video feedback noise (left) and improved quality (right). ..... 49
Figure 67. Tether-induced video noise (left) and noise eradication (right). ..... 49
Figure 68. Candidate sampling mechanism designs. ..... 50
Figure 69. Conceptual sampling mechanisms. ..... 50
Figure 70. Candidate sampling arms. ..... 50
Figure 71. Sampling mechanism (A), rear-mounted motor actuators (B), and functionality (C). 51
Figure 72. Sampling arm and base prototypes. ..... 51
Figure 73. FIU's Miniature Magnetic Rover's sampler arm. ..... 52
Figure 74. Sampler's prismatic joint. ..... 52
Figure 75. First design iteration of rover's sampler. ..... 53
Figure 76. Second design iteration of rover's sampler. ..... 53
Figure 77. FIU miniature rover's sampling systems. ..... 53
Figure 78. Flexible connection angle. ..... 54
Figure 79. Chassis length and height calculation ..... 54
Figure 80. Optimal chassis angle. ..... 54
Figure 81. Current design iteration of rover's sampler. ..... 55
Figure 82. Cold Test Facility deployment. ..... 56
Figure 83. Extender module current design (left) and hollow redesign (right). ..... 57
Figure 84. Redesigned module guides using compliant material. ..... 57
Figure 85. Crawler's gripper modules. ..... 57
Figure 86. Improved gripper module with independent blades. ..... 58
Figure 87. Crawler's gripper module gripping test. ..... 58
Figure 88. Pipe crawler improved modules. ..... 59
Figure 89. Tether quick disconnect. ..... 59
Figure 90. Lateral Gamma Scanner's operator interface. ..... 60
Figure 91. Operator Graphical Interface's main layout. ..... 60
Figure 92. Lateral gamma scanner's behavior tree automation. ..... 61
Figure 93. Tracking of deployed-tether length. ..... 62
Figure 94. Updated LGS's behavior tree. ..... 62
Figure 95. LGS deployment featured on Hanford social media. ..... 63
Figure 96. Off-riser sampler's conceptual design. ..... 64

Figure 97. Sampler manipulator's conceptual design. ..... 64
Figure 98. Pneumatic joint design. ..... 65
Figure 99. Off-riser sampler pneumatic joint. ..... 65
Figure 100. FEM analysis of assembly component. ..... 65
Figure 101. Pneumatic joint core's exploded view. ..... 66
Figure 102. Pneumatic joint's driving ends. ..... 66
Figure 103. Linear motion carriage assembly. ..... 66
Figure 104. Pneumatic joint's actuator core assembly. ..... 67
Figure 105. Pneumatic joint's idler sprocket driving end. ..... 67
Figure 106. Pneumatic joint's encoder. ..... 68
Figure 107. Sampler arm's design. ..... 68
Figure 108. Pneumatic joint's functional prototype. ..... 69
Figure 109. Pneumatic joint's three-position control schematic (left) and prototype (right). ..... 69
Figure 110. Laboratory's newly acquired machining equipment. ..... 69
Figure 111. Laboratory's newly acquired resin printers. ..... 70
Figure 112. Pneumatic joint's payload testing. ..... 70
Figure 113. Off-riser sampler's testing mockup. ..... 71
Figure 114. DOE Fellow's summer results at SRNL. ..... 71
Figure 115. Printing nozzle's conceptual design. ..... 72
Figure 116. Printing nozzle's design. ..... 72
Figure 117. Auger nozzle's prototype. ..... 73
Figure 118. Piston Nozzle's conceptual design. ..... 73
Figure 119. Motion system's design. ..... 74
Figure 120. Auger nozzle printer's prototype. ..... 74
Figure 121. 3D printer's upgraded control panel. ..... 75
Figure 122. Pipe components shipped to SRNL for material characterization. ..... 79
Figure 123. Ultrasonic waveforms for 3-inch pipe sections – elbow (left) and straight (right). ..... 79
Figure 124. Ultrasonic waveforms for 2-inch pipe sections – elbow (left) and straight (right). ..... 79
Figure 125. Permasense sensor data for the 3-inch elbow section on the engineering scale loop. 80
Figure 126. Vickers Hardness Tester (left), sample indentation (center) and surface imaging (right). ..... 81
Figure 127. Microscopic images of the coupon surface (Coupon 1) showing diamond indent and pits. ..... 82

Figure 128. Microscopic images of Coupon 2 showing the indent and pits. ..... 82

Figure 129. Hardness Tester (left), microscopic image of the coupon surface (eroded - center and polished - right). ..... 84

Figure 130. Microscopic images of the coupon surface during hardness testing with 100gf of applied load. ..... 84

Figure 131. Microscopic images of the coupon surface during hardness testing with 200gf of applied load. ..... 85

Figure 132. Pipe coupons (6-inch) for making the erosion coupons (left) and manual pump in the reservoir tank (right). ..... 86

Figure 133. Pipe adapter - 3D printed part (left), fitted borescope (center) and in the pipe section (right). ..... 87

Figure 134. Borescope images - internal pipe surface (left), straight section with glass bed (center) and clogged glass particles (right). ..... 87

Figure 135. Degradation in coupon placed near the elbow. ..... 89

Figure 136. Degradation in coupon placed on bottom 3-inch section of the pipe. ..... 90

Figure 137. Degradation in coupon placed at the top 3-inch section of the pipe. ..... 90

Figure 138. Degradation in coupon placed at the bottom of 3-inch section closer to the reducer. ..... 91

Figure 139. Degradation in coupon placed at the top 3-inch section of the pipe. ..... 91

Figure 140. Erosion pattern in all 5 coupons. ..... 92

Figure 141. Critical data points on the loop for thermal stability experiments. ..... 93

Figure 142. Temperature variation in the loop components. ..... 93

Figure 143. Temperature variation in the pipe sections. ..... 94

Figure 144. Pipe loop with critical data points identified for degradation study. ..... 95

Figure 145. UT measurement of the coupon using two separate sensors (inner and outer coupon surface). ..... 97

Figure 146. Coupon #1 through #5 (left to right) images taken after completion of the test cycles. ..... 100

Figure 147. Coupon # 1 Microscopic image before polishing (left) and polished (right). ..... 100

Figure 148. Coupon # 2 Microscopic image before polishing (left) and polished (right). ..... 101

Figure 149. Coupon # 3 Microscopic image before polishing (left) and polished (right). ..... 101

Figure 150. Coupon # 4 Microscopic image before polishing (left) and polished (right). ..... 101

Figure 151. Coupon # 5 Microscopic image before polishing (left) and polished (right). ..... 102

Figure 152. Caustic simulant solution in the tank (left) and after 3 weeks of settling (right). ... 104

Figure 153. Pipe test section with markings for shipping to SRNL. ..... 104

Figure 154. Simulant mass measurement (left) and experimental set up for mixing the salt simulants (right). ..... 105

Figure 155. Coupon mass measurement (left) and UT thickness measurement (right)..... 106

Figure 156. Thermal images during the salt mixing process. ..... 107

Figure 157. Significant salts and solvent images (sodium hydroxide, aluminum nitrate and sodium nitrate). ..... 107

Figure 158. Sodium sulphate during dissolution. ..... 108

Figure 159. Caustic loop thermal images during operation with temperature changes over time (75.2 to 93.2°F). ..... 108

Figure 160. Thermal images of the coupon sections (3-inch pipe) with temperature rise from 90.3 to 110°F..... 109

Figure 161. Pump thermal profile with highest temperature reaching 161°F..... 109

Figure 162. Visual images showing caustic corrosion in the coupons under static conditions.. 110

Figure 163. Chemical handling pump (left), disassembled impeller (center) and pump's volute (right). ..... 112

Figure 164. Slip ring (left), volute showing chemical corrosion (center) and pump's shaft (with casing removed) (right). ..... 112

Figure 165. Static immersion test results for SRNL coupons (stainless coupons with 2, 4 and 6 M salt solutions). ..... 113

Figure 166. Static immersion test results for the SRNL coupons (stainless and carbon steel data comparison)..... 113

Figure 167. Static immersion test results for the SRNL coupons (4 M solution details of mass changes). ..... 114

Figure 168. Sample COMSOL simulations for particle erosion (left) and detailed particle trajectories (right)..... 116

Figure 169. Branched pipe geometry. ..... 117

Figure 170. FEA mesh of the pipe model. ..... 117

Figure 171. Velocity flow field with cut planes normal to the flow direction..... 118

Figure 172. Velocity flow field depicting the split in flow due to pipe branching. ..... 118

Figure 173. Volumetric representation of flow velocity. ..... 119

Figure 174. Pressure distribution in the pipe material. ..... 119

Figure 175. Pipe geometry for turbulent flow simulation..... 120

Figure 176. FEA mesh of the pipe model. ..... 121

Figure 177. Convergence plot of velocity, pressure, and turbulence variables. ..... 121

Figure 178. Velocity flow field with curved streamlines due to turbulence. ..... 122

Figure 179. Velocity slice plot. ..... 122

Figure 180. Pressure distribution in the pipe. ..... 123
Figure 181. Wall resolution (surface) in viscous units indicating the mesh refinement accuracy. ..... 123
Figure 182. Pipe geometry for turbulent flow and particle tracing simulations. ..... 124
Figure 183. Particle erosion using CFD in a pipe with turbulent flow conditions showing particle trajectories. ..... 125
Figure 184. Simulation of the surface erosion rate using the DNV erosion model. ..... 125
Figure 185. Simulation of the surface erosion rate using the ECRC erosion model. ..... 126
Figure 186. Simulation of the surface erosion rate using the Finnie erosion model. ..... 126
Figure 187. Pipe flow results – velocity contours (left) and shear stress (right). ..... 127
Figure 188. Flow through an elbow - velocity flow lines (left) and pressure distribution (right). ..... 127
Figure 189. Flow through an expander-reducer – velocity lines (left) and total pressure (right). ..... 128
Figure 190. Pipeline flow results – flow path lines. ..... 128
Figure 191. Pressure distribution due to the flow in the pipeline with bends and expander-reducer sections. ..... 129
Figure 192. Wall shear stress distribution in the pipeline with bends and expander-reducer sections. ..... 129
Figure 193. Pipe section – CAD model (left) and FE mesh (right). ..... 130
Figure 194. Surface pressure and velocity distribution (left) and total flux as streamlines (right). ..... 131
Figure 195. Velocity slice plots depict distribution along the longitudinal and radial directions. ..... 131
Figure 196. Erosion loop CAD model (left) and Finite Element Mesh (right). ..... 132
Figure 197. Erosion loop flow (laminar) with surface velocities (left) and critical section detailed surface velocity (right). ..... 132
Figure 198. Surface velocity variation at the reducer (left) and at the second elbow (right). .... 132
Figure 199. Pressure variation in the loop (left) and surface velocity variation at the bend (right) under turbulent flow conditions. ..... 133
Figure 200. Surface velocity variation at the bend (left) and at the T-section (right) for the erosion loop. ..... 133
Figure 201. Convolutional neural network composed of single 2DConv layer per block. ..... 134
Figure 202. Convolutional neural network composed of two 2DConv layers per block. ..... 134
Figure 203. Algorithm parameters for anomaly detection. ..... 135

Figure 204. Anomaly detection of corroded and non-corroded surfaces of the sample coupons. ..... 136
Figure 205. Anomaly score and histogram of outliers for the corrosion model. ..... 136
Figure 206. Machine Learning framework (left) and Convolutional Neural Network (CNN) Architecture for Corrosion Classification. ..... 137
Figure 207. Comparison of the inside of unaged and aged HIHTL specimens. ..... 140
Figure 208. X-Ray Diffraction (XRD) analysis results from the 12.5% NaOH specimens. ..... 141
Figure 209. X-Ray Diffraction (XRD) analysis results from the 25% NaOH specimens. ..... 142
Figure 210. Baseline hose sodium penetration scan results. ..... 143
Figure 211. Scan results of 25% NaOH hose specimen. ..... 143
Figure 212. Scan results of 12.5% NaOH hose specimen. ..... 144
Figure 213. Scan results of 6.25% NaOH hose specimen. ..... 145
Figure 214. Map scan results of 25% NaOH hose specimen. ..... 146
Figure 215. Map scan results of 12.5% NaOH hose specimen. ..... 146
Figure 216. Scan results of 6.25% NaOH hose specimen. ..... 146
Figure 217. Quincy Lab Analog Oven Model 30. ..... 147
Figure 218. Stainless steel pan. ..... 148
Figure 219. ¼” stainless steel half-round rod. ..... 148
Figure 220. EPDM squares cut from a 3/16” sheet. ..... 148
Figure 221. EPDM specimens after removal from aging vessel. ..... 149
Figure 222. Solution level gauge. ..... 149
Figure 223. Level gauge being used on a vessel. ..... 150
Figure 224. Baseline (unaged) sodium ion count results. ..... 150
Figure 225. Sodium ion count results after 1 week of aging in 6.25% NaOH solution. ..... 151
Figure 226. Sodium ion count results after 1 week of aging in 12.5% NaOH solution. ..... 151
Figure 227. Sodium ion count results after 1 week of aging in 25% NaOH solution. ..... 151
Figure 228. Sodium ion count results after 9 weeks of aging in 6.25% NaOH solution. ..... 152
Figure 229. Sodium ion count results after 9 weeks of aging in 12.5% NaOH solution. ..... 152
Figure 230. Sodium ion count results after 9 weeks of aging in 25% NaOH solution. ..... 152
Figure 231. Test setup for coatings exposure to acid solutions. 1. acrylic tube with acid solution, 2. coating (brown color) covering the top surface of the sample, 3. concrete sample. ..... 158
Figure 232. Images of top view of Sherwin-Williams-coated samples, with (ST1-1, ST7-1) and without (ST3-2, ST5-1) surface preparation, before and during accelerated aging. ..... 161

Figure 233. Average thickness of selected coated samples, with (ST1, ST7) and without (ST3, ST5) surface preparation during accelerated aging. Group 1 (ST1 - ST4) and Group 2 (ST5 - ST8)..... 162

Figure 234. Bode plot comparison graph for selected coated samples with (ST1) and without (ST3) surface preparation of group 1. ..... 163

Figure 235. Bode plot comparison graph for selected coated samples with (ST7) and without (ST5) surface preparation of group 2. ..... 164

Figure 236. Comparative images of the top view of Belzona-coated specimens with rebar, with (BT1-1, BT7-1) and without (BT3-1, BT5-1) surface preparation, before and after aging conditions. ..... 165

Figure 237. Bode plot comparison graph for selected coated samples with (BT1) and without (BT3) surface preparation. ..... 167

Figure 238. View of the potentiostat, the Faraday Cage and computer (left image) used for electrochemical measurements. Zoom of the experimental setup (right image). ..... 171

Figure 239. Nyquist (left) and Bode (right) plots for the 304 stainless steel canister material exposed to Solution 1 and Solution 2 at different immersion times. ..... 174

Figure 240. Potentiodynamic graphs for 304 stainless steel canister material when immersed in simulated Hanford groundwaters, solution 1 (top) and solution 2 (bottom)..... 175

Figure 241. Nyquist (left) and Bode (right) plots for the 316 stainless steel canister material exposed to Solution 1 and Solution 2 at different immersion times. ..... 176

Figure 242. Potentiodynamic graphs for 316 stainless steel canister material when immersed in simulated Hanford groundwaters, Solution 1 (top) and Solution 2 (bottom). ..... 177

Figure 243. Images of the 304 stainless steels before (reference) and after the potentiodynamic test in Solution 2 at different magnifications. Top images for the reference sample and bottom images for the sample after test. ..... 178

Figure 244. Images of the 316 stainless steel before (reference) and after the potentiodynamic test in Solution 2 at different magnifications. Top images for the reference sample and bottom images for the sample after test. ..... 179

# LIST OF TABLES

Table 1. Flush-to-Line Volume Ratio Results, One-Day Sedimentation ..... 14
Table 2. Flush-to-Line Volume Ratio Results – Extended Settlement ..... 14
Table 3. Powertrain gearbox material properties ..... 43
Table 4. Prismatic Joint Actuator Selection ..... 52
Table 5. Vickers Hardness Test Results for Erosion Coupon 1 ..... 83
Table 6. Vickers Hardness Test Results for Erosion Coupon 2 ..... 83
Table 7. Vickers Hardness Test Results for Eroded Coupon (No Surface Preparation) ..... 85
Table 8. Vickers Hardness Test Results for Eroded Coupon (with Surface Preparation) ..... 85
Table 9. Results of Particle Erosion Experiment 1 ..... 88
Table 10. Results of Particle Erosion Experiment 2 ..... 88
Table 11. Results of Particle Erosion Experiment 3 ..... 88
Table 12. Pipe Degradation Experiment (Pre-Test Thickness) ..... 95
Table 13. Pipe Degradation Experiment (Post-Test Thickness) ..... 96
Table 14. Coupon Erosion with UT Measurements ..... 97
Table 15. Coupon Weights - Post Extraction from the Loop ..... 98
Table 16. SRNL Coupon Mass and Thickness Results Under Post-Test Conditions (Erosion Testing) ..... 98
Table 17. Coupon Visual Inspection (Internal and External Images) for Post-Test Conditions .. 99
Table 18. Caustic Simulants and Proportions for 6M Salt Solution Preparation ..... 105
Table 19. SRNL Coupon – Baseline Conditions Prior to 6M Simulant Testing ..... 106
Table 20. Mass Loss in Coupons due to Static Corrosion ..... 111
Table 21. Thickness Change in Coupons due to Static Corrosion ..... 111
Table 22. Test Plan for Accelerated Aging of Coatings ..... 155
Table 23. Potential Coatings for the Accelerated Aging Tests ..... 156
Table 24. Measurements to Evaluate Coating Behavior ..... 159
Table 25. Average thickness and average thickness loss of Belzona coating with rebar ..... 166
Table 26. Test Plan ..... 170
Table 27. Candidate Materials Type for Canister/Container and Reason ..... 170

# PROJECT 1 EXECUTIVE SUMMARY

The Department of Energy's (DOE's) Office of Environmental Management (EM) has a mission to clean up the contaminated soils, groundwater, buildings, and wastes generated over the past 60 years by the R&D and production of nuclear weapons. The nation's nuclear weapons complex generated complex radioactive and chemical wastes. This project is focused on tasks to support the safe and effective storage, retrieval, and treatment of high-level waste (HLW) from tanks at Hanford and Savannah River-sites. The objective of this project is to provide the sites with modeling, pilot-scale studies on simulated wastes, technology assessment and testing, and technology development to support critical issues related to HLW retrieval and processing. Florida International University (FIU) engineers work directly with site engineers to plan, execute, and analyze results of applied research and development. In addition, efforts focus on addressing waste disposal challenges at the sites and issues related to preserving the structural integrity of the H-Canyon Exhaust Tunnel at Savannah River.

DOE Fellows supporting this project include Brendon Cintas (graduate, Ph.D., Mechanical Engineering), Bryant Pineda (graduate, M.S., Mechanical Engineering), David Rojas (undergraduate, Mechanical Engineering), Desmond Sinnott (undergraduate, Mechanical Engineering), Douglas Baptiste (Undergraduate, Civil Engineering), Gabriel Cerioni (Graduate, M.S., Mechanical Engineering), Joel Adams (graduate, Ph.D., Mechanical Engineering), Josue Estrada Martinez (graduate, M.S., Mechanical Engineering), Nicholas Espinal (undergraduate, Mechanical Engineering), Philip Moore (graduate, M.S., Mechanical Engineering), Rafael Velasquez (Undergraduate, Electrical Engineering), Sebastian Story (graduate, M.S., Mechanical Engineering) and Theophile Pierre (undergraduate, Mechanical Engineering).

The following ARC researchers are supporting this project and mentoring the DOE-EM Fellows: Dwayne McDaniel (Ph.D., Engineering Mechanics, Project Manager), Anthony Abrahao (M.S., Mechanical Engineering, Task 18.4, 18.5, Task Manager), Amer Awwad (M.S., Mechanical Engineering, Task 19.2, Task Manager), Aparna Aravelli (Ph.D., Mechanical Engineering, Task 19.1, Task Manager), Jose Rivera (B.S., Civil Engineering, Task 19.2, Research Analyst), Mackenson Telusma (M.S., Mechanical Engineering, Task 18.3, Task Manager), Mayren Echeverria (Ph.D., Chemical Engineering, Task 20, Task Manager), Leonel Lagos (Ph.D., PMP®, Mechanical Eng./Civil/Env. Engineering, PI).

Although several tasks have been initiated and completed over the course of the cooperative agreement, at the end of this past year, there were 4 active tasks. These tasks are listed below, and this report contains a detailed summary of the work accomplished for FIU's Performance Year 3.

### Task 17: Advanced Topics for HLW Mixing and Processes

In the U.S. Department of Energy's (US DOE) Savannah River Site (SRS) and Hanford site, systems of pipelines transport high-level radioactive liquid waste for waste processing and storage. After transporting the waste, the lines are flushed with water to ensure that no sludge or sludge solid sediments remain in the transfer line. Current guidelines that establish a minimum flush volume and flush water velocity required for post-transfer flushing operations to achieve a satisfactory cleanliness exist; however, the Defense Nuclear Facilities Safety Board (DNFSB) indicated a need for further investigation on the technical basis for the prescribed guidelines. Consequently, further studies that will assist SRS and Hanford in waste remediation are being done

to optimize the operational conditions. This optimization would minimize the flush volume and consequent downstream waste, which ultimately would assist in preserving tank storage, preventing secondary waste processing, and minimizing changes to the waste's chemistry and rheology.

To perform these investigations, an expandable, 3-inch carbon steel experimental pipe loop was designed and constructed at Florida International University (FIU) to simulate flushing operations of non-Radioactive slurries. The test loop was designed to simulate sediment beds of solid materials and bed heights to investigate what parameters affect the efficiency of flushing operations at various concentrations. Testing was then conducted using non-Radioactive kaolin-water slurry simulants at various concentrations with various flush volume and flush modes to determine the effect of flush volumes for each configuration. These concentrations offer repeatability within the sediment beds inside the pipeline for fully flooded and gravity-drained conditions with one day, one week, and two-week sedimentation. By parametrizing the sediment height and conditions, the flush volume and flush velocity values could be optimized, which leads to satisfactory cleaning of transport lines of varying length with a minimal use of flush water.

This report presents the latest efforts in flush analyses to determine the efficiency of flushing operations. The test matrix with the various configurations for the first expansion of the test loop at 330 feet has been completed and presented in this report. This data, which approximates a flush-line volume ratio (FTLV) for fully flooded and gravity-drained conditions with one day, one week, and two-week sedimentation at a range from 2.48 to 3.08, will be compared to the results from the 165 feet loop to assess any trends with the longer pipe length. Additionally, engineers at Savannah River have requested that we alter the plan for expanding the loop to longer lengths, to assist in understanding how much slurry volume is needed to resuspend settle solids after a transfer has already occurred.

**Task 18: Technology Development and Instrumentation Evaluation**

Scientists and engineers from the Hanford and Savannah River sites are constantly evaluating innovative technologies to alleviate the operational issues related to inspecting, sampling, and repairing aging nuclear infrastructure and tanks containing highly radioactive nuclear waste. In close collaboration with WRPS and SRNL, the Applied Robotics Laboratory at FIU has developed and deployed several specialized robotics tools tailored to the needs of the Hanford and Savannah River sites.

In collaboration with SRNL, FIU has developed a wall-crawler system (Subtask 18.3) to evaluate the H-Canyon exhaust tunnel for degradation and potentially apply a protective coating. The H-Canyon is America's only remaining chemical processing facility capable of reprocessing plutonium, highly enriched uranium, and other radioactive materials. Robotic inspections of the facility's exhaust tunnel revealed significant degradation of the reinforced concrete structure, primarily associated with acid attack compromising the tunnel's structural stability. Applying a protective coating on the degraded tunnel walls could mitigate and prevent further deterioration. During this performance period, vectored thrust capabilities were integrated into the wall-crawling platforms, the onboard electronic package footprint was minimized in the five-fan wall-crawling platform, and using an IMU, current, and temperature sensor, the platforms' semiautonomous control was also improved.

In collaboration with WRPS, FIU has investigated mobile robotic platforms (Subtask 18.4) and state-of-the-art field-deployable sensory suitable for emergency first response, surveying, and

long-term monitoring. Continuous surveillance of nuclear facilities and repositories is critical in successfully controlling and understanding radiological environmental impact, planning cleanup efforts, and meeting quality assurance objectives established by the U.S. Department of Energy standards and guidelines. When surveying nuclear facilities and repositories, advanced mobile surveillance systems are safe, efficient, and labor-saving tools that safely deploy state-of-the-art instrumentation without exposing workers to radiation risks. Given the large size of many facilities, the high cost of radiation sensors, and the nature of radiological sources, mobile systems provide a cost-effective solution versus on-site sensor networks or monotonous routine measurements performed by site personnel. During this performance period, the team further improved the robust navigation, radiation mapping, digital twin capture, and reconstruction of FIU's surveillance robots. During the summer, an FIU's all-terrain ground robot was successfully deployed at WRPS's Cold Test Facility, demonstrating potential uses of mobile robotic platforms to automate above-ground routine operations and possibly assist first responders at tank farms. The deployment lessons learned and WRPS engineers' feedback guided the technology development at FIU, which will be redeployed at Hanford in the summer, demonstrating new features requested by WRPS's technicians.

In another collaboration with WRPS, FIU has developed several specialized inspection tools (Subtask 18.5) tailored to single-shell and double-shell tanks. The effort is part of the WRPS's Engineering and the Chief Technology Officer (CTO) partnership with FIU to develop technologies to alleviate operation burdens at Hanford's tank farms. During this performance period, sampling capability was successfully incorporated into the miniature rover (Subtask 18.5.1). The system improvements will continue with the objective of redeploying at Hanford to retrieve sample material under the DSTs in 2025. The lateral gamma scanner (Subtask 18.5.2) was successfully demonstrated and tested for the second time at Hanford's Cold Test Facility. The system streamlining will continue, and the gamma radiation sensor integration will be finalized. The discussions regarding a possible 2024 deployment of the LGS at Hanford's tank farm will continue with WRPS. An off-riser sampler system (Subtask 18.5.3) prototype will be finalized and demonstrated at Hanford's Cold Test Facility during the upcoming summer. The team will continue streamlining the pneumatic arm's components, resume designing a deployment cable hoist system, and start implementing a stabilization mechanism.

Finally, in collaboration with SRNL, FIU researched in-situ 3D printer techniques (Subtask 18.5.4) to dispose of and contain nuclear waste in concrete structures. Radiation containment for short-term storage is vital in protecting health and the environment from damage. Current storage of nuclear wastes relies on standard-size metal containers. Irregular or large objects generally occupy precious volume. Implementing 3D printing with concrete tailored to absorb radiation will help reduce wasted volume, potentially alleviating operational burdens. During this performance period, the task investigated potential 3D printer and nozzle designs to build prototypes and optimize concrete recipes and processes suitable for nuclear waste containment. The research collaboration will continue exploring different mixes and optimized processes in conjunction with the DOE Fellow's summer internship, resuming his research at SRNL in the summer.

**Task 19: Pipeline Integrity and Analysis**

Structural integrity of non-metallic materials is being investigated under the current research work. Nonmetallic materials used in the Hanford Site Tank Farm waste transfer system include the inner primary hoses in the hose-in-hose transfer lines (HIHTLs), Garlock® gaskets, ethylene propylene diene monomer (EPDM) O-rings, and similar other nonmetallic materials. These materials are

exposed to radiation, caustic solutions and elevated temperature and pressure stressors. While the individual effect of these stressors has been well established, their combined effect is of significance to the Hanford site. FIU has been supporting this task by developing a test loop and testing the non-metallic materials under simultaneous stressor exposures.

The objective of this task is also to provide the Hanford Site with data obtained from experimental testing of the hose-in-hose transfer lines, Teflon® gaskets, EPDM O-rings, and other nonmetallic components used in their tank farm waste transfer system under simultaneous stressor exposures. The experiments will be limited to various combinations of simultaneous stressor exposure to caustic solutions, high temperatures and high pressure. Evaluation of baseline materials will be conducted for comparison to materials that have been conditioned with the various simultaneous stressors.

Previous testing included aging of HIHTL and EPDM dog-bone specimens at various concentrations of NaOH as well as water only at the elevated temperatures. Four test loops were developed at FIU allowing for the aging of HIHTL as well as dog-bone specimens utilizing 6.25%, 12.5% and 25% v/v NaOH and only water respectively at 170°F. After the exposure, the material properties of the specimens were measured and compared to the baseline (unaged) samples. Material properties evaluated included the tensile strength of the EPDM dog-bone samples and the burst pressure of the HIHTL. Both the tensile strength of the EPDM dog-bone samples and the burst pressure of the HIHTL specimens exposed to the 6.25% NaOH solution exhibited the most significant deterioration and those exposed to 25.00% NaOH solution had the least deterioration. Examination of the HIHTL and the EPDM dog-bone specimens with scanning electron microscopy showed that the deterioration for the specimens exposed to 6.25% NaOH solution were the most severe and the samples exposed to 25.00% NaOH solution had the least deterioration. Additionally, an interesting observation was made regarding a white material coating the inner surface of the HIHTL hoses after aging with different concentrations of NaOH solutions. It was found that the HIHTL aged with only the higher concentrations (12.50% and 25.00%) of NaOH solutions exhibited this white coating, whereas the HIHTL aged with the 6.25% NaOH solution did not show the same phenomenon. It is thought that at higher concentrations, precipitate forms and emerges from the solution of NaOH, subsequently coating the inside of the hoses. Furthermore, it is suggested that once the hoses are coated with the precipitate, the coating may act as a blocking agent. This blocking effect could potentially hinder or limit the further diffusion of NaOH solution into the EPDM, subsequently reducing the extent of degradation.

In order to obtain a better understanding of what is the white material coating the inner surface of the HIHTL hoses is and its effect on the degradation of the hoses, this phase of testing included XRD analysis of the white material. In addition, to determine the level of NaOH ion penetration into the HIHTL material, SEM-EDX analysis was conducted on specimens cut from the aged HIHTLs. To better understand the formation rate of the white material coating on the inside of the HIHTLs, FIU engineers worked with Hanford personnel to develop an experimental test plan that involved aging EPDM material coupons in sodium hydroxide solutions at concentrations of 6.25%, 12.5% and 25% at 170°F.

This task will provide information that will assist engineers with understanding the wear rates in metal pipes and transfer lines along with the effect of various stressors on nonmetallic components. The research will aid in determining the remaining useful life of both metallic and non-metallic components by establishing more detailed/accurate guidelines and avoiding unexpected failures in transfer lines.

**Task 20: Corrosion Protection and Characterization of EM Infrastructure**

FIU is assisting the Savannah River site engineers with investigations that can assist in the mitigation of degradation of the concrete walls in the H-Canyon exhaust tunnel. The degradation observed could compromise the mechanical strength of the structure. Hence, the search for solutions to mitigate and prevent further degradation is necessary. The identification, evaluation and selection of the best coating candidate that can be applied to the tunnel's degraded concrete walls constitute the main goal of this investigation. The investigation has been divided into different phases: 1) development and evaluation of aged concrete surfaces under accelerated aging conditions, 2) identification and evaluation of potential coatings applied on aged and non-aged concrete under accelerated aging conditions (preliminary results presented in this report) and 3) selection of best coating candidates from research findings.

Previous efforts were focused on the identification and preliminary evaluation of potential coating candidates for the protection of the degraded concrete walls of the HCAEX tunnel. A comprehensive test plan for the evaluation of the coated surfaces was developed and executed including key variables such as 1) surface preparation, 2) aging conditions of the substrate and 3) presence of rebar. Two of the four potential coatings, Carboline and Belzona (without rebar), to protect the degraded tunnel walls, initiated the accelerated aging and evaluation. The accelerated aging of the samples consisted of exposing the top surface to a 0.5M nitric acid solution and erosion.

In this year, Belzona, and Sherwin-Williams coatings, completed the accelerated aging tests and evaluation. Visual inspection, failure analysis, thickness and impedance measurements results showed slower degradation for the coating systems compared with the single coating. The degradation of the coatings was characterized by color change, loss of coating particles and in some cases, detachment of some coarse aggregates. The coating systems showed the highest impedance values indicative of good-excellent protective properties. In general, coated samples with surface preparation depicted less thickness loss. The reduction of thickness over time, for all tested coatings, indicated degradation and loss of protective properties. The erosion of the surfaces played a key role in the degradation of the coatings.

FIU is also working on a new task with the Hanford Site. A current challenge for DOE and relevant DOE sites is to understand the durability of the steel canisters/containers that will contain low-activity waste (LAW) and secondary waste forms, encapsulated in glass and grout respectively, and that will be placed within the Integrated Disposal Facility (IDF) at Hanford. Currently, corrosion data of the steel and weld regions of the canisters at Hanford that is exposed to groundwater is limited. In addition, there is limited information on groundwater in contact with waste forms. The primary technical need is to study the corrosion rate of the steel canister's exterior that is exposed to Hanford groundwater and determine how well it shields the waste form that is inside the canister from exposure. During this year, efforts were concentrated on completing the evaluation of 304 and 316 stainless steels in contact with a Hanford simulated groundwater solution through electrochemical measurements. For comparative purposes, another solution containing only the chloride ions of the previous recipe was also used. Electrochemical measurements were conducted including corrosion potential (Ecorr), potentiodynamic polarizations (PDP) and impedance in the two different Hanford groundwater solutions. Corrosion data such as corrosion and current potential were obtained from Tafel slopes. It was also observed the effect of chloride ions on pitting corrosion through the analysis of the potentiodynamic graphs.

# MAJOR TECHNICAL ACCOMPLISHMENTS

**Task 17: Advanced Topics for HLW Mixing and Processes**

- FIU presented 5 professional track posters and oral presentations based on Project 1 research results at the WM2023 Symposia in Phoenix in March 2023.
- The test matrix that was defined for the 330 ft flushing loop, was completed. This included completing tests for the 20% solids one day sedimentation and 10% one-week sedimentation.
- Results from the flushing trials indicated flush volume line ratios between 2.48 and 3.08 were needed for the various trials.
- After the WM2023 conference engineers from Savanah River Solutions approached FIU to see if the flushing loop could be used to test the resuspension of settled solids with a slurry as opposed to the typical flushing approach with water. This requires stopping the expansion of the loop and potential modification of the test loop to accommodate the new request. In addition, the goal would be to understand how much volume of slurry would be needed to resuspend the settled particles but not completely clear the loop.

**Task 18: Technology Development and Instrumentation Evaluation**

- The first DOE, FIU, and Washington River Protection Solutions (WRPS) Technology Development Collaboration Meeting was hosted at FIU on February 7 and 8, 2023. Officials from the DOE-EM TD Office, WRPS, Central Plateau Engineering, Savannah River National Laboratory, and the US Army Corps of Engineers attended the meeting.
- Six professional track posters and oral presentations based on Project 1 research results were presented at the WM2023 Symposia in Phoenix, AZ in March 2023.
- Four DOE Fellows continued researching their FIU robotic projects at SRNL and WRPS during their summer internships.
- The wall-crawler systems were improved, vectored thrust capabilities were integrated, the onboard electronic package footprint was minimized, and the platforms' semiautonomous control was improved, fusing sensors from IMU, electrical current, and temperature.
- FIU’s in-house autonomous mapping and surveillance was enhanced and expanded to legged robots.
- An all-terrain ground robotic platform was successfully deployed at WRPS's Cold Test Facility, demonstrating potential uses of mobile robotic platforms to automate above-ground routine operations and possibly assist first responders at tank farms.
- Sampling capabilities were successfully prototyped into the magnetic miniature rover.
- The lateral gamma scanner system was successfully demonstrated and tested for the second time at Hanford's Cold Test Facility, and discussions regarding a possible 2024 deployment at Hanford's tank farm ware started with WRPS.

- A pneumatic joint for the off-riser sampler manipulator was successfully designed, prototyped, and tested.
- In-situ 3D printer techniques to dispose of and contain nuclear waste in concrete structures were investigated, a printer and a nozzle were designed, prototyped, and tests started. Cost-effective concrete mixes were also explored based on SRNL recipes and available local sources.

**Task 19: Pipeline Integrity and Analysis**

- Previous year's research results showed that after aging HIHTL as well as EPDM material coupons for 1 year at 170°F with three concentrations of NaOH (6.25, 12.5 and 25%), the greatest degradation occurred at the lowest concentration of NaOH. This year's research focused on understanding why this phenomenon occurred.
- SEM-EDX analysis of the aged specimens revealed that the penetration depth of sodium ions was 60% and 70% greater in the specimens aged with 12.50% and 6.25% NaOH solutions, respectively, compared to the specimen exposed to the 25.00% NaOH solution. This indicates that the specimens aged with the lower concentration solutions had the greatest sodium ion penetration and thus the greatest degradation.
- White crystalline deposits were observed on the interior of the dry HIHTL specimens aged with the highest NaOH solutions (25.00% and 12.50%), while no such deposits were found on the specimens exposed to the 6.25% solution. Through XRD analysis, these deposits were identified as Thermonatrite, a mineral form of sodium carbonate ($Na2CO3{\cdot}H2O$). The presence of Thermonatrite appears to have acted as a barrier, restricting the further diffusion of NaOH solution into the EPDM material, subsequently reducing the extent of degradation.
- Experiments were conducted to determine the Thermonatrite rate of formation. An experimental test plan that involved aging EPDM material coupons in sodium hydroxide solutions at concentrations of 6.25%, 12.5% and 25% at 170°F for a 9-week period. One coupon was removed every week from each solution. After the 9-week aging period, a total of 27 coupons were collected and were analyzed using SEM-EDX analysis to determine how far sodium ions had penetrated into the EPDM material. Results did not show a significant increase in ion penetrations between the coupons aged for 1-week and those aged 9-weeks. This indicated that the 9-week maximum aging period was not enough time to allow the sodium hydroxide to penetrate the EPDM material.
- Findings from previous year's research were published in the *Engineering Failure Analysis Journal* titled, "Effect of solution concentration on ethylene propylene diene monomer (EPDM) nonmetallic components used in caustic liquid waste transfer lines".

**Task 20: Corrosion Protection and Characterization of EM Infrastructure**

- FIU presented an oral presentation and a poster with some research results of the tasks at the WM2023 Symposia in Phoenix, Arizona.
- Two potential coatings (coating systems and single coats) for the protection of the tunnel concrete walls were evaluated.

- Belzona-coated samples with rebar initiated the accelerated aging and evaluation.
- Sherwin Williams-coated samples completed the accelerated aging and evaluation.
- Impedance measurements supported the evaluation of the coating's protective properties.
- Completed the evaluation of 304 and 316 stainless steels exposed to simulated Hanford groundwater solutions.
- Corrosion parameters such as corrosion potential, corrosion current and corrosion current density were obtained from Tafel slopes and calculations.
- Completed a preliminary surface characterization of the samples before and after testing using optical microscopy.
- Evaluated the effect of chloride ions in a simulated Hanford groundwater solution on the corrosion behavior of 304 stainless steel and 316 stainless steel canister materials.

# TASK 17: ADVANCED TOPICS FOR HLW MIXING AND PROCESSES

## Subtask 17.2: Evaluation of Pipeline Flushing Requirements for HLW at Hanford and Savannah River Site

### Subtask 17.2: Introduction

US DOE sites within the DOE-EM complex, though especially at Savannah River Site's (SRS) Defense Waste Processing Facility (DWPF) and Hanford's Direct-Feed Low-Activity Waste (DFLAW) and Waste Treatment and Immobilization Plant (WTP) are prescribed recommended flushing parameters that establish a minimum flush volume and flush velocity of water required to ensure proper cleaning. This prescription ensures that the pipelines that transfer the high-level radioactive waste are flushed without the solids eroding the pipe, and to also ensure that the post-transfer flushing operations result in a satisfactory cleanliness of the pipes, where there are no residual solids remaining inside the pipeline post-flush. The Defense Nuclear Facilities Safety Board (DNSFB) has indicated a need for vigorous investigation on the technical basis for prescribing flush velocity in pipelines to determine the optimal performance at the Department of Energy sites. The DNFSB justifies this need because transfer of the waste must be operated at a critical velocity of fluid flow to: (a) prevent residual formations from solids sedimentation within the pipe bed and (b) ensure that during the transfer operation, the insoluble solids within the sludge waste do not erode the pipe walls. Additionally, the correct amount of water is used to effectively clean the pipeline without producing surplus secondary waste that would also need to be treated. If flushed improperly, partial, or full granular plugs and H-gasses can build up, which result in process upsets, costly delays and potential need for line repair or line abandonment, equipment overloads, or possible destruction of equipment such as a rupture at the pump or within the pipeline [4]. The pretreatment facility design strategy requires that each slurry transfer in the process lines be followed by a flush with water to minimize the chances of a partial or full line plug.

Several studies were done to determine the current prescribed flushing guidelines at Pacific Northwest National Laboratory (PNNL) at the Hanford Site. These studies revealed that the minimum required flush volumes were more than the minimum required values provided by certain design guidelines. The flush velocity that was recommended for a slurry up to 30 Pascals of yield stress is 10 ft/sec to adequately flush the system. Flush velocities in the pipeline exceeded the maximum velocity stated in the flushing guidelines [1] that ensure that the interior of the pipeline does not erode due to the solid particles within the slurry that are agitated during transfer and flushing. In the same study, it was demonstrated that "a flush-to-line volume (FTLV) ratio of 3 was needed to remove the sediment bed whereas design guide provides a minimum flush-volume ratio of 1.7" [2]. From the design guidelines and the study, the prescribed minimum is 1.7 times the volume of the pipeline (an FTLV of 1.7), whereas the actual flush volumes to ensure cleanliness were closer to nearly triple the FTLV.

At Florida International University's – Applied Research Center (FIU-ARC), investigations to determine effective flushing operations using a minimal amount of water and to provide additional guidelines in support of recently developed flushing standards indicated by TFC-ENG-STD-26 [3] have been underway. Effective execution of the work requires creation and characterization of sediment beds and their solids concentrations, flushing in different modes, and evaluation of operation effectiveness through post-flush sampling. To extend previous flushing studies, the focus was to create different case studies targeting different materials and pipe lengths. Focus was on

influential parameters set for one simulant in a fixed pipe length for each round of testing. These parameters include varying the initial conditions of the sediment such as the concentration of the solid and its corresponding settlement height, settlement time of one day and one-week flush operation (fully-flooded and gravity-drained).

## Subtask 17.2: Objectives

The objective of this effort is to provide a technical basis for flush volume used in the waste transfer process. This includes:

- Implementing optimal flush operations that minimize waste production, pipeline erosion, and ensure satisfactory cleaning of pipelines based on an established criterion for thorough discussions between FIU and personnel at the waste sites and national laboratories.
- Developing a correlation for flush parameters based on characteristics of the system at the start of flushing (initial conditions). Data and correlations will be useful for determination of pumping requirements improving existing guidelines.

## Subtask 17.2: Methodology

The experimental set up consists of a test loop composed of 3-inch schedule 40 carbon steel pipes and fittings (Figure 1). This test loop can perform various functions such as slurry circulation, pump cleaning, flushing, sediment and water retrieval, and post-flush circulation. The pipeline was sloped at the rate of 0.15% (to emulate conditions at Hanford Site and facilitate gravity draining) [5]. A 15 HP centrifugal pump controlled by a variable frequency drive (VFD) is used to circulate the simulant, flush with water, and conduct post-flush analyses. The fluid level, flow speed, and fluid density are monitored using sensors – the VEGAPULS 11 radar sensor and the Krohne Optimass 1000 Coriolis meter, respectively - that report the status of these parameters in real time.

**Figure 1. Major components for flushing experiments.**

Several changes were made to the flushing loop to implement the first phase of the loop expansion from 165 feet to 330 feet of length without altering the general configuration of the loop, as shown in Figure 2 and Figure 3. To expand the loop, the ninety-degree intersection was temporarily removed, and eight 20-foot sections (four per side) were added. After ensuring each 20-foot section was at the correct slope to simulate the elevation changes at Hanford and SRS' transfer lines, the ninety-degree section was replaced.

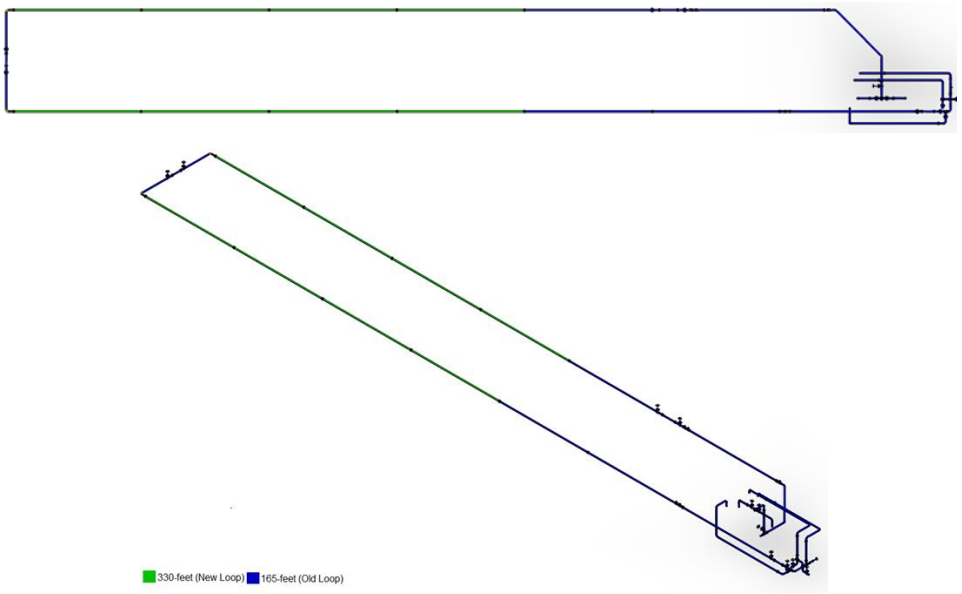


**Figure 2. CAD model of the updated 330-foot flush loop.**

**Figure 3. Constructed 330-foot extension used for flushing.**

### Improvements to Data Analysis

Previously, code logic was implemented to approximate the FTLV by inspecting the dataset and determining when the density curve reaches a steady state. These improvements to the code logic determined the rate of change of the density curve (its slope value). When the code was initially written, it was tested using controlled data sets and preliminary results of 'accepted' data from the flushing loop in which a long steady-state was achieved. This performance period focused on further development of the code in which it was tested using the other data sets from fully flooded and gravity-drained conditions. When the code was tested, incidents such as when there was a short steady-state would return an artificially low FTLV value. Additionally, for the fully-flooded data sets, the code erroneously predicted the FTLV where there was little to no change to the density during the intermediate density where it was above the density of water. To address this, a threshold was done where it would only predict the FTLV when the density slope is below the tolerance and the density values were also below a certain level of plus or minus 2% of the density of water.

*Flushing Operation*

EPK kaolin with a 2.65 specific gravity was used in trials with both the gravity-drained and fully-flooded conditions. The test matrix included trials with system loads of 10, 15, and 20% vol of kaolin-water mixtures using a pump frequency of 35Hz to target a flow velocity below 10 ft/s. Tests were performed using two initial conditions: a fully-flooded condition and a gravity-drained condition. In the fully-flooded condition, the test loop was flooded with a simulant of a specified concentration and left to settle for approximately one day after stopping the slurry pump and without any changes to configurations or system environment. After the settling period, water from flush tanks was flushed through the system using the 15HP pump into a 500-gallon collection tank. In the gravity-drained condition, similar to the fully-flooded condition, the test loop was flooded with a simulant of specified concentration and left to settle for one day for nominal testing.

For the 10% gravity-drained condition, studies were also conducted with variable settling times to determine the effect of prolonged sedimentation times on flush volume requirements. In these trials, the gravity-drained condition was created as described above, but the settling time was increased to one and two weeks before being drained, and the test conducted. After the amount of time had passed, a drain valve was opened to remove the water from the settled kaolin, leaving behind a layer of sediment exposed to air within the pipeline. Water was then flushed through the system back into the collection tank.

## Subtask 17.2: Results and Discussion

For this performance period, efforts focused on completing the defined test matrix. This included running trials for the 20% fully flooded and gravity drain cases. In addition, after discussions with engineers at Savannah River, the 10% extended dwell time of 1 week was removed from the text matrix. This was because the 2-week FTLV ratio was low (2.71) and shorter dwell times were not needed.

During the trials, the slurry pump was run long enough to ensure complete flushing, and the data collected was analyzed to determine the actual volume required to clean the system. The calculation of the flush-to-line volume ratio is shown in the next section. For the analysis, the clean condition was determined by the Coriolis meter's density reading (showing approximately the

density of water). Flow quantities such as mass flow rate and density were also recorded using a data acquisition (DAQ) module (NI USB6001) and a PRO-FLO200 totalizer. Results from the completed trials are shown in Figure 4 and Figure 5. The plots show both the density and flow rates verses time for the three concentrations and for each initial condition.

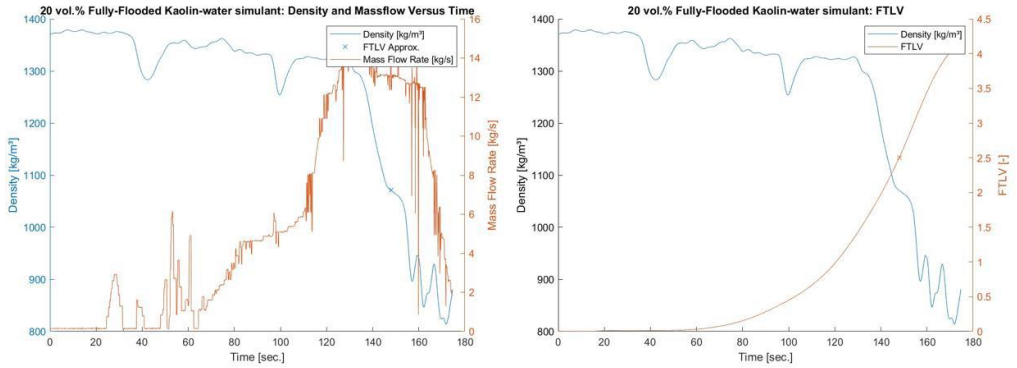


**Figure 4. 20 vol.% Fully-flooded (left), Density and mass flow verses time (right), approximate FTLV.**

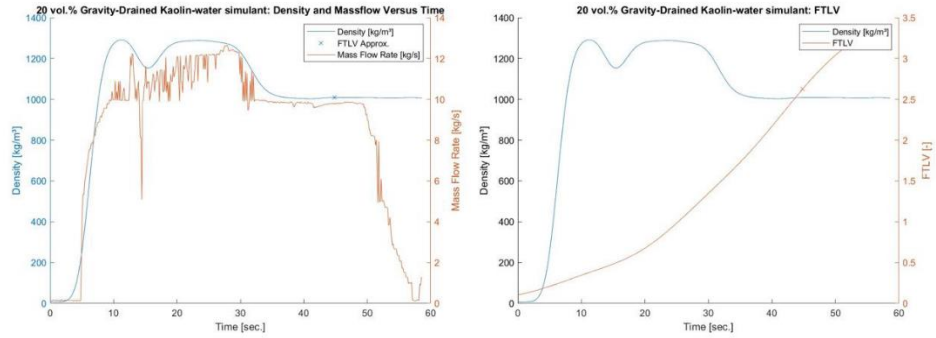


**Figure 5. 20 vol.% Gravity drained (left), Density and mass flow verses time (right), approximate FTLV.**

For the fully-flooded test, the density curve starts above 1,000 kg/m$^3$, and decreases as the particles are removed. For the gravity-drained condition, the density starts at zero and increases as the slurry moves through the meter. When the pipe is flushed, the density again returns to just below or just above 1,000 kg/m$^3$.

*Flush-Line Volume Ratio*

The flush-to-line volume ratio is a ratio of the volume of water being used to flush the line, with respect to the volume of the pipeline.

$$FTLV = \frac{\text{volume used to flush}}{\text{pipeline volume}}$$

In the test loop, the level sensor was installed on the top of the water reservoir tank to monitor the change in volume of the water within the reservoir tank. This parameter was then utilized to determine the volume of water used to flush by detecting a change of water level within the water tank. During the flushing operation, this variable is monitored coincidentally with density and mass flow rate and saved onto a file for analysis via a script. Results (Table 1 and Table 2) show the FTLV ratios determined by the post-processing script for (a) default settlement time and (b) extended settlement. The results in the tables indicate there is no substantial change when varying the solids concentration for the fully-flooded condition. This is likely to do with the separation of

the column of water and the solids; because water is already present, it is possible that this contributes to the resuspension of the solids, removing it from the line faster and therefore not requiring as much water to flush. This is further exemplified with the gravity-drained condition, where the difference between the 10 vol.% and 15 vol.% for gravity-drained tests showed no considerable difference in the amount of water needed to clean the loop; however, when comparing the gravity-drained to fully-flooded – particularly for 15 vol.%, nearly 5% more water is needed to effectively clean the same amount of solids.

**Table 1. Flush-to-Line Volume Ratio Results, One-Day Sedimentation**

| One Day Sedimentation FTLV Results | | |
|---|---|---|
| | Fully Flooded | Gravity Drain |
| **10%** | 2.479 | 2.586 |
| **15%** | 2.544 | 2.617 |
| **20%** | 3.081 | 2.814 |

**Table 2. Flush-to-Line Volume Ratio Results – Extended Settlement**

| 10 vol% Variable Sedimetation Results | |
|---|---|
| One Day | 2.586 |
| 2 Weeks | 2.751 |

## Subtask 17.2: Conclusions

Results were presented that demonstrate flushing of 10% vol and 15% vol concentrations of kaolin-water slurry sediments within a 3-inch diameter, 330-foot pipe loop using fully-flooded and gravity-drained conditions. Results demonstrated that flushing with these conditions required a flush-line volume ratio of approximately 2.5 using data from the Krohne Optimass 1000 Coriolis meter and VEGAPULS11 level sensor. Via post-processing and code logic, the flush-line volumes were determined.

Future work for this research had included expanding the test loop to 495 feet, however, after discussions with Savannah River Solutions engineers, it was requested to redirect this effort. The flushing loop task will next consider how effectively slurry can be used to resuspend settled sediment. In this new direction, efforts will be made to quantify how much slurry is needed to resuspend settled particles after various dwell times in various length pipes. If successful, there is potential for eliminating flushing waste stream in cases where the slurry can be used to flush the pipe.

## Subtask 17.2: References

1. A. Poloski, M. L. Bonebrake, A. M. Casella, M. D. Johnson, P. J. MacFarlan, J. J. Toth, H. E. Adkins, J. Chun, K. M. Denslow, M. L. Luna, J. M. Tingey, “Deposition Velocities of Newtonian and Non-Newtonian Slurries in Pipelines”, PNNL-17639, WTP-RPT-175 Rev. 0, (2009)
2. S. T. Yokuda, A. P. Poloski, H. E. Adkins, A. M. Casella, R. E. Hohimer, N. K. Karri, M. Luna, M. J. Minette, J. M. Tingey, “A Qualitative Investigation of Deposition Velocities of a Non-Newtonian Slurry in Complex Pipeline Geometries”, PNNL-17973, WTP-RPT-178 Rev. 0, (2009)
3. N. Hall, “Minimum Flow Velocity for Slurry Lines”, 24590-WTP-GPG-M-0058, Rev 0 (2006)

4. Kazban, A., “Plugging and Wear of Process Piping at The Waste Treatment and Immobilization Plant”, DNFSB/TECH-40 (2016)

# TASK 18: TECHNOLOGY DEVELOPMENT AND INSTRUMENTATION EVALUATION

## Subtask 18.3: Development of a Coating Deployment Platform for the H-Canyon Exhaust Tunnel

### Subtask 18.3: Introduction

The H-Canyon is the only remaining chemical processing facility in America capable of reprocessing plutonium, highly enriched uranium, and other radioactive materials [1]. The exhaust air flow from the H-canyon chemical processing areas and HB-line is transported through the H-Canyon Exhaust (HCAEX) tunnel, where radioactive contamination is removed. Robotic inspections of the tunnel have revealed significant ongoing degradation of the reinforced concrete structure that was associated with acid attack. The degradation observed could compromise the mechanical strength of the structure. Hence, the search for solutions to mitigate and prevent further degradation is necessary [2-3]. The application of a protective coating on the degraded tunnel walls could mitigate and prevent further degradation, which constitutes the main goal of this investigation. This research effort has been divided into two phases: 1) Development and evaluation of aged concrete under accelerated aging conditions and 2) Evaluation of potential coatings applied on aged and non-aged concrete under simulated aggressive conditions.

In the preliminary stage of the investigation, a comprehensive literature review was performed and major findings included: 1) the characterization of the tunnel degradation conditions, 2) the identification of the chemical attack and erosion as the primary degradation mechanisms affecting the tunnel concrete walls, 3) the identification of the acid-type immersion tests as a well-known method for evaluating the materials' resistance to acid attack and, 4) the preliminary selection of potential coatings for aggressive environments similar to the tunnel [3].

Lessons learned and research findings of the initial testing of concrete in acid solutions supported the development and ongoing execution of a comprehensive test plan that will be presented in this report. The test plan execution is an ongoing task allowing the development and evaluation of aged concrete surfaces, with 1) protruded aggregates, 2) exposed steel rebar, and 3) chemically damaged, similar to the tunnel walls after more than 60 years of operation. The degraded (aged) concrete surfaces were developed through various accelerated aging conditions including the effect of some variables such as acid concentration, erosion, mode of action of the aggressive agent, and the presence of steel rebar [3]. Finally, the developed aged concrete surfaces will be used as the substrate for the evaluation of potential coatings in a further stage of the investigation. Because this is an ongoing investigation, preliminary results of the accelerated aging of concrete specimens will be presented in this report.

Due to the hostile environment of the HCAEX tunnel, the ability to enter the tunnel and perform any type of investigative, or in this case damage mitigation to the concrete walls, have been restricted to the use of robotic platforms equipped with the tools necessary to accomplish said goals. The robotic platform would need to work in tandem with another larger ground platform capable of traversing the difficult terrain of the tunnel. The ground platform would need to deploy the secondary platform onto the concrete walls to apply a down selected coating.

The secondary robotic platform will need to be capable of traversing the HCAEX tunnel concrete walls in a manner that does not further damage the surface of the walls and allows accurate positioning of the platform to apply the coating. A literature review regarding the different methods available that would allow a mobile platform to maintain contact with the walls, regardless of the platform's orientation, will be highlighted in this report.

After developing and testing a single fan-based platform, which creates the appropriate adhesion mechanism, the results obtained from constructing a multi-fan omnidirectional platform will be detailed in this report. The goal of the report will also be to show the viability of the platform as an option to a unit capable of traversing a concrete surface without introducing further damage to the wall's surface and at the same time, maneuvering across the surface to reach a desired location when tele-operated.

### Subtask 18.3: Objectives

The primary objective is to develop a robotic mobile platform capable of traversing vertical walls with varying surface conditions and applying a coating to the walls with the aim of preventing further surface degradation inside the HCAEX tunnel. The aim is to develop a robotic mobile platform capable of traversing vertical walls with varying surface conditions using a thrust based adhesion mechanism [4,5].

A scaled mockup concrete wall will be constructed using the information from Savannah River Site engineers, and the platform will be evaluated for its ability to maneuver along walls with varying surface conditions. The performance of the platform will also be quantified and used as a baseline to compare to future iterations of the platform as improvements are made during the project cycle.

The platform will be equipped with a coating application system which will be developed for the purpose of applying a selected coating to the concrete walls of the HCAEX tunnel. The application system will be designed to be modular in nature so that it can be incorporated into mobile platforms of varying sizes and configurations.

### Subtask 18.3.1: Improvement of Mobile Platform Efficiency

### Subtask 18.3.1: Methodology

A thrust vector unit, Figure 6, consisting of an EDF unit and a gimbal like mechanism was developed and used to control the direction of the generated thrust. A testing apparatus was assembled which included a load cell to measure the force generated by the vectored EDF unit at different angles and servos to actuate the unit at the different pitch and yaw angles. The combination of those angles would have the vectored thrust interact with the wall crawling platform by making use of a force perpendicular and parallel to the platform's motion.

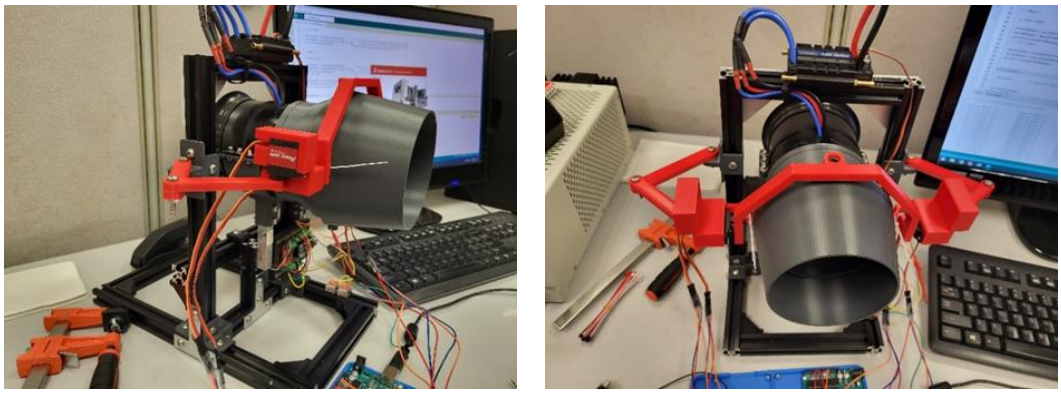

**Figure 6. Vector thrust testing setup.**

Next, the vector units were attached to the dual EDF unit, Figure 7, to test the efficacy of the platform performing transitions and energy consumption during motion along a vertical surface. The addition of vector thrust modules added to the complexity of the controls of the platform since the angel of the directed thrust needs to be adjusted depending on the orientation of the platform during transition changes from horizontal to vertical, vertical motion and vertical to upside-down.

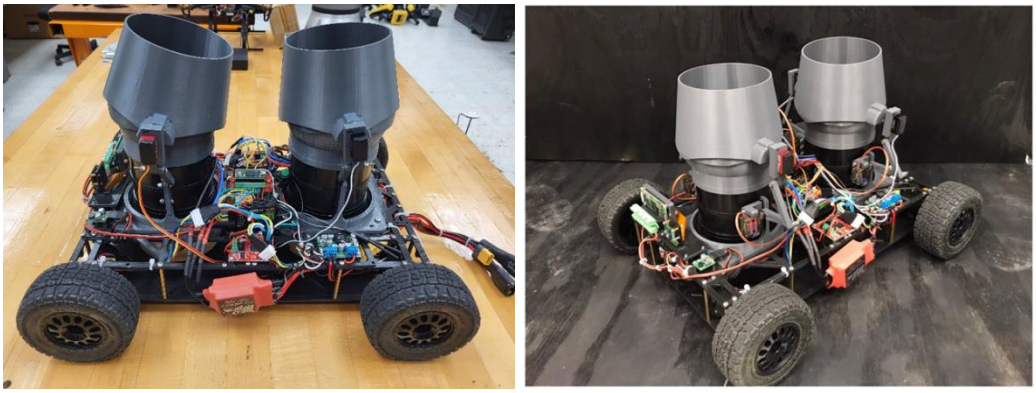

**Figure 7. Dual EDF unit equipped with vector thrust units.**

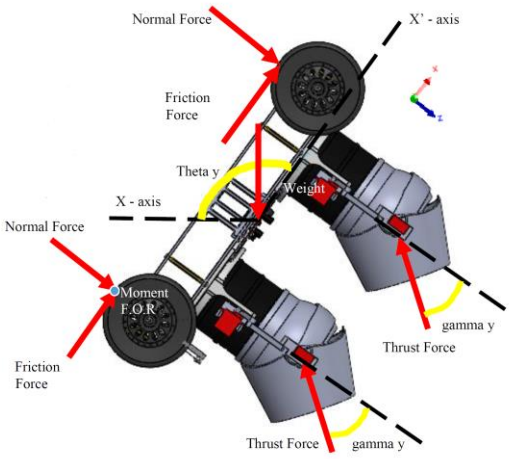


**Figure 8. Free body diagram of vector thrust unit and platform interaction.**

The relationship between the platform's orientation and angle of attack for the vector thrust units was derived using the free body diagram depicted in Figure 8 above. An IMU attached to the center of the platform plays a crucial role measuring the angular changes, specifically roll, pitch and yaw. The corresponding angles are used as inputs to determine the required angle the vector thrust unit needs to be directed to aid the platform in moving along a vertical surface while still creating the required adhesion forces.

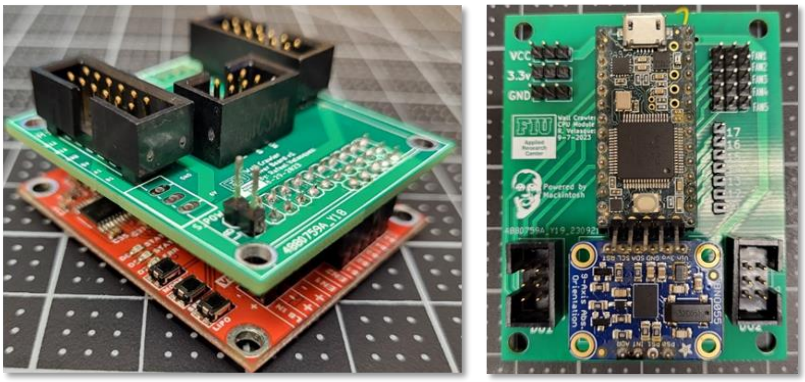

**Figure 9. PCB modules for motor controller, microcontroller and IMU integration.**

Another improvement was the development of the PCB modules that are used on the large EDF platform to minimize the amount of wiring required for communication to the different electronic components on the platform along with increasing the robustness of the electrical layout. The PCB modules consist of the motor controller module, servo PCB module and a microcontroller and IMU module. Two of which are depicted above in Figure 9. The ability to ingrate the electronic package onto a more configurable package makes the entire setup very modular and creates an easier layout for troubleshooting.

**Figure 10. Small-scale wall mockup.**

Finally, a small-scale mockup, Figure 10, was constructed with the idea of having a modular testbed which can be used for rapid testing of the different wall crawling platforms. The rapid testing would aid in providing data to improve the overall performance of the mobile platforms while transitioning and moving along a surface at different orientations.

## Subtask 18.3.1: Results and Discussion

The vector thrust unit was tested using a test setup that was developed and assembled in-house, which measured the thrust generated by the unit at different angles. Figure 11, shows the measured load from the load sensor, which falls in line with the observation of the thrust being restricted due to the small exit diameter of the vectored nozzle. For this setup, a maximum thrust of 2.2kg was measured at an angle of 30 degrees about the horizontal axis.

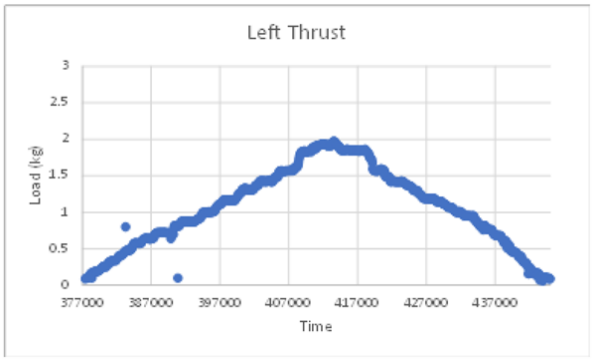


**Figure 11. Graph of thrust force generated at maximum thrust angle of 30 degrees.**

Next, the vector thrust units were integrated onto the dual EDF platform and successfully tested on the small-scale wall mockup, Figure 12. It was observed that servos that were used on the platform did not provide the required torque to maintain the necessary vectored angle while thrust being generated after an extended period. However, it was also observed that the vectored thrust created a parallel force which aided the DC drive motors by reducing the amount of torque required for platform motion.

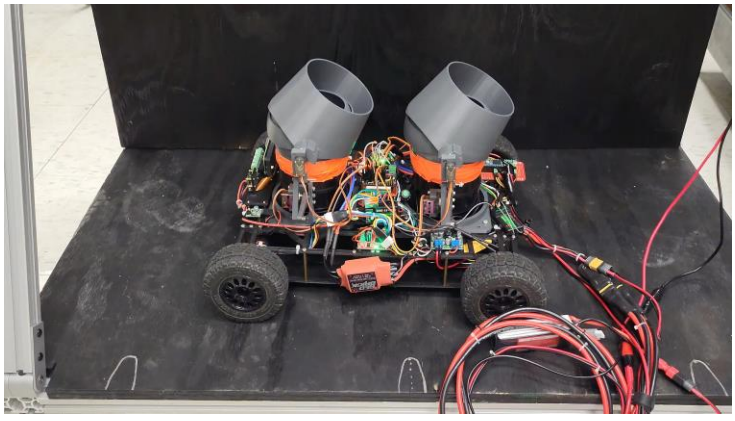

**Figure 12. Dual EDF platform being tested with vector thrust units.**

Finally, after verifying the electrical safety of the PCB modules, they were integrated on to the 5-fan platform, Figure 13 below. The proper voltage and current draw for the DC motors were two

factors that played a role in the choice of electronic components and form factor for the PCB modules, along with implementing means of easing troubleshooting.

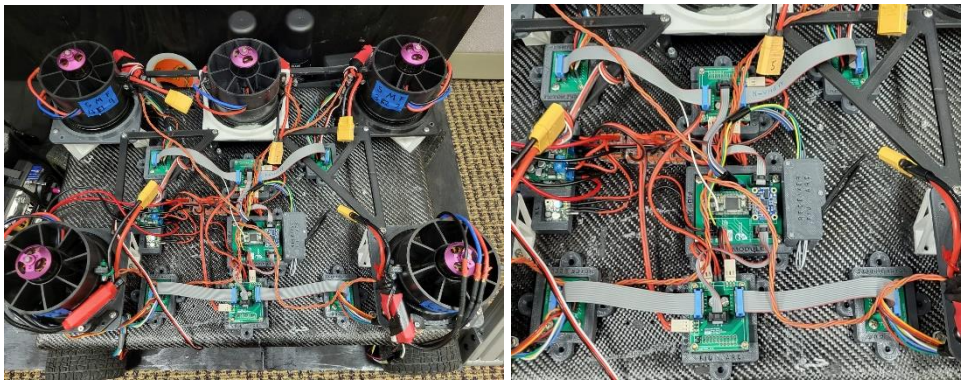

**Figure 13. Large wall crawler platform integrated with PCB modules.**

## Subtask 18.3.1: Conclusions

Multiple technologies were prototyped and assembled to improve the efficiency and performance of the EDF based platform. A vector thrust unit was tested and integrated onto the dual EDF platform and then successfully tested on the small-scale wall mockup developed for rapid test. Next, PCB modules were developed to reduce the wiring onboard the platform and eliminate electrical issues associated to power and signal reliability. The development of these technologies has increased the overall performance of the wall crawling platform along with aiding in creating a more robust mobile platform that is more energy efficient.

## Subtask 18.3.1: References

1. Gilliam, Bob J., Ray, J., and Giddings, B. "Inspection and assessment of the H-Canyon ventilation system at The Savannah River Site". Phoenix, Arizona, 2015. Waste Management Conference.
2. Staff Report, Defense nuclear facilities safety board. "H-Canyon exhaust tunnel fragility analysis input and assumptions". 2018.
3. Echeverria, M., Nunez Abreu, A., Lagos, L., McDaniel, D. "Aging of concrete for the evaluation of repair materials to protect the HCAEX tunnel at Savannah River". Waste Management 2020 Conference, Phoenix, AZ, March 2020. (Best Poster of Track). Paper # 20301
4. Telusma, M., Natividad, J., Lagos, L., McDaniel, D. “Development of an Omnidirectional Wall Crawling Mobile Platform, Designed to Aid in the Repair of H-Canyon’s Concrete Walls”. Waste Management 2021 Conference, Phoenix, AZ, March 2021.
5. Lattanzi, D., Miller, G. “Review of Robotic Infrastructure Inspection Systems”. Journal of Infrastructure Systems Vol. 23, Issue 3 (September 2017)

## Subtask 18.3.2: Integration of the Coating Application System

### Subtask 18.3.2: Methodology

An experiment was designed to determine the efficacy of equipping the large 5-fan EDF unit with a spray mechanism and instruct the unit perform a set of routines to create a desired pattern. The wall crawling platform, Figure 14, was initially tested on a horizontal surface to determine the appropriate controls required to complete the task and then transferred to a vertical surface. The controls for completing this task will rely on a combination of the platform speed, direction of platform, viscosity of coating material and time required for the coating to set to move on to the next section. The chassis design for the large EDF platform includes a barrier section which aids in preventing the coating material from entering the inlets of the EDF units atop the chassis.

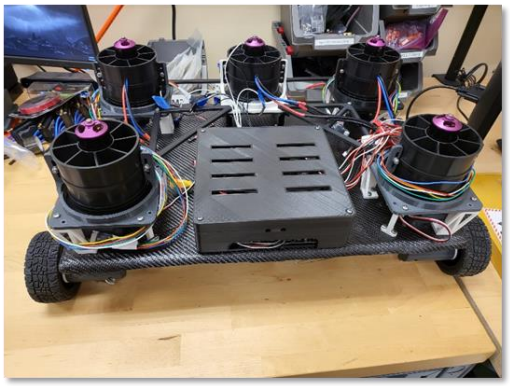

**Figure 14. Large 5-Fan wall crawler.**

The platform was equipped with a basic spray mechanism, Figure 15, which is actuated with a 25kg-cm servo, with the goal of creating a pattern on the horizontal surface. The spray mechanism was installed on the underside of the large EDF platform, Figure 16, where there is a 4-inch distance from the nozzle of the spray to the flat surface. Figure 16 also depicts the chassis barrier which aids in minimizing the amount of debris entering the inlet of the EDF units from the underside, ensuring that the deployed coating will not be disturbed by the relatively high velocity air from the fans.

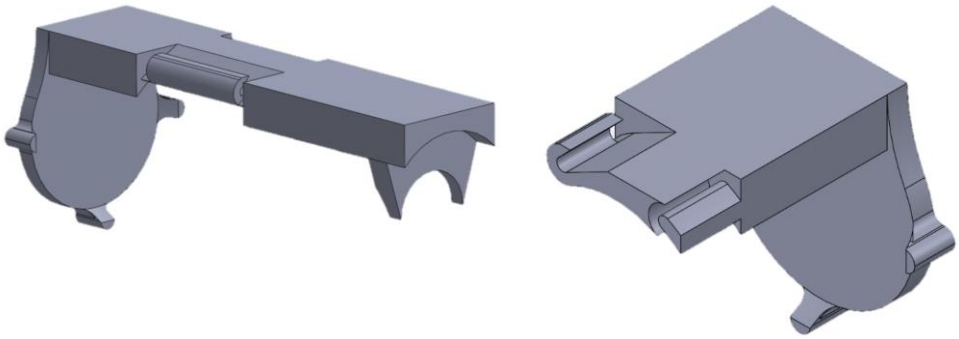

**Figure 15. Spray enclosure pieces.**

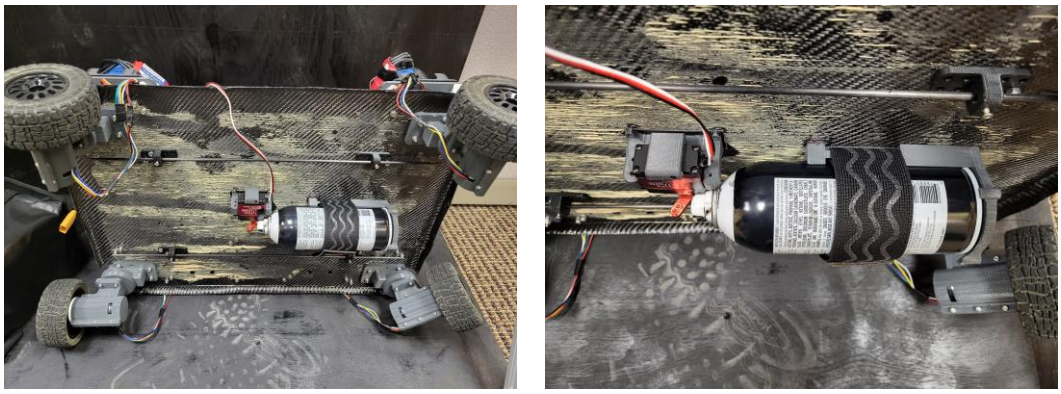

**Figure 16. Spray mechanism installed on large EDF platform.**

Using the large EDF platform which has been integrated with a spray mechanism, experimental data can now be collected regarding the time required to complete a spray pattern and the controls required to complete the task while improving the overall performance of the unit.

## Subtask 18.3.2: Results and Discussion

Experiments were carried out to determine the efficacy of equipping the underside of the large EDF platform with a simple spray mechanism and create a pattern on a horizontal surface and translate that information to the same task completion on a vertical surface. Figure 17 depicts the large EDF positioned to deploy the spray material with a timed delay to create the desired pattern, in this case a rectangle. The clear spray lines also indicate that the chassis barrier allows for the deployment of the spray material onto the surface with minimal effects from the EDF units with the flow at the bottom of the pattern caused by excess material building up on the spray nozzle.

**Figure 17. Testing of large EDF platform and pattern creation using aerosol spray.**

The completion of the initial testing indicated that system integration of the spray mechanism and the 5-fan EDF platform was a success and tested then began on a vertical surface. Figure 18 below, depicts the large EDF platform completing the transitioning onto a vertical of the small-scale mockup and then deploying the spray material onto the white surface.

**Figure 18. Deployment of spray material on vertical surface.**

### Subtask 18.3.2: Conclusions

In conclusion, it was shown that the large EDF platform can be equipped with a spray mechanism to aid in the deployment of a selected coating material onto either a horizontal or vertical surface. A simple actuated spray mechanism was developed and attached to the underside of the platform's chassis where a pattern was created on a horizontal surface using a fixed spray angle. Results indicate that the maneuverability of the platform and nozzle spray angle will aid in coating areas effectively.

### Subtask 18.3.2: References

1. Telusma, M., Natividad, J., Lagos, L., McDaniel, D. "Development of an Omnidirectional Wall Crawling Mobile Platform, Designed to Aid in the Repair of H-Canyon's Concrete Walls". Waste Management 2021 Conference, Phoenix, AZ, March 2021.

## Subtask 18.4: Long-Term Surveillance of Nuclear Facilities and Repositories using Mobile Systems

### Subtask 18.4: Introduction

Continuous surveillance of nuclear facilities and repositories is critical in successfully controlling and understanding radiological environmental impact, planning cleanup efforts, and meeting quality assurance objectives established by the U.S. Department of Energy standards and guidelines. When surveying nuclear facilities and repositories, advanced mobile surveillance systems are safe, efficient, and labor-saving tools that safely deploy state-of-the-art instrumentation without exposing workers to radiation risks. Given the large size of many facilities, the high cost of radiation sensors, and the nature of radiological sources, mobile systems provide a cost-effective solution versus on-site sensor networks or monotonous routine measurements performed by site personnel. In addition, mobile systems deployed in more frequent periodic surveillance missions can provide continuous radiation measurements, simultaneously fusing data from several other embedded sensors. Long-term environmental changes can be

tracked over time, which is needed to assess and document the condition of nuclear facilities during operation, decommissioning, and end-state assessments.

In collaboration with Washington River Projection Solutions site engineers, this subtask has investigated robotic platforms and state-of-the-art field-deployable sensory systems suitable for long-term monitoring of nuclear facilities and repositories. Finally, efforts were dedicated to training a new DOE Fellow hired to support the research conducted under this task.

### Subtask 18.4: Objectives

This task's primary goal is to investigate fully autonomous off-the-shelf multi-use robotics technologies adequate for surveying nuclear facilities and repositories across the DOE complex. Our investigations pursued the following objectives:

- Develop an agnostic field-deployable sensor package coupled with a robust autonomous radiological survey framework to be deployed at Hanford's mobile platforms during the summer.
- Continue customizing and testing FIU's ground and aerial mobile platforms, integrating perception sensors to navigate nuclear facilities, developing digital twins, and fusing data from synthetic gamma measurements, surrounding imagery, and lidar mapping, among other field sensors.

FIU also implemented geospatial data analysis frameworks driven by Machine Learning in our in-house autonomous radiological survey. These frameworks will provide site engineers with tools suitable for automating the analyses of massive amounts of data collected over time in subsequent surveillance.

### Subtask 18.4: Methodology

Fully autonomous surveillance technologies are valuable tools for decision-making because they permit taking many spatial data and trends into account so managers can make more optimal and safer decisions based on updated, abundant, and reliable information. Mobile platforms have great potential in automating data collection, providing comprehensive quality data usually necessary for Artificial Intelligence and Big Data systems. These statistical learning tools are sensitive to random errors, abnormal events, and inadequate or insufficient data, where potential human errors can compromise the accuracy and performance of trained systems. Therefore, automated data collection strategies play a significant role in successfully deploying upcoming modern technologies driven by Machine Learning. The proposed subtask will provide a case study applying crewless inspections for long-term surveillance of nuclear waste facilities and repositories.

Conventional surveying methods of taking radiation measurements by hand within or around the containment areas and analyzing the collected data to obtain the result are ineffective and have put scientists at risk of unnecessary radiation exposure. On the other hand, the current state of autonomy for field-deployed autonomous radiological survey systems is mobile robots with waypoint navigation capabilities. Usually, a scientist selects a series of waypoints on a map, directing the robot to travel autonomously between points. Advanced systems often support obstacle detection and local collision avoidance using LiDAR imagers. However, current surveillance robots in nuclear facilities and repositories do not have a high degree of onboard

autonomy to cope with dynamic environments changing over time due to operations, weather events, and site deterioration currently presented in DOE sites.

As exemplified by Figure 19, changes in Hanford's Tank Farm due to retrieval operations [1] and the constant need to manually reconfigure the surveillance mobile platform's mission plan could burden site engineers, which would also be the case in analyzing the captured data over time.

**Figure 19. Hanford's Tank Farm retrieval operations in September 2016 (left) and 2018 (right).**

The proposed methodology expands traditional autonomous navigation frameworks implementing a novel onboard information-driven planning and control tailored to radiological surveillance of extensive facilities. The online adaptive planning algorithm [2] considers not only navigation goals and battery constraints but also includes sensing objectives such as increasing coverage and routing the optimal path that would decrease the uncertainty in the overall radiation map and reduce geometric uncertainties in the mapped environment over time. The framework will also implement basic terrain risk awareness and advanced perception, a crucial issue in taking fully autonomous surveillance systems out of the structured laboratory and mockup environments and deploying them into existing facilities and repositories.

The core areas of development of FIU's Mapping and Robust Localization Framework are:

1) information-driven planning and control in radiological environments,
2) terrain risk awareness in dynamic and unstructured environments, and
3) advanced perception in complex environments.

### Information-driven planning and control in radiological environments

The proposed framework uses fully autonomous robots as intelligent agents for sensing locations, actively defining an optimal sequence of consecutive measurements, and controlling acquisition parameters of the radiation sensor in real-time (basically dwell time and surface proximity), to improve the accuracy of the radiation map and address common issues with irregularly spaced, noisy, low count data, obstructions, and existing background radiation.

### Terrain risk awareness in dynamic and unstructured environments

The proposed framework implements a computer vision module, assisted by a semi-supervised machine learning system that uses surrounding camera video images to classify the floor's terrain conditions segmented by LiDAR data elevation. A convolutional neural network is trained to classify surface types (carpet, vinyl, water, grass), where unknown conditions (low classification probability) are treated as obstacles. Unknown surfaces can be later manually classified by an operator bringing a human in the loop. The proposed framework improves terrain awareness over

time, keeping the platforms safe in unexpected floor conditions, which is critical in unsupervised robots working in outdoor repositories, especially after weather events.

### Advanced perception in complex environments

**The proposed framework uses several heterogeneous imaging sensors and gamma radiation detectors to construct an immersive environmental map, as illustrated by Figure 20. Mobile platform integration.**

. The framework stores high-resolution maps for digital twin reconstruction and keeps reduced-order ones for navigation and control. The framework also innovates using a robust localization algorithm fusing many sources of odometry (basically ICP, IMU, and visual), suitable in monotonous environments such as hallways and tunnels.

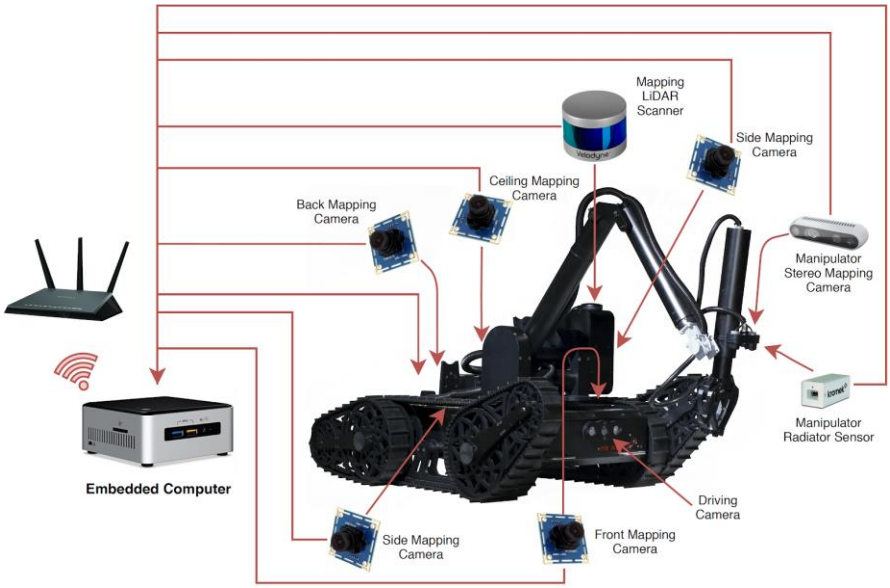


**Figure 20. Mobile platform integration.**

Figure 21 shows the ground mobile platforms used in our in-house tests. The platforms have been customized, integrating several perception and gamma radiation sensors to navigate nuclear facilities and generate high-fidelity tridimensional environmental maps.

**Figure 21. FIU's mobile ground platforms.**

## Subtask 18.4: Results and Discussion

During this performance period, FIU continued the effort to improve our in-house autonomous surveillance framework, allowing routine inspection tasks and data capture safely, accurately, and frequently. The enhancements focused on covering large areas and increasing accuracy in digital

twin reconstruction. Efforts also were dedicated to improving rough terrain navigation, perception, and environmental risk awareness. Furthermore, legged mobile platforms were incorporated into our unmanned aerial and ground vehicles fleet. Legged robots are agile, navigating challenging terrains with unprecedented mobility.

**System Improvement**

The embedded computer of FIU's small mobile platform was upgraded. The task was cumbersome, compiling and migrating the robot firmware from the original Robot Operating System (ROS) to its new version ROS2.

Figure 22 shows the original embedded computer and the upgrade, which is more suitable for processing onboard machine learning containing integrated multiple graphical process units (GPUs) and dual camera serial interfaces (CSIs).

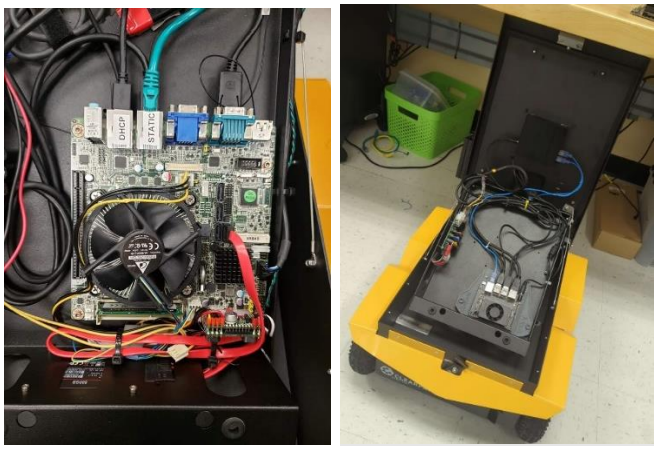

**Figure 22. FIU's mobile platform original (left) and upgraded (left) embedded computer.**

To finalize the onboard computer upgrade and Robotic Operating System update to ROS2 of our indoor unmanned ground vehicle (UGV).

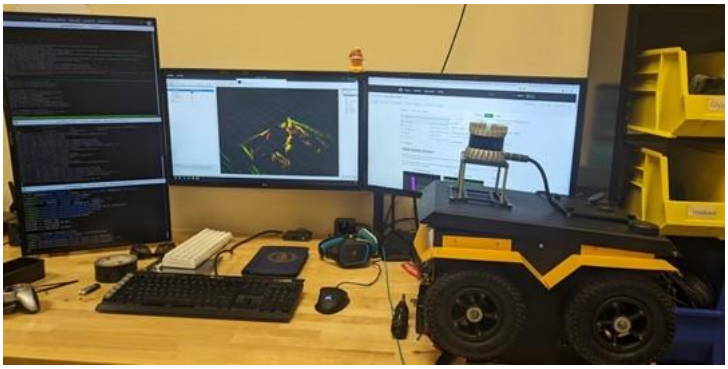

**Figure 23. Ground platform lidar integration.**

The system upgrade required exhaustive testing and software tweaks to stabilize the platform control. Figure 23 illustrates the final customization integrating a 3D lidar into the robot.

Additionally, the team troubleshooted an all-terrain ground platform donated by WRPS. As illustrated in Figure 24, all the previous robot modifications were disassembled to isolate and determine the causes of malfunction, leading to issues in the platform's embedded computer, which is being upgraded. Ongoing communication with the manufacturer is being maintained to restore the robot to its original state, including missing batteries, mounts, and cover plates.

**Figure 24. All-terrain ground platform donated by WRPS (left) and troubleshooting (right).**

FIU also coordinated the all-terrain ground platform transfer with WRPS. The plans included repairing, upgrading, and instrumenting the robot for deployment at Hanford's cold test facility in the summer, demonstrating the potential uses of mobile robotic platforms to automate routine above-ground tasks at tank farms and emergency response scenarios.

After determining the source of the platform's malfunction, the all-terrain platform’s embedded computer was replaced with a more capable system. The retrofit included mounting the computing unit onto the robot's chassis and installing an operating system. The required support software and drivers were also set up. The overall system was tested, and the motor control units functioned successfully, actuating the robot's wheels. Presented in Figure 25, efforts addressed wiring issues powering the embedded instrument.

**Figure 25. All-Terrain ground platform donated by WRPS.**

## Improved Navigation

The simultaneous localization and mapping (SLAM) toolboxes were revisited with a specific focus on evaluating the performance of the manufacturer's toolbox integrated into our mobile platform in contrast to open-source ones. Traditional SLAM's algorithm depends on extended Kalman filters to estimate robot position by fusing conventional odometry sources from wheel encoders and inertial measurement units (IMUs) dead reckoning.

Our robust navigation framework also addressed issues related to robust robot localization, fusing many other sources of odometry when available, such as GPS, vision odometry from tracking cameras, and ICP odometry from live lidar mapping point clouds. Further localization improvements considered fusing semantic map cognition and environmental landmarks tracked by onboard unsupervised machine learning classifiers based on vision.

Figure 25 shows tests conducted with the all-terrain UGV in a controlled indoor environment, driving around an office space. The UGV captured data on its surroundings, generated maps, and simultaneously understood its position within the facility.

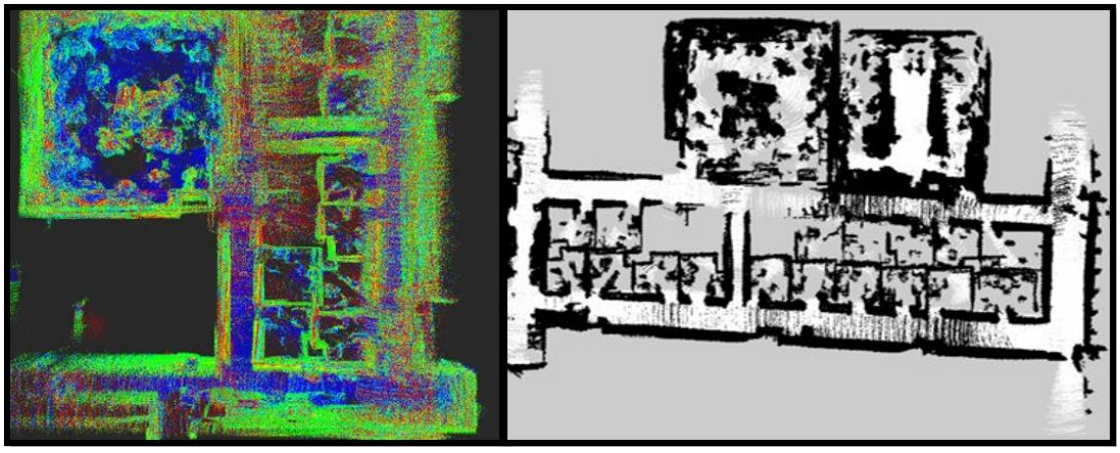

**Figure 26. Captured 3D point cloud (left) and 2D Map Generated using SLAM (right).**

Figure 27 shows the initial efforts of integrating FIU's quadruped robot into our autonomous navigation framework.

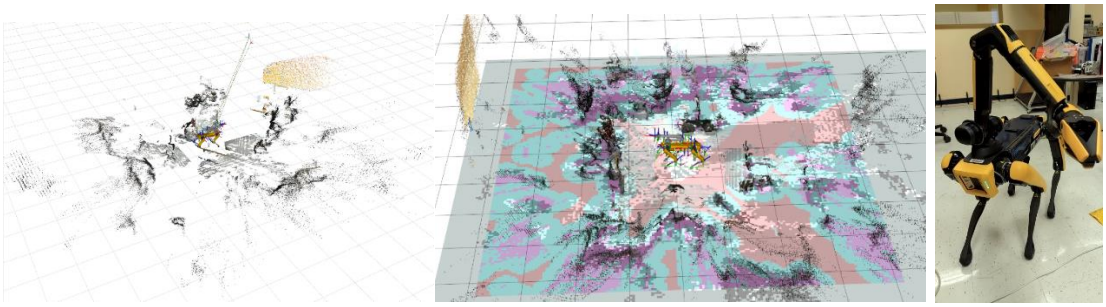

**Figure 27. Legged robot autonomous mapping.**

## Gamma Radiation Sensor Integration

Radiation sensors were selected and purchased, suitable to deploy at Hanford tank farms using ground and aerial platforms, an effort coordinated with WRPS engineers. The sensor package

combines low-dose and high-dose measurement capabilities, in contrast to the dosimeter current being used at Hanford. The selected gamma detectors are Cs(Tl)I-based and CZT-based micro gamma spectrometers for low-dose and high-dose environmental surveys. The team started developing a gamma field reconstruction based on GIS, photogrammetry, and lidar data supported by FIU's Autonomous Surveillance Framework.

**Summer Deployment at Hanford**

FIU received, repaired, upgraded, and instrumented the all-terrain ground platform donated by WRPS and deployed the robot at Hanford's cold test facility by the DOE Fellow working on the task during his summer internship. Figure 28 shows FIU's technology being received at Hanford's CTF.

**Figure 28. FIU's technology delivered at WRPS's CTF.**

Figure 29 shows FIU's technology deployed at CTF. The deployment demonstrated potential uses of mobile robotic platforms to automate above-ground routine operations at tank farms. The effort is part of the WRPS's Engineering and the Chief Technology Officer (CTO) partnership with FIU to develop technology that can possibly assist first responders at Hanford's tank farms.

**Figure 29. FIU's technology deployed at Hanford's CTF.**

Figure 30 shows an outdoor map generated during the summer demonstration.

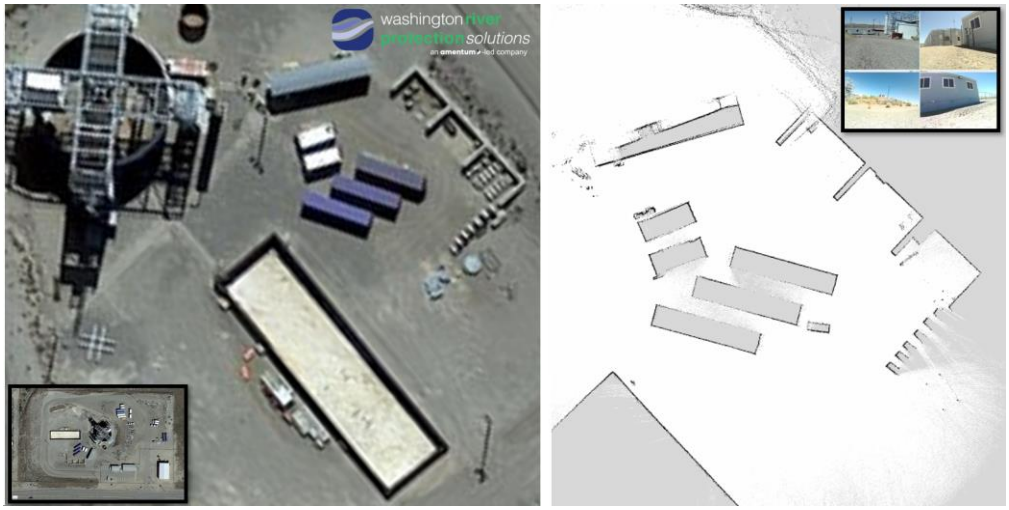


**Figure 30. Deployment at Hanford's CTF.**

The lessons learned from the summer deployment and WRPS engineers' feedback guided the technology development when the Fellow returned to FIU.

### Waste Segregation Task Support

The team also supported Project 3, Task 9, controlling a waste segregation robotic manipulator. The efforts mainly included the construction of a computer vision application and furthering our research in reinforcement and learning training methods for robot manipulators.

### Testbed

Figure **31** shows a test bench adapted to support the task.

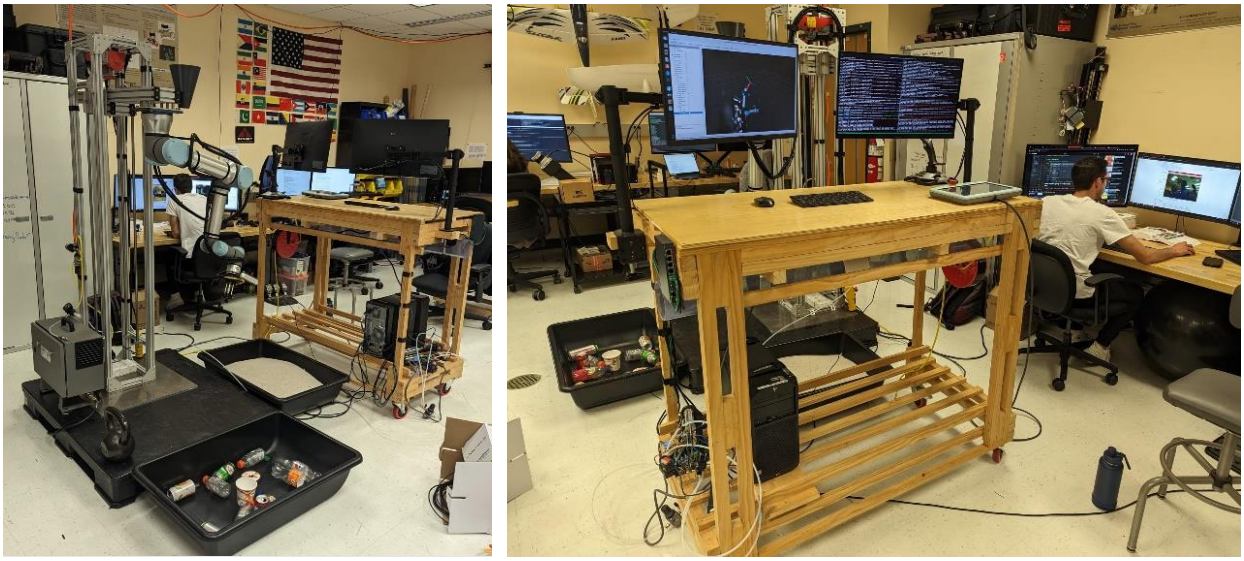

**Figure 31. Waste segregation test bench.**

A pneumatic gripper was integrated to the robotic manipulator to pick up solid waste. The gripper shown in Figure 32 uses a pneumatic vacuum venturi controlled by a solenoid valve to actuate a vacuum cup.

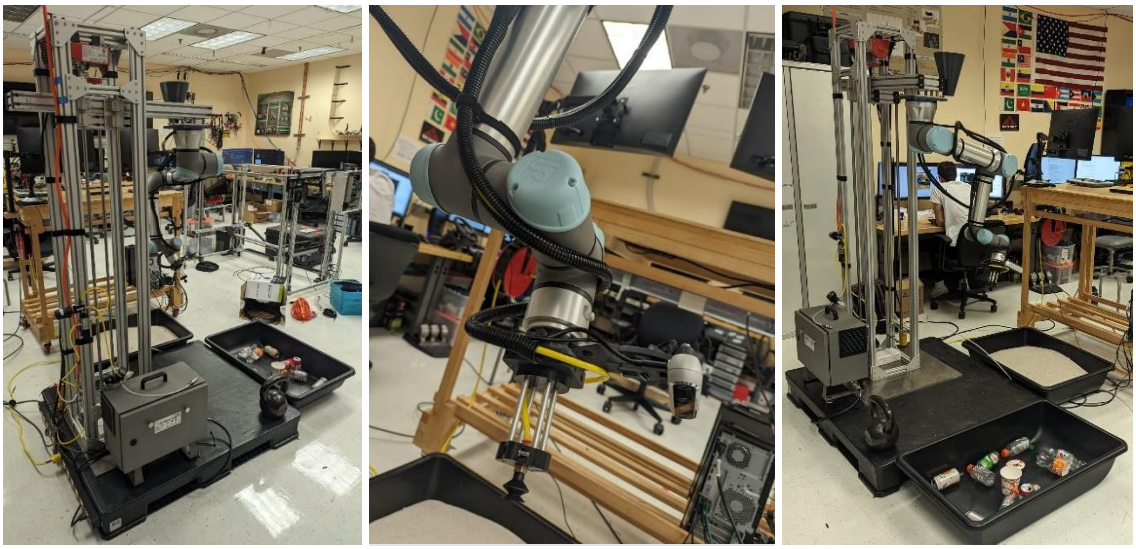

**Figure 32. Pneumatic gripper.**

Figure 33 shows the pneumatic gripper controller developed at FIU to control pick-and-place operations.

**Figure 33. Pneumatic gripper controller.**

## Vision System

Multiple decision-making methods using single-camera views for controlling robotic manipulators were investigated. The two primary perception methods were color masking and quick response (QR) code recognition.

For the QR code approach, numerous libraries were tested for their recognition capabilities at various angles and lighting conditions. Preliminary tests in Figure 34 illustrate QR code detection in an image to provide four key points related to real-world dimensions.

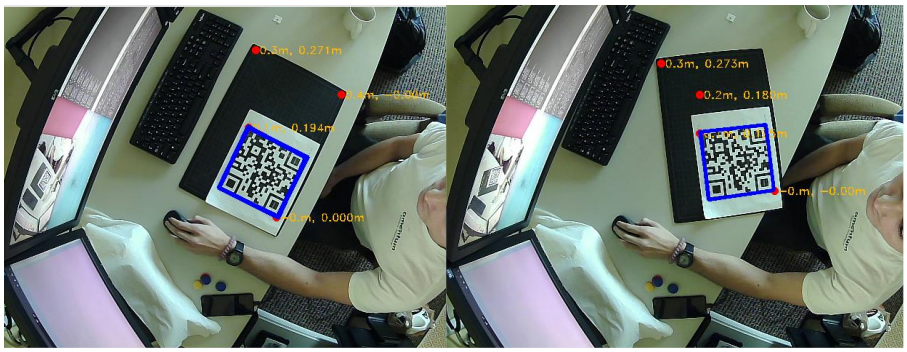


**Figure 34. QR code automated calibration.**

In contrast, as illustrated by Figure 35, the color masking technique has many limitations related to lighting. The method identifies objects specifying ranges of color intensities for thresholding. Objects that lie outside the selection range are rejected.

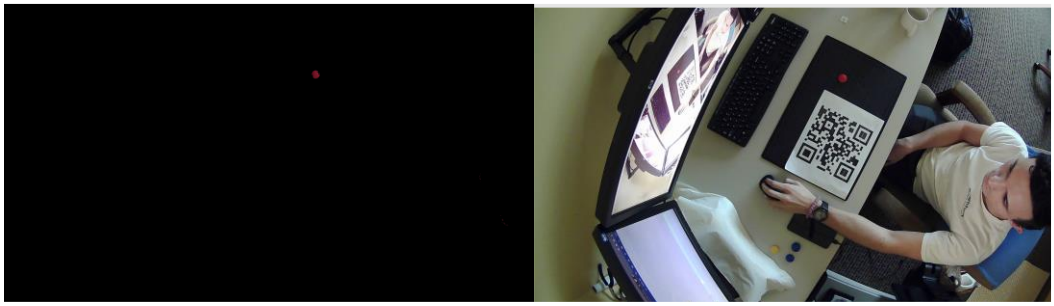

**Figure 35. Color masking identification technique.**

The QR code for automated image registration with robot position calibration and color for object detection was replaced by an unsupervised Machine Learning vision system to classify solid waste.

The waste is categorized using a 3D depth camera installed at the robot's end effector. Project 3's team oversees developing an unsupervised Machine Learning vision system to classify solid waste. Figure 36 demonstrates the waste segregation manipulator successfully performing a pick-and-place operation using this pneumatic gripper autonomously.

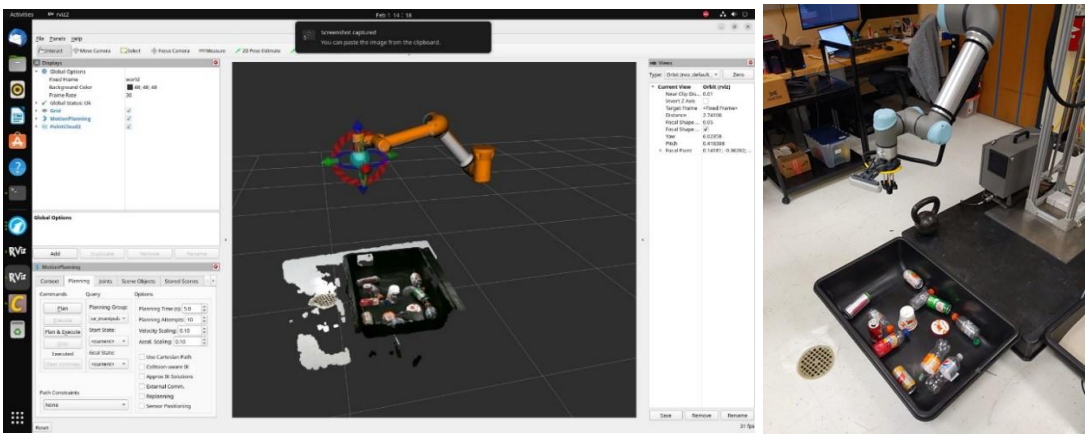

**Figure 36. Waste segregation pick-and-place demonstration.**

The team has also provided training photos of selected waste to create a machine-learning prediction model. The prediction model will be used to classify waste items based on their visual characteristics, which could also aid in grasping gestures and sorting the objects.

**Figure 37. Sample of waste images for training machine-learning prediction model.**

## Sorting Automation

A behavior tree was developed with numerous logic control features to automate the object detection coordinated with picking-and-placing operations. The behavior tree was developed to organically model more complex behavior without involving hard code similar complex behavior. The tree, consisting of leaves that run individual behaviors, allows performing asynchronous actions, which provides greater flexibility than finite state machines. Figure 38 shows a basic behavior tree implemented to command the manipulator to locate and hover over objects in its workspace.

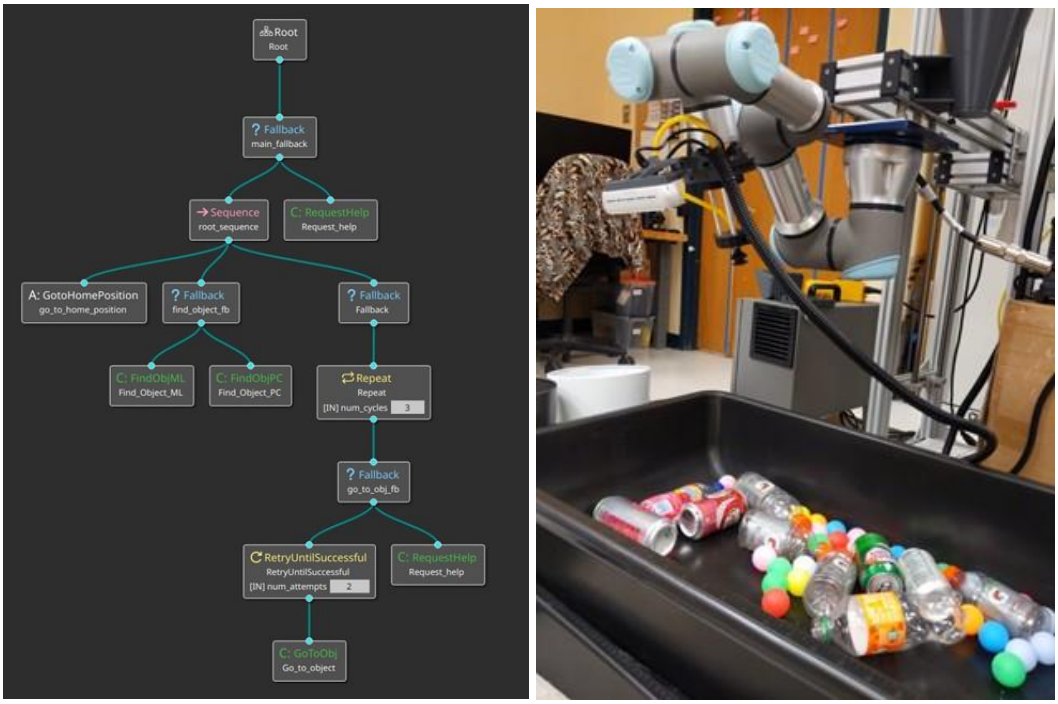


**Figure 38. Locate and rover behavior tree.**

Two specific behaviors were implemented, "GotoHomePosition" and "RequestHelp," that make the robot reach an ideal viewing position on its workspace and request help. Future behaviors are being implemented to command the manipulator to locate objects using the end effector 3D camera, activate the gripper suction cup, and place the items in specifically labeled bins.

The robot's behavior tree was further developed, adding more task programs (nodes). First, the machine learning segmentation model implemented by Project 3's group was integrated into our manipulation framework. The node passes images from the robot manipulator's live camera feed through this model and publishes the resulting array of points from identified objects to a custom message.

Figure 39 below shows the model working on a single entity, but the program can locate multiple instances simultaneously.

**Figure 39. Object detection using FIU's machine learning segmentation model.**

The implemented perception node was then integrated into the behavior tree to segment objects at any time during more complex logic flows. Figure 40 shows additional tests performed to observe the robustness of the machine-learning model. Rare misidentification instances were observed, although they have not yet been quantified.

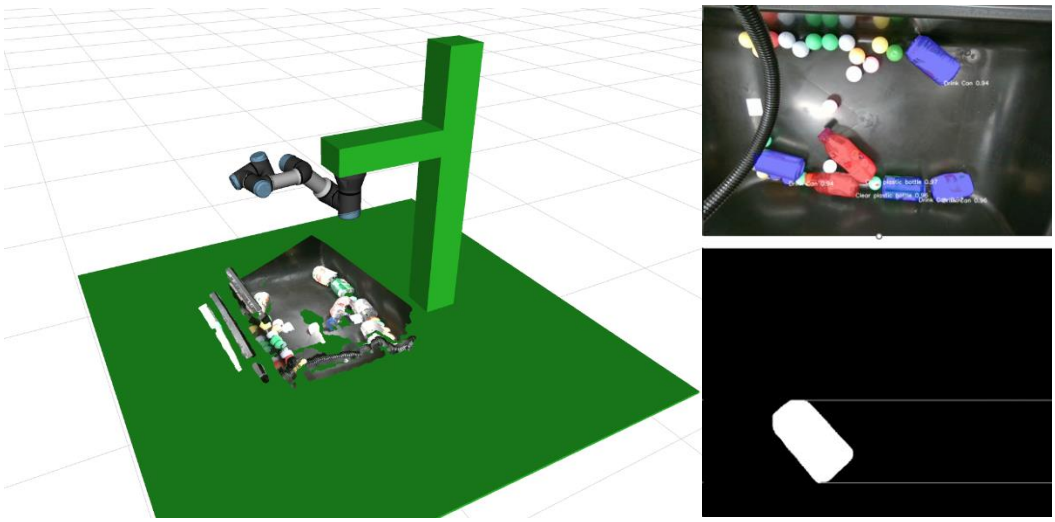

**Figure 40. Waste sorting automation.**

Since a pick-and-place robotic manipulation framework was successfully implemented for waste segregation, the Task 9 development continues by Project 3's team.

### Subtask 18.4.1: Conclusions

The Long-Term Surveillance of Nuclear Facilities and Repositories using Mobile Systems efforts will continue to improve robust navigation, radiation mapping, digital twin capture and reconstruction. The improvements will continue:

a) integrating additional sensory relevant to surveillance of tank farms,
b) incorporating Machine Learning into the framework,
c) automating digital twin tasks such as segmentation, object detection, and automatic registration,
d) implementing information-driven planning and control techniques and comparing their performance with traditional ones, and
e) fusing close-range data captured by 3D cameras with mid-range ones imaged by LiDAR, combining local accuracy with far-field awareness.

Instructions from the Multi-Agency Radiation Survey and Site Investigation Manual (MARSSIM) will be incorporated in our autonomous mapping algorithms to provide detailed guidance for planning, implementing, and evaluating environmental and radiological facility surveys conducted to demonstrate compliance with a dose-based or risk-based regulation.

During the 2024 summer, the FIU mobile platforms will be potentially redeployed at Hanford. The lessons learned and interactions with scientists and engineers will guide the development of robotics technologies that can automate above-ground routine operations and possibly assist first responders at Hanford's tank farms.

### Subtask 18.4.1: References

1. S. Ferrari and T. A. Wettergren. (2021). Information-Driven Planning and Control. The MIT Press.
2. C. Miskinis (2018, January). Combining digital twin simulations with virtual reality – what can we expect?. https://www.challenge.org/insights/virtual-reality-and-digital-twin
3. M. Berger, A. Tagliasacchi, L. Seversky, P. Alliez, G. Guennebaud, J. Levine, A. Sharf, C. Silva (2016). A Survey of Surface Reconstruction from Point Clouds. Computer Graphics Forum.

## Subtask 18.5: Development of Robotic Systems for DOE Sites

### Subtask 18.5: Introduction

Hanford's site scientists and engineers are constantly evaluating innovative technologies to alleviate the operational issues related to inspecting and sampling aging single-shell and double-shell tanks containing highly radioactive nuclear waste. In close collaboration with WRPS, the Applied Robotics Laboratory at FIU has developed and deployed specialized inspection tools tailored to Hanford's needs.

FIU's magnetic rover was successfully deployed at the Hanford tank farm, inspecting the AP-105 double-shell tank. WRPS's site personnel successfully operated the miniature inspection tool, navigating along the tank's inner liner walls from above ground to the tank's bottom floor, reaching the central plenum, and providing video feedback along the way. The miniature inspection tool's design incorporates several innovative features that are patent pending, from a flexible body tailored to overcoming oblique weld seams to magnetics wheel scups removing accumulated rust deposits.

FIU has also developed a lateral gamma scanner to autonomously monitor leaks underneath Hanford's single-shell tanks. The tool is designed to scan existing lateral pipelines underneath the tanks running across the diameter, measuring changes in the gamma radiation baseline. The device uses a pneumatic peristaltic crawler synchronized with an automated cable reel, providing a viable option for leak detection, does not require operator supervision, and reduces operational burdens on site personnel. The tool was successfully demonstrated at WRPS's cold test facility last summer.

FIU has also developed an off-riser sampler manipulator to support Hanford's tank retrieval operations. The system uses existing small diameter tank risers to cable deploy a dexterous teleoperated robotic manipulator coupled with multiple end-effector tooling to sample ample residual waste material in single-shell tanks. The idealized concept was successfully demonstrated at WRPS's Cold Test Facility last summer using an industrial robotic manipulator scooping simulant sand.

In addition, FIU started a new task in collaboration with Savannah River National Laboratory, in-situ 3D printing concrete structures for waste containment and disposal.

### Subtask 18.5: Objectives

This task aims to develop and deploy novel inspection and sampling tools for tank integrity assessments, removal, and storage of residual waste. FIU engineers and DOE Fellows will continue to work directly with site engineers to build, and test systems that can improve site personnel's operational efficiency and safety. Specific subtasks include:

- Continue streamlining, adding functionalities, and strengthening the multiple tools developed at FIU.
- Leverage lessons learned from site personnel interactions and deployments.
- Deploy and demonstrate technologies at the Hanford and SRNL sites during the summer.

In collaboration with WRPS, the proposed subtasks will continue supporting FIU's current efforts in developing and deploying novel tools at Hanford tank farms to alleviate operational burdens on tank integrity assessments and residual waste removal. The developed devices can also be outfitted with additional sensors providing environmental information within SSTs and DSTs and essential details on tank floor health.

In collaboration with SRNL, FIU will support SRNL’s vision of creating 3D printing in situ concrete structures for waste containment and disposal.

### Subtask 18.5: Methodology

The approach taken to develop inspection tools for use at the Hanford Site has been to start with concepts that address the necessary issues and work with Hanford engineers to down-select from

the ideas and focus on the concepts. Once a concept has been vetted, FIU engineers design and develop an initial prototype. Bench scale tests are then conducted to demonstrate the validity of the concepts and develop an understanding of where improvements are needed. After a prototype has been developed and determined to be functional, the system is tested in a mockup built at FIU. Typically, after trying in our mockups, improvements are made to address issues noted during testing. Issues such as improved functionality and durability are discussed then. Once engineers at Hanford or SNRL are satisfied that the system meets the requirements, the units are taken to the DOE site to test in their Cold Test Facility or for deployment.

To further foster joint efforts, FIU hosted the first DOE, FIU, and WRPS Technology Development Collaboration Meeting on February 7 and 8, 2023. Officials from the DOE-EM TD Office, Washington River Protection Solutions, Central Plateau Engineering, Savannah River National Laboratory, and the US Army Corps of Engineers attended the meeting. The meeting agenda mainly included the following:

- Current project updates.
- Facilities tours.
- Technology demonstrations.
- Project technical discussions
- Summer interns' activities.
- Future on-site training.
- Potential projects for the 2024 upcoming performance period.

Figure 41 shows images from the demonstration of technologies developed at FIU sponsored by DOE-EM at the Applied Robotics Laboratory during the meeting.

**Figure 41. DOE, FIU, and WRPS Technology Development Collaboration Meeting at FIU.**

## Subtask 18.5: Results and Discussion

### Subtask 18.5.1 – Incorporation of Sampling Capability to Miniature Rover

FIU continued enhancing the miniature inspection tool's capabilities. WRPS site engineers requested that FIU incorporate a sampling mechanism at the front of the rover to retrieve samples of deposit material along the bottom during routine inspections in Hanford's double-shell tanks. Finally, considered efforts were also dedicated to training a new DOE Fellow taking over the task,

replacing the Fellow who defended his master's thesis on the FIU's Miniature Rover System Development and started working at Los Alamos National Laboratory.

**Design Improvement**

Figure 42 shows the miniature inspection rover deployed at Hanford to inspect the bottom of the AP-105 DST in 2022.

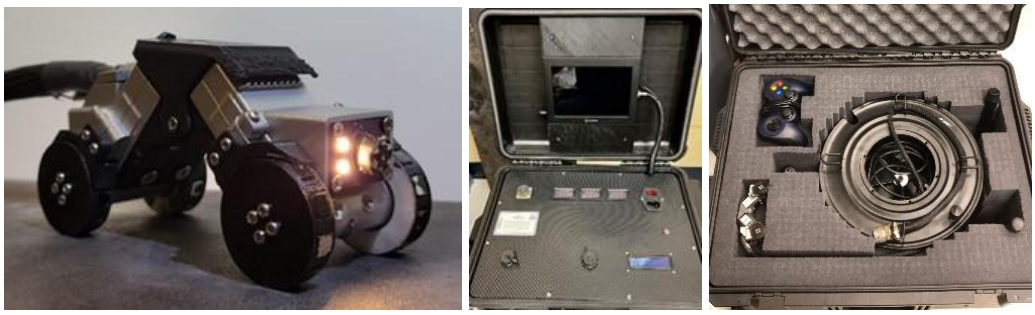

**Figure 42. Deployed miniature inspection rover at AP-105 tank.**

Figure 43 shows images of the tank farm deployment. WRPS technicians operated the rover through the riser located at grade and lowered it down via the deployment tray. Upon being lowered to the appropriate length, the rover traversed down the tank wall in the annulus and entered the refractory air slot. Upon the successful inspection of the refractory slot, the rover returned to the deployment tray and was retrieved successfully.

**Figure 43. FIU's miniature inspection rover deployment at AP-105 DST.**

After the AP-105 tank deployment, the technology was transferred to Hanford engineers, and an improved replacement, shown in Figure 44, was rebuilt at FIU, including the rover, tether, and control box. The rover's chassis was built utilizing stereolithography (SLA) resin-printed parts,

replacing the costly 3D-printed aluminum. The modification also required converting some hardware to resin material compatible ones.

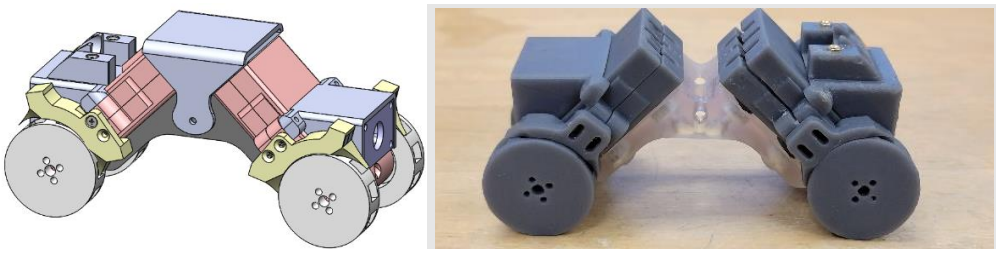

**Figure 44. Resin-printed rover in partial assembly.**

Figure 45 shows the miniature magnetic rover chassis printed using a Stereolithography (SLA) 3D Printer. The finish and resolution of printed surfaces are exceptional, showing promising results in replacing the 3D-printed aluminum components. The selected resin material is very rigid; however, it is brittle. Over-sized components, such as bearings, could not be press-fit without cracking or chipping the chassis, which has required minor redesigning and tolerance tuning.

**Figure 45. Miniature Rover resin parts before post-processing.**

Additional efforts include printing parts in draft resin to assess strength, press-fit hardware, and print-in-place capabilities. The print-in-place components require tight tolerances for the respective elements, causing unwanted adhesion beyond the printer's resolution. Figure 46 demonstrates a test piece for installing threaded inserts in rigid printing resin. Hole diameters are in increments of 0.05 mm to select an ideal fit, considering strength, material stiffness, and insert failure. Due to the resin rigidity, excessively tight tolerances cause the part to fracture. Plans include using different resins to print the miniature rover's chassis and varying the material stiffness according to each component's mechanical function.

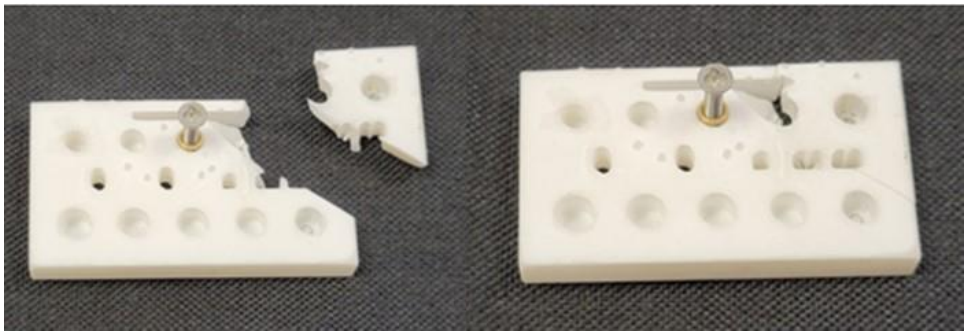

**Figure 46. Press-fit insert tolerance testing on rigid resin.**

Figure 47 shows images of the team's efforts to alternatively manufacture the miniature rover's chassis in Aluminum 6061 using the Pocket NC 5-Axis CNC to achieve better mechanical performance and eliminate the costly original 3D-printed aluminum parts. Aluminum 3D printed parts are brittle and heavier compared to machined components from solid blocks.

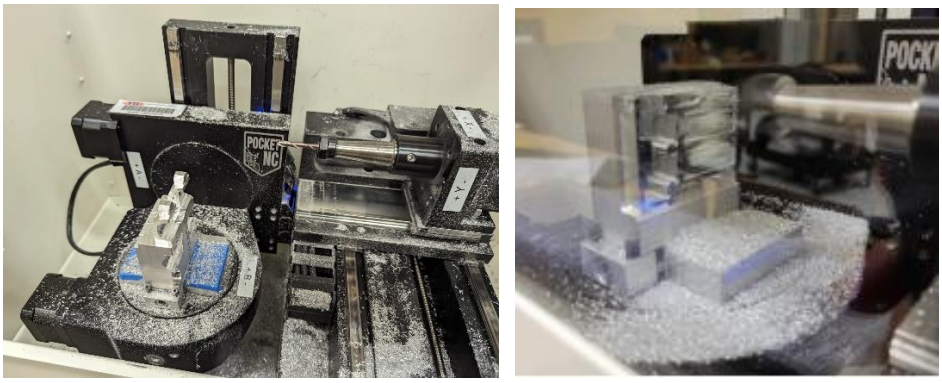


**Figure 47. Chassis CNC machining.**

The machining efforts also included redesigning the chassis to accommodate manufacturing. Figure 48 shows the promising results CNC results.

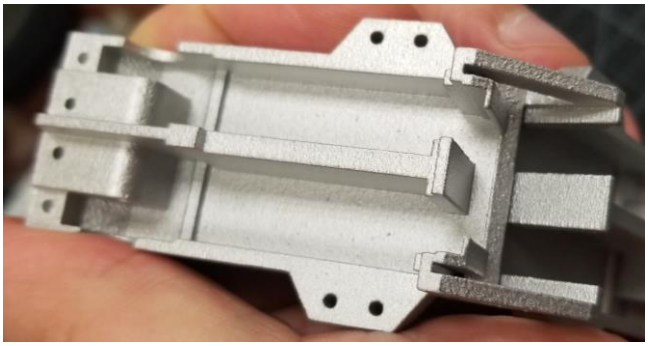

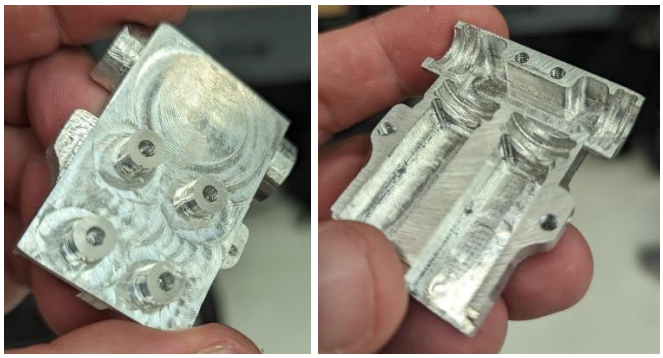

**Figure 48. 3D Printed (top) and machined (bottom) chassis components.**

The chassis flexible connection was also optimized for better compliance in tackling eventual buildups, corrosion, and oblique weld seams along DST inspections. Figure 49 shows a finite element analysis study to maximize torsion without compromising chassis strength.

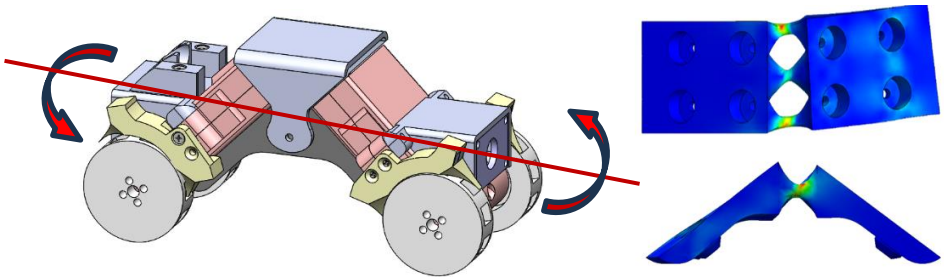

**Figure 49. Chassis's complaint connection.**

The powertrain gears of the rover wheels were also upgraded from brass to carbon steel, as shown in Figure 50.

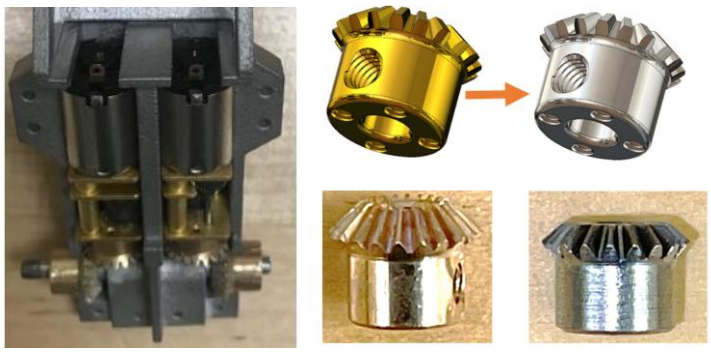

**Figure 50. Drivetrain gearbox upgrade.**

The upgraded carbon steel gears have better manufacturing, tolerances, dimensional quality control, and mechanical performance (presented in Table 3) than the original brass.

**Table 3. Powertrain gearbox material properties**

| Property | Brass | Carbon Steel |
|---|---|---|
| **Density (g/cm³)** | 8.4 - 8.7 | 7.7 - 8.1 |
| **Young's Modulus (GPa)** | 100 - 125 | 200 - 210 |
| **Tensile Strength (MPa)** | 200 - 550 | 370 - 870 |
| **Shear Strength (MPa)** | 110 - 370 | 240 - 390 |

| | | |
|---|---|---|
| **Hardness (Brinell)** | 80 - 110 | 120 - 300 |
| **Coefficient of Friction (Dry)** | 0.15 - 0.35 | 0.3 - 0.6 |
| **Thermal Conductivity (W/m·K)** | 109 - 120 | 43 - 60 |
| **Machinability** | Excellent | Good to Excellent |
| **Corrosion Resistance** | Excellent | Moderate to Poor |

The miniature rover's embedded electronics were redesigned to expand its sampling functionality. The plan involved the addition of an onboard microcontroller to handle multiple actuators and possible future sensors. Four small footprint printed circuit boards (PCB) were designed:

- tether distribution,
- microcontroller,
- camera, and
- motor boards.

All PCBs are interconnected via a set of JST connectors, streamlining current issues with cable management.

The tether distribution board, shown in Figure 51, is the primary entry point for the tether supplying electric power and communication to the miniature rover. The PCB distributes the cat6 tether cable's strands, dispersing them into multiple JST connectors. Additionally, the distribution board contains voltage regulators and a CAN bus communication interface.

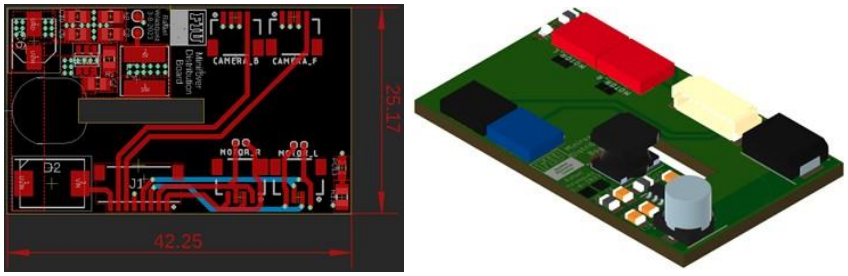


**Figure 51. Tether distribution board (units in mm).**

Figure 52 shows the microcontroller board of the central nervous system for the forthcoming miniature inspection rover. It incorporates the microcontroller and the motor drivers for the wheels and sampling system.

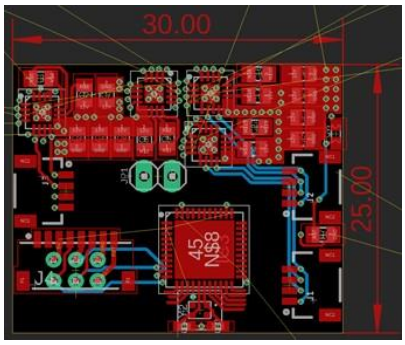


**Figure 52. Microcontroller board schematic (units in mm).**

The camera board, shown in Figure 53, upgrades the previous LED board. The camera module connection is relocated to the tether distribution board to improve the inspection tool's serviceability.

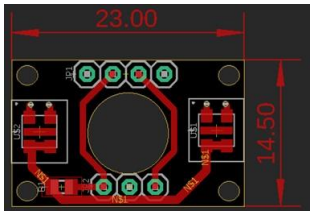


**Figure 53. Camera board schematic (units in mm).**

Figure **54** show the motor board simplifies troubleshooting the motors, eliminating soldering or de-soldering. These boards are outfitted with a JST connector, allowing for easy and efficient motor connections.

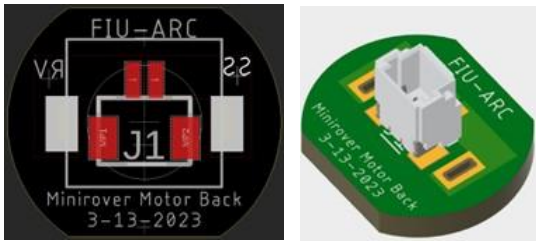


**Figure 54. Motor Board (units in mm).**

The designed PCB incorporates future expansions, with provisions for accommodating current and forthcoming miniature rover models incorporating onboard microcontrollers. The board includes automatic detection that accurately differentiates between rover versions, alerting operators in case of miswiring.

Figure 55 shows the miniature rover's redesigned tether distribution board. The PCB integrates a voltage regulator for compensating voltage drops on long cables.

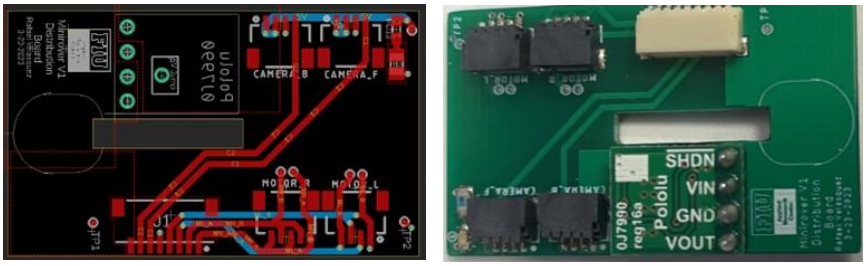


**Figure 55. Miniature rover's redesigned self-regulated tether distribution board.**

Figure 56 shows the miniature rover’s current controller board for integrating the sampling systems and potential other attachments. The PCB includes an onboard microcontroller, motor controllers, and CAN bus communication required to operate additional attachments without incorporating extra lines to the current tether.

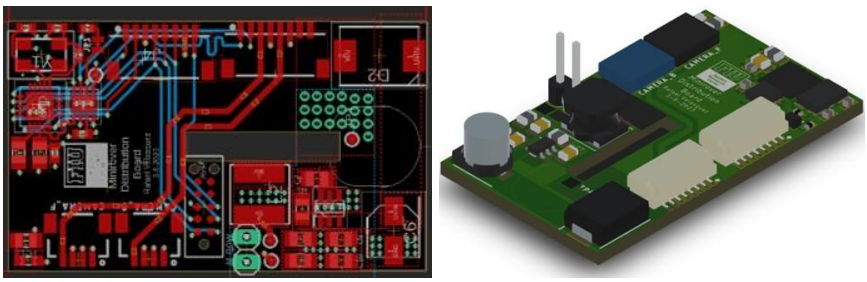

**Figure 56. Miniature rover's controller board.**

Figure 57 show the redesigned miniature rover's motor board to accommodate the connectors adequately, correcting the previous design.

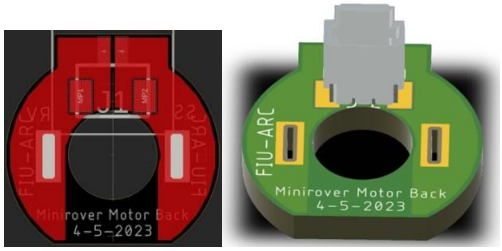


**Figure 57. Miniature rover's motor board.**

Figure 58 shows the final prototype of the miniature inspection rover equipped with the designed PCB boards.

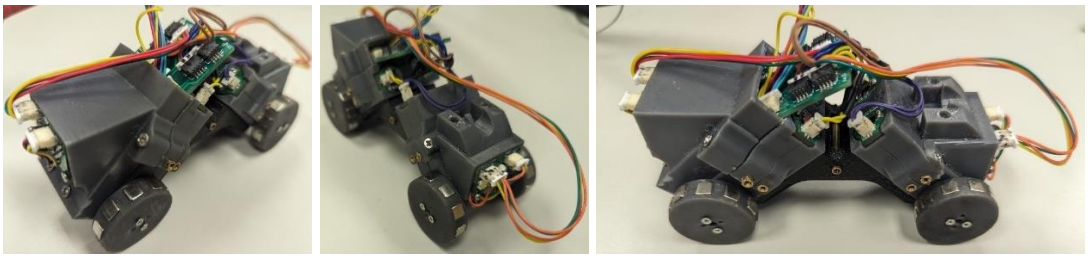

**Figure 58. Improved Miniature Inspection Rover.**

The new control box was also upgraded with an embedded computer and a touchscreen monitor running a custom graphical interface (GUI) developed at FIU, replacing the commercial video recorder in the previous model. FIU's GUI was tailored to the inspection tool, providing a more organic user-operator interface.

In addition, printed circuit boards (PCBs) were designed to optimize components and electric layout. s 1-13 show a low-voltage DC electronics PCB successfully developed to improve cable management. Subsequent plans include integrating the remaining high-voltage AC/DC circuits and voltage regulators, creating a robust monolithic system that is relatively easy to troubleshoot and maintain.

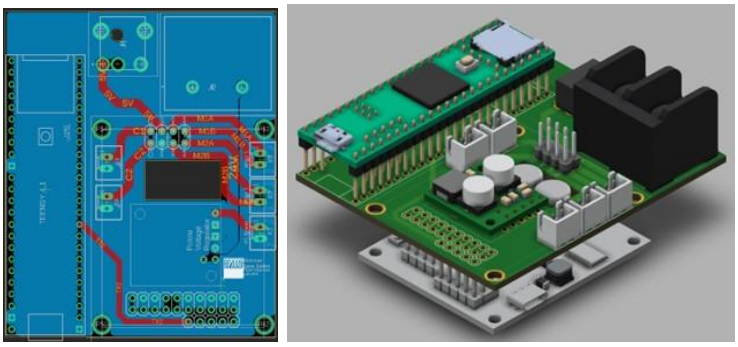

**Figure 59. Control box's main circuit board.**

The revised control box has undergone significant improvements to reduce the wiring complexity prevalent in previous designs. Figure 60 shows a designed PCB for cable management and power distribution. The distribution board effectively splits the required voltages into multiple levels, featuring integrated fan regulators safeguarding against potential overheating.

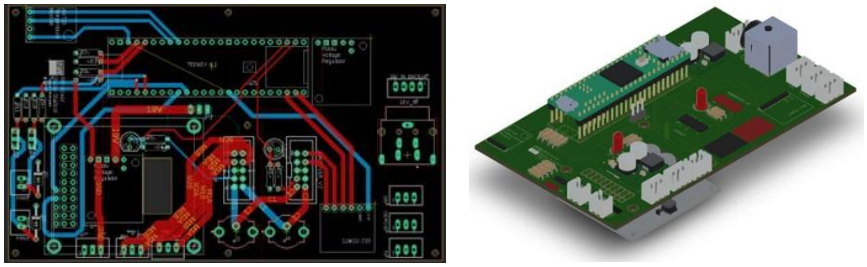

**Figure 60. Miniature rover control box board.**

Figure 61 shows the final prototype of the miniature rover control box board, implementing electrical ground isolation to eradicate video noise feed.

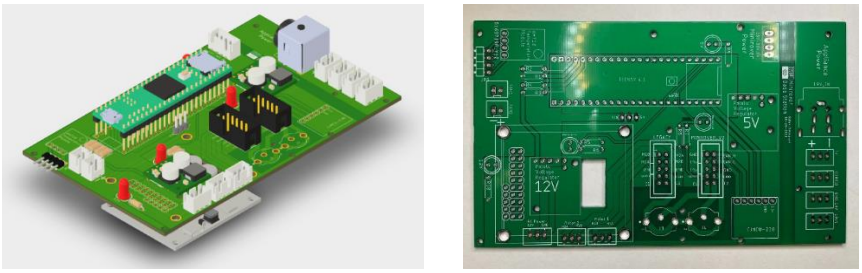


**Figure 61. Miniature rover control box board final prototype.**

Figure 62 shows the tether connection board's final prototype, an integral part of the video feed noise removal, also implementing extra electrical ground isolation from the tether signals.

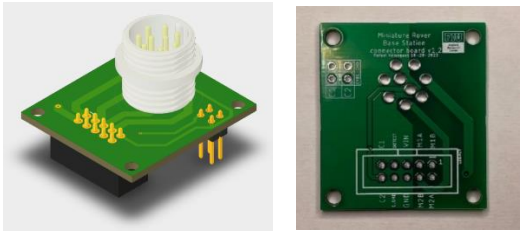

**Figure 62. Tether connection board final prototype.**

Figure 63 shows the system's upgraded control box. The new PCBs design and customization also address video feedback noise and electrical grounding issues in previous systems.

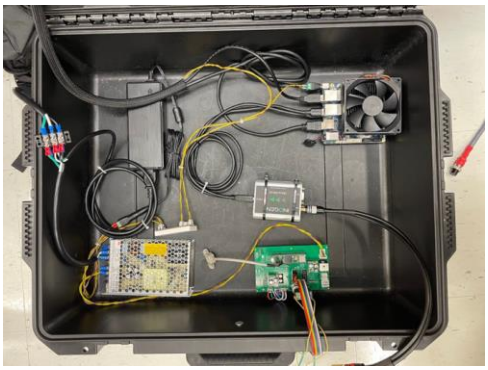

**Figure 63. Upgraded Control Box.**

Efforts were dedicated to eradicating the induced noise in the device's video feed. Motor control signals sent through the 200 feet tether cause artifacts in the analog video feedback, resulting in unclear images. Figure 64 shows digitized waveforms analyzed using an oscilloscope. The team explored several filtering and grounding solutions to the noise problem.

**Figure 64. Grounded (left) and ungrounded (right) video feed.**

Figure 65 shows video signals collected from the rover's cameras during operation in an ongoing systematic approach to determine the source of image distortions and mitigating noise interference.

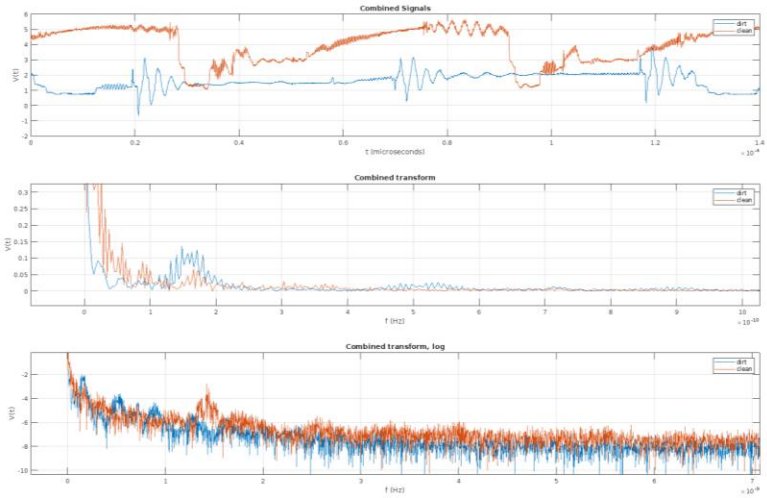


**Figure 65. Rover video feedback spectrum analysis.**

Figure 66 shows the improved rover's video feedback where electrical grounding issues were addressed. Although the cameras still show overlapping images, interference from the motors when the unit is moving was drastically suppressed.

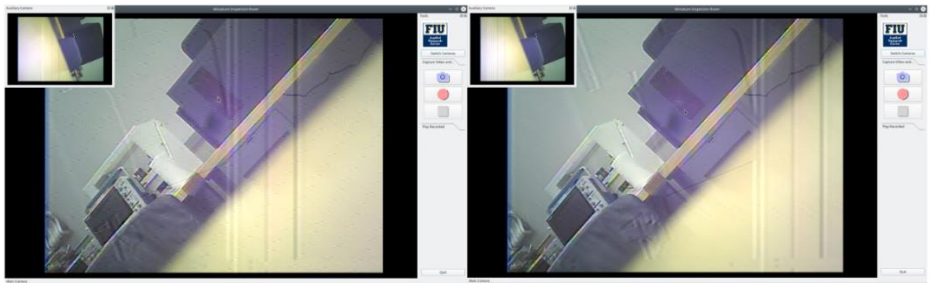

**Figure 66. Minitower's video feedback noise (left) and improved quality (right).**

Figure 58 shows the miniature inspection rover's video feed before and after implementing grounding and complete noise eradication.

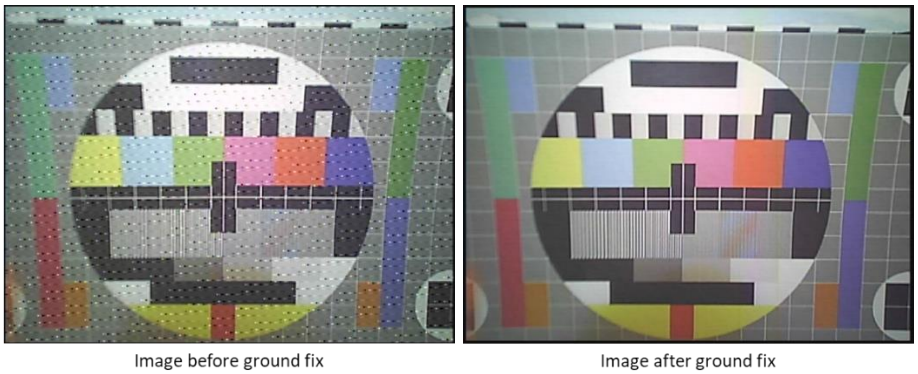


Figure 67. Tether-induced video noise (left) and noise eradication (right).

**Sampling Mechanism Design**

Figure **68** shows candidate designs for the miniature magnetic rover's sampling mechanism requested by WRPS. The team envisions several attachments and end effectors according to the material consistencies expected at the bottom of the DST's primary liner, such as dust, calcified deposits, and flaking corrosion. The figure also illustrates the proposed mechanism differences in actuation and control.

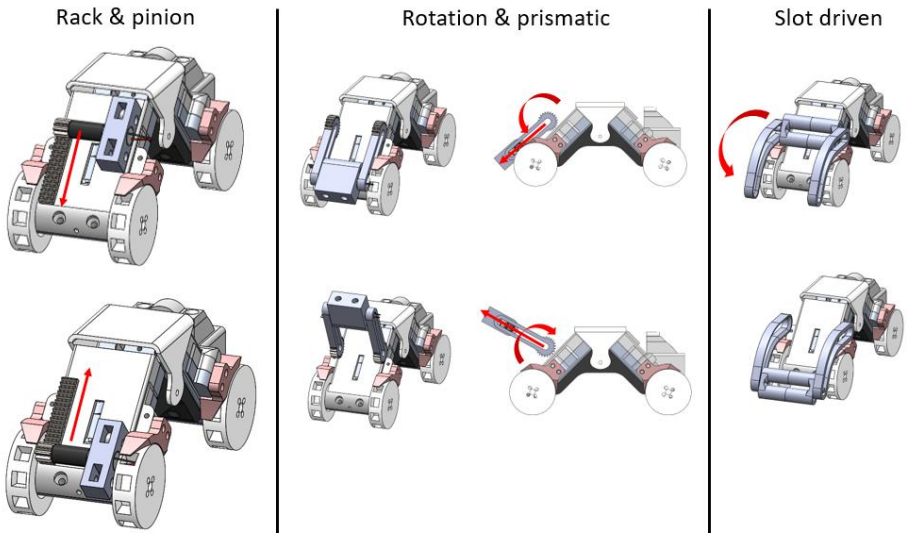


**Figure 68. Candidate sampling mechanism designs.**

Efforts were dedicated to developing several sampling systems beyond the previous conceptual stages and starting viability studies for manufacturing and testing individual components.

Figure 69 shows three distinct robotic arms considered for their ability to interact with both the primary liner and surrounding refractory concrete channel surfaces. Each design's overall reach, strength, and robustness is vital in selecting a candidate system for deployment.

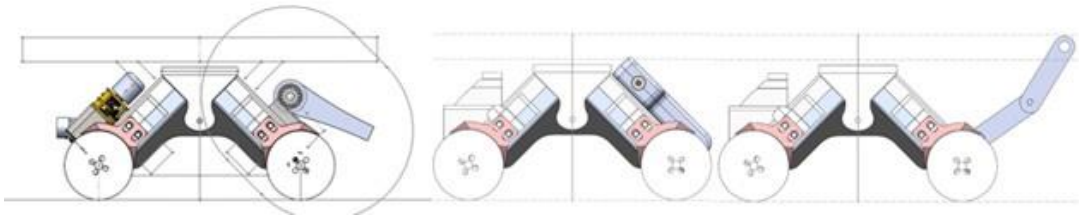

**Figure 69. Conceptual sampling mechanisms.**

The workspaces and motion of the candidate sampling arm designs are also shown in

Figure **70**.

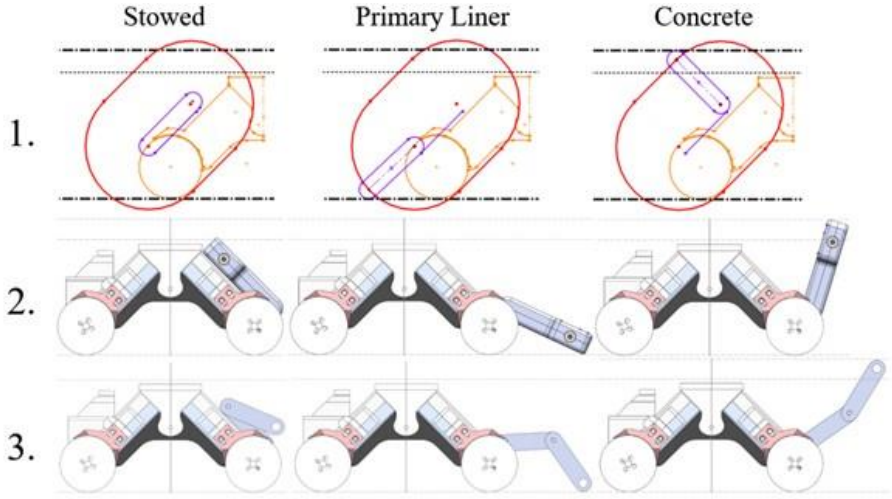


**Figure 70. Candidate sampling arms.**

The sampling system's components were prototyped to assess assembly, tolerance fitting, and resin printing compatibility.

Figure 71 (A and B) shows a two-degree freedom cable-driven arm using two rear-mounted motors to actuate a leadscrew and a rotate joint powering the frontal sampler. States of the mechanism are shown stowed, touching the refractory channels, and touching the primary liner in Figure 71(C).

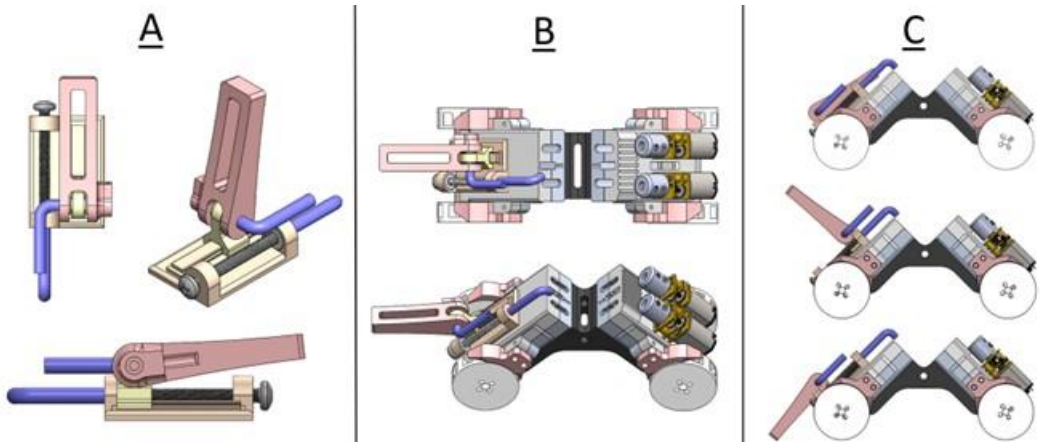


**Figure 71. Sampling mechanism (A), rear-mounted motor actuators (B), and functionality (C).**

Additional efforts included printing parts in draft resin to assess strength, press-fit hardware, and print-in-place capabilities. The print-in-place components require tight tolerances for the respective elements, causing unwanted adhesion beyond the printer's resolution. Figure 72 shows the parts of an early candidate sampling mechanism and their typical areas of failure.

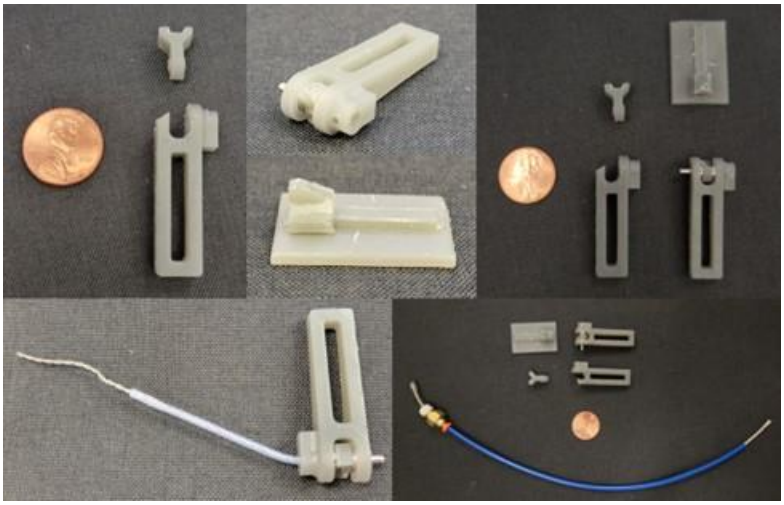

**Figure 72. Sampling arm and base prototypes.**

Figure 73 shows the selected candidate design, a two degrees of freedom sampler arm, that uses a motorized rotational joint and a prismatic joint to probe material deposit at the primary liner and the DST's concrete refractory channels.

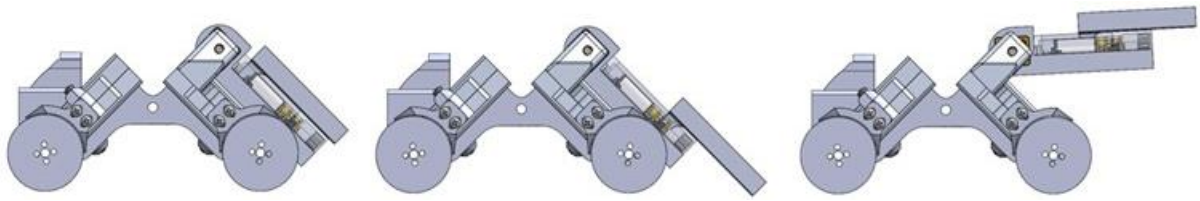

**Figure 73. FIU's Miniature Magnetic Rover's sampler arm.**

Figure 74 shows the prismatic joint powered by a lead screw. The lead screw forces were analyzed to ensure the sampler mechanism could withstand scraping reactive forces.

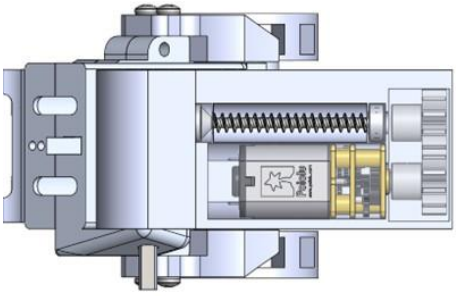

**Figure 74. Sampler's prismatic joint.**

Table 4 presents the candidate actuators for the prismatic joint. The calculations neglect potential losses due to friction and eventual misalignment.

**Table 4. Prismatic Joint Actuator Selection**

| | M2 Lead Screw | | | | M3 Lead Screw | | |
|---|---|---|---|---|---|---|---|
| | Plastic (900:1) | Metal(380:1) | Metal(1000:1) | | Plastic (900:1) | Metal(380:1) | Metal(1000:1) |
| dm | 0.001774 | 0.001774 | 0.001774 | dm | 0.0027195 | 0.0027195 | 0.0027195 |
| f | 0.51 | 0.51 | 0.51 | f | 0.51 | 0.51 | 0.51 |
| l | 0.0004 | 0.0004 | 0.0004 | l | 0.0005 | 0.0005 | 0.0005 |
| Tl | 0.009 | 0.05 | 0.1 | Tl | 0.009 | 0.05 | 0.1 |
| F [N] | 24.0011372 | 133.3396511 | 266.6793022 | F [N] | 15.09805898 | 83.87810543 | 167.7562109 |
| F [lbf] | 5.395670286 | 29.97594603 | 59.95189207 | F [lbf] | 3.394178682 | 18.85654823 | 37.71309646 |

Figure 75 shows the first design iteration of rover's sampler system after months of prototyping and research. The design also included space for electronics, lights, and front and rear camera modules.

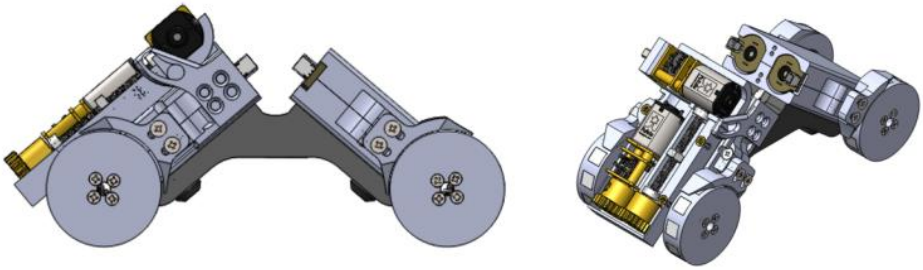

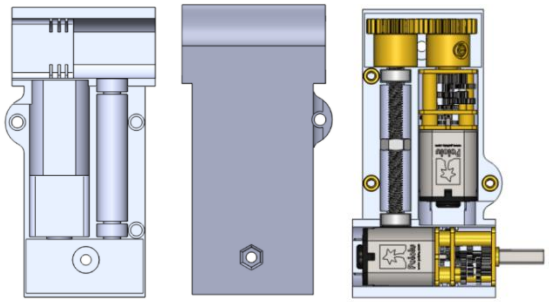

**Figure 75. First design iteration of rover's sampler.**

Figure 76 illustrates subtle changes made to the sampler gearbox to maximize space for the new hardware and modifications to the sampler mechanism.

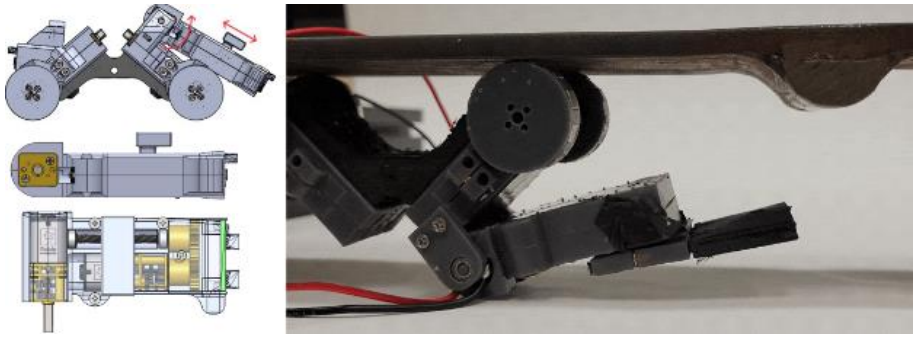

**Figure 76. Second design iteration of rover's sampler.**

Figure 77 shows a sampling system's functional prototype. The articulated arm has an ample workspace and can sample material from the tank's primary liner and reach deposits on the concrete refractory channels.

**Figure 77. FIU miniature rover's sampling systems.**

To enhance the rover's performance and maneuverability based on the constraints of the DST's refracture channel geometry on Hanford's DSTs, the team focused on two key aspects:

- optimizing the rover's length and
- minimizing its height to ensure it could effectively navigate a 30-degree turn.

The flexible connection angle characteristic of the U-shape chassis frame governs the rover's overall length and height, as illustrated in Figure 78.

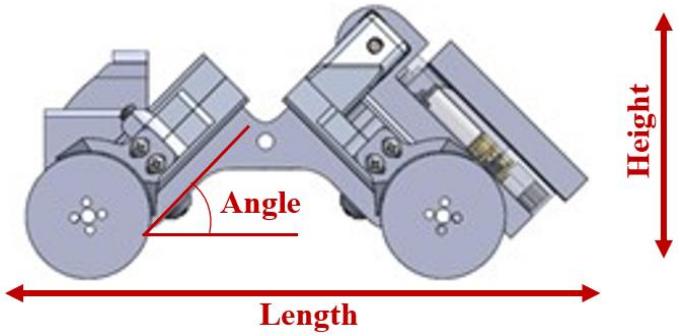


**Figure 78. Flexible connection angle.**

Figure 79 presents the chassis' maximum length and height calculations based on the flexible connection angle.

$$x_{Channel\ Width} = 2(-\frac{y_{Channel\ Height}}{3.33} + 31.75)$$

$$\{y_{Channel\ Height} | 0 \le y_{Channel\ Height} \le 63.5\}$$

$$l(\theta) = x_{Channel\ Width}(\csc\theta + \sec\left(\theta + \frac{\pi}{3}\right))$$

$$\{\theta | 0 < \theta < \frac{\pi}{3}\}$$

$$l'(\theta) = x_{Channel\ Width}\left(-\csc\theta\cot\theta + \sec\left(\theta + \frac{\pi}{3}\right)\tan\left(\theta + \frac{\pi}{3}\right)\right)$$

Critical point and minimum @ $l'(\theta) = 0$

Simplified solution:

$$1 = \sin\theta\tan\theta\cot(\frac{\pi}{6} - \theta)\csc(\frac{\pi}{6} - \theta)$$

$$\theta = \frac{\pi}{12} + \pi k, \quad Where\ k = \mathbb{R}$$

$$l\left(\frac{\pi}{12}\right) = x_{Channel\ Width}(\csc\frac{\pi}{12} + \sec\left(\frac{5\pi}{12}\right))$$

$$l\left(\frac{\pi}{12}\right) = x_{Channel\ Width}(2\sqrt{2}(1+\sqrt{3}))$$

$$l(y_{Channel\ Height}) = (2(-\frac{y_{Channel\ Height}}{3.33} + 31.75))(2\sqrt{2}(1+\sqrt{3}))$$

@ the channels highest point the width is 63.5 mm and the maximum length is 490.690 mm

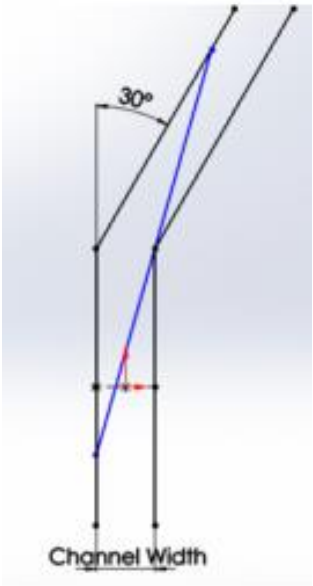


**Figure 79. Chassis length and height calculation.**

Figure 80 shows the current flexible connection angle optimized to maneuver through the refractory channel turns, considering the rover's ideal length and height, including the sampler addition.

**Figure 80. Optimal chassis angle.**

Figure 81 shows the current design iteration of the rover's sampler system. The innovative chassis design strategically incorporates three hinges to provide structural support and promote moment bending when subjected to vertical or horizontal loads, significantly enhancing the rover's ability to handle various terrains and navigate buildup, corrosion spots, oblique weld seams, and other potential eventual obstacles along DST floor inspections.

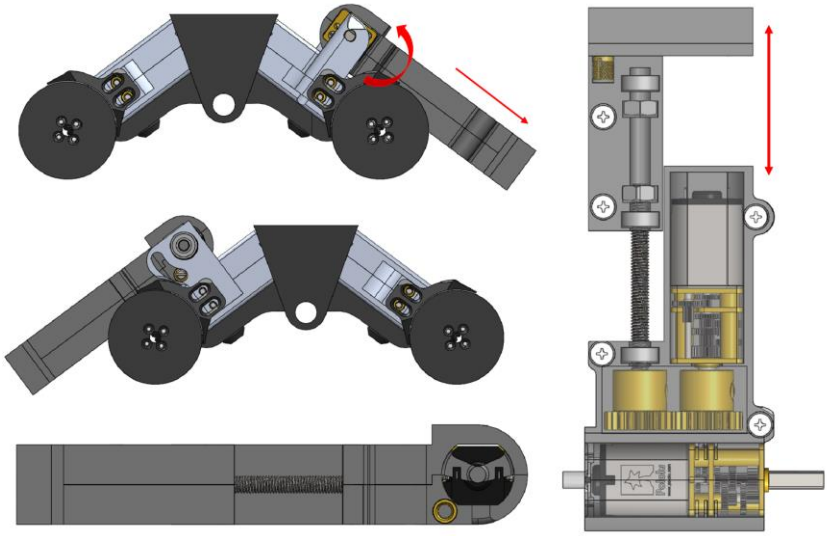

**Figure 81. Current design iteration of rover's sampler.**

The restrictive geometry and existing floor conditions of DSTs' refractory channels at Hanford tank farms impose multiple challenges to designing and integrating a robust sampler system into FIU's miniature inspection rover. FUI's sampler system development will continue in the 2024 performance period, and there are plans to deploy the retrofitted inspection tool at Hanford in the summer of 2025.

## Subtask 18.5.2 – Lateral Gamma Scanner Development and Support

FIU continued to support the lateral gamma scanner task, streamlining the crawler and reel synchronization and improving localization accuracy during the proposed automated inspections of SSTs' laterals. The crawler and reel's components were streamlined based on lessons learned from Hanford's Cold Test Facility deployment. FIU started supporting the integration of the radiation sensors in close coordination with WRPS scientists. The LGS system was redeployed at Hanford's Cold Test Facility during the summer. Finally, efforts were dedicated to training a new DOE Fellow taking over the task, replacing the Fellow who defended his master's thesis on the FIU's Lateral Gamma Scanner System Development and started working at WRPS at Hanford.

### Design Improvement

Figure 82 shows the successful deployment of the LGS system in March 2022 at WRPS's Cold Test Facility in Hanford, Washington.

**Figure 82. Cold Test Facility deployment.**

The tests simulated FIU's peristaltic crawler carrying gamma sensor modules being deployed through a single shell tank's lateral. The sensor payload is a mockup based on a sensor deployed in 2005. The weight and size of the payload were coordinated with Hanford's engineers and scientists.

After Hanford's Cold Test Facility deployment, the primary development focused on streamlining the pipe crawler design, addressing issues learned from the summer deployment. Cable management is a significant issue due to the pipe crawler's compact design, especially inserting and removing the main ethernet cable through the modules, which is currently cumbersome, requiring module disassembly, cutting, and re-soldering of multiple ethernet connectors.

Figure 83 shows a preliminary design of a hollow-core extender module, which uses four pistons equally spaced around the diameter instead of the current configuration where a single central piston per module is used. A hollow core and the possibility of routing the cables through the center will eliminate the need to cut and resolder the cable connectors, a very specialized task not feasible for field operators.

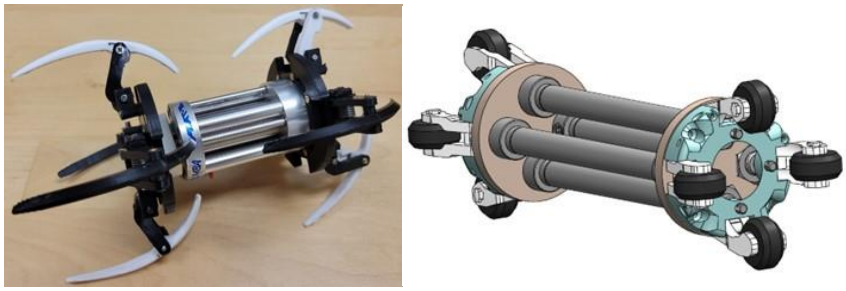

**Figure 83. Extender module current design (left) and hollow redesign (right).**

Another addressed concern was the hinged guides' structural reliability. During inspections, the guides keep the crawler suspended at the pipe center, minimizing drag, wear, and tear. Figure 84 shows a preliminary monolithic redesign, replacing the current spring-loaded arms with compliant ones using 3D-printed flexible materials. Compliant components eliminate hinges and springs, reducing the number of small and moving parts and potentially removing points of failure.

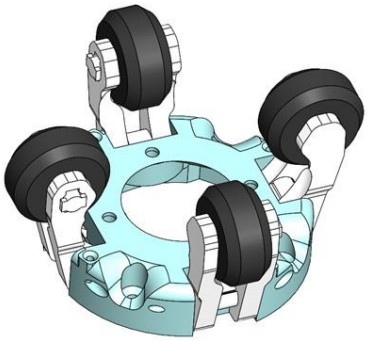

**Figure 84. Redesigned module guides using compliant material.**

Figure 85 shows the redesigned gripper modules, four smaller pneumatic pistons laid out evenly in a radial configuration, replacing the single central piston that actuated the grippers, making the pipe crawler more modular and maintainable.

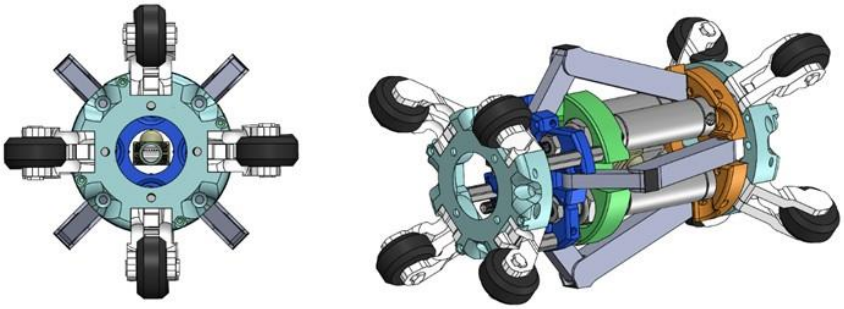

**Figure 85. Crawler's gripper modules.**

Figure 86 shows a functional prototype for the improved gripper design. The gripper uses a rubber blade per pneumatic piston instead of the single flange, attaching the four actuators that move the blades simultaneously. The independent blades better conform to pipe walls, gripping evenly on curved surfaces.

**Figure 86. Improved gripper module with independent blades.**

The design improvements on the crawler's gripper module enhanced the previous gripping force from approximately 20 pounds to 45 pounds per module, as demonstrated in Figure 87.

**Figure 87. Crawler's gripper module gripping test.**

Figure 88 shows the most current prototypes of the pipe crawler modules, including all improved modules. The improvements also include strengthened wheel guides. The guides center the crawler module, minimizing friction and potential debris accumulation during inspections.

**Figure 88. Pipe crawler improved modules.**

Figure 89 shows a tether quick-disconnect attachment integrated into the inspection tools to improve maintenance.

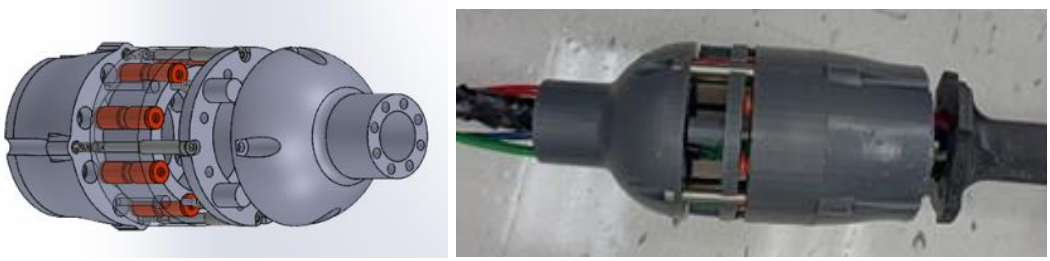

**Figure 89. Tether quick disconnect.**

## Automation Improvement

The functionality of the LGS system was extended, and its graphical user interface (GUI) improved, allowing Hanford's operators to monitor and interact with the system’s components during automated inspections. The added functionalities provide user feedback on the state of the crawler, sensory payload, tether reel, and estimated location in real time, making the system more flexible and reliable during operation.

The FIU’s Miniature Inspection Rover operator interface uses a slightly modified version of the GUI developed for the LGS system, sharing more intuitive and friendly controls to WRPS's field operators by adopting conventional visual controls, such as toggleable menus and media buttons, used in popular camera and video capture programs. The application implemented video recording functionalities, inspection video playbacks, and addressed eventual hardware issues such as camera and sensor malfunction, network and tether connectivity, and abnormal electrical voltages and pneumatic pressures to ensure robustness during field deployment.

Illustrated in Figure 90, in the LGS, a touchscreen integrated into the system's mechanized reel displays the user interface. The operator activates and tests any individual crawler modules by touching the respective visual control in the GUI.

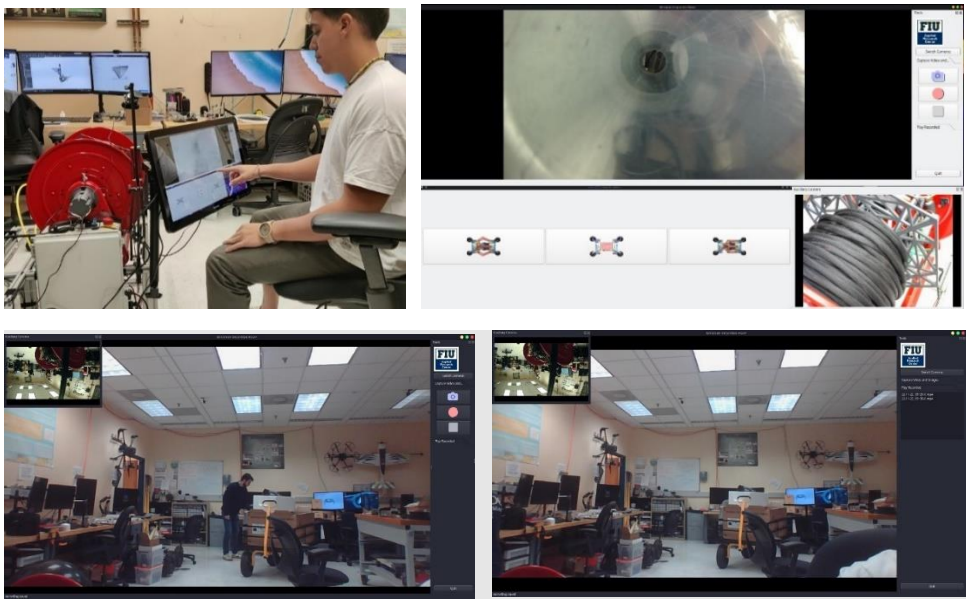

**Figure 90. Lateral Gamma Scanner's operator interface.**

Figure 91 shows the GUI's main layout, most prominently displaying sensor data and video feed from cameras at the front of the crawler and the top of the tether reel. The default GUI's view shows both camera videos simultaneously. However, the interface is fully customizable, and the operator can rearrange and resize any graphical component.

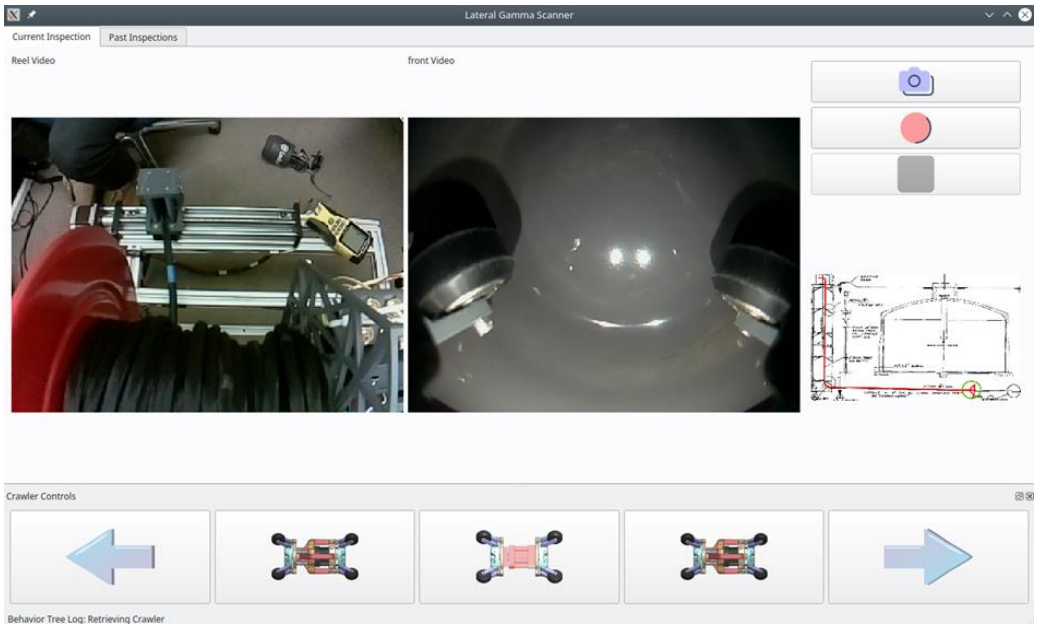


**Figure 91. Operator Graphical Interface's main layout.**

The LGS system is fully autonomous, the implemented field-ready GUI encapsulates all automation details, data acquisition, logging, crawler movements, reel synchronization, tool retrieval, and status monitoring during inspections. However, site operators can override the autonomous process if needed, monitoring and controlling the inspection progress graphically and intuitively.

The LGS system is implemented in C++ and integrated using the Robotic Operating Systems (ROS2). The GUI is also built in C++ and ROS2 using the Qt graphical library, not requiring the operator to have any specialized knowledge of programming, networking, or command-line tools characteristic of the first deployment and proof of concept demonstration at WRPS. Additionally, the system integration using ROS2 allows the GUI to run on any computer connected to the LGS's ethernet network, making it convenient to supervise and operate the system from outside the tank farm.

The system's automation employs the ROS2 BehaviorTreeCPP library to perform sensor probing, decision-making, and actuation commanding. Figure 92 shows the LGS behavior tree's algorithm depicting all actions during a complete automated inspection cycle. In the tree model, each element in the system (the reel, the crawler, the sensors, etc.) is controlled separately as a *"branch"* in the tree, which makes the system more flexible and reliable over time.

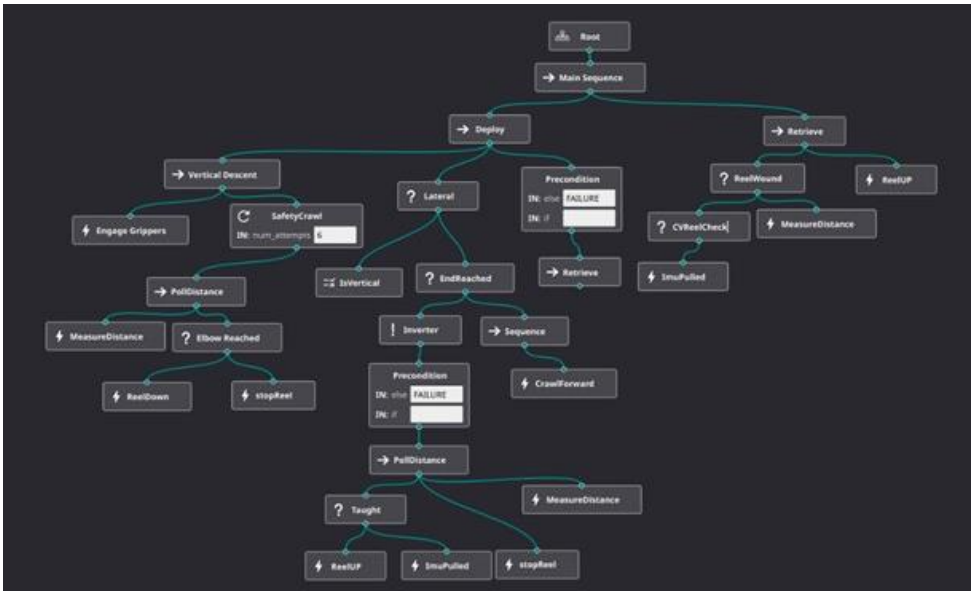


**Figure 92. Lateral gamma scanner's behavior tree automation.**

A behavior tree automation model runs as hierarchical structures comprising a root node representing the overall behavior and multiple child nodes defining sub-behaviors. Each child node can be another tree or a simpler control structure, such as a sequence or a selector. This hierarchy is *"ticked"* node by node, starting at the root until a tick reaches a node at the bottom of the tree. At this point, the node executes its role and returns one of three statuses (success, failure, or running) as a signal to its parent node. Behavior trees tend to be more natural for decision-making and goal planning than the finite state machine controller previously implemented. The tree outwards-branching structure results in more complex decision-making, allowing the system to consider multiple options simultaneously. State Machines, in contrast, are typically flat structures whose fixed number of states limits their complexity.

Behavior tree models are traditionally composed of reusable and modular nodes. In the LGS automation, rewinding the tether up using the mechanized reel is employed at different points in the inspection and under different conditions. Although this action is identical every time, it has various purposes depending on how it is structured in the tree and paired with other conditions.

Efforts were also dedicated to improving the crawler's localization during lateral inspections, using additional position estimation tracking tether marks placed at regular intervals along the cable using computer vision, as shown in Figure 93. Previous estimations relied on integrating discrete acceleration measurements to calculate a position and counting the number of times the crawler has inched forward.

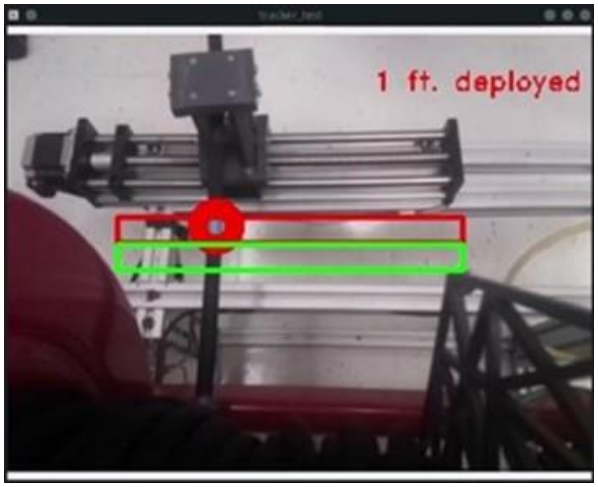


**Figure 93. Tracking of deployed-tether length.**

The current position estimation routine ensures that the tether is taut during measurements by reeling back the cable until the frontal module's IMU detects crawler jerks. Similar combinations of actions are used at many inspection points; thus, they are saved as reusable subtrees. Figure 94 shows the behavior tree's current state of development.

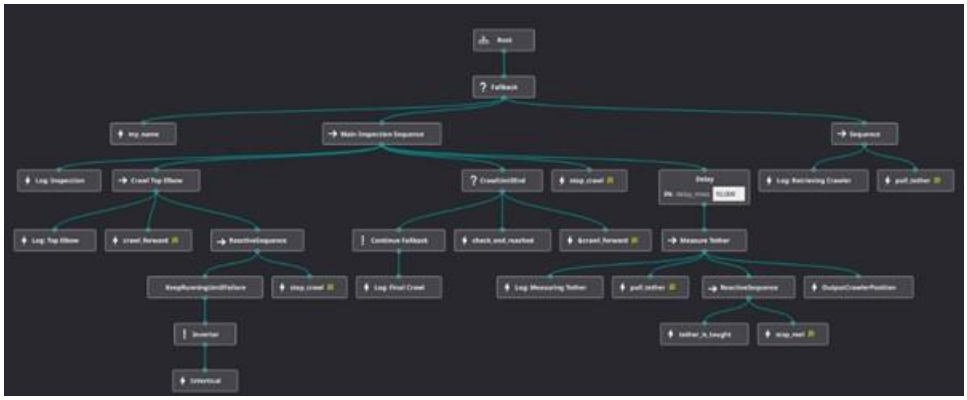

**Figure 94. Updated LGS's behavior tree.**

## Summer Redeployment at Hanford

In the summer of 2023, the LGS was redeployed at Hanford's Cold Test Facility. The effort was part of the WRPS's Engineering and the Chief Technology Officer partnership with FIU to develop a technology that can detect possible leaks under single-shell tanks. The deployment received positive feedback from site engineers for a potential 2024 deployment at Hanford's SST tank farm.

Figure 95 illustrates details of FIU's deployment efforts featured on WRPS social media.

# WRPS collaborates with FIU to design tool for detecting single-shell tank leaks

Engineering and the Chief Technology Office (CTO) are continuing their partnership with Florida International University (FIU) to develop technology that can detect possible leaks under single-shell tanks (SSTs).

The "Lateral Gamma Scanner" project is one of three summer internships currently being sponsored by WRPS. The crawler moves through existing horizontal pipes by using mechanical grabbers that push and pull it along the inside of the pipe, while sensors detect possible leaks by measuring gamma radiation from cesium-137.

Josue Estrada, a WRPS intern and Department of Energy (DOE) Fellow, is part of the team continuing work from last year. He was present to help lead a recent demonstration at the Cold Test Facility (CTF).

"This year, we've furthered development of the system in its reliability, operability, and maintenance," he explained.

The crawler's gripper module has undergone significant design improvements, enhancing the previous gripping force from approximately 20 pounds to 45 pounds per module. The upgrade will allow the tool to crawl through more debris with relative ease. The improvements also include strengthened wheel guides. The guides center the crawler module to minimize friction and potential debris accumulation during inspections.

"We also enhanced operability by adding a more user-friendly interface that shows a video feed of the crawler moving forward and allows the operator to pause and resume the operation with a touchscreen button on a display monitor," said Estrada.

The design team integrated a quick-disconnect attachment into the inspection tools and redesigned the crawler's modules, which previously had wires soldered in place around the crawler's central piston. The new modules have hollow centers that allow cables to be inserted or removed as needed without soldering.

The recent demonstration tested the improved device in front of several WRPS engineers.

"I am impressed by the exceptional talent and unwavering dedication displayed by the students of the DOE Fellowship program at FIU," said Doug Reid, a WRPS mechanical engineer who is Estrada's mentor in CTO. "As a proud corporate sponsor, I have witnessed the remarkable partnership between academia and industry. The students' intelligence, creativity, and technical prowess have benefitted WRPS. Their passion for learning and innovation is a true testament to their potential as future leaders in technology."

"We are honored to have collaborated with these talented individuals and remain committed to supporting their continued success," he added.

In the upcoming fall semester, the robotics team at FIU's Applied Research Center will begin the integration and testing of a preliminary gamma sensor into the crawler system. This development aims to deliver a prototype ready for tank deployment in 2024.

*The "Lateral Gamma Scanner" crawler bot is lowered down the pipe and retracted using a reel and cable system.*

*DOE Fellow and WRPS intern Josue Estrada explains how the design team has improved the crawler bot's ability to navigate debris in pipes during a demonstration at CTF.*

*The new interface allows an operator to interact with the crawler's automation system more easily.*

*The crawler bot uses small, mechanical grippers to push and pull itself along the inside of a pipe.*

Page 5

**Figure 95. LGS deployment featured on Hanford social media.**

The lessons learned from the summer deployments and WRPS engineers' feedback guided the design improvement presented in previous sections.

## Subtask 18.5.3 – Off-riser Sampler Development

As requested by WRPS, FIU concentrated on designing, building, and testing a nimble manipulator equipped with appropriate end-effector tooling to sample 4-inch risers. Commercially available industrial manipulators typically have wider than 4-inch footprints that cannot fit through small risers in single-shell tanks. The considered operational scenarios include scooping mud or chipping off hard specimens. The plans to deploy the system at the single-shell tank full-scale mockup at Hanford's Cold Test Facility during the summer of 2023 were postponed to 2024 due to challenges in developing such a small-footprint mechanical arm with relevant dexterity and payload capacity.

Figure 96 shows the conceptual design of the off-riser sampling system. The development poses several challenges, including the tank sampling height, small riser diameter, inside high radiation doses, and waste viscosity itself.

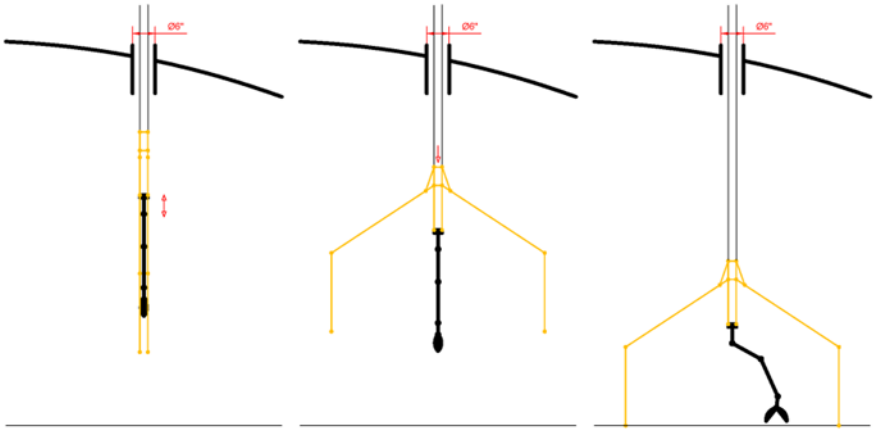

**Figure 96. Off-riser sampler's conceptual design.**

Figure 97 illustrates the conceptual design of a four-degree-of-freedom pneumatic-driven mechanical manipulator. Pneumatics actuators are inherently radiation hardening and are cost-effective compared to hydraulics. Even though hydraulic systems are more powerful, tend to be more precise, and are less likely to be affected by changes in temperature, pneumatic systems are easier to maintain. However, the team is still debating the benefits of pneumatics versus hydraulics for the final systems, and preliminary tests involving payload handling and dexterity tests will be critical in guiding the design.

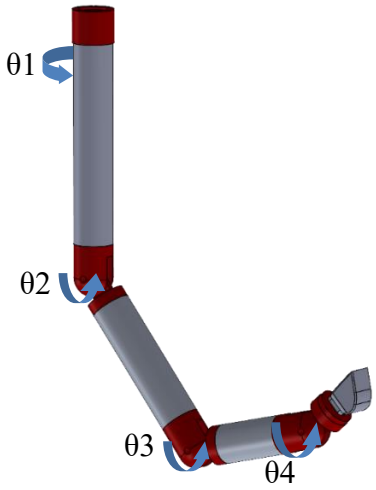


**Figure 97. Sampler manipulator's conceptual design.**

## Mechanical Design

Figure 98 shows an early design for a pneumatic chain-driven 3.5-inch diameter joint. The assembly uses a single pneumatic actuator to reach 5 feet, lifting approximately 10 lbs.

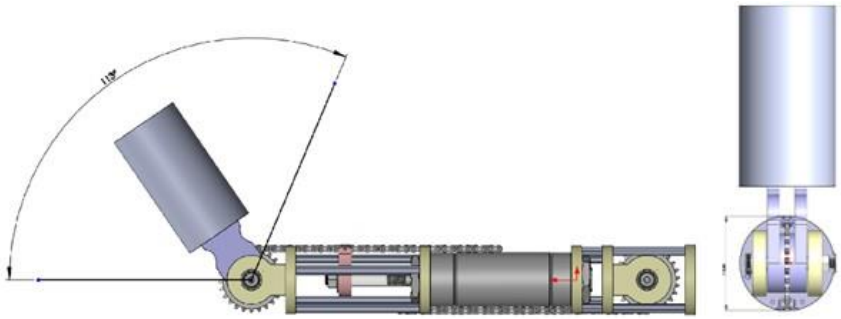

**Figure 98. Pneumatic joint design.**

The joint was designed during the summer of 2023 by the DOE Fellow working on the task, continuing his research as an intern at WRPS in Hanford. The effort is part of the WRPS's Engineering and the Chief Technology Officer (CTO) partnership with FIU to develop technology that can sample waste inside Hanford's SSTs through small risers.

As illustrated by Figure 99, designing a pneumatic joint with the required compact footprint is challenging, involving multiple component redesign interactions to address assembling and manufacturing issues.

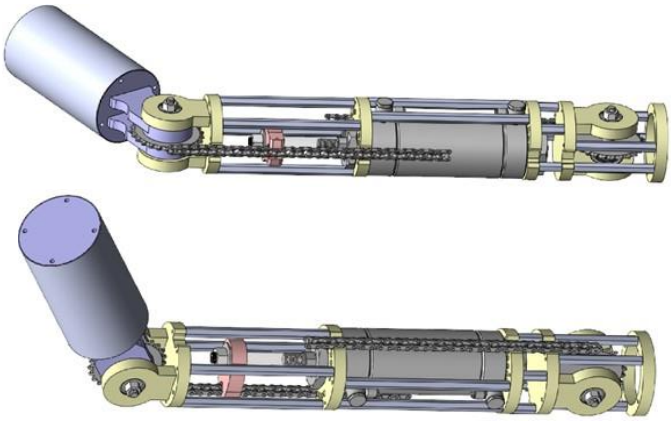

**Figure 99. Off-riser sampler pneumatic joint.**

Finite Element Analysis (FEA) was implemented to optimize each component in the assembly for maximum strength and minimum weight. To illustrate the interactive process, Figure 98 shows a streamlined bearing mount under load.

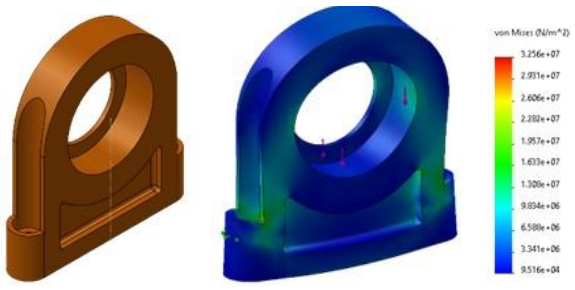

**Figure 100. FEM analysis of assembly component.**

Figure 101 shows an exploded view of the joint core. The modular design consists of a:

- driving end,
- motion carriage,
- idler end, and
- the actuator core.

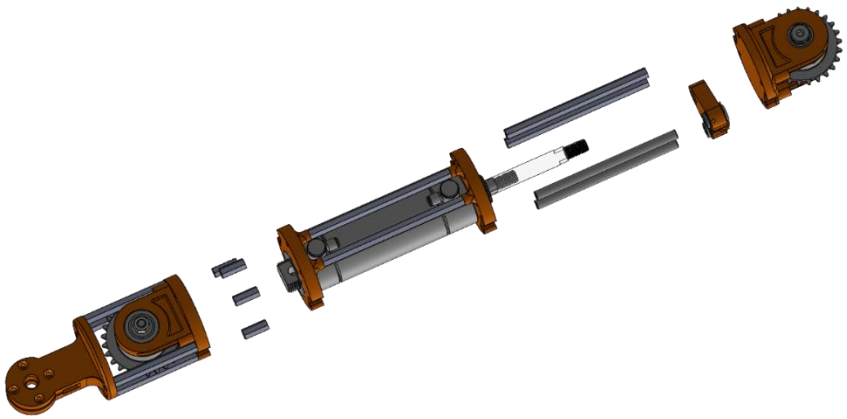

**Figure 101. Pneumatic joint core's exploded view.**

The joint's strength and rigidity come from the use of aluminum stand-offs and steel linear motion rails. Figure 102 shows the joint's first driving end. The assembly utilizes a flat ANSI 35 roller-chain sprocket. The sprocket is bolted to the nest joint.

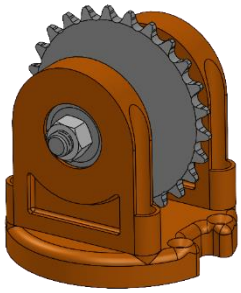

**Figure 102. Pneumatic joint's driving ends.**

The linear motion carriage, shown in Figure 103, transfers the motion of the air cylinder to the chain and is supported by two linear rods. The rods ensure smooth movement, resisting the torque that the chain and cylinder would exert on the carriage, and serve as structural members of the design. The carriage also contains an integrated chain tensioner to ensure smooth operation.

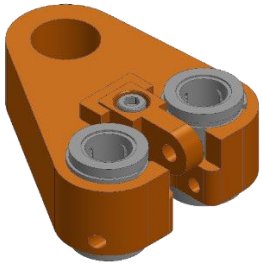

**Figure 103. Linear motion carriage assembly.**

Figure 104 shows the actuator core assembly designed. The core uses the air cylinder as a structural member, reducing weight and saving space. More miniature actuators are used in joints closer to the end effector, requiring less torque along the arm.

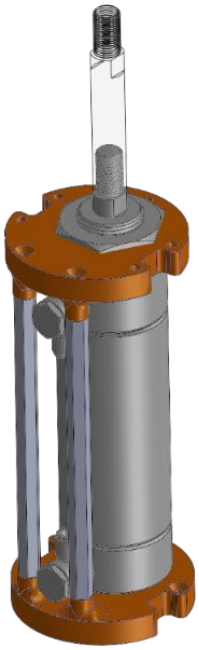

**Figure 104. Pneumatic joint's actuator core assembly.**

Figure 105 shows the joint's second driving end. The idler sprocket connects and drives the other limbs.

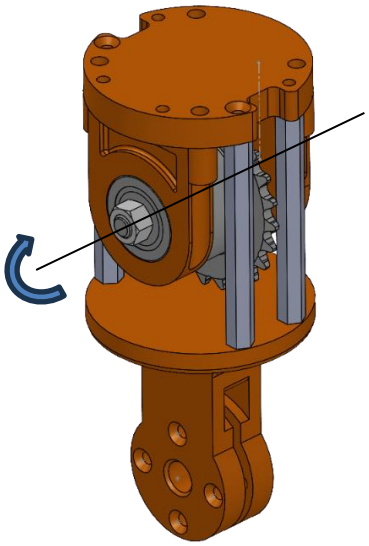

**Figure 105. Pneumatic joint's idler sprocket driving end.**

The idler end also contains the encoder, making precise control of this pneumatic system possible. Magnetic encoders were chosen for their resistance to radiation. A belt and two pulleys link The

encoder to the idler shaft. The tension of the pulley can be adjusted by moving the encoder and tightening it in place, as seen in Figure 106.

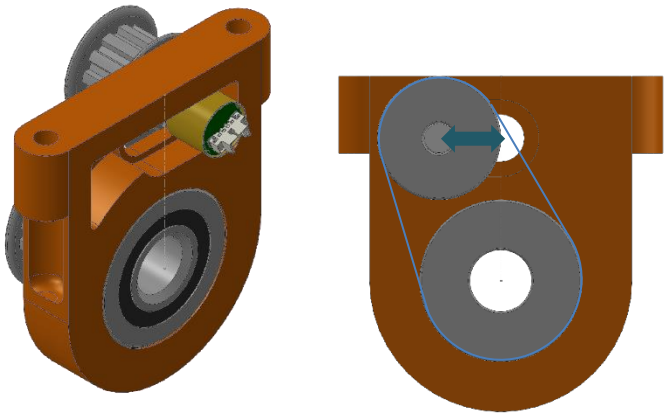

**Figure 106. Pneumatic joint's encoder.**

Figure 107 shows the sampler manipulator's complete design, not including the pivoting joint at the base. The arm's reach is currently approximately 4 feet. There are plans to design an end effector containing a tool changer for interchange tooling to address wastes of different consistencies and under other conditions. The base pivoting joint design and arm integration are part of the research efforts in the upcoming performance period 2024.

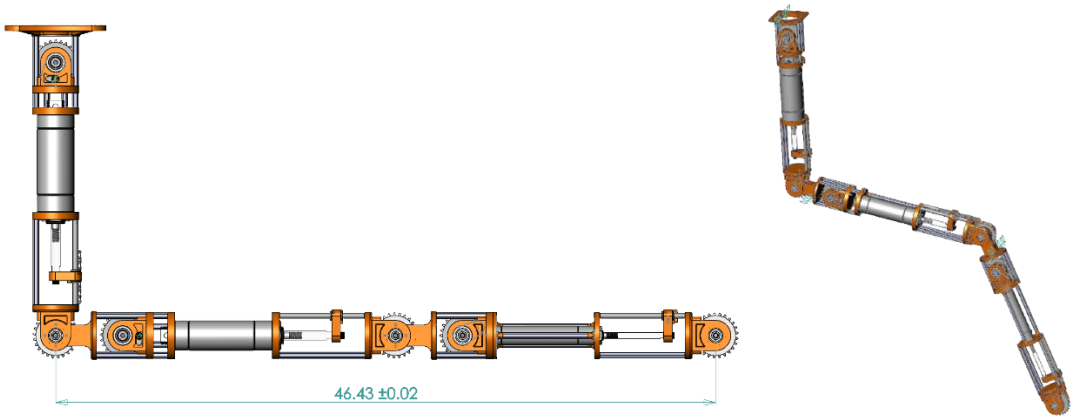


**Figure 107. Sampler arm's design.**

Figure 108 shows a functional prototype of the pneumatic joint assembled and demonstrated at Hanford's Cold Test Facility. The lessons learned from the summer interaction with WRPS engineers, and their feedback were crucial to guide the technology development when the Fellow returned to FIU.

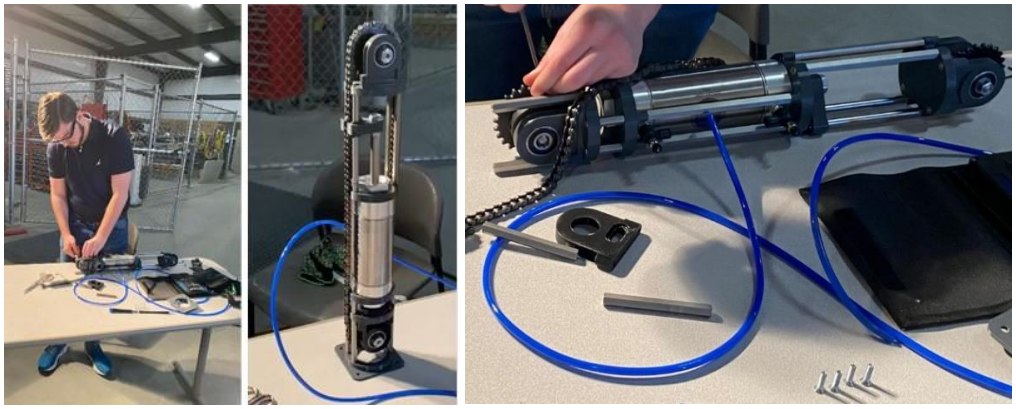

**Figure 108. Pneumatic joint's functional prototype.**

## Controls

Each pneumatic joint's cylinder is actuated by a three-position solenoid valve controlled by solid-state relays commanded by a microcontroller receiving position feedback for a rotary encoder. As illustrated in Figure 109, the solenoids allow the cylinders to stop partway through their motion.

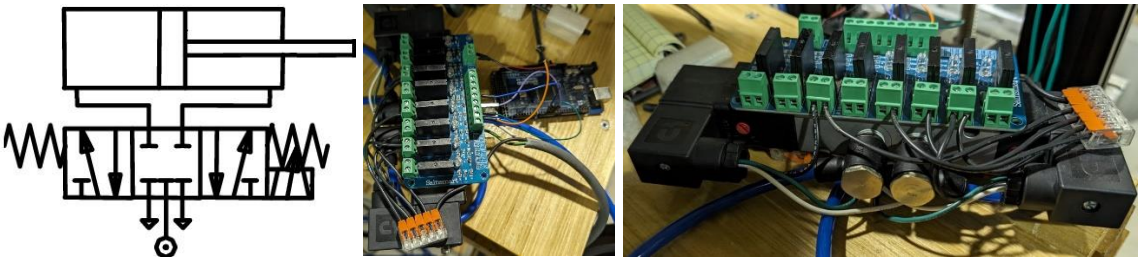

**Figure 109. Pneumatic joint's three-position control schematic (left) and prototype (right).**

## Manufacturing

The team also focused on improving the robotics laboratory manufacturing capabilities to construct a robust off-riser sampler prototype. CNC software, tooling, calipers, and materials were purchased for the laboratory. As illustrated by Figure 110, the list also includes benchtop equipment to machine aluminum parts, mainly a CNC 5-axis mill, a manual mill, and a CNC router.

**Figure 110. Laboratory's newly acquired machining equipment.**

Figure 111 shows two stereolithography (SLA) resin printers acquired to provide rapid prototype components with greater strength, precision, and detail accuracy than our current fused deposition modeling (FDM) filament printers.

**Figure 111. Laboratory's newly acquired resin printers.**

The team's manufacturing improvement efforts included training on design for manufacturing, machining equipment, and safety to support other DOE-EM tasks supported by the laboratory.

## Bench Scale Testing

Figure 112 shows preliminary joint tests lifting 45 pounds to simulate the equivalent required payload.

**Figure 112. Pneumatic joint's payload testing.**

Figure 113shows the test testbed developed to demonstrate the off-riser sampler capabilities. The frame is motorized to simulate the arm's vertical movement during sampling operation at SST.

**Figure 113. Off-riser sampler's testing mockup.**

## Subtask 18.5.4 – In-Situ 3D Printing Concrete Structures for Waste Containment

In collaboration with SRNL, FIU researched in-situ 3D printer techniques to dispose of and contain nuclear waste in concrete structures. The task investigated potential 3D printer and nozzle designs to build prototypes, optimize concrete recipes and processes suitable for nuclear waste containment.

Radiation containment for short-term storage is vital in protecting health and the environment from damage. Current storage of nuclear wastes relies on standard-size metal containers. Irregular or large objects generally occupy precious volume. Implementing 3D printing with concrete tailored to absorb radiation will help reduce wasted volume, potentially alleviating operational burdens.

During the 2023 summer, the DOE Fellow working on the task continued his research interning at SRNL on their 3D printing project, using SRNL's concrete recipes and printers, presented in Figure 114.

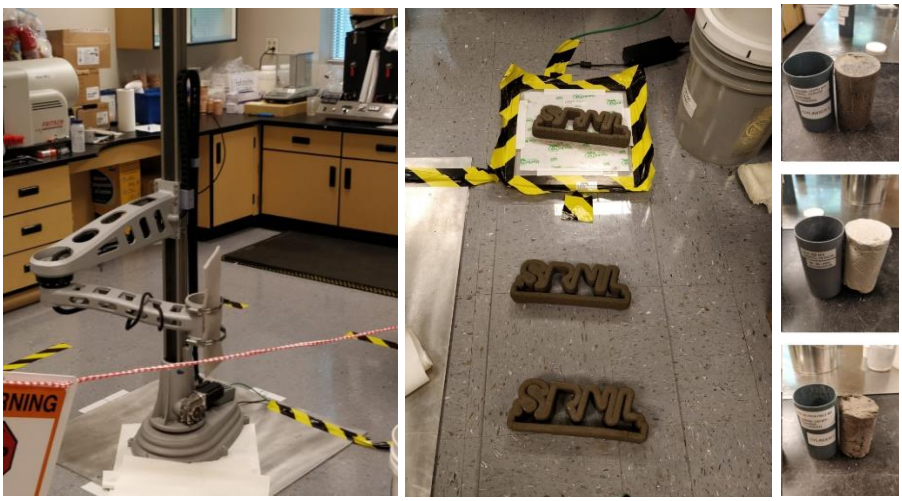


**Figure 114. DOE Fellow's summer results at SRNL.**

The lessons learned from the summer interaction with SRNL's scientists, and their feedback were crucial to guide the project development when the Fellow returned to FIU.

## Nozzle Design

Figure 115 shows our preliminary nozzle design. Standard circular profile nozzles typically do not provide the most adequate layer adhesion. Extrusion from a nozzle with fins that smooth the layers as it usually prints allows for a better surface finish and interlayer adhesion closer to poured concrete.

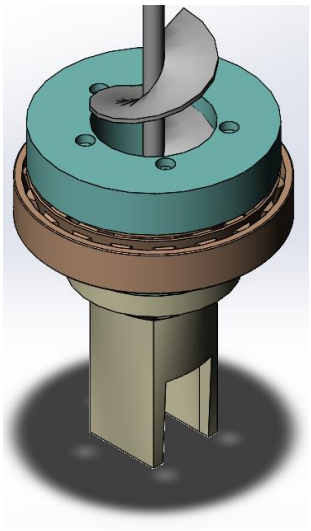

**Figure 115. Printing nozzle's conceptual design.**

Figure 116 shows our nozzle's final design. The nozzle maintains a divergent path to the print geometry curve while smoothing the layer lines.

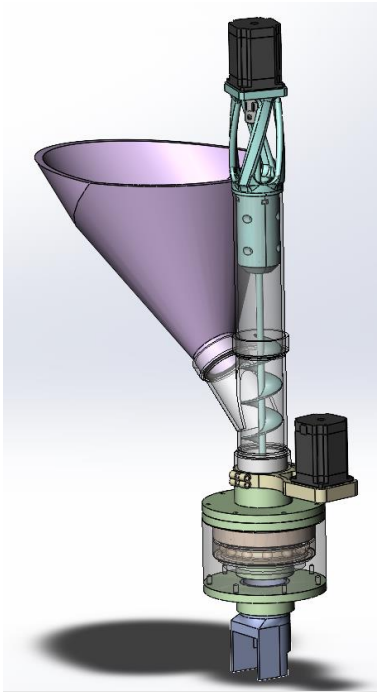

**Figure 116. Printing nozzle's design.**

Figure 117 shows a functional nozzle prototype built for a FIU. All components were successfully 3D printed and tested for fitment. The thermoplastic part presented adequate structural reliability and accurate dimensional tolerance.

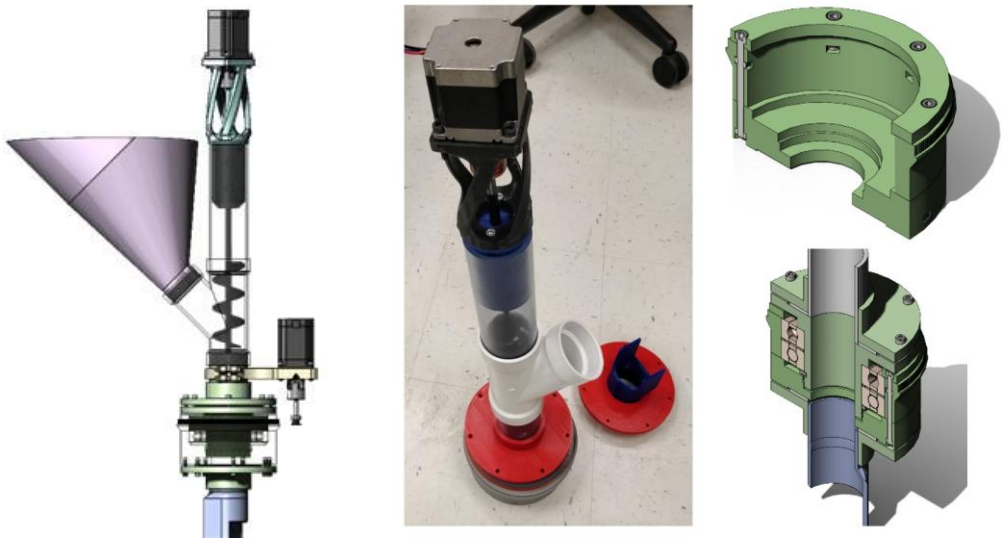

**Figure 117. Auger nozzle's prototype.**

Figure 118 shows a piston-type nozzle, designed as baseline performance for extrudability comparisons with our designed continuous print nozzle. The piston nozzle design was based on a concrete printer successfully tested by the DOE Fellow during his summer internship at SRNL.

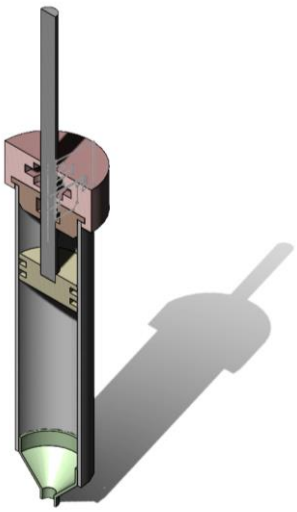

**Figure 118. Piston Nozzle's conceptual design.**

**Motion System Design**

The current state-of-the-art 3D concrete manufacturing technology was investigated, and various printer system configurations were researched to provide a viable alternative for implementing a future large-scale engineered barrier printing at FIU.

Figure 119 shows a two-axis linear system designed for testing 3D printing nozzles at FIU.

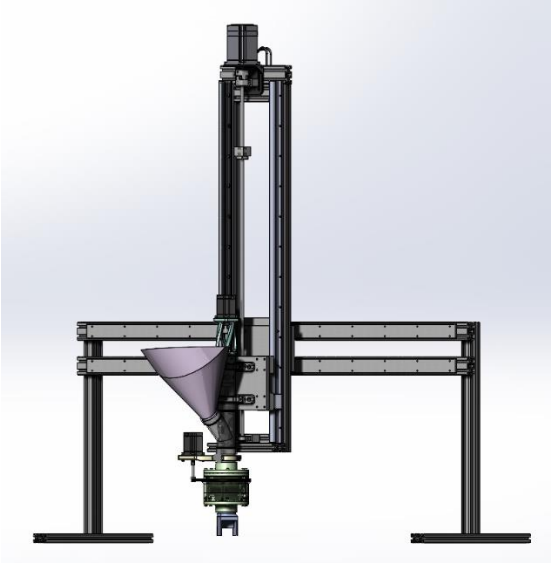

**Figure 119. Motion system's design.**

Figure 120 shows our auger nozzle's prototype mounted onto a retrofitted linear motion system built at FIU.

**Figure 120. Auger nozzle printer's prototype.**

The system's motor controls were upgraded with modern components, shown in Figure 119, for more precise and coordinated movements during printing using a microcontroller running open-source computer numerical control (CNC) machining software.

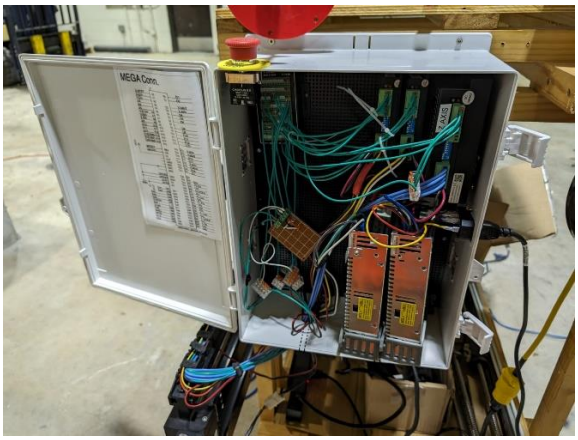

**Figure 121. 3D printer's upgraded control panel.**

The control software was fine-tuned, and the extruder's motor was successfully calibrated to ensure accurate millimeter printing. Printing performance issues were addressed through troubleshooting and maintenance procedures to ensure proper operation and preparation for testing with concrete mixtures.

### Printable Concrete Receipt Optimization

Significant efforts were dedicated to exploring different material options to find better mixes for printable concrete to optimize the printing process, quality, and structural and shielding performance.

Coordinated by SRNL, a concrete formulation to produce 3D printable concrete was concluded, including contacting suppliers to obtain quotes and samples. After encountering difficulty sourcing fly ash, a common material in 3D printable concrete mixes, alternatives were researched, making pumice an acceptable replacement for a pozzolan. Since pumice is more expensive, initial tests will use cement instead.

## Subtask 18.5: Conclusions

The successful incorporation of sampling capability to FIU's miniature rover will continue with the objective of redeploying at Hanford to retrieve sample material under the DSTs in 2025.

The Lateral Gamma Scanner was successfully demonstrated and tested for the second time at Hanford's Cold Test Facility. The system streamlining will continue, and the gamma radiation integration, including other potential sensors requested by WRPS, will be finalized. The discussions regarding a possible 2024 deployment of the LGS at Hanford's tank farm will continue with WRPS.

The Off-riser Sampler System prototype will be finalized and demonstrated at Hanford's Cold Test Facility during the upcoming 2024 summer. The team will continue streamlining the pneumatic arm's components, resume designing a deployment cable hoist system, and start implementing a stabilization mechanism.

The 'In-Situ 3D Printing Concrete Structures for Waste Containment' research collaboration with SRNL will continue exploring different mixes and optimized processes in conjunction with the DOE Fellow's summer internship, resuming his research at SRNL in the summer of 2024.

## Subtask 18.5: References

1. Randall, R. and Price, R. K., 2006, Gamma Surveys of the Single-Shell Tank Lateral for A and SX Tank Farms, CH2M Hill, RPP-RPT-27605, Rev. 0.
2. Engeman, J.K., Girardot, C.L., Harlow, D.G., Rosenkrance, C.L. , 2012, Tank 241-AY-102 Leak Assessment Report, Washington River Protection Solutions, RPP-ASMT-53793, Rev.
3. Stanford Artificial Intelligence Laboratory et al., Robotic Operating System, https://www.ros.org.
4. The Qt Company, Qt Cross-Platform Graphical User Interfaces, https://www.qt.io.
5. DOE (2018, November). Post-Retrieval Activities Changing Hanford Tank Farm Footprint. https://www.energy.gov/em/articles/post-retrieval-activities-changing-hanford-tank-farm-footprint

# TASK 19: PIPELINE INTEGRITY AND ANALYSIS

## Subtask 19.1: Pipeline Corrosion and Erosion Evaluation

### Subtask 19.1: Introduction

The Hanford Site Tank Farm has implemented a Fitness-for-Service (FFS) program for the Waste Transfer System. The FFS program, based on API-579-1/ASME FFS-1, examines structural parameters of the waste transfer systems in order to develop erosion/corrosion rates for relevant system components. The FFS information is acquired from opportunistic evaluations of pipelines that have been removed from service. FIU-ARC engineers work closely with key Hanford high level waste (HLW) personnel and the contractor, Washington River Protection Solutions, LLC (WRPS), to support the FFS program, deliver solutions for sensor evaluations, conduct bench-scale testing followed by data acquisition and analysis for corrosion and erosion assessment. Previous efforts at Hanford included the installation of sensors on a number of the POR 104 components, to provide real time pipe wall thickness measurements. Due to various limitations, alternative approaches for remote permanently mounted pipe wall ultrasonic thickness measurement systems are being investigated.

FIU's efforts to support this scope have included investigating key options available in the market for remote, permanently mounted ultrasonic transducer (UT) and other sensor systems for HLW pipe wall thickness measurements and wear. Specific applications include straight sections, elbows and other fittings used in jumper pits, evaporators, and valve boxes. FIU assessed the use of various ultrasonic systems that are either commercially available or used previously at Hanford and selected the most promising systems for further evaluation. Two sensor systems were down selected. The Permasense UT sensor system and the fiber optic sensors from Cleveland Electric Laboratories (CEL) were acquired, and initial bench-scale validation testing was conducted. Following the initial bench scale tests, engineering scale testing was implemented on an in-house designed and installed test loop. The design loop has been established using 2- and 3-inch diameter straight and bend pipe sections to mount the sensors. The loop was eroded using a sand-water slurry and the Permasense sensors and the CEL sensors were used for thickness measurements [1,2,3,4,5,6]. The Permasense sensors were also tested for their performance in extreme environmental conditions under high humidity and temperatures. Finally, the feasibility of conducting radiation testing on those sensors was considered and a test plan was developed for implementation. Permasense UT sensors were used for thickness detection while the CEL sensors were used for anomaly detection. In addition, SRNL mass loss coupon erosion systems were evaluated for erosion and corrosion detection in the pipe loop at FIU. These included the SRNL coupons with the Pencil UT sensor [4,5].

FIU has successfully completed the sand water erosion tests on both carbon and stainless-steel coupons. Currently, FIU is investigating the effect of glass frit particle erosion and caustic simulant corrosion on the SRNL coupons. A bench scale mockup has been constructed and initial caustic simulant testing has been conducted. The static coupon immersion tests are also being performed in parallel. Benefits of this research include providing validation for new methods and technologies that will assist engineers in understanding the fault potential of HLW nuclear waste transfer components due to corrosion and erosion. By providing insights into determining if and when lines need to be removed/replaced, the unneeded excavation of transfer lines can be avoided, saving valuable time and resources. Also, more detailed and accurate guidelines can be developed

governing the life expectancy of the transfer system and its components. By being able to have accurate predictions of points of failure from erosion, and by being able to monitor an entire pipeline's status in real-time, resources can be targeted to tackle preventative measures instead of reactive.

### Subtask 19.1: Objectives

The motivation for this subtask is to assist DOE, WRPS and SRNL in providing realistic estimates of the remaining useful life of the components, to incorporate those estimates into future design plans and to automate the erosion corrosion monitoring. This subtask includes the investigation of various sensor systems and fluid flow dynamics to detect thinning in pipes and tanks along with real-time evolution of the wear using SRNL's mass loss/erosion coupons. Hence, there are three objectives for this task for structural health monitoring using various types of sensors. Including:

- Evaluation of SRNL's carbon and stainless-steel coupons for erosion testing.
- Caustic simulant-induced corrosion evaluation on FIU's custom bench scale flow loop.
- Development of data analytics and fluid flow dynamics-based models for automated erosion and corrosion detection.

## Subtask 19.1.1: Evaluation of SRNL Stainless Steel Coupons for Erosion Testing using DWPF Glass Frit

### Subtask 19.1.1: Methodology

The purpose of this research was to test and demonstrate that the SRNL erosion and mass loss coupons could provide an in-situ method for collecting erosion and mass loss rates from a pipeline using the stainless steel and carbon steel coupons during operation. Previous work included initial testing with the first set of carbon steel coupons provided by SRNL to FIU [4]. The application of these coupons was experimentally tested in an engineering scale pipe loop by circulating sand-water slurries of varying densities and grit sizes. The intended advantage of the replaceable coupons is their ability to easily calculate mass loss/gain and to gain insights into qualitative data such as erosion patterns on the inside of the pipes.

Past year's work included the feasibility investigation and initial testing of DWPF glass frit as a material for accelerated erosion in the pipe sections using the SRNL mass loss coupons and the Permasense Sensors. The present work evaluates:

- The structural integrity of the pipeline (FIU's Engineering scale test loop)
- Thermal integrity of the pipe loop under erosion experiments
- Erosion with multiple particles – sand and DWPF glass frit combination
- SRNL coupon material for hardness

### Subtask 19.1.1: Research Results and Discussion

In October 2022, coupons and a sample pipe section were shipped to SRNL. The Permasense UT sensor system was troubleshooted and erosion data was acquired over a period of 3 years. Additionally, efforts were dedicated to analyzing the erosion data. A sample carbon steel pipe section (2-inch diameter nipple), one mildly used low carbon steel and one high carbon steel

maximally corroded coupon, were shipped to SRNL for analysis. SRNL scientists will examine the coupon material and manufacture new coupons for further sand, glass, and chemical tests to be conducted in FIU laboratories. The shipped components are shown in Figure 122.

**Figure 122. Pipe components shipped to SRNL for material characterization.**

The Permasense ultrasonic sensors were not collecting the thickness data due to instrumentation and software issues. All sensors were checked, and troubleshooting was conducted to get the system up and running. Erosion data was then successfully collected. The A-scans of the 4 Permasense UT sensors are shown in Figure 123 and Figure 124.

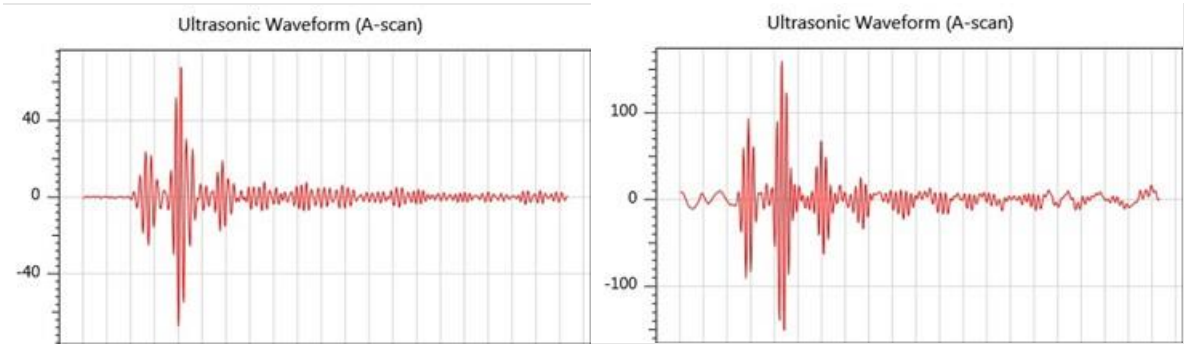


**Figure 123. Ultrasonic waveforms for 3-inch pipe sections – elbow (left) and straight (right).**

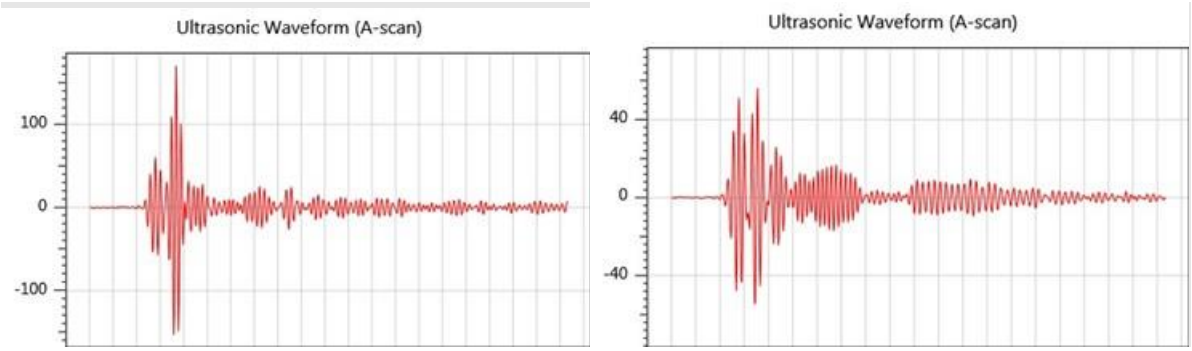


**Figure 124. Ultrasonic waveforms for 2-inch pipe sections – elbow (left) and straight (right).**

In November 2022, the glass frit testing was conducted intermittently to erode the pipe sections and Permasense UT sensor data was obtained for a period of 4 years. The thickness data plotted over time is shown in Figure 125 for the 3-inch elbow section. It is evident from the data that the

erosion has reduced the thickness from 5.77 mm to 5.73 mm over a period of 4 years with intermittent accelerated erosion (during testing) and rest periods (particle accumulation durations). Similar data is acquired for the other 3 Permasense sensors.

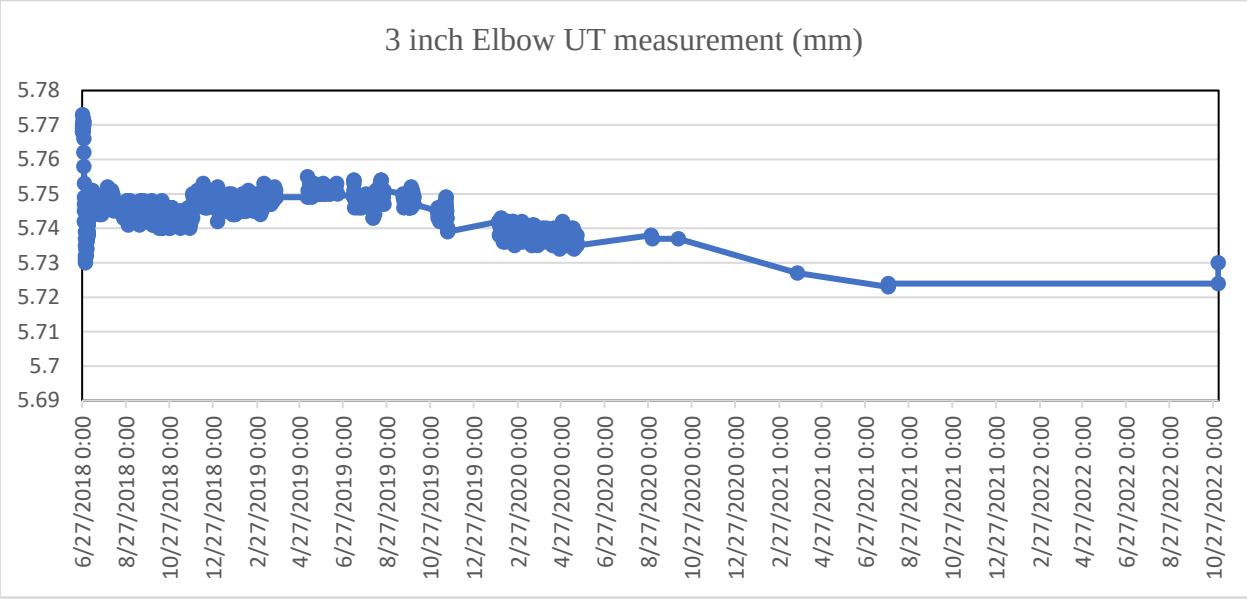


**Figure 125. Permasense sensor data for the 3-inch elbow section on the engineering scale loop.**

In December 2022, material specification was verified with SRNL scientists for future erosion tests with glass frit and sand. The experimental results obtained from tests with sand and glass particles up to this performance period were analyzed and conclusions were made. Based on the sand and glass test erosion data, the pipe sections showed a greater extent of erosion than the coupon material. Hence, a hardness test of the pipe material and the coupon material was conducted at SRNL by their scientists. Results indicated that the hardness of the pipe material was 82 HRB, while the hardness of the coupon material was found to be 104 HRB. HRB is the Hardness Rockwell B test number that indicates the hardness of a material. The higher the number, the harder is the material. As such, the coupon material was found to be harder than the pipe material. Moving forward, SRNL will manufacture and provide softer coupons (hardness matching schedule 40 carbon steel pipe material). Currently, FIU is waiting on the new coupons and will resume testing when obtained. FIU is in the process of combining the pencil UT sensor data and the Permasense pipe thickness data and developing data analytics models to predict the thickness changes over time. Additionally, glass tests will be continued for the next 6 months.

Previously, SRNL scientists conducted a hardness test on 1 coupon and pipe material and informed hardness values of 82 HRB and 104 HRB respectively. In the month of January 2023, FIU conducted in-house hardness tests on 2 other erosion coupons to validate the hardness values of various coupon materials and to inform the SRNL scientists. Surface hardness of the stainless steel and carbon steel (used and new) coupons was determined using Vickers microhardness testing equipment. The instrument - model *LECO LM 110AT* (Figure 126) determines the hardness of a material using the micro indentation technique. Hardness is the resistance of a material to plastic indentation, scratching, surface penetration or wear. This resistance is measured by penetrating the material with another harder material. In this case, an indentation is made using a square-shaped, 136-degree diamond pyramid indentation probe. An external load is also applied. The penetration depends on the applied load (magnitude and duration) and geometry of the indent. Depth of the

indentation provides a measure of hardness expressed as a number. A load of 100gf was applied for 10-15 seconds to conduct the experiments. Vickers hardness number is calculated using the following formula.

$$VHN = \frac{2Psin(\frac{\theta}{2})}{D^2}$$

where P is the applied test load, θ is the angle (136°) and D is the average diagonal length of the indentation. The instrument includes software for direct measurements and calculations. The sample (old coupon) placed on the Vickers hardness tester for indentation is shown in Figure 126.

**Figure 126. Vickers Hardness Tester (left), sample indentation (center) and surface imaging (right).**

Two coupons were tested. The microscopic images generated with the indentation are captured by the instrument and are shown in Figure 127 and Figure 128. The diamond shaped penetration on the surface of the coupon is evident in the figures. Also, the pits (corrosion and impact) and scratches (erosion) are visible in the same figures. The surface erosion in the case of the sand tested coupon (#1) had lines (scars) while the sand and glass beads tested coupon (#2) had more pits due to the rounded glass bead particle impact on the material. These are due to the sand and glass testing conducted on the engineering scale test loop with these coupons placed on the 3-inch pipe section.

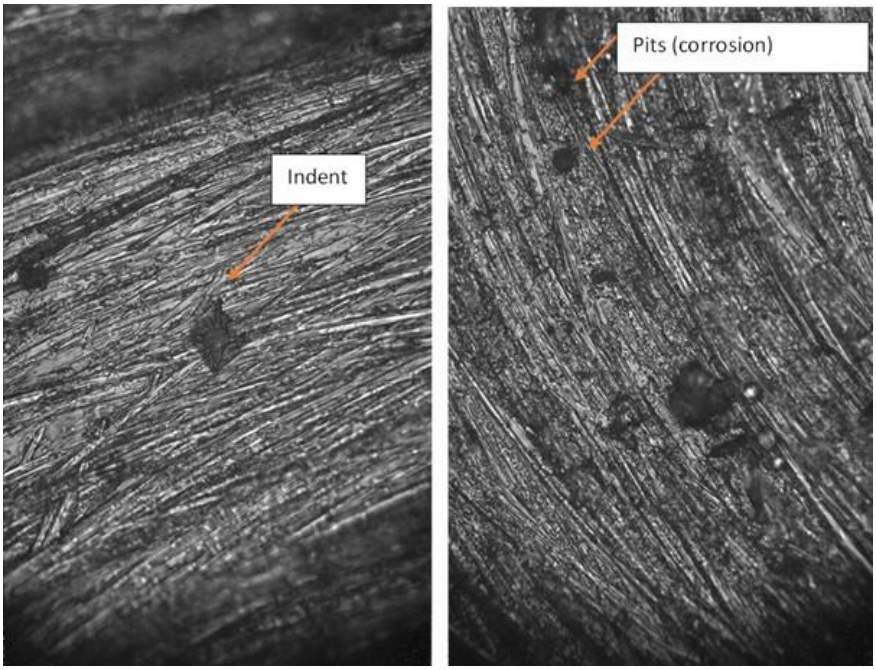


**Figure 127. Microscopic images of the coupon surface (Coupon 1) showing diamond indent and pits.**

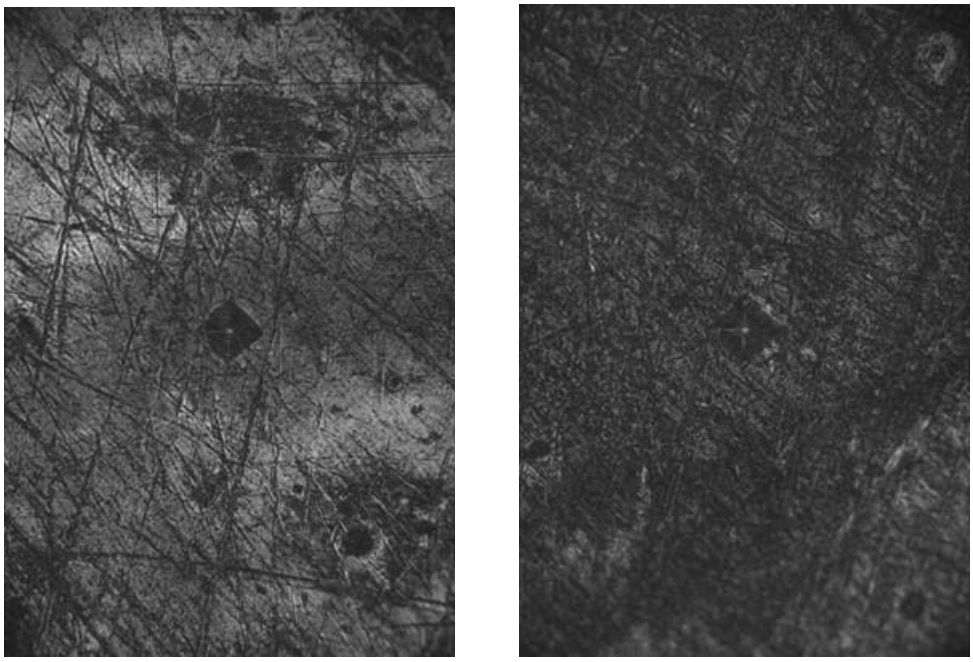

**Figure 128. Microscopic images of Coupon 2 showing the indent and pits.**

Details of the experiments - hardness number, applied load and indentation diameters are provided in Table 5 and Table 6. The results show that the average hardness for Coupon 1 is 301 HV and for Coupon 2 is 329 HV. This, when converted to Hardness Rockwell B (HRB) test results, provide 105 HRB and 107 HRB, respectively. These values agree with the numbers provided by SRNL scientists (104 HRB) indicating the validity of our hardness testing process. In future, the coupons will be polished to smoothen the surface and images will be captured for the coupons as pre-test conditions for the next sand/glass testing.

**Table 5. Vickers Hardness Test Results for Erosion Coupon 1**

| Indent Test # | Hardness (Vickers) | Load | D1 | D2 |
|---|---|---|---|---|
| 1 | 302 HV | 200 gf | 35.0 µm | 35.1 µm |
| 2 | 276 HV | 100 gf | 26.8 µm | 25.0 µm |
| 3 | 370 HV | 100 gf | 22.5 µm | 22.3 µm |
| 4 | 267 HV | 100 gf | 25.8 µm | 26.9 µm |
| 5 | 292 HV | 100 gf | 24.5 µm | 25.9 µm |

**Table 6. Vickers Hardness Test Results for Erosion Coupon 2**

| Indent # | Hardness | Load | D1 | D2 |
|---|---|---|---|---|
| 1 | 275 HV | 100 gf | 26.8 µm | 25.2 µm |
| 2 | 475 HV | 100 gf | 19.6 µm | 19.9 µm |
| 3 | 386 HV | 100 gf | 21.3 µm | 22.5 µm |
| 4 | 301 HV | 100 gf | 25.6 µm | 24.0 µm |
| 5 | 387 HV | 100 gf | 23.7 µm | 20.0 µm |
| 6 | 333 HV | 100 gf | 24.1 µm | 23.2 µm |
| 7 | 292 HV | 100 gf | 25.8 µm | 24.6 µm |
| 8 | 209 HV | 100 gf | 29.9 µm | 29.6 µm |
| 9 | 301 HV | 100 gf | 23.9 µm | 25.8 µm |

In February, hardness testing on two erosion coupons was conducted to determine the hardness of the coupon material. The accuracy of the hardness value needed confirmation due to a rough (eroded-corroded) surface and the SRNL coupons needed preparation for the next set of engineering scale testing. Hence, in February, the surface preparation and re-testing of the coupons was conducted. The initial sample testing using Vickers Hardness Tester showed highly rough surfaces with scars (Figure 129 center). Hence, the coupon was completely polished with rough (220 grit) and fine (4000 grit) sandpaper to obtain a smooth surface for indentation. Surface hardness testing with Vickers Hardness Tester (model LECO LM 110AT, Figure 129 left) was conducted with a 136-degree diamond indenter. Surface hardness is determined as a number dependent on the applied load, average diameter of the indenter and the angle of indentation with diamond (material). The new surface obtained after polishing is shown in (Figure 129 right). It is evident that the previous surface had large lines due to particle erosion in addition to pits. The polished surface removed most of the erosion, but certain scars are still visible.

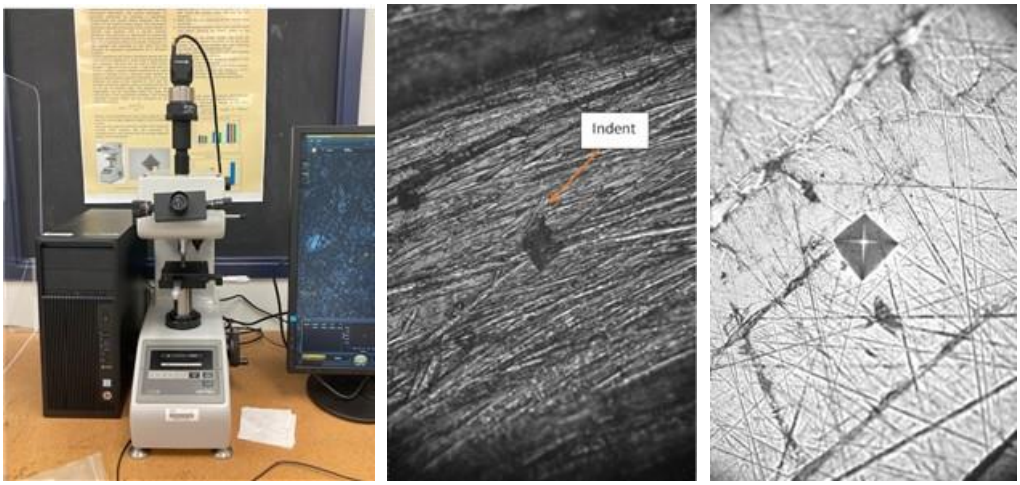


**Figure 129. Hardness Tester (left), microscopic image of the coupon surface (eroded - center and polished - right).**

The hardness testing was conducted with variation in loads. Two sets of loads (100gf and 200gf) were applied on the SRNL sample coupon using the diamond indenter. Coupon surface images with 110gf load are shown in Figure 130 and those with 200gf are shown in Figure 131. The images are lighter compared to the unpolished sample due to the reflection of light from the polished surface. Also, noticed in the images is the size of the default indenter diameters (rhombus size). Further, the scars (lines) are due to the sandpaper and remaining eroded scars on the surface.

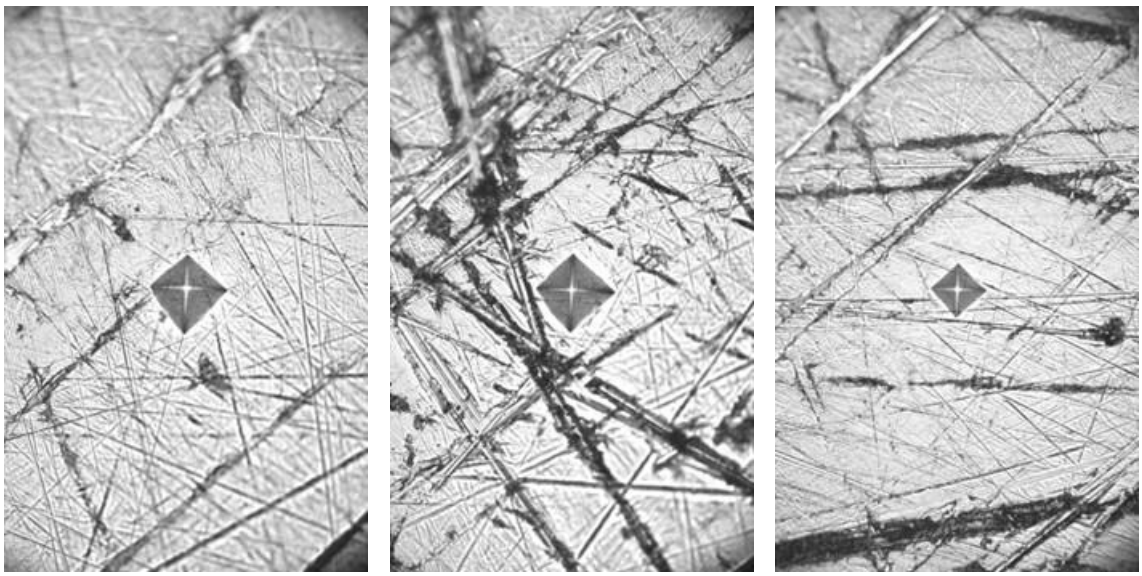

**Figure 130. Microscopic images of the coupon surface during hardness testing with 100gf of applied load.**

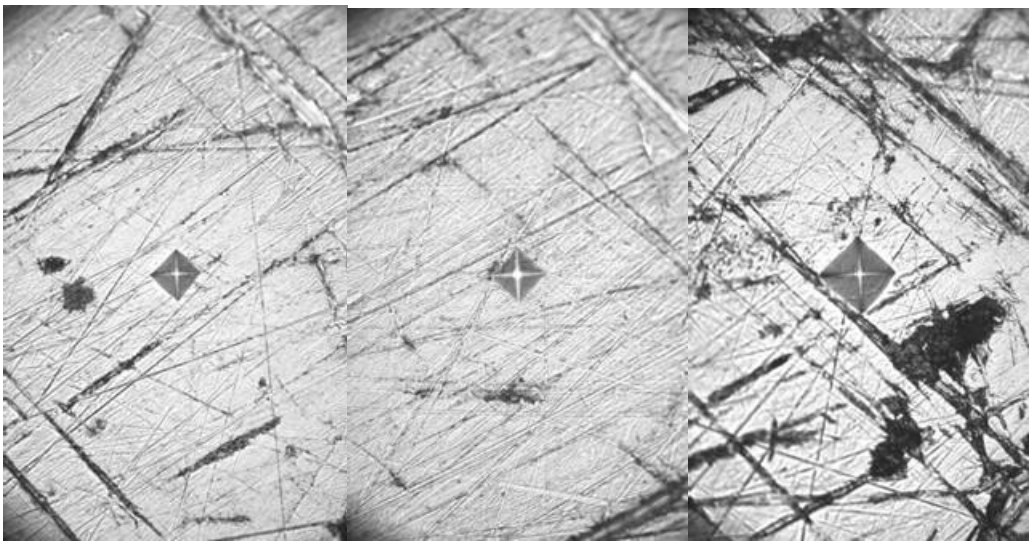

**Figure 131. Microscopic images of the coupon surface during hardness testing with 200gf of applied load.**

Results obtained were compared for both cases (eroded and polished) and are provided in Table 7 and Table 8. Results indicate a decrease in the hardness value with an increase in load. This is also affected by the average diagonal length D of the indentation rhombus (shown in the picture). The average hardness value obtained with an eroded surface was 314HV and the average hardness value with a polished surface showed a slightly higher value of 316HV. The range is within limits and hence, it is concluded that eroded coupons can directly be used in the Vickers Hardness Tester to obtain material hardness. Surface preparation is optional to a certain level of corrosion.

**Table 7. Vickers Hardness Test Results for Eroded Coupon (No Surface Preparation)**

| Indent # | Hardness | Load | D1 | D2 |
|---|---|---|---|---|
| 1 | 275 HV | 100 gf | 26.8 µm | 25.2 µm |
| 2 | 475 HV | 100 gf | 19.6 µm | 19.9 µm |
| 3 | 386 HV | 100 gf | 21.3 µm | 22.5 µm |
| 4 | 301 HV | 100 gf | 25.6 µm | 24.0 µm |
| 5 | 387 HV | 100 gf | 23.7 µm | 20.0 µm |
| 6 | 333 HV | 100 gf | 24.1 µm | 23.2 µm |
| 7 | 292 HV | 100 gf | 25.8 µm | 24.6 µm |

**Table 8. Vickers Hardness Test Results for Eroded Coupon (with Surface Preparation)**

| Indent # | Hardness | Load | D1 | D2 |
|---|---|---|---|---|
| 1 | 307 HV | 100 gf | 24.3 µm | 24.8 µm |
| 2 | 332 HV | 100 gf | 23.3 µm | 23.9 µm |
| 3 | 328 HV | 100 gf | 24.2 µm | 23.3 µm |
| 4 | 306 HV | 200 gf | 35.0 µm | 34.6 µm |
| 5 | 318 HV | 200 gf | 34.2 µm | 34.1 µm |
| 6 | 319 HV | 200 gf | 33.4 µm | 34.8 µm |
| 7 | 298 HV | 200 gf | 34.9 µm | 35.7 µm |

The month of March included finalizing new coupon material for machining, preparing the test area and test matrix for the next phase of erosion tests, and finalizing the coupon machining schedule with the SRNL team.

Material hardness tests (with and without surface preparation) revealed hardness values of the current coupons to be about 315HV (average), which is higher than the pipe material. Hence, after discussions with SRNL scientists, new material is being procured for the coupons. In this regard, the ingots made of carbon steel will be used. These are typically pipe coupons with thick walls (schedule 160). The walls will be used to machine the erosion coupons needed for FIU loop testing. Sample ingots are shown in Figure 132 (left). They are made of SA53/A53 Gr. B carbon steel material and are 6-inch in nominal diameter with 0.719-inch thickness. Currently, the samples are being procured and machined at SRNL and will be shipped to FIU for further erosion tests.

Additional efforts included cleaning the test area in the labs and conducting water tests in the engineering scale loop. Water in the tank has been pumped using a manual pump (Figure 132, right). Additionally, a UT sensor has been calibrated for measurements.

**Figure 132. Pipe coupons (6-inch) for making the erosion coupons (left) and manual pump in the reservoir tank (right).**

Coupon images have been captured using a borescope in the pipe. During image capturing, the second set of coupons (in the 3-inch straight section) were not accessible due to the camera being physically unstable at the pipe center. To avoid this, an adapter has been designed and 3D printed so it can be attached to the borescope and the entire pipe internal surface can be easily captured via the camera. The designed adapter and its usage in the pipe with the borescope are shown in Figure 133. The images captured with the stabilized borescope using the designed adapter are shown in Figure 134. These represent the pipe's internal structure (left) with coupon, the straight section (channel) with glass particle bed (center) and the glass deposits in the pipe at a particular section (right).

**Figure 133. Pipe adapter - 3D printed part (left), fitted borescope (center) and in the pipe section (right).**

**Figure 134. Borescope images - internal pipe surface (left), straight section with glass bed (center) and clogged glass particles (right).**

Extensive testing of sand and glass mixtures was conducted to summarize the findings and report to SRNL and DOE as deliverables. The engineering scale test loop was also evaluated for its thermal stability performance and structural integrity under the testing conditions.

Previous testing with glass-beads depicted minute wear in pipes and coupons due to the rounded bead surface. To obtain more realistic erosion patterns, sand and glass beads were mixed to a total of 10% by volume, based on the densities of sand and glass particles. Hence, the set of experiments included addition of the mixture of sand and glass particles. Sample test results for the SRNL coupon degradation as well as the pipe material degradation are presented next.

Three sets of experimental tests are provided in Table 9, Table 10 and Table 11. These data represent coupon thickness measurements using the ultrasonic pencil sensor. The three experiments were conducted on separate days. The tank containing glass beads from previous experiments was agitated and additional sand was added to the mixture with water to obtain a 10% by volume of sand water and glass mixtures. Addition of sand was conducted in phases for uniform mixing and is shown in Table 9. It is evident from all three tables below that the thickness slightly fluctuated for Coupons 1, 2 and 3. This is due to the fact that Coupon 1 is at the elbow with maximum erosion, and Coupons 2 and 3 are in the straight sections with fully developed flow. Coupons 4 and 5 have not shown any change since they are farther away from the elbow and reducer section.

**Table 9. Results of Particle Erosion Experiment 1**

| Coupon Experiment 1 - Thickness in mm. | | | | | |
|---|---|---|---|---|---|
| Time (s) | Coupons (1) | Coupon (2) | Coupon (3) | Coupon (4) | Coupon (5) |
| 12:00 PM | 3.1496 | 3.175 | 2.0828 | 2.3622 | 1.9558 |
| 12:30 PM | 2 Gallons of (20/30) Sand added to glass-water mixture | | | | |
| 1:00 PM | 3.1496 | 3.0988 | 2.1082 | 2.3368 | 1.9558 |
| 1:30 PM | 2 Gallons of (20/30) Sand added to glass-water mixture | | | | |
| 2:00 PM | 3.1242 | 3.0988 | 2.1082 | 2.3622 | 1.9558 |
| 2:30 PM | 2 Gallons of (20/30) Sand added to glass-water mixture | | | | |
| 3:30 PM | 3.0988 | 3.1496 | 2.1082 | 2.3876 | 1.9558 |
| 4:30 PM | 3.0734 | 3.1242 | 2.1082 | 2.3876 | 1.9558 |
| 5:10 PM | 3.0734 | 3.1242 | 2.1082 | 2.3876 | 1.9558 |

**Table 10. Results of Particle Erosion Experiment 2**

| Coupon Experiment 2 - Thickness in mm. | | | | | |
|---|---|---|---|---|---|
| Time (s) | Coupon (1) | Coupon (2) | Coupon (3) | Coupon (4) | Coupon (5) |
| 9:05 AM | 3.1242 | 3.175 | 2.1082 | 2.3622 | 1.9558 |
| 11:30 AM | 3.1242 | 3.175 | 2.0828 | 2.3622 | 1.9558 |
| 12:00 PM | 3.1242 | 3.2004 | 2.0828 | 2.3622 | 1.9558 |
| 12:30 PM | 3.1242 | 3.175 | 2.0828 | 2.3622 | 1.9558 |
| 1:00 PM | 3.0734 | 3.1496 | 2.0828 | 2.3622 | 1.9558 |
| 1:30 PM | 3.1242 | 3.175 | 2.0828 | 2.3622 | 1.9558 |
| 2:00 PM | 3.0734 | 3.2004 | 2.0828 | 2.3622 | 1.9558 |
| 2:30 PM | 3.1242 | 3.1496 | 2.0828 | 2.3622 | 1.9558 |
| 3:00 PM | 3.0988 | 3.2004 | 2.0828 | 2.3622 | 1.9558 |
| 3:30 PM | 3.0734 | 3.1496 | 2.0828 | 2.3622 | 1.9558 |

**Table 11. Results of Particle Erosion Experiment 3**

| Coupon Experiment 3 - Thickness in mm. | | | | | |
|---|---|---|---|---|---|
| Time (s) | Coupons (1) | Coupon (2) | Coupon (3) | Coupon (4) | Coupon (5) |
| 9:30 AM | 3.1242 | 3.1496 | 2.0828 | 2.3622 | 1.9558 |
| 10:00 AM | 3.048 | 3.175 | 2.0828 | 2.3622 | 1.9558 |
| 10:30 AM | 3.1242 | 3.2004 | 2.0828 | 2.3622 | 1.9558 |

| | | | | | |
|---|---|---|---|---|---|
| 11:00 AM | 3.048 | 3.2004 | 2.0828 | 2.3622 | 1.9558 |
| 11:30 AM | 3.048 | 3.1496 | 2.0828 | 2.3622 | 1.9558 |
| 12:00 PM | 3.1242 | 3.2004 | 2.0828 | 2.3622 | 1.9558 |
| 12:30 PM | 3.0734 | 3.175 | 2.0828 | 2.3622 | 1.9558 |
| 1:00 PM | 3.0734 | 3.175 | 2.0828 | 2.3622 | 1.9558 |
| 1:30 PM | 3.1496 | 3.175 | 2.0828 | 2.3622 | 1.9558 |
| 2:00 PM | 3.175 | 3.175 | 2.0828 | 2.3622 | 1.9558 |
| 2:30 PM | 3.1242 | 3.2004 | 2.0828 | 2.3622 | 1.9558 |
| 3:00 PM | 3.1242 | 3.2004 | 2.0828 | 2.3622 | 1.9558 |

Further, pattern variation in each of the coupons was analyzed by the graphs in Figure 135 to Figure 140. Coupon 1, placed close to the elbow, showed uniform erosion with time. Coupon 2, placed at the bottom, had an initial reduction in the thickness reading. This can be due to the erosion of the bottom deposited layer. Next, the increase in thickness could be due to the particle deposition forming a moving bed at the bottom. The final section remains uniform in thickness with a stationary bed. Coupon 3, placed at the top, showed initial erosion of the particles with sudden flow which stabilized after the initial stages. Coupon 4 behaved similarly to Coupon 2 with reduction, increase and stabilized measurements over time. Coupon 5 showed no change. As explained earlier, it can be due to the formation of a thick particle bed layer. Finally, all the results of the coupons are shown in the graph in Figure 140. It is to be noted that the coupons have varying initial thicknesses due to their pre-eroded conditions obtained from previous testing.

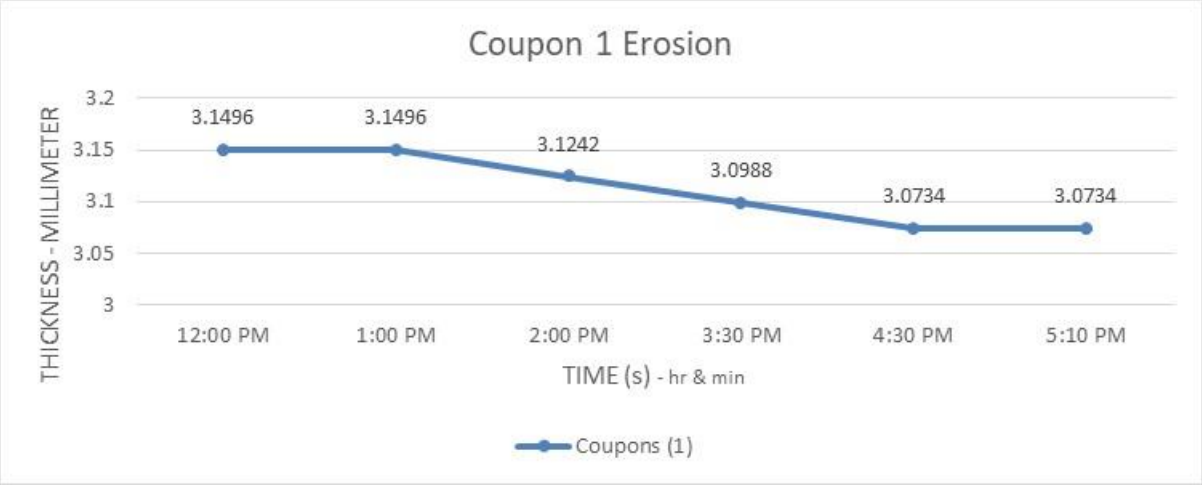


**Figure 135. Degradation in coupon placed near the elbow.**

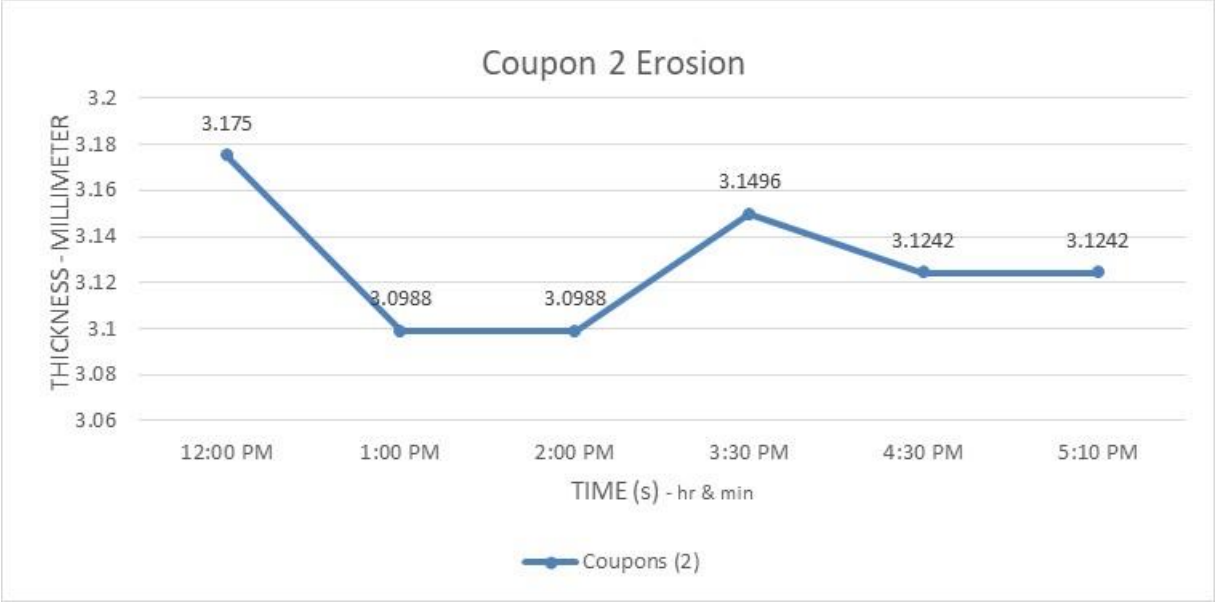


**Figure 136. Degradation in coupon placed on bottom 3-inch section of the pipe.**

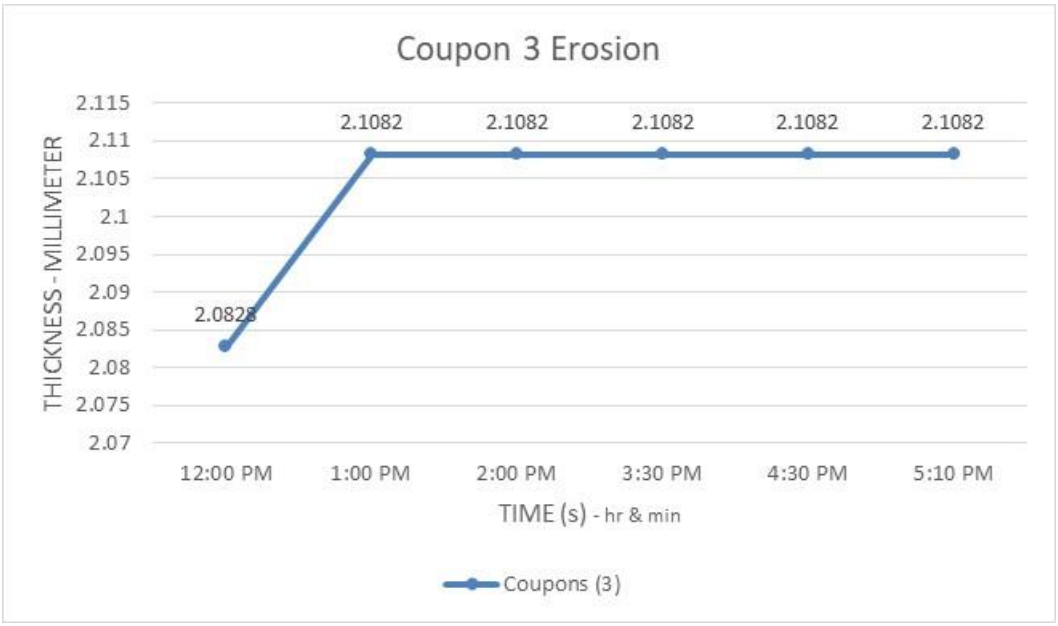


**Figure 137. Degradation in coupon placed at the top 3-inch section of the pipe.**

**Figure 138. Degradation in coupon placed at the bottom of 3-inch section closer to the reducer.**

**Figure 139. Degradation in coupon placed at the top 3-inch section of the pipe.**

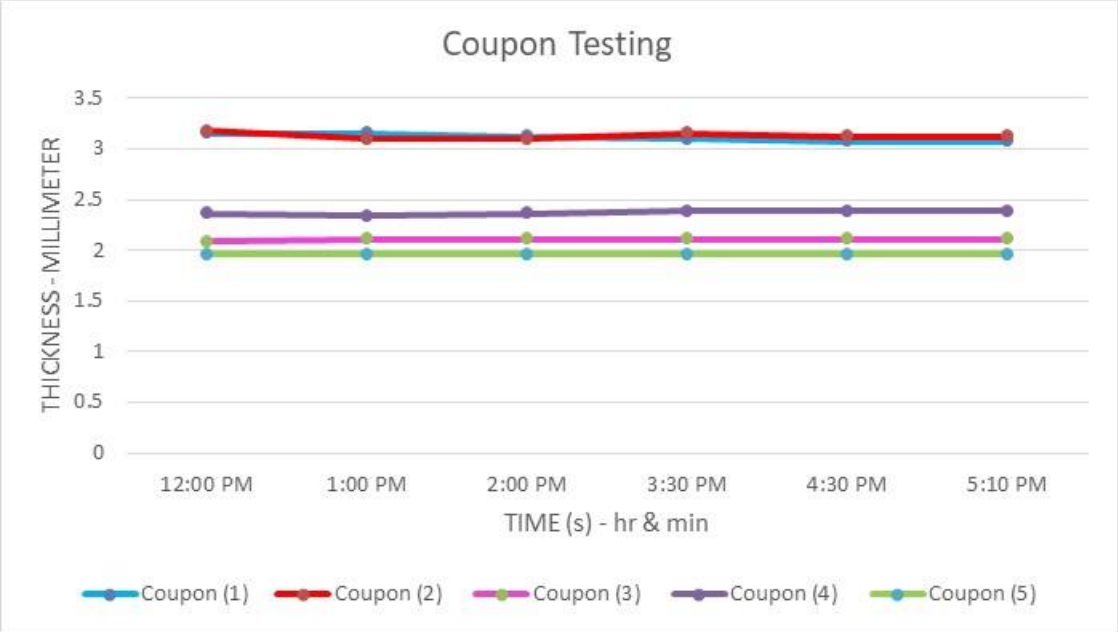


**Figure 140. Erosion pattern in all 5 coupons.**

## Loop Thermal Stability Evaluation

Erosion tests result in heating of the pipes, pump, tank, and other loop system components. Hence, thermal stability is significant during the tests. All experiments have been conducted under temperature monitored conditions. Twelve data points were traced for their thermal profile during the experiments. These included pump, mixer, tank (water), 2- and 3-inch pipe sections at various points and the atmosphere (ambient temperature). The loops with critical data points for thermal evaluation are shown in Figure 141. Variation over a period of 5-6 hrs of a sample test is shown in Figure 142 and Figure 143. The first figure shows the rise in temperature of the pump, tank, and the mixer components. It is evident that maximum increase in temperature occurs in the pump and mixer during operation with a maximum temperature of 70°C. Water temperature rise was about 15°C. Figure 143 shows the temperature variation in the pipe material (carbon steel). It is evident that the heating was almost uniform in all pipes with a temperature change from 23°C to 45°C. All these values are within working conditions and hence validate the testing process.

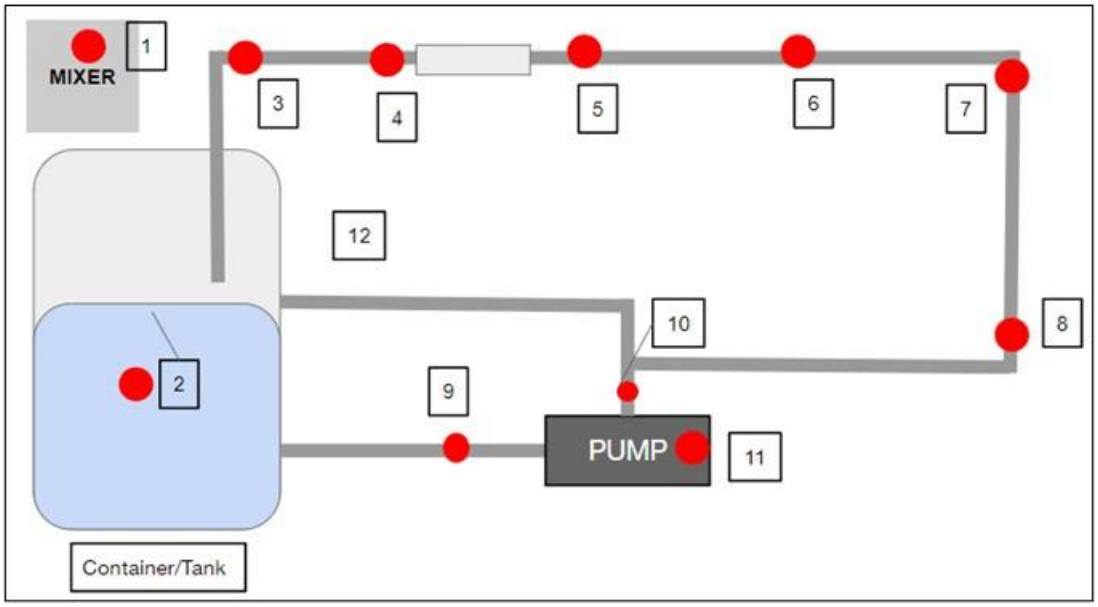


**Figure 141. Critical data points on the loop for thermal stability experiments.**

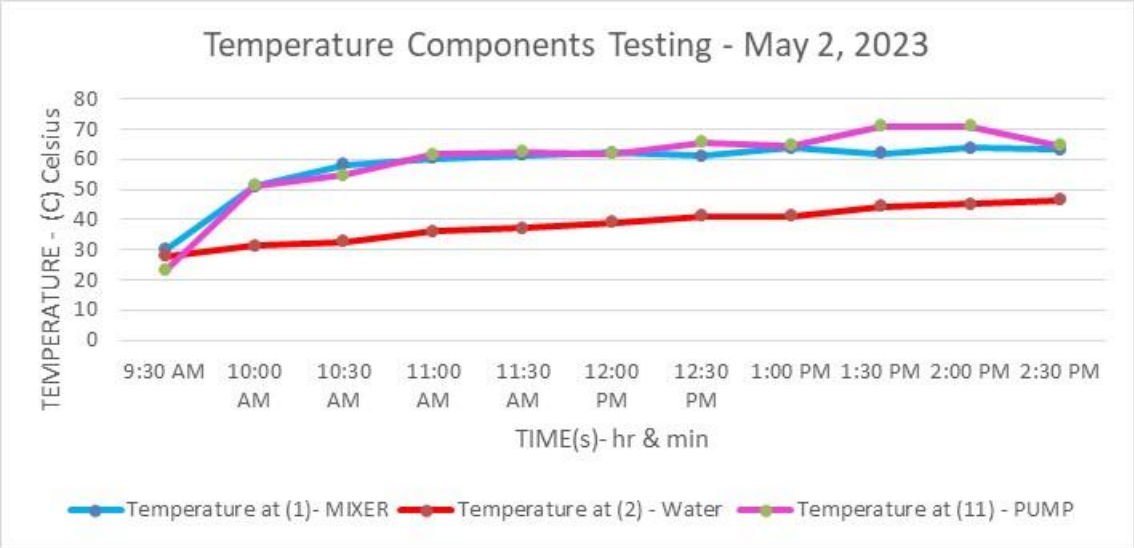


**Figure 142. Temperature variation in the loop components.**

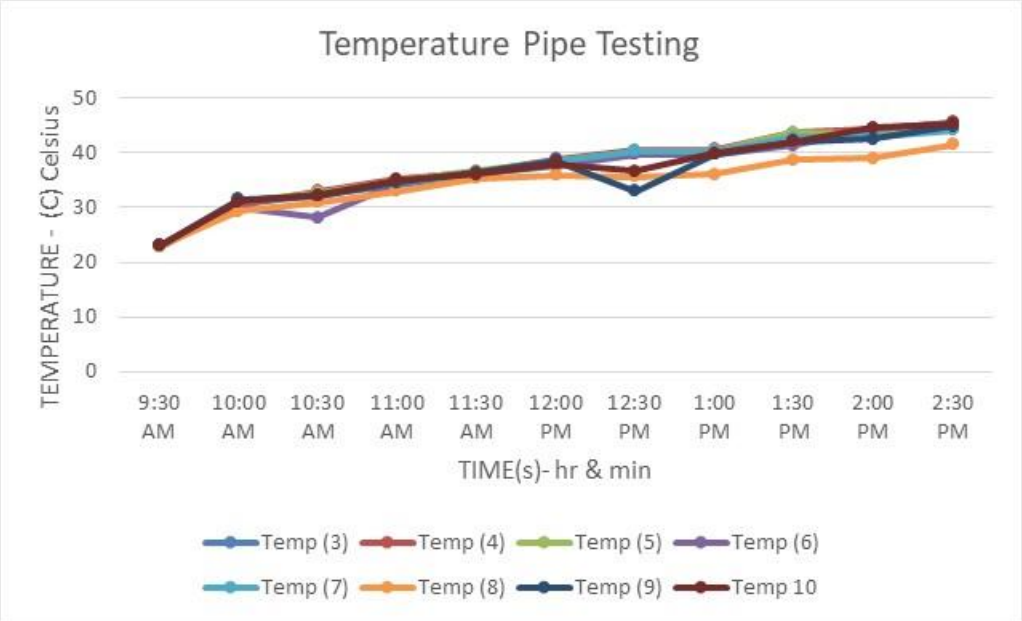


**Figure 143. Temperature variation in the pipe sections.**

Additionally, post-test structural integrity assessment of the pipe loop was conducted. Finally, the coupons were extracted from the pipe loop to conduct UT, weight loss measurements and visual inspection to quantify the erosion.

## Structural Integrity Assessment of the Pipe Loop

In addition to the erosion in the SRNL coupons, the pipe decay over time during and due to the testing was investigated. The material of the piping is carbon steel with schedule 40 2- and 3-inch sections. To examine the pipe degradation, 12 different points in the pipe loop have been identified as critical points. The locations are shown in Figure 144. At each location, 4 peripheral data points are measured for thickness. A handheld ultrasonic sensor (Olympus D790SM) is used for this purpose. Thickness results before and after a series of glass-sand tests are presented in Table 12 and Table 13. It is evident from the tables, that the point near the pump exit (point 2) depicted considerable erosion at p (1) indicating the side of the vertical tube. This is due to the maximum velocities occurring at that location. Also, it is to be noted that the erosion on the sides of the pipes is least at p (3) and p (4) and it is considerable at the top and bottom peripheral points at most horizontal locations. This is according to the physics of the problem, since flow is turbulent in the pipes with maximum velocities at the center and gradually reducing towards the pipe walls. Additionally, there is an increase in thickness in some bottom points on the horizontal pipes. This is due to the particles tending to deposit at the bottom due to gravity, forming beds.

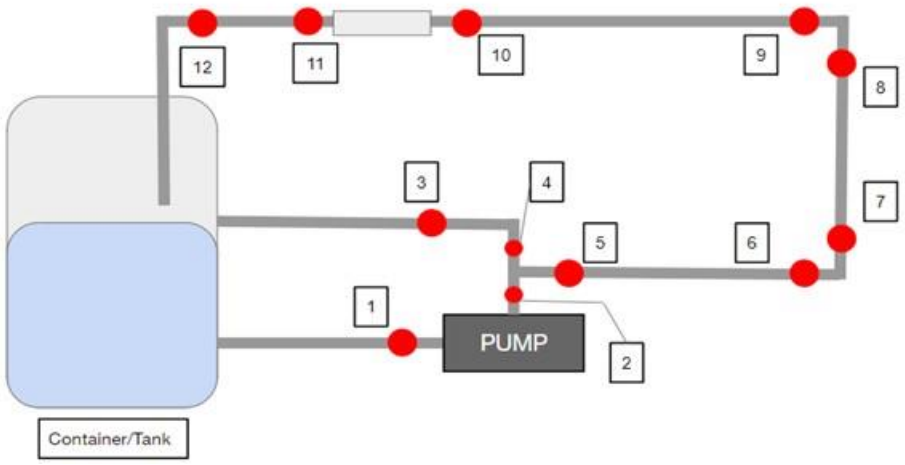


**Figure 144. Pipe loop with critical data points identified for degradation study.**

**Table 12. Pipe Degradation Experiment (Pre-Test Thickness)**

| Pipe Degradation Experiment 1 (UT measurements) | | | | |
|---|---|---|---|---|
| Position (s) | P (1) - mm | P (2) - mm | P (3) - mm | P (4) - mm |
| Position (1) | 3.2258 | 3.2766 | 3.2766 | 3.2766 |
| Position (2) | 3.5814 | 3.1496 | 3.2004 | 3.3782 |
| Position (3) | 5.1308 | 4.9022 | 5.0292 | 5.1816 |
| Position (4) | 3.302 | 3.81 | 3.5306 | 3.7084 |
| Position (5) | 2.9718 | 3.2004 | 3.2004 | 2.8702 |
| Position (6) | 4.826 | 4.7244 | 4.9022 | 4.7244 |
| Position (7) | 2.9464 | 3.2258 | 3.0988 | 2.9718 |
| Position (8) | 3.7592 | 3.8862 | 3.8608 | 3.8608 |
| Position (9) | 3.556 | 3.7084 | 3.6322 | 3.4544 |
| Position (10) | 5.3594 | 5.4102 | 5.4864 | 5.2832 |
| Position (11) | 5.4864 | 5.5118 | 5.2832 | 5.1816 |
| Position (12) | 5.3594 | 5.5626 | 5.334 | 5.3848 |

**Table 13. Pipe Degradation Experiment (Post-Test Thickness)**

| Pipe Degradation Experiment 2 (UT measurements) | | | | |
|---|---|---|---|---|
| Position (s) | Side (1) - mm | Side (2) - mm | Side (3) - mm | Side (4) - mm |
| Position (1) | 3.2258 | 3.2512 | 3.2512 | 3.302 |
| Position (2) | 3.5306 | 3.2512 | 3.2512 | 3.5052 |
| Position (3) | 5.0038 | 5.08 | 5.1562 | 5.0546 |
| Position (4) | 3.302 | 3.4036 | 3.4544 | 3.4036 |
| Position (5) | 3.0734 | 3.1496 | 3.1496 | 2.9972 |
| Position (6) | 4.7498 | 4.826 | 4.9276 | 4.8006 |
| Position (7) | 2.9718 | 3.1496 | 3.0734 | 2.9718 |
| Position (8) | 3.81 | 3.9116 | 3.8862 | 3.8862 |
| Position (9) | 3.81 | 3.6576 | 3.6576 | 3.556 |
| Position (10) | 5.4102 | 5.461 | 5.3086 | 5.3086 |
| Position (11) | 5.4102 | 5.4356 | 5.2578 | 5.2578 |
| Position (12) | 5.4356 | 5.4356 | 5.3594 | 5.3848 |

## Post-test Coupon Extraction and Erosion Evaluation

All 5 coupons (3 carbon steel and 2 stainless steel) were extracted from the pipe loop and evaluated for weights, visual and thickness changes. For thinning in coupons, the thickness was measured both internally and externally using two separate UT sensors. The inner section of the coupon was measured using the pencil sensor and the outer section with the handheld sensor (Figure 145). The reason is to assure accuracy of measurements with both sensors and accessibility of the surface.

**Figure 145. UT measurement of the coupon using two separate sensors (inner and outer coupon surface).**

Thickness data for the coupons is provided in Table 14. Coupons 1, 2 and 4 are made of carbon steel and placed at the elbow, top and bottom straight sections closer to the elbow. Coupons 3 and 5 are made of stainless steel and are in the straight sections away from the elbow. From the thickness data it is evident that there is no change in the stainless-steel coupon thickness when measured from the inside and outside. In the case of the carbon steel coupons, there has been an increase in the outside measurements with the highest thickness change in Coupon 4, that was placed in the bottom section of the pipe. This is due to the sand and glass mixture deposited and hardened on the coupon surface, hence leading to increased thickness when measured using the handheld device. It is concluded that the pencil sensor only measured the metal thickness, while the handheld device is capable of measuring the metal as well as the solid deposit on the surface. Coupon weights are also provided in Table 14.

The maximum weight is with Coupon 5, placed at the bottom and the minimum weight is for Coupon 4 placed closer to the elbow. The difference in weights is due to the machining to fit in the pipe holes and the material type. Next, the pre- and post-test conditions will be compared and reported.

**Table 14. Coupon Erosion with UT Measurements**

| Coupon Erosion – Thickness (UT measurement) | | |
|---|---|---|
| Coupon # | Inside Measurement (mm) | Outside Measurement (mm) |
| Coupon #1 | 3.1496 | 3.2766 |
| Coupon #2 | 3.175 | 3.5052 |
| Coupon #3 | 2.0828 | 2.0828 |
| Coupon #4 | 2.3622 | 3.9878 |
| Coupon #5 | 1.9558 | 1.9304 |

**Table 15. Coupon Weights - Post Extraction from the Loop**

| Coupon # | Weight Average (g) |
|---|---|
| Coupon #1 | 8.1949 |
| Coupon #2 | 8.32937 |
| Coupon #3 | 7.41573 |
| Coupon #4 | 6.91373 |
| Coupon #5 | 10.47243 |

During the next quarter, post-test evaluation of the erosion coupons was conducted and completed to determine the effects of sand and glass particle-based erosion. Vicker's hardness tester was used to obtain microscopic images of the coupon surfaces to compare with pre-test conditions. The Erosion Loop system has been continuously testing the flow of water and the effect of particle erosion with sand, glass, and water mixtures. These elements in contact with the flushed coupons led to the erosion and eventual corrosion in the carbon and stainless-steel pipe material. Understanding this important process of corrosion-erosion could lead to better estimation of the life expectancy of the material and circuit design. Without having the need to dissemble an entire section to study the erosion pattern effected by the flow and simulants, the mass-loss coupons allow for better investigation process. Results obtained from several weeks of testing to determine the thickness and weight changes of the coupons, are shown in Table 16. Each coupon was carefully removed and studied for accuracy in weight and wall thickness values.

**Table 16. SRNL Coupon Mass and Thickness Results Under Post-Test Conditions (Erosion Testing)**

| **Coupon (#)** | **Material** | **Position** | **Weight** | **UT Thickness** |
|---|---|---|---|---|
| **Coupon (1)** | Carbon Steel | 90 Degree Elbow | 8.195 | 0.124 |
| **Coupon (2)** | Carbon Steel | Top (Section 1) | 8.329366667 | 0.125 |
| **Coupon (3)** | Stainless Steel | Top (Section 2) | 7.415733333 | 0.093 |
| **Coupon (4)** | Carbon Steel | Bottom (Section 1) | 6.913733333 | 0.077 |
| **Coupon (5)** | Stainless Steel | Bottom (Section 2) | 10.47243333 | 0.082 |

**Table 17. Coupon Visual Inspection (Internal and External Images) for Post-Test Conditions**

| Coupon(s) | Material | Step (Outside) | Inside |
|---|---|---|---|
| Coupon #1 | Carbon | | |
| Coupon #2 | Carbon | | |
| Coupon #3 | Stainless | | |
| Coupon #4 | Carbon | | |
| Coupon #5 | Stainless Steel | | |

**Figure 146. Coupon #1 through #5 (left to right) images taken after completion of the test cycles.**

Coupon post-test conditions in the form of images (top view and side view) are shown in Table 17 and Figure 146. To investigate the detailed corrosion and erosion effects on the surface of the coupons, the specimens were placed on a high-resolution microscopic camera in the Vicker's hardness tester. The images obtained are shown in Figure 147 to Figure 151. The left images are actual results from the surfaces after testing and the right-side images are taken after polishing the surfaces with sandpaper. It is observed that Coupons 1, Coupons 2, and Coupons 4 are the carbon steel coupons that are mostly affected by the sand and glass particles and the flow conditions. By identifying the position of the coupon, we can determine which specific coupons are highly damaged. For example, Coupon 1 is on the long radius 90-degree elbow and has the most build up and corrosion effect compared to the rest. Coupon 4 has the most buildup of the simulant particles. This is due to being located at the bottom of the pipe section and being in constant contact with flow and settlement of the simulants. Coupon 2 has the least corrosive effect due to the placement being on the top surface of the pipe. From the regular camera images, stainless steel coupon did not evidently show any particle erosion or erosive damage. But the detailed microscopic images identify the surface erosion and pitting corrosion. Also, within the stainless-steel coupon images, the polished images still show pitting corrosion after the removal of external corrosive layer. This confirms that after long period of testing and long periods of exposure with both glass frit and 20/30 sand both carbon steel and stainless steel have undergone a corrosive stage.

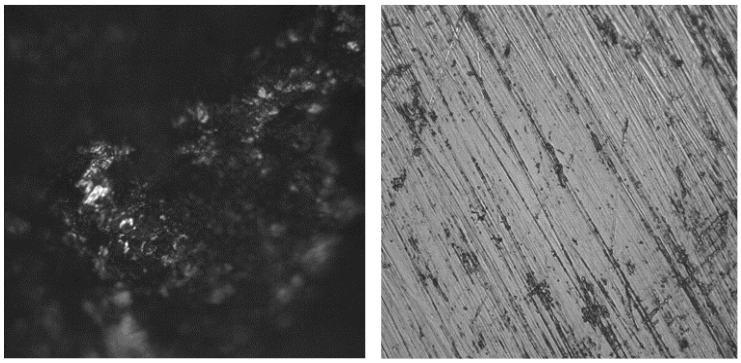

**Figure 147. Coupon # 1 Microscopic image before polishing (left) and polished (right).**

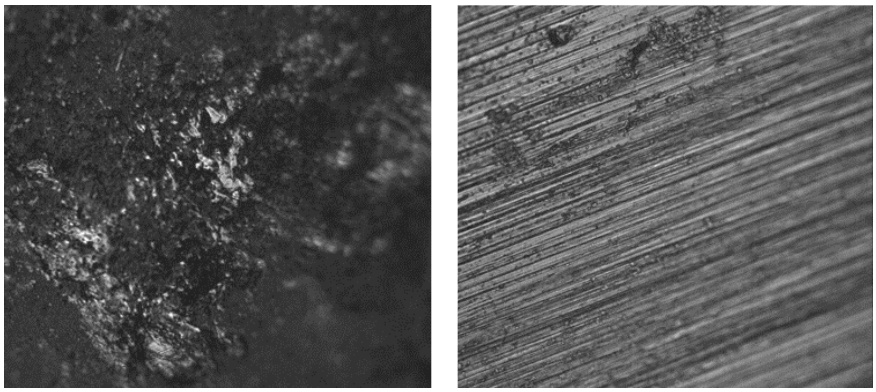

**Figure 148. Coupon # 2 Microscopic image before polishing (left) and polished (right).**

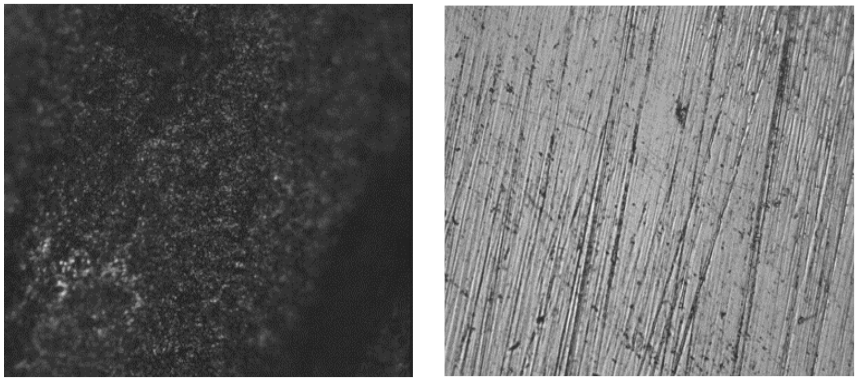

**Figure 149. Coupon # 3 Microscopic image before polishing (left) and polished (right).**

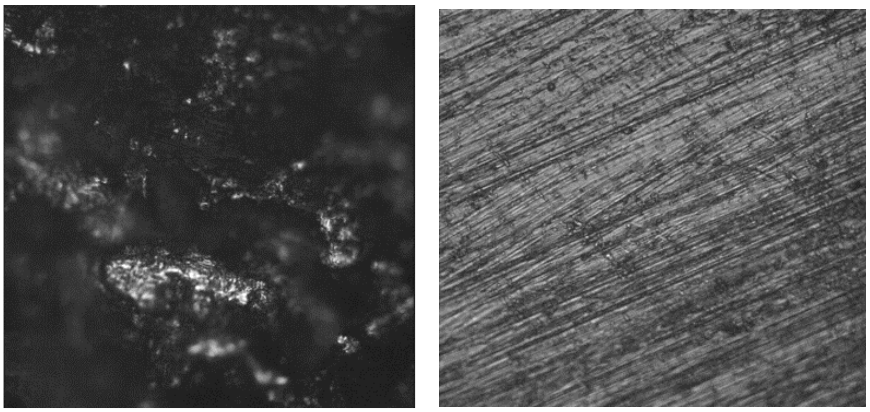

**Figure 150. Coupon # 4 Microscopic image before polishing (left) and polished (right).**

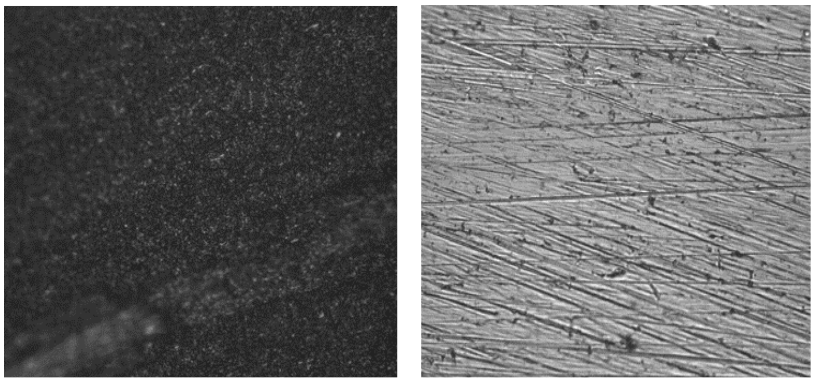

**Figure 151. Coupon # 5 Microscopic image before polishing (left) and polished (right).**

Currently, FIU is in the process of data analysis of all the structural integrity data obtained for the pipelines and the SRNL coupons to transmit the research findings to SRNL for making future erosion predictions and design conclusions.

## Subtask 19.1.1: Conclusions

The real-time particle erosion effect on the SRNL coupons has been verified and validated on an engineering scale test bed using a combination of sand and glass replicating SRNL's DWPF glass frit. Experimental results showed much less change in erosion in stainless steel when compared to the carbon steel coupons. The integrity assessment of the pipe loop resulted in drastic changes in the carbon steel sections, particularly the elbow joints. In addition, the material evaluation of the coupons was conducted for hardness. The hardness tests will further be continued in future to suggest and evaluate the right material for the HLW transfer pipes.

## Subtask 19.1.1: References

1. Aravelli A., McDaniel, D., Davila, C., "Real-time Erosion-Corrosion Detection in Waste Transfer Pipelines using Guided Wave Ultrasonic Sensors", Proceedings of the Waste Management Symposia 2018, Phoenix, AZ, March 18-22, 2018.
2. Aravelli, A., Thompson, M., McDaniel, D., Krutsch, M., McNeilly, M., Imrich K., Wiersma B., "Advanced Fiber Optic and Ultrasonic Sensor Systems for Structural Health Monitoring of Pipes in Nuclear Waste Sites", IMAPS 52nd International Symposium on Microelectronics (IMAPS), Boston, MA, Sep 30-Oct 3, IMAPS (2019).
3. https://srnl.doe.gov/tech_transfer/tech_briefs/SRNL_TechBriefs_UltrasonicThicknessMassLossMeasurement.pdf.
4. Aravelli, A., McDaniel, D., Thompson, M., Imrich, K., Wiersma, B., "Erosion-Corrosion Detection in Carbon Steel Pipe Loops using SRNLs Thickness and Mass Loss Measurement Coupons", Waste Management 2020 Conference, Phoenix, AZ, March 2020.
5. https://www.olympus-ims.com/en/shop/item/269-productId.570437480.html
6. Thompson, M., McDaniel, D., Wiersma, B., Aravelli, A. "Structural Health Monitoring Technologies for Wear and Anomaly Detection in Nuclear Waste Transfer Systems", Waste Management 2021 Conference, Phoenix, AZ, March 2021.

## Subtask 19.1.2: Caustic Simulant Testing using the Bench Scale Flow Loop

### Subtask 19.1.2: Methodology

The purpose of this subtask is to test and demonstrate that the SRNL coupons could provide static and dynamic methods for collecting corrosion rates from pipelines using stainless steel and carbon steel coupons. For this, a bench scale loop was custom designed and installed for testing replicate caustic simulants with various concentrations. The recipe for the salt solutions was prepared by SRNL scientists and transmitted to FIU for testing in the bench loop [1]. Static testing was conducted by immersing the coupons in bottles with 2, 4 and 6 Molar salt solutions, while the dynamic testing is conducted by placing the bench scale loop in a fume hood.

Past years' work included construction of the caustic bench loop and initial loop validation experiments using the 2M caustic solutions. This year's work includes:

- Static evaluation of the coupons under 2, 4 and 6 Molar solutions – Experiments and data analysis.
- Bench loop troubleshooting and pump repair.

### Subtask 19.1.2: Research Results and Discussion

Caustic corrosion was experimentally determined under static and dynamic conditions. In order to conduct both tests, chemical solutions were prepared using the simulant recipe provided by the SRNL scientists. The volume of solution prepared was scaled according to the requirements. Static testing and results are discussed next followed by the bench loop results.

In the first quarter, corrosion settling characteristics of the 2M salt solution was studied, a pipe test section and sample coupons were shipped to SRNL for new coupon manufacturing, additional chemicals were procured from Fisher Scientific, 6M salt solutions were prepared and bench loop testing with 6M solutions was initiated.

The first stage of bench scale caustic testing with 2M salt solution was completed, and the tested solution was removed from the tank and stored in a container for settling. The storage container was kept undisturbed for a 3-week period to check the separation and settlement of corrosion particles and salts at the bottom. After 3 weeks, it was observed that the corrosion/rust particles were completely settled at the bottom of the container while the rest of the solution was crystal clear, clearer than the static solution in the bottles with coupons. Hence, the clear solution is currently being examined to check for pH and other chemical characteristics for its reusability. The plan is to decant the fluid and weigh the corroded solid material. Figure 152 depicts the solution before recovery from the pipe loop's tank (left) and after 3 weeks of settlement (right). It is a very significant observation that can be used to measure the corrosion in terms of material loss (mass/weight) of the entire pipe loop.

**Figure 152. Caustic simulant solution in the tank (left) and after 3 weeks of settling (right).**

Next, the 3-inch test section of the bench scale loop was shipped to SRNL for drilling holes for coupons. The new coupons will be inserted in 5 locations as shown in Figure 153. The locations are determined based on the flow features of the fluid during dynamic conditions. Two locations are close to the junction between the 2- and 3-inch attachment to ensure full flow conditions and to capture any dead volume (air gaps). Two locations are equally distanced from the pipe ends (center) to obtain the erosion at the top and bottom, and one location is on the side for partial flow conditions.

**Figure 153. Pipe test section with markings for shipping to SRNL.**

In November, 6M salt solutions were prepared, SRNL coupons were installed in the loop and the next stage of caustic testing on the bench scale loop has been initiated. 6M salt solution has been prepared in 10 batches using the proportions and recipe provided by SRNL (Figure 154). The total amount of the simulants required for 18L and amount per batch is provided in Table 18. Each of the chemicals is proportioned to a batch size, weighed, and dissolved in distilled water using a mechanical stirrer. The weighing process and experimental setup are shown in Figure 154.

**Table 18. Caustic Simulants and Proportions for 6M Salt Solution Preparation**

| **Chemical (name)** | **Chemical (Symbol)** | **Quantity Required Total (gm) per 18L** | **Quantity (gm) per batch (1800 ml)** |
|---|---|---|---|
| Sodium Hydroxide | NaOH | 2181.6 | 218.16 |
| Aluminum Nitrate | Al $(NO_3)_3$*$9H_2O$ | 1490.4 | 149.04 |
| Sodium Sulfate | $Na_2SO_4$ | 113.04 | 11.304 |
| Sodium Carbonate monohydrate | $Na_2CO_3$*$H_2O$ | 561.6 | 56.16 |
| Sodium Nitrate | $NaNO_3$ | 2376 | 237.6 |
| Sodium Nitrite | $NaNO_2$ | 835.2 | 83.52 |
| Sodium chloride | NaCl | 208.08 | 20.808 |
| **Mass Total (gm)** | | 7765.92 | 776.592 |

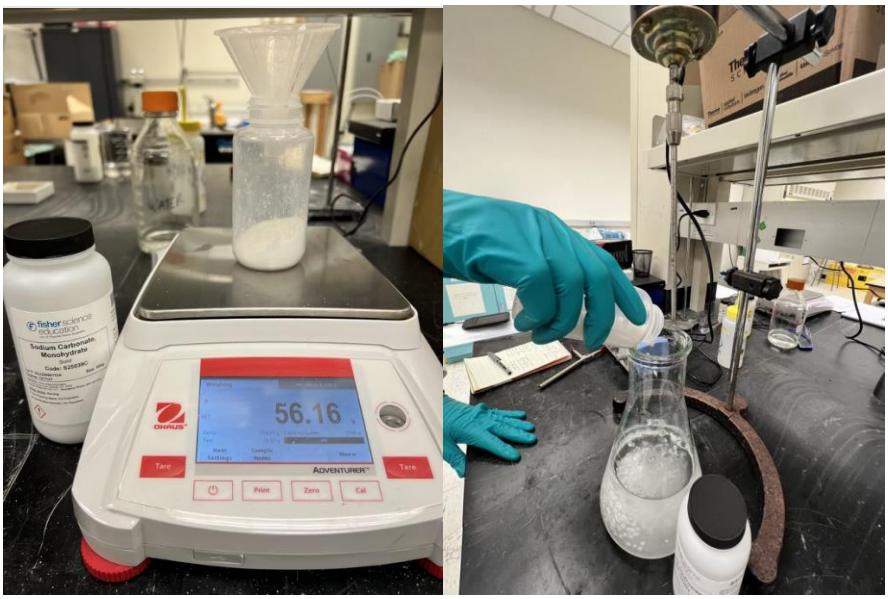


**Figure 154. Simulant mass measurement (left) and experimental set up for mixing the salt simulants (right).**

Once the solution is prepared, the loop was cleaned, and water was circulated to remove any residual corrosion in the pipes and particles deposited in the tank and near the pump inlet and outlet. Following the loop clean up, coupons were installed at 4 sections in the 3-inch diameter test section. Two stainless and two carbon steel coupons have been used. Prior to installation, the initial weight, image data and UT thickness data have been taken. Coupon masses and thickness data is provided in Table 19 and the procedure is shown in Figure 155. These conditions were considered as the baseline conditions for the SRNL coupons. The 6M testing was conducted by circulating the fluid for 4-5 hours per day over a period of 3 months. UT thickness data was measured at intervals of once per week.

**Table 19. SRNL Coupon – Baseline Conditions Prior to 6M Simulant Testing**

| Coupon | Mass (gm) | Thickness (mm) | Initial Condition |
|---|---|---|---|
| CS (W1) | 9.4386 | 2.5 | New |
| CS (W2) | 9.3071 | 2.18 | New |
| SS (W3) | 9.3500 | 2.01 | New |
| SS (W4) | 9.2678 | 2.07 | New |

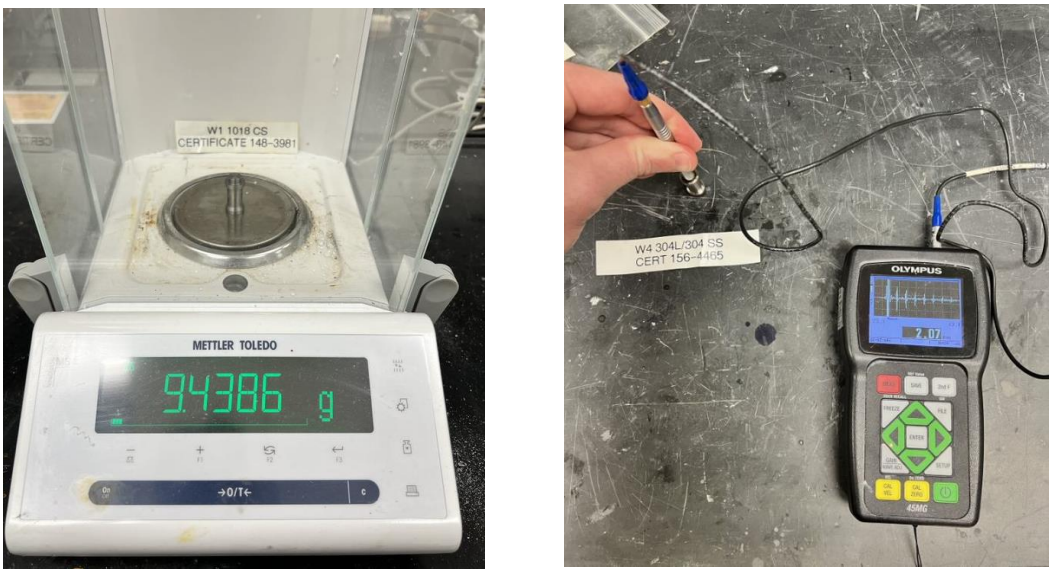


**Figure 155. Coupon mass measurement (left) and UT thickness measurement (right).**

In December, 6M salt solutions prepared in the previous performance period were analyzed for thermal measurements and the solution was tested in the bench scale loop for temperature variations during short durations of operation. Temperature fluctuations due to the chemical reactions occurring in the solutions during the mixing process were studied prior to testing the concentrated 6M solution in the loop. Thermal images during the mixing process revealed elevated temperatures. Sample thermal images collected during mixing of solvents are shown in Figure 156. The initial temperature of the water in the beaker was at 66 °F. Addition of the first solvent (sodium hydroxide) resulted in a temperature rise of ~102 °F. The solution was left undisturbed to cool for ~30 minutes and then the second solvent, aluminum nitrate, was added. This resulted in a pungent smell and excessive heat was generated with temperatures rising to 130 °F (Figure 156). Thereby the solvent was added in small quantities with continuous mixing. The solution was allowed to cool for ~1 hr for complete dissolution, ensuring the formation of sodium nitrate. Next, the remaining chemicals were added.

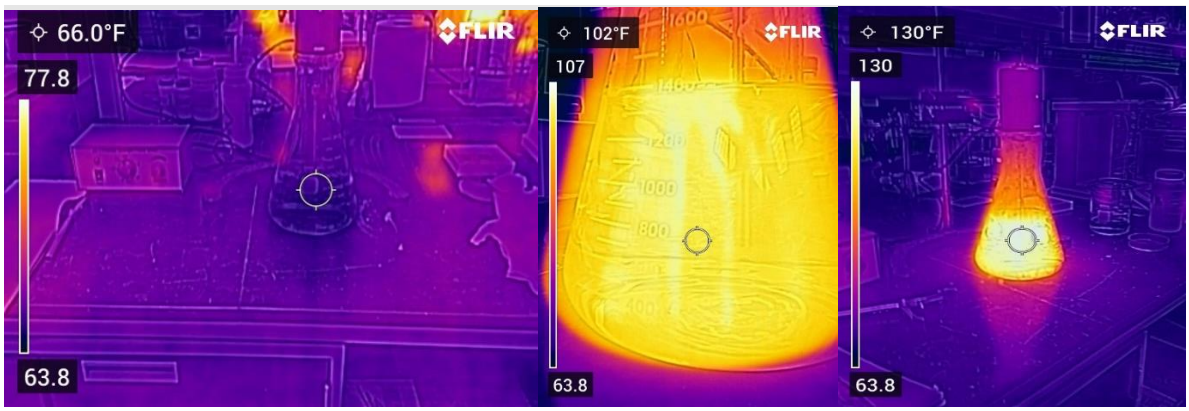


**Figure 156. Thermal images during the salt mixing process.**

During the addition of sodium sulphate, a deposit was formed at the bottom of the beaker due to its powdered structure (Figure 158). The settlement was mechanically blended into the solution. Sodium nitrate took a longer duration to dissolve as it is in the form of large circular balls and is to be added in large quantities compared to the other salts (Figure 207). It resulted in an initial opaque solution followed by a yellowish tint to the liquid. A volume of 18 liters of solution was prepared in 10 batches. Initial batches took longer durations (~4.5 hrs) and after 2 iterations, the time of preparation was reduced to ~ 2 hrs per batch as the process was optimized.

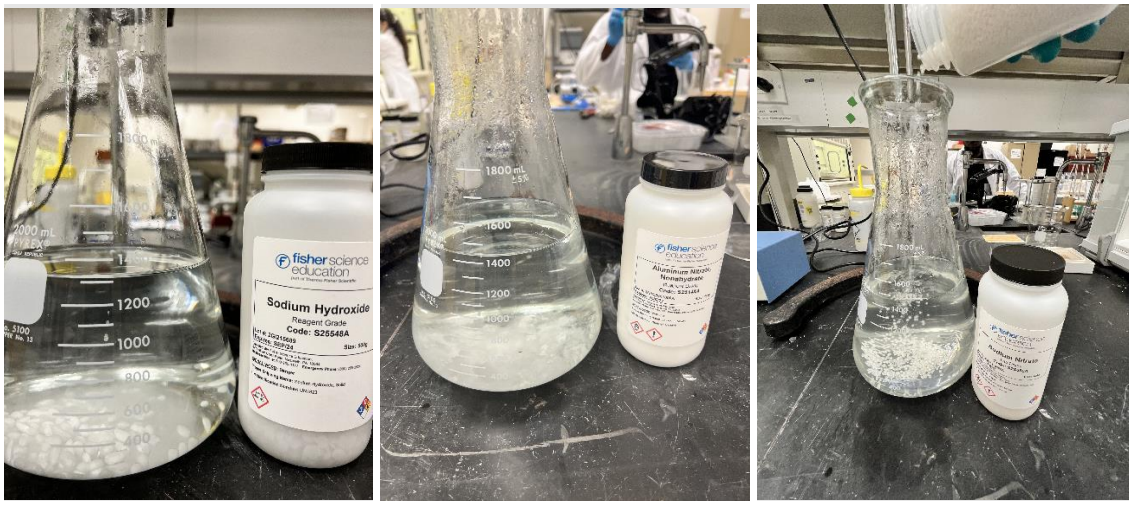


**Figure 157. Significant salts and solvent images (sodium hydroxide, aluminum nitrate and sodium nitrate).**

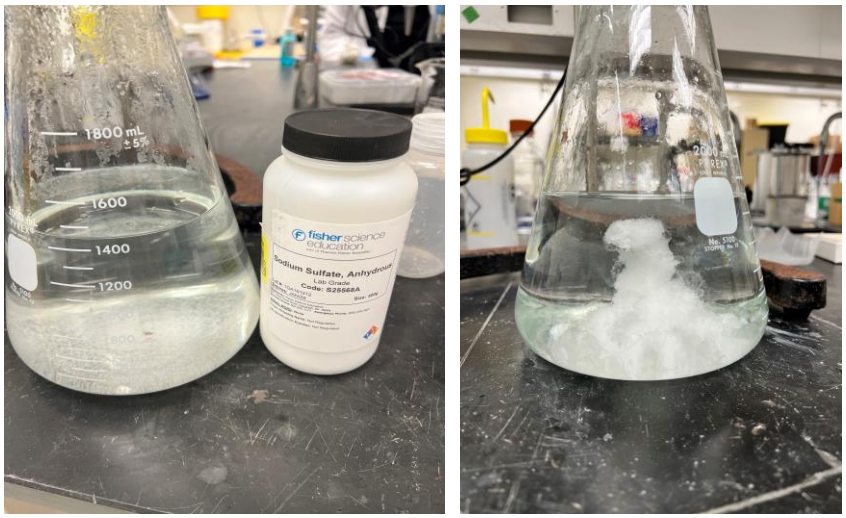


**Figure 158. Sodium sulphate during dissolution.**

The 18L 6M salt solution was pumped into the reservoir tank in the loop and tests were conducted to investigate the temperature rise in the loop. The thermal profiles on the loop under dynamic conditions are shown in Figure 159. From the figures, it is evident that the initial loop temperature was 75°F and it reached a highest temperature of 110°F over a period of 6 hrs during continuous fluid circulation. The coupon section (3-inch pipe) showed a high temperature (~110°F) (Figure 160). It is to be noted that the elbows made of stainless steel were cooler with lower temperatures when compared to the carbon steel sections. The maximum difference in temperatures between the two metals was observed to be ~50°F indicating the suitability of stainless steel under thermal variations. The pump showed the highest temperature rise to a maximum value of 161°F (Figure 161). This limits the operation of the loop on a continuous duration in addition to the heating of metal pipes. FIU is currently investigating the temperature effects on the loop to optimize the testing time per day/week and conducting intermittent tests for caustic corrosion.

**Figure 159. Caustic loop thermal images during operation with temperature changes over time (75.2 to 93.2°F).**

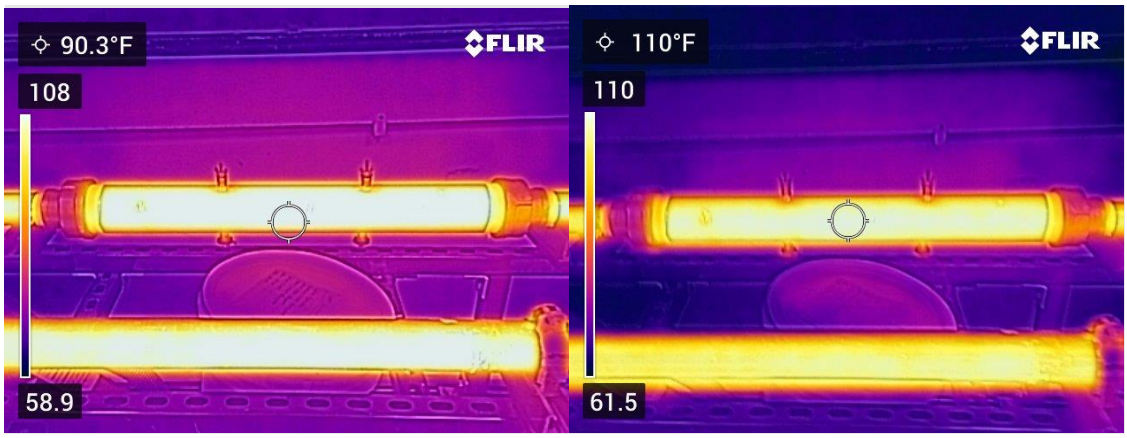


**Figure 160. Thermal images of the coupon sections (3-inch pipe) with temperature rise from 90.3 to 110°F.**

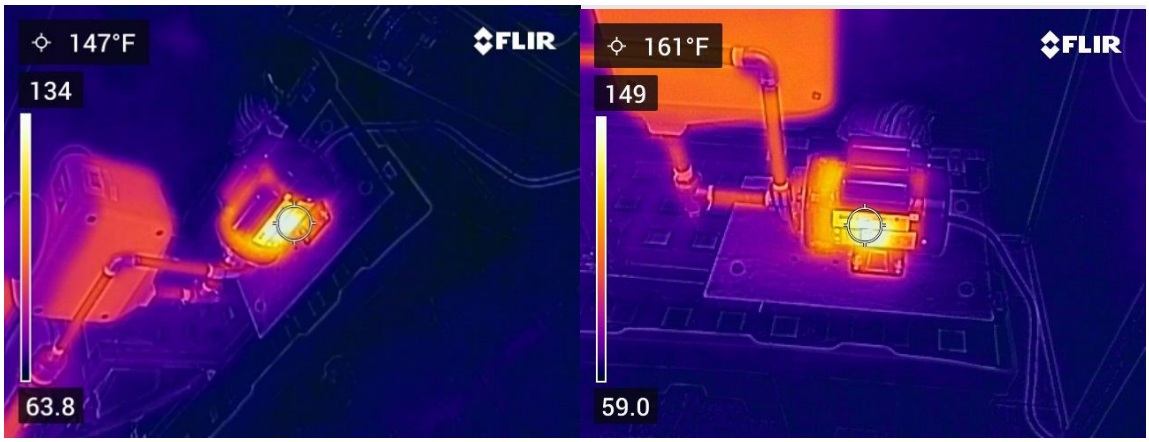


**Figure 161. Pump thermal profile with highest temperature reaching 161°F.**

During the next quarter, coupon evaluations under static test conditions with the simulated waste recipe, were continued for caustic corrosion monitoring. FIU was waiting for the procurement of new coupons from the SRNL team to test on the bench scale loop for dynamic tests. Under static testing conditions, all 5 coupons under complete immersion state were recovered and evaluated for visual images, weight changes, and thickness values. Images of caustic corrosion are shown in Figure 162. Coupon weights are shown in Table 20 and UT readings are shown in Table 21. The time difference between the data presented is a period of 7 months (October till May). As expected, carbon steel is the most corroded with a 6M salt solution while stainless steel showed the least change. FIU will be receiving a new set of coupons for chemical evaluations with a 6M concentrated simulant solution.

| Chemical Corrosion Testing of Steel Coupons (static testing) | | | | | |
|---|---|---|---|---|---|
| Date(s) | Molarity | Carbon (Step) | Carbon (Inside) | Stainless (Step) | Stainless (Inside) |
| 05/23/23 | 4M | | | 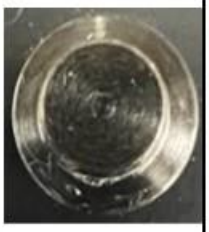 | |
| 05/23/23 | 6M | 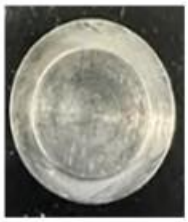 | | | |
| 06/07/23 | 4M | | | 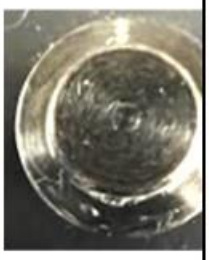 | |
| 06/07/23 | 6M | | | | |

**Figure 162. Visual images showing caustic corrosion in the coupons under static conditions.**

**Table 20. Mass Loss in Coupons due to Static Corrosion**

| Chemical Corrosion - Weight Comparison | | | |
|---|---|---|---|
| Coupon Properties | Weight (g)-Before | Weight (g) - After | Change in Weight (g) |
| 6M Carbon Steel | 9.57553 | 9.46117 | 0.11436 |
| 6M Stainless Steel | 9.14073 | 9.07733 | 0.0634 |
| 4M Carbon Steel | 9.49041 | 9.4511 | 0.03931 |
| 4M Stainless Steel | 9.04392 | 9.03313 | 0.01079 |
| 2M Stainless Steel | 9.20587 | 9.1524 | 0.05347 |

**Table 21. Thickness Change in Coupons due to Static Corrosion**

| Chemical Corrosion - UT measurements | | | |
|---|---|---|---|
| Coupons Properties | Measurement (mm) Before | Measurement (mm) After | Change in thickness (mm) |
| 6M Carbon Steel | 1.1684 | 0.635 | 0.5334 |
| 6M Stainless Steel | 0.6096 | 0.6858 | 0.0762 |
| 4M Carbon Steel | 1.143 | 0.6604 | 0.4826 |
| 4M Stainless Steel | 0.6096 | 0.5842 | 0.0254 |
| 2M Stainless Steel | 0.7366 | 0.6604 | 0.0762 |

The coupon evaluations, under static test conditions with the simulated waste recipe, were continued for caustic corrosion monitoring. FIU received the pipe section and coupons from SRNL and assembled the section into the loop. Testing was initiated but the pump started leaking and thus had to be repaired. The pictures of the disassembled pump, damaged slip ring, pump's volute and impeller are shown in Figure 163 and Figure 164.

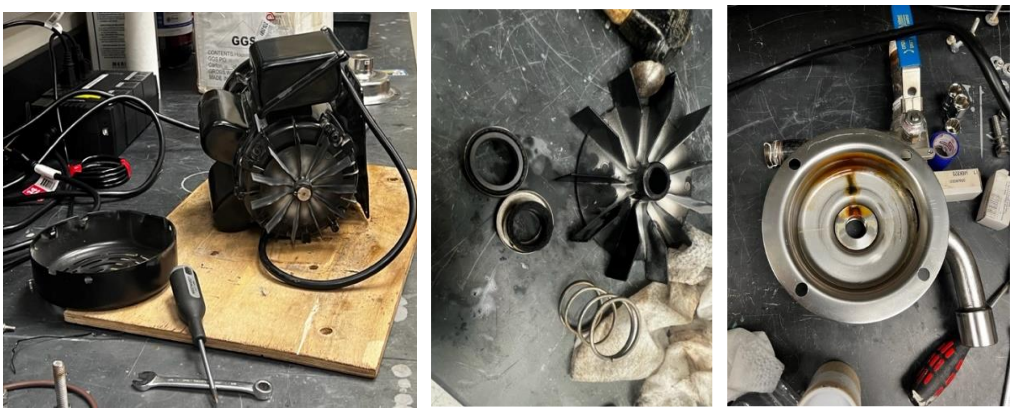

**Figure 163. Chemical handling pump (left), disassembled impeller (center) and pump's volute (right).**

**Figure 164. Slip ring (left), volute showing chemical corrosion (center) and pump's shaft (with casing removed) (right).**

In addition, the static test results for 2, 4 and 6 M solutions were compared for the carbon and stainless-steel coupons for a duration of 3 years. Results are shown in Figure 165 to Figure 167. The mass loss is evident over the duration of 3 years. The first graph shows variation of mass in the coupons immersed in 2, 4 and 6 Molar salt solutions. It is evident that the trend (behavior) of the mass change is uniform in all three cases. The peaks and valleys in data are predicted to be due to the solids deposited inside the coupons that were eventually cleaned. Maximum mass loss was observed in the case of carbon steel and with 6M salt solutions. The details of the collected data will be transmitted to SRNL for their documentation and future use.

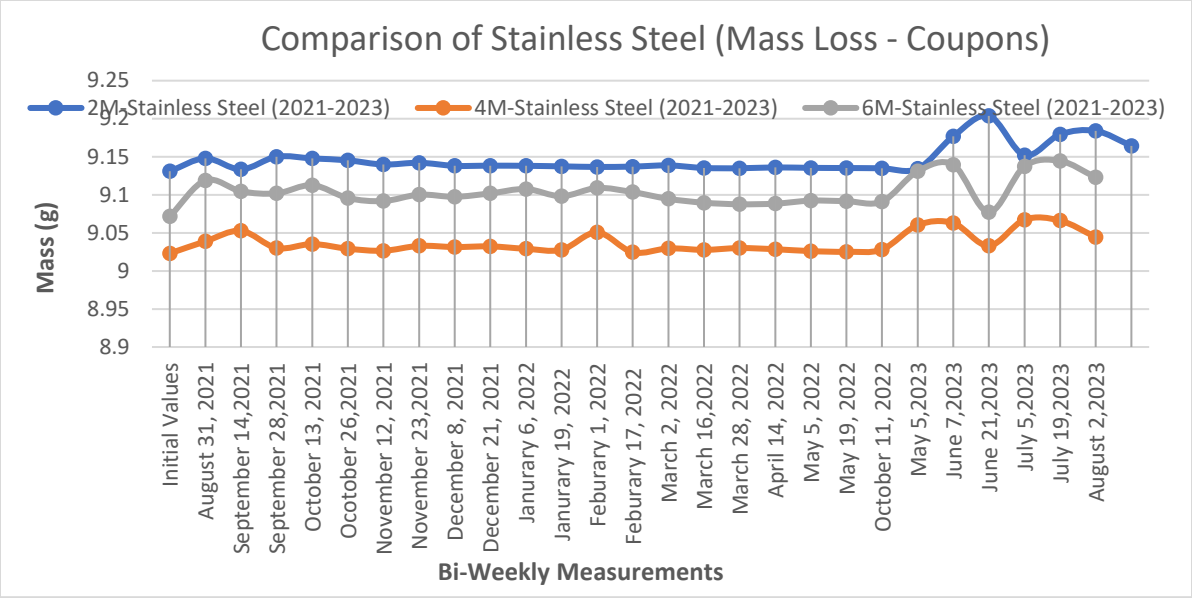


**Figure 165. Static immersion test results for SRNL coupons (stainless coupons with 2, 4 and 6 M salt solutions).**

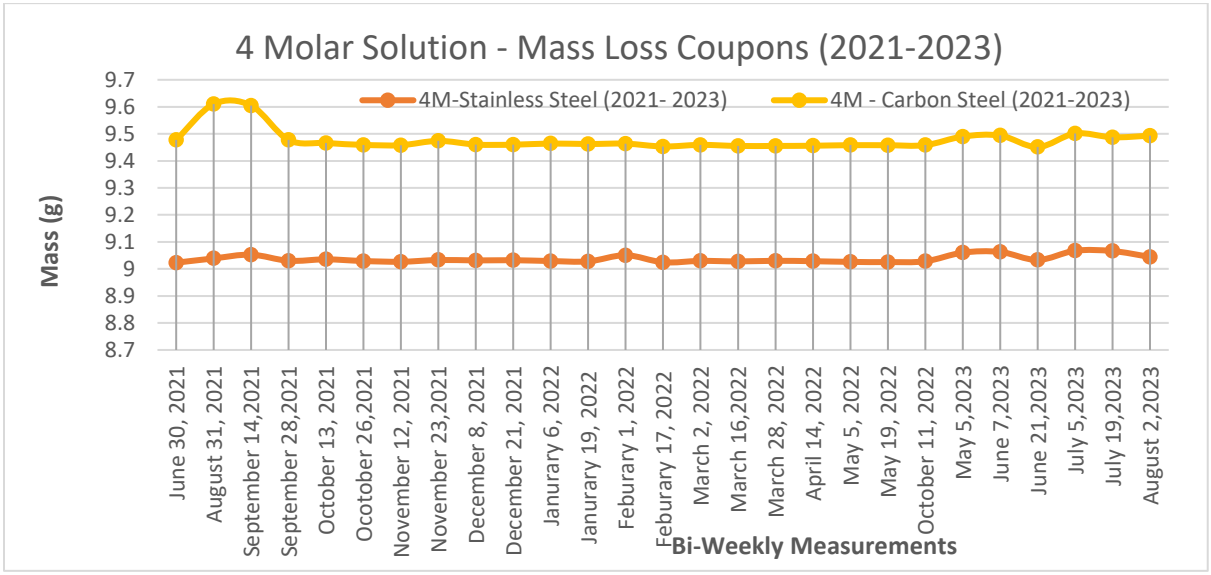


**Figure 166. Static immersion test results for the SRNL coupons (stainless and carbon steel data comparison).**

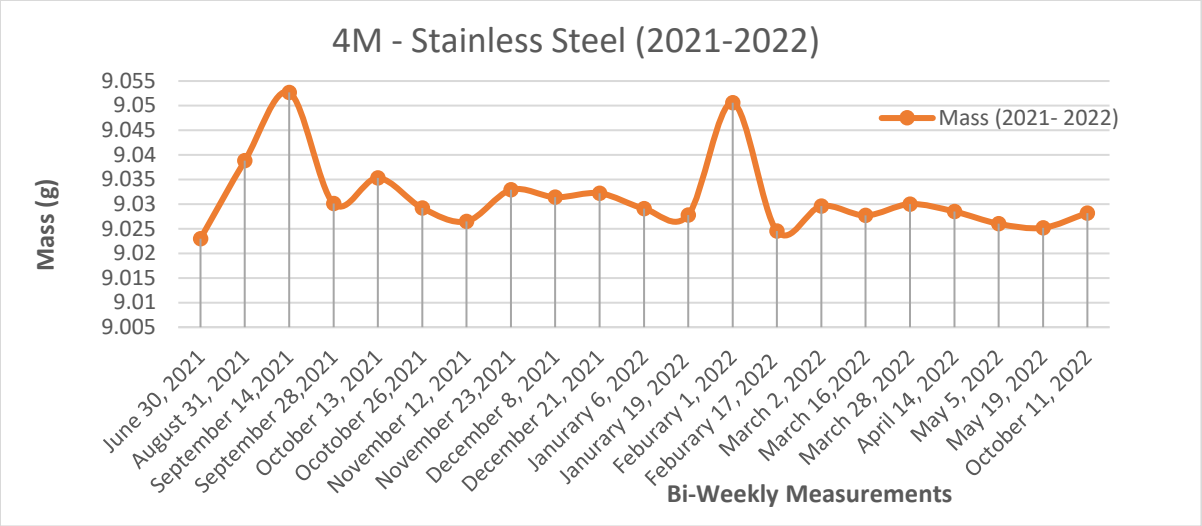


**Figure 167. Static immersion test results for the SRNL coupons (4 M solution details of mass changes).**

## Subtask 19.1.2: Conclusions

The effect of simulated caustic solutions replicating the chemical composition of HLW at Hanford and Savannah River sites is studied on waste transfer pipes. Two materials have been considered for corrosion due to the varying molar concentrations of the chemical simulants. Immersion experiments were conducted using SRNL's patented coupons. Visual inspection, weight change and thickness changes are quantified. Finding of the research summarize that carbon steel underwent high levels of caustic corrosion with 6M salt simulants over a period of 3 years. Results of static testing will be shared with SRNL for future material and design considerations. Based on the static test results, bench loop testing will be conducted with high concentrations of the chemical simulants and SRNL obtained new coupons.

## Subtask 19.1.2: References

1. Wiersma, B. J., Peters, T. B., Poirier, M., "Simulant Recipes for Flow-loop Testing at Florida International University", SRNL-L3000-2020-00017, December 18, 2020.
2. https://www.olympus-ims.com/en/shop/item/269-productId.570437480.html\
3. Aravelli, A., McDaniel, D., Thompson, M., Imrich, K., Wiersma, B., "Erosion-Corrosion Detection in Carbon Steel Pipe Loops using SRNLs Thickness and Mass Loss Measurement Coupons", Waste Management 2020 Conference, Phoenix, AZ, March 2020.
4. Aravelli, A., Thompson, M., McDaniel, D., Krutsch, M., McNeilly, M., Imrich K., Wiersma B., "Advanced Fiber Optic and Ultrasonic Sensor Systems for Structural Health Monitoring of Pipes in Nuclear Waste Sites", IMAPS 52nd International Symposium on Microelectronics (IMAPS), Boston, MA, Sep 30-Oct 3, IMAPS (2019).
5. Thompson, M., McDaniel, D., Wiersma, B., Aravelli, A. "Structural Health Monitoring Technologies for Wear and Anomaly Detection in Nuclear Waste Transfer Systems", Waste Management 2021 Conference, Phoenix, AZ, March 2021.

6. A. Aravelli, D. Sinnott, R. Piloto, D. McDaniel, L. Lagos, B. Wiersma, “Simulant Based Particle Erosion and Chemical Corrosion in HLW Pipe Components”, Waste Management 2023 Conference, Phoenix, AZ, March 2023.

## Subtask 19.1.3: Automated Erosion and Corrosion Detection using fluid flow dynamics and advanced data analytics

### Subtask 19.1.3: Introduction

Erosion and corrosion testing in the flow loop provides adequate data for developing automated erosion and corrosion detection process; and condition monitoring of the HLW pipe system components. This subtask investigates the use of experimental and flow simulation data to develop advanced algorithms for preventive and predictive maintenance of the tanks and transfer lines. This year’s scope of work included:

- Computational Fluid Dynamics (CFD)-based flow model development in pipe components and loops using COMSOL and ANSYS.
- Machine learning model development for erosion corrosion detection in HLW transfer pipes.

### Subtask 19.1.3: Methodology, Results and Discussion

During the beginning of the year, collaboration with Project 3 team members was initiated for the machine learning algorithm development and CFD simulations with COMSOL multi-physics software were conducted. The database with images obtained from some of the sand erosion experiments and salt-based corrosion tests was shared. The team also worked on appropriate architecture development for the erosion/corrosion models.

COMSOL Multiphysics software’s 2 new modules were investigated. They were the particle tracing module and the pipe flow and CFD module. Both were needed for this current task. The particle tracing module can be used for sand and glass particles suspended in the flow, while the CFD and pipe flow module can be used to formulate the experimental test bed and flow conditions with fluids. FIU worked on the procurement of the additional modules. Sample applications found in literature of the particle tracing process for erosion rate and particle tracing are shown in Figure 168. The module uses Euler-Lagrange multiphase flow models in which particles are modeled as discrete entities.

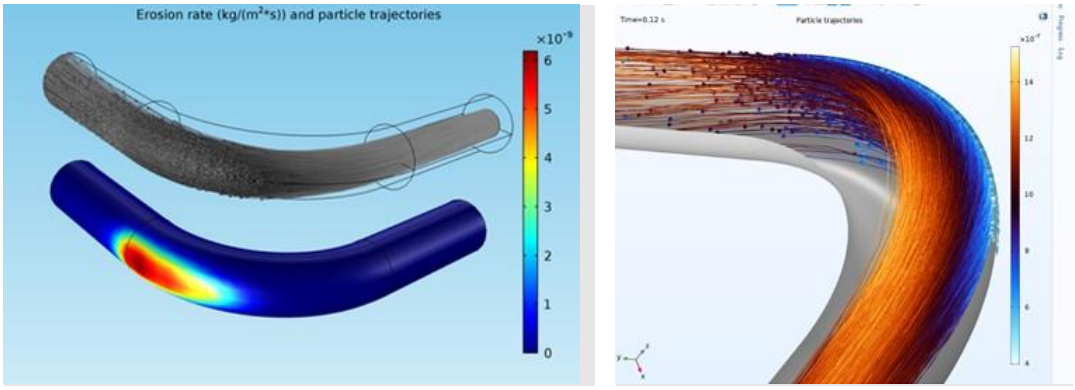


**Figure 168. Sample COMSOL simulations for particle erosion (left) and detailed particle trajectories (right).**

***(https://www.comsol.com/model/pipe-erosion-due-to-contaminant-particles-16655)***

In December, flow simulations were initiated using the software COMSOL 6.0. A computational fluid dynamic (CFD) simulation of flow in a pipe section, with branching, was conducted to study the effect of water flow in a pipe with one inlet and two outlets. The geometry of the pipe was created using cylindrical and sectioned torus sections forming a union to achieve the branching. A finite element model was generated using triangular elements in a physics-controlled mesh according to the geometry. Flow in the pipe for the initial study was assumed to be laminar, with flow velocity and pressure as dependent variables. Water was used as a working fluid and incompressible fluid conditions were considered. Laminar flow conditions were evaluated using Navier-Stoker's equation to calculate the flow velocities and pressure distribution in the pipe material. The pipe geometry and mesh are shown in Figure 169 and Figure 170. The velocity profile is shown Figure 171. It is evident that the velocity profile is according to the physics of the problem - depicting higher velocities at the core/center of the pipe and reduced velocities observed radially outwards reaching zero at the surface. Figure 172 indicates the velocity profile at the branched surfaces (Y-Z plane) with split flow. Reduced velocities due to the split are evident in the two branched sections. The volume graph (Figure 173) of velocity indicates a zero surface-velocity and the cut planes at different sections show a maximum velocity of 0.16 m/s in about 60% of the core. Full flow conditions are assumed in the simulations. The pressure profile is shown in Figure 174 and the contours also show a maximum pressure of 17.50 Pa at the inlet and decreasing towards the outlet (default atmospheric pressure). Currently, FIU is working on turbulent flow conditions with varied pipe geometry.

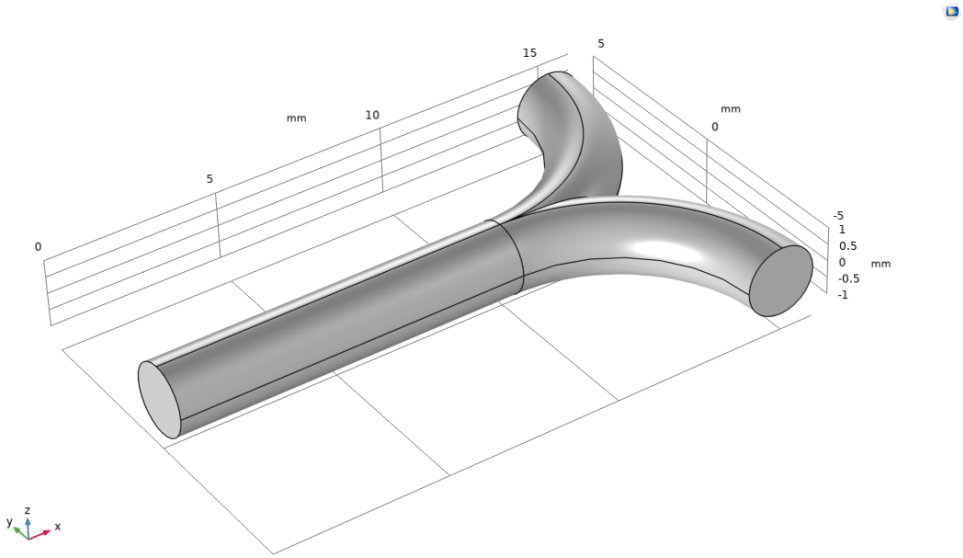


**Figure 169. Branched pipe geometry.**

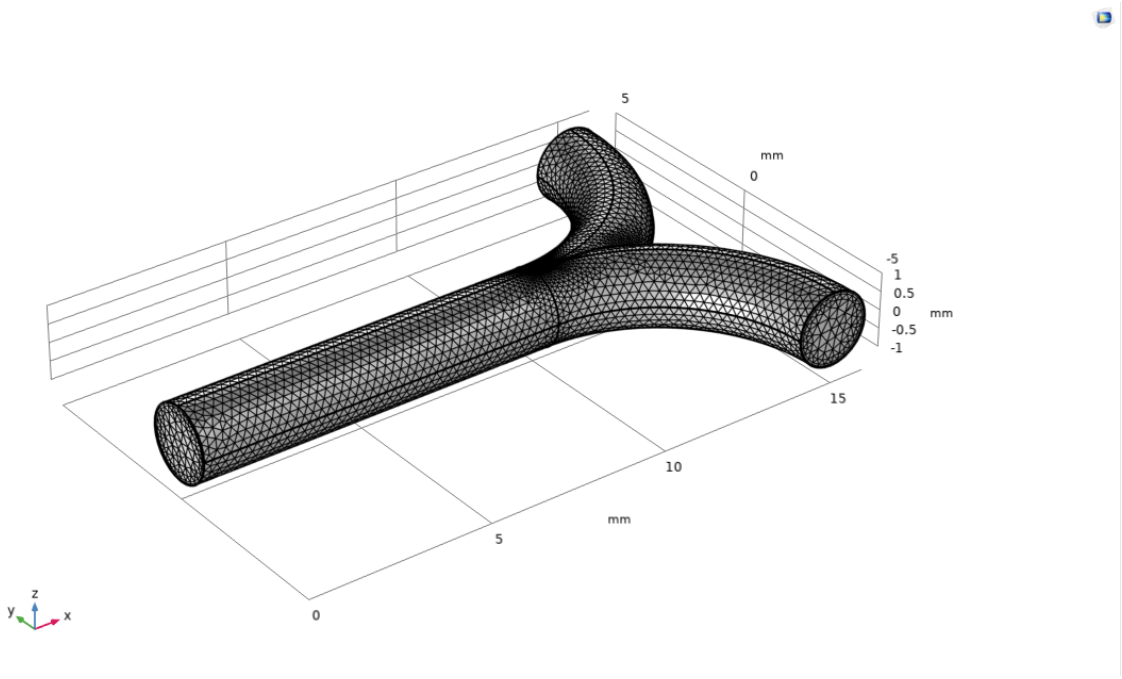


**Figure 170. FEA mesh of the pipe model.**

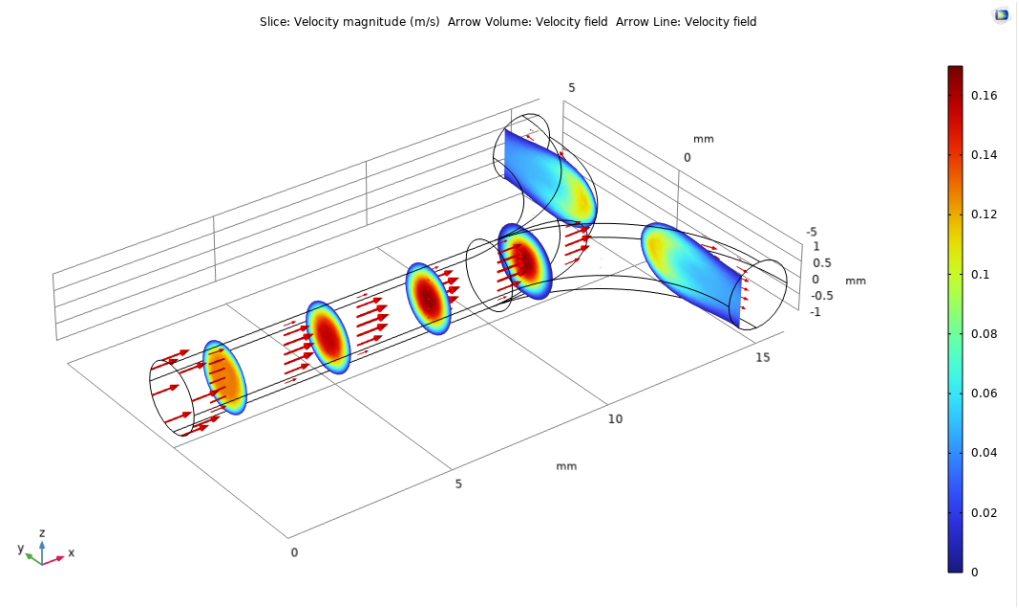


**Figure 171. Velocity flow field with cut planes normal to the flow direction.**

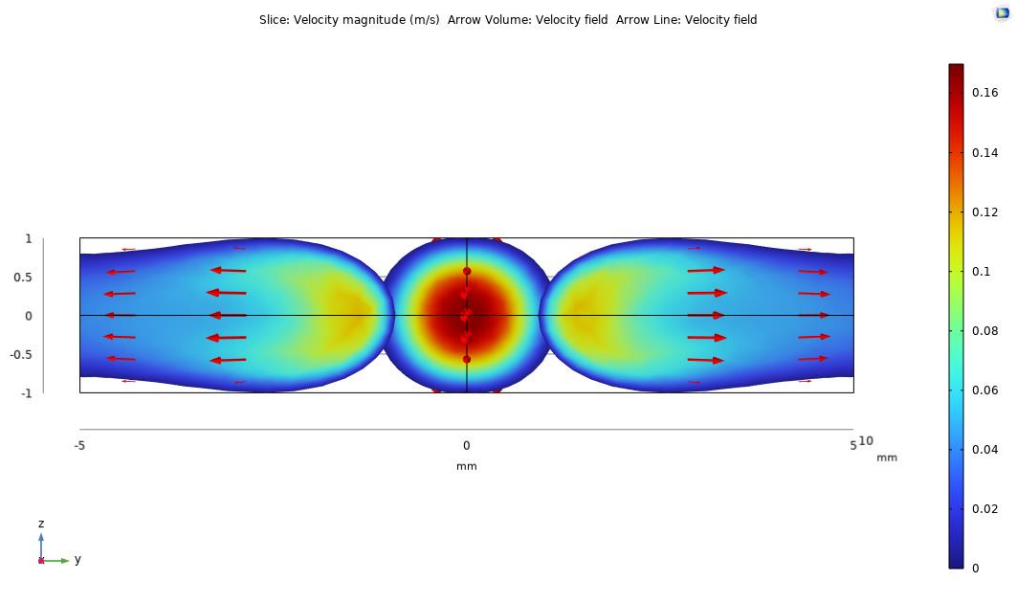


**Figure 172. Velocity flow field depicting the split in flow due to pipe branching.**

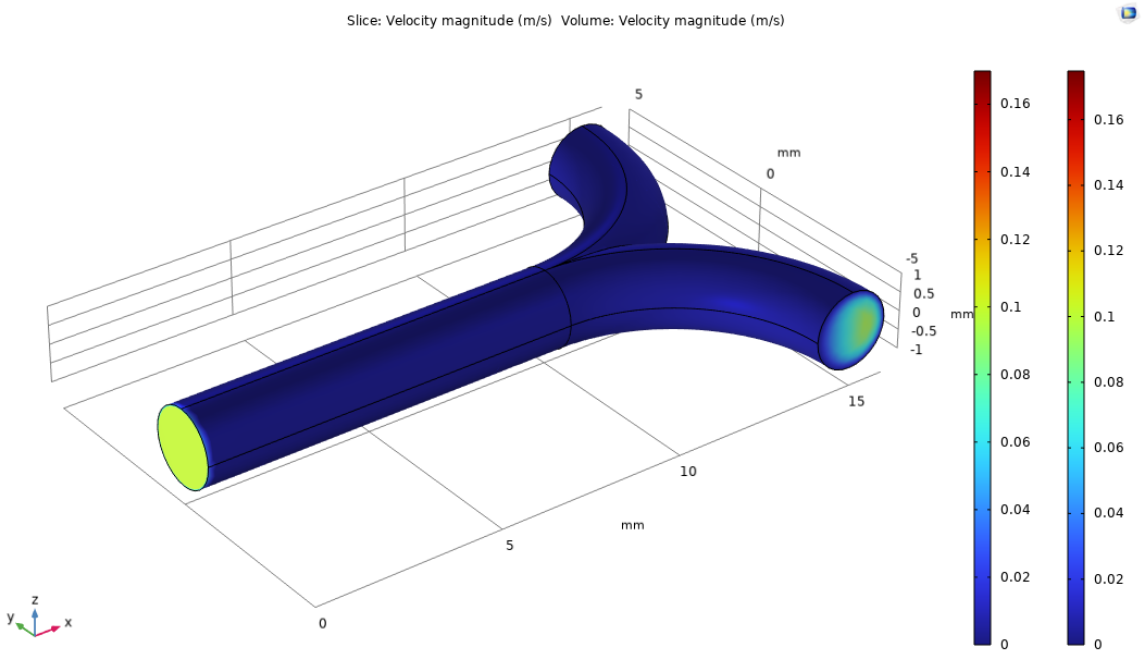


**Figure 173. Volumetric representation of flow velocity.**

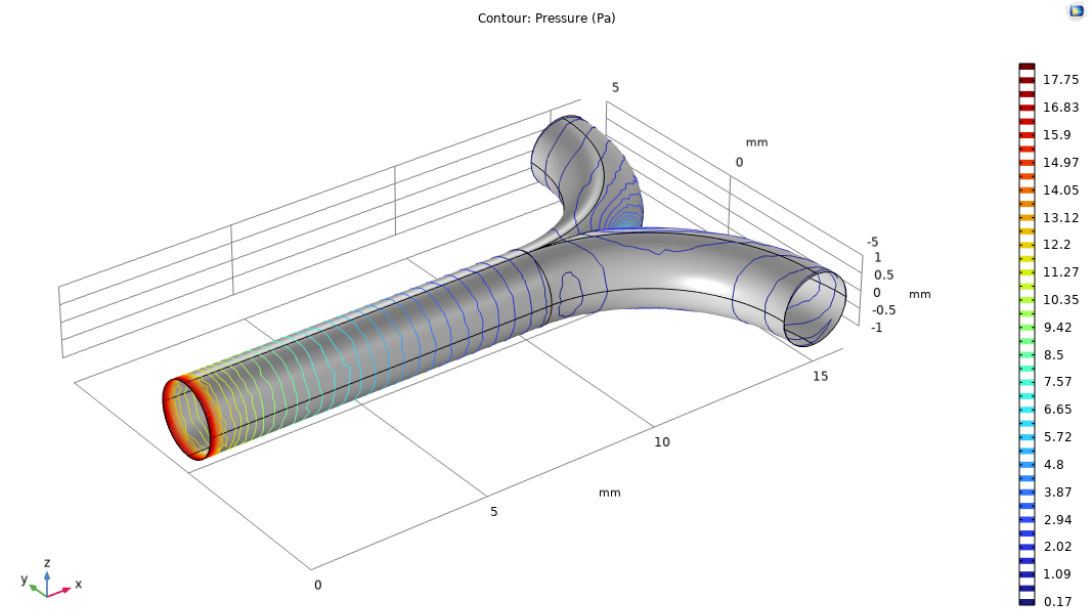


**Figure 174. Pressure distribution in the pipe material.**

Initially, CFD simulations were conducted using the available version of COMSOL. This version was basic and limited to laminar flow analysis. Since the flow in the FIU pipe loops is turbulent, the full CFD version of COMSOL was needed to proceed with the computational work. Discissions were held with the COMSOL representatives and a trial version of COMSOL 6.1 (latest full version) was obtained for two weeks to test. Turbulent flow analysis in a pipe section

was conducted to determine the COMSOL modules needed for the erosion and corrosion-based Multiphysics analysis in the pipe loops under various mixture conditions.

A cylindrical pipe section replicating straight sections and bend (90 degree) was used for the flow simulations. Each straight section of the pipe was 50 cm in length and 20 cm in diameter. Bend radius of curvature was 50 cm. Fluid transported in the pipe section was water with a flow velocity of 20 m/s. Liquid is treated as incompressible and only half of the pipe section was modeled taking advantage of the symmetry and computational benefits. The plane of symmetry was considered as an x-y plane as shown in Figure 175 (geometry).

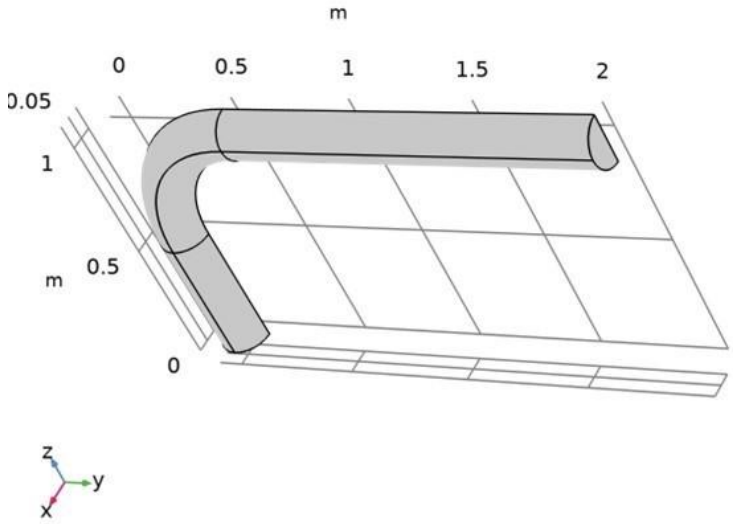


**Figure 175. Pipe geometry for turbulent flow simulation.**

The Reynold's number calculated based on the pipe geometry was Re = 3.96 X $10^6$ and hence defining the flow to be turbulent. For the CFD modeling, the Reynolds-average Navier-Stokes (RANS) k-ω turbulence model was selected since it is recommended for flows with curved streamlines near the bends. A structured finite element mesh with varying element sizes and fine resolution was used to account for accurate analysis at each section of the pipe. A boundary layer mesh condition ensured adequate resolution of the flow close to the pipe walls. The finite element mesh is shown in Figure 176. The solver took about 75 iterations to converge for the optimum velocity and turbulent parameters. Minimization error with iteration during convergence is depicted in Figure 177.

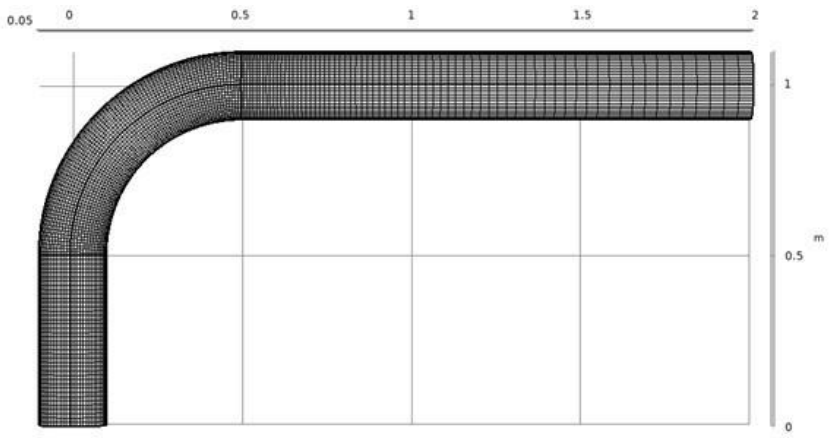


**Figure 176. FEA mesh of the pipe model.**

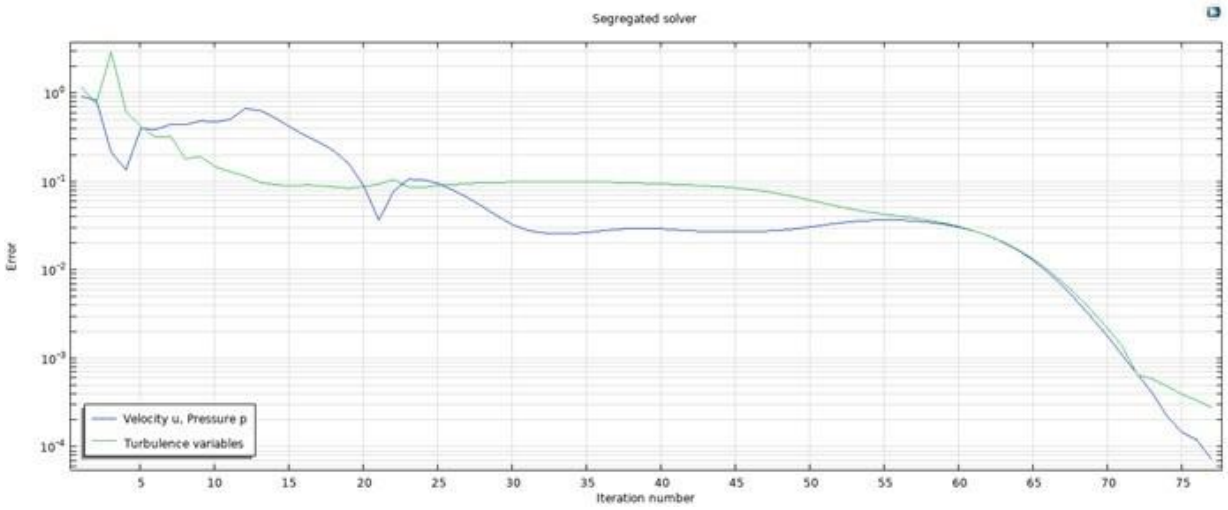


**Figure 177. Convergence plot of velocity, pressure, and turbulence variables.**

The resulting velocity distribution is shown in Figure 178 and Figure 179. A pressure plot is shown in Figure 180. It is evident from the velocity plots that the streamlines are curved after the bend depicting the influence of the bend radius of curvature on the turbulent flow. Also, the velocity slice plot shows a maximum velocity of approximately 19.5 m/s at the region after the bend indicating a fully developed flow field and turbulence effected by the pipe geometry. The pressure plot shows negative pressure at the inner radius of the bend indicating a small dead volume. The wall resolution in viscous units is shown in Figure 181 with a value less than 100 indicating an adequately refined mesh.

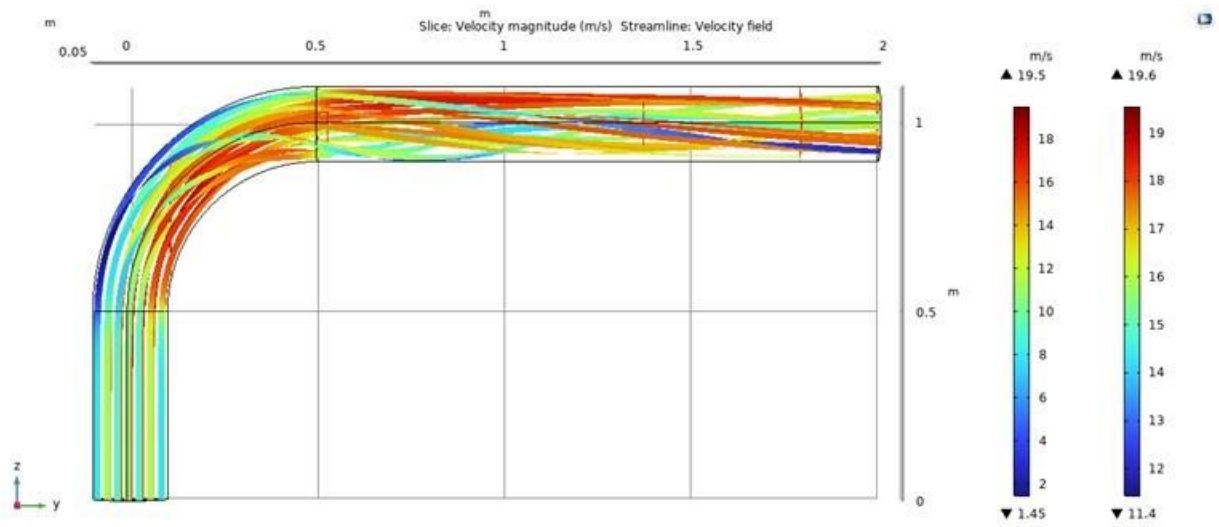


**Figure 178. Velocity flow field with curved streamlines due to turbulence.**

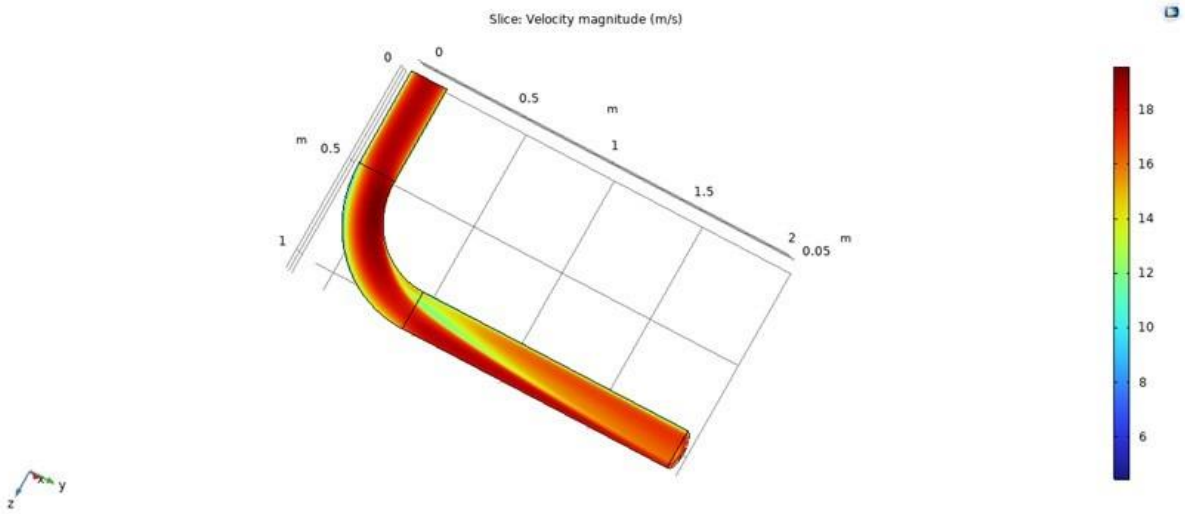


**Figure 179. Velocity slice plot.**

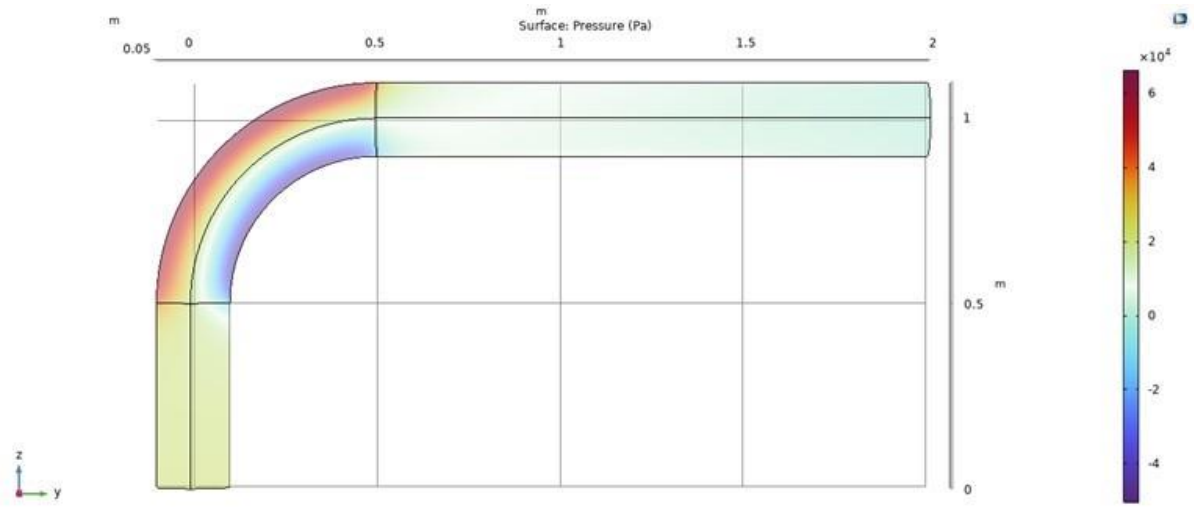


**Figure 180. Pressure distribution in the pipe.**

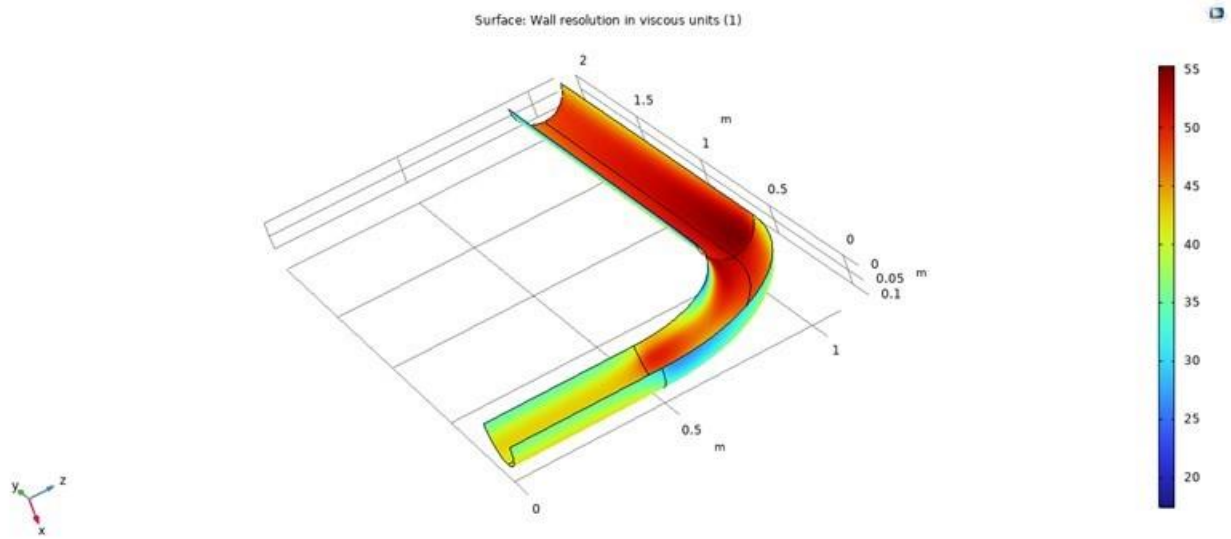


**Figure 181. Wall resolution (surface) in viscous units indicating the mesh refinement accuracy.**

## ***Fluid Dynamics Simulations for Particle Erosion***

During the month of February, CFD simulations were conducted to detect the effect of particle erosion in pipes. Previously, a pipe model was developed, a finite element mesh was generated and CFD simulations were conducted for laminar and turbulent flow conditions with water as the working fluid. During this period, the particle tracing module in COMSOL was used to generate erosion in the pipe bend which is the critical section prone to maximum erosion.

Pipe geometry used for model development is shown in Figure 182 (geometry) which consists of straight sections of 50 cm in length and 20 cm in diameter. Bend radius of curvature taken was 50

cm. Fluid transported in the pipe section was water with a flow velocity of 20 m/s. Liquid is treated as incompressible and only half of the pipe section was modelled taking advantage of the symmetry and computational benefits.

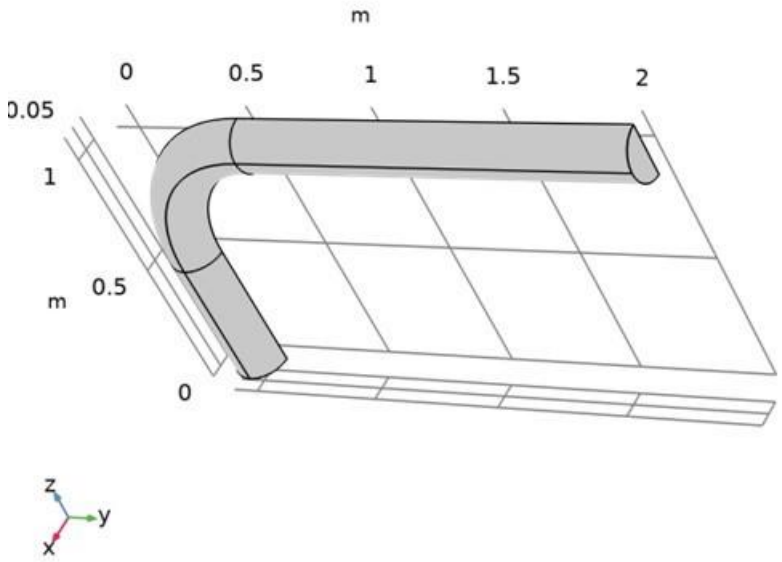


**Figure 182. Pipe geometry for turbulent flow and particle tracing simulations.**

Turbulent flow was modeled using the Reynolds-average Navier-Stokes (RANS) k-ω turbulence model in CFD and velocity contours were plotted. Next, the system was modelled by introducing the circular solid particles into the pipe and erosion rate was calculated. Particle trajectories replicating erosion at the bends is shown in Figure 183. Three different erosion models were used to detect the erosion rate on the pipe model. Results obtained by the three models (DNV, ECRC and Finnie) are provided in Figure 184, Figure 185 and Figure 186. It is evident that the erosion rate predicted is highest in the DNV model with a value of 18 nano kg/m$^2$s. The ECRC model has a maximum erosion value of 8 nano kg/m$^2$s and the Finnie model predicted a maximum erosion rate of 5 nano kg/m$^2$s. The difference in prediction is due to the parameters used for calculations of the erosion rate.

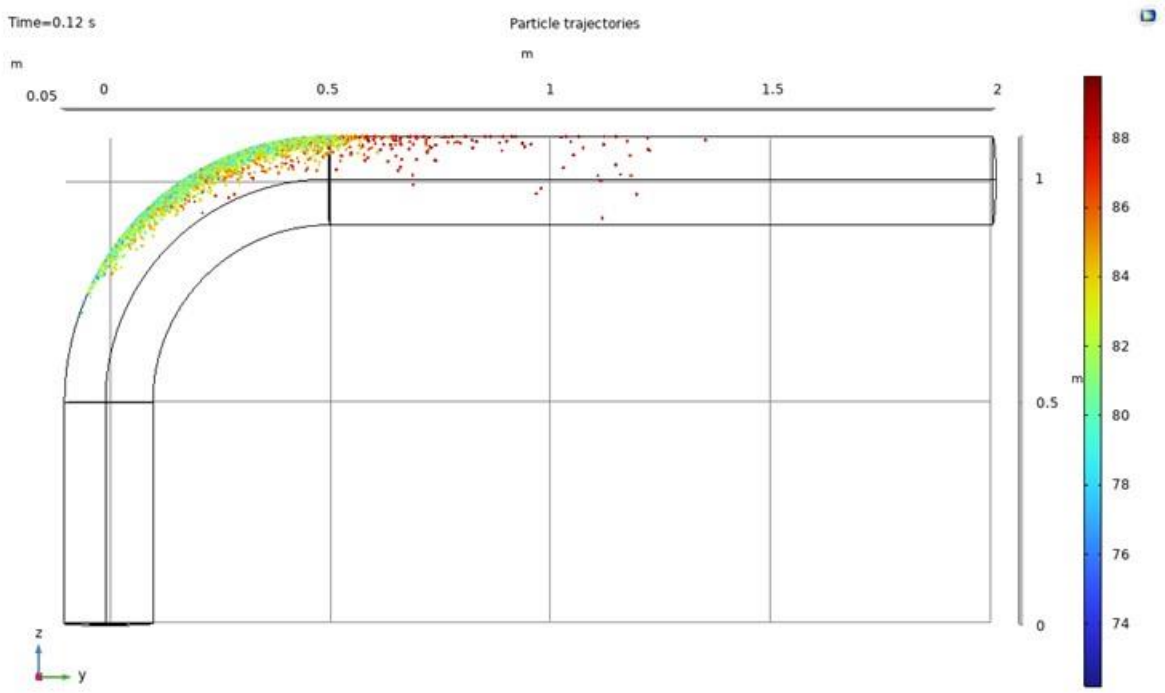


**Figure 183. Particle erosion using CFD in a pipe with turbulent flow conditions showing particle trajectories.**

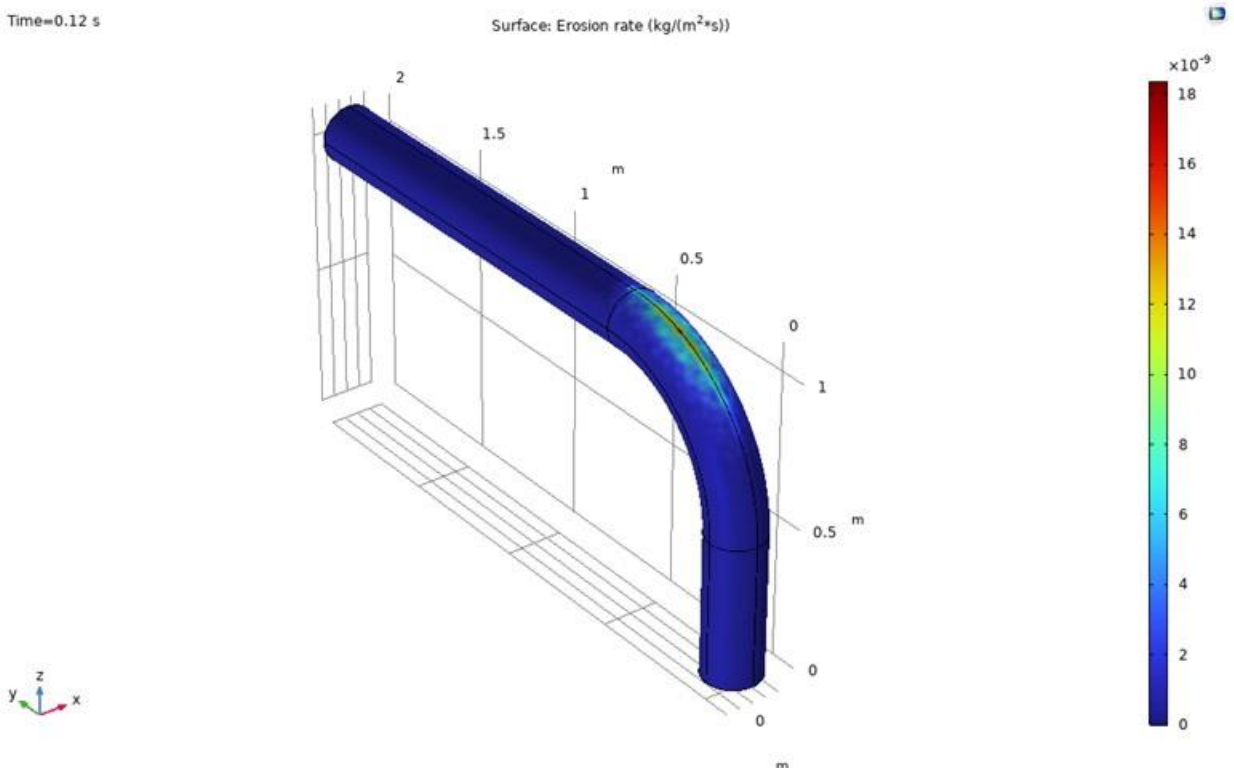


**Figure 184. Simulation of the surface erosion rate using the DNV erosion model.**

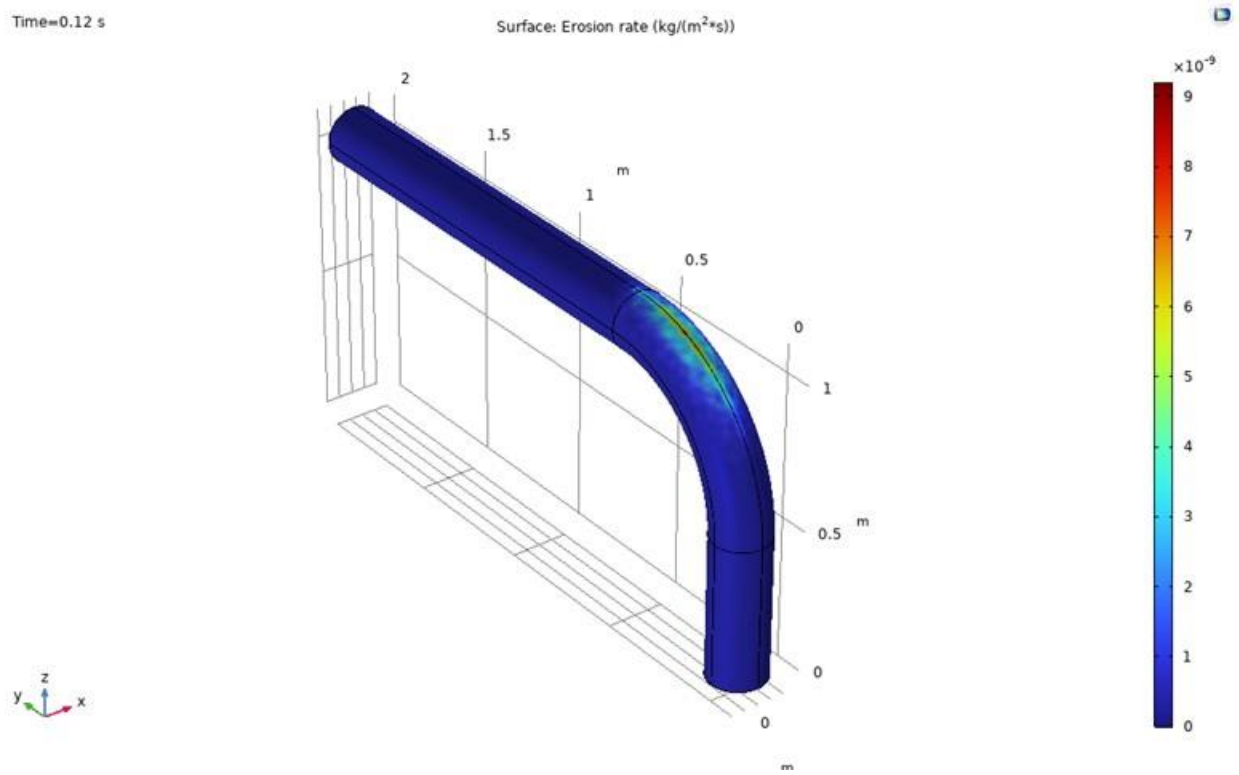


**Figure 185. Simulation of the surface erosion rate using the ECRC erosion model.**

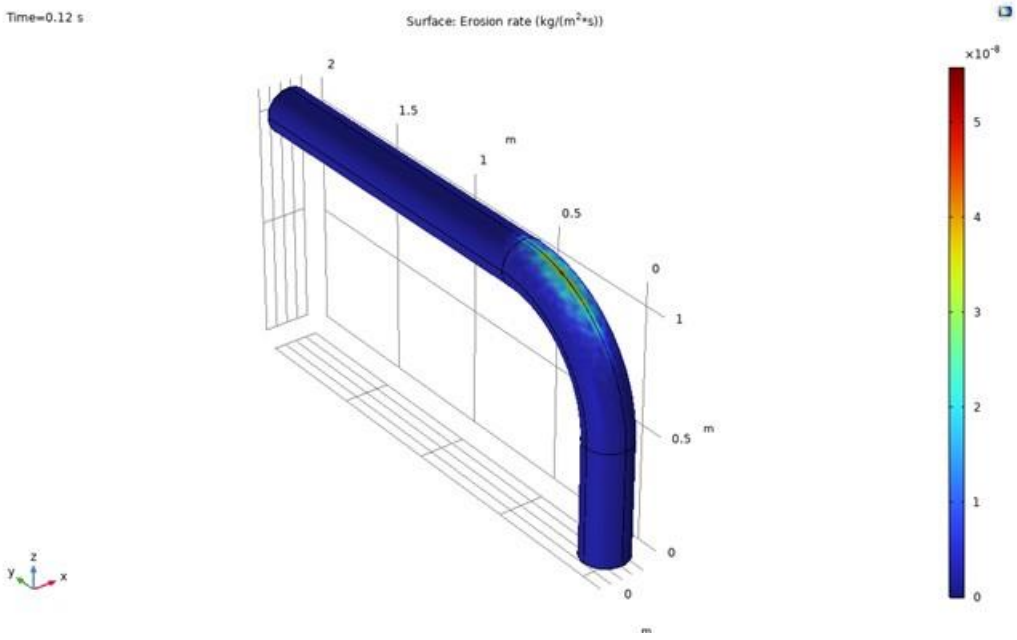


**Figure 186. Simulation of the surface erosion rate using the Finnie erosion model.**

***Fluid Dynamics Simulations for various pipe sections***

In the month of March, ANSYS 2022 R2 was used to simulate flow in various pipe sections – straight section, bend, and expander-reducer, replicating the change in pipe flow velocities during laminar flow conditions. Flow velocities and stresses on the pipe sections were computed.

Three pipe sections (geometries) were used for model development. The Nominal Diameter of the pipe was chosen to be 2 inches with a length of 1 ft. The material is carbon steel with schedule 40 dimensions. The Velocity Magnitude at the entrance is 1 m/s with an outer atmospheric pressure of 101,325 Pa on the surroundings of the pipe. Flow liquid is water and is treated as incompressible. Results shown in Figure 187 are for the straight section. The sketches are the result of a simulation test that covered the range of laminar fluid flow in a horizontally straight pipe. The left-side picture shows the velocity contours while the right-side image is the wall shear stress due to the liquid flow.

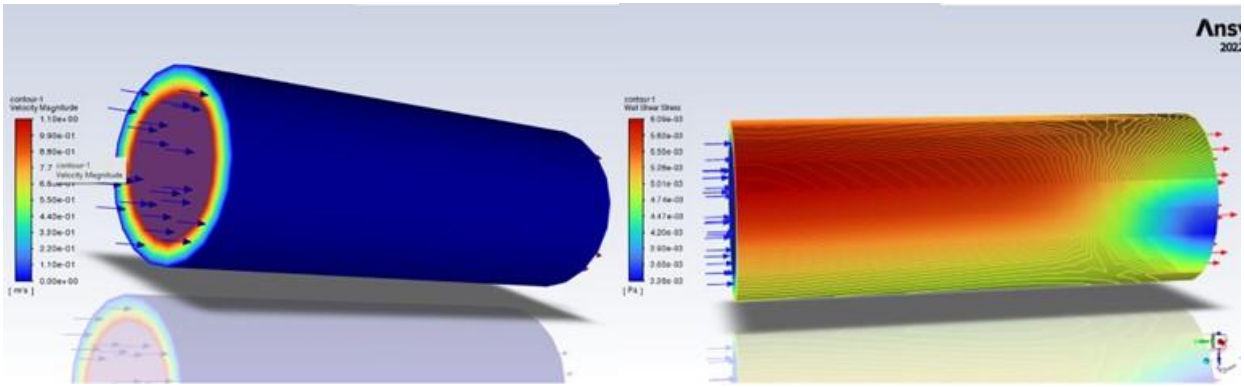

**Figure 187. Pipe flow results – velocity contours (left) and shear stress (right).**

Similar computations on a pipe bend are shown in Figure 188. The left image shows the velocity flow lines while the right image shows the pressure distribution on the bend. It is evident that the magnitude of the velocity is highest at the inner side of the bend while the pressure is lowest. The highest pressure is at the outer side of the bend.

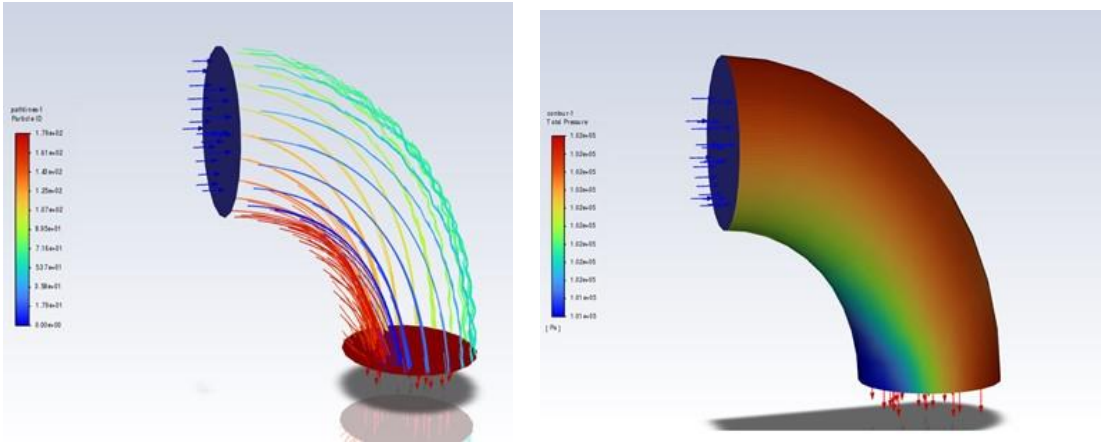

**Figure 188. Flow through an elbow - velocity flow lines (left) and pressure distribution (right).**

Laminar flow simulations were also conducted using an expander-reducer section. Results are provided in Figure 189 for the velocity and the total pressure. It is evident that the pressure is highest at the inlet side of the pipe, reduces as the pipe expands to a higher diameter and finally reaches values close to the outlet (atmospheric pressure).

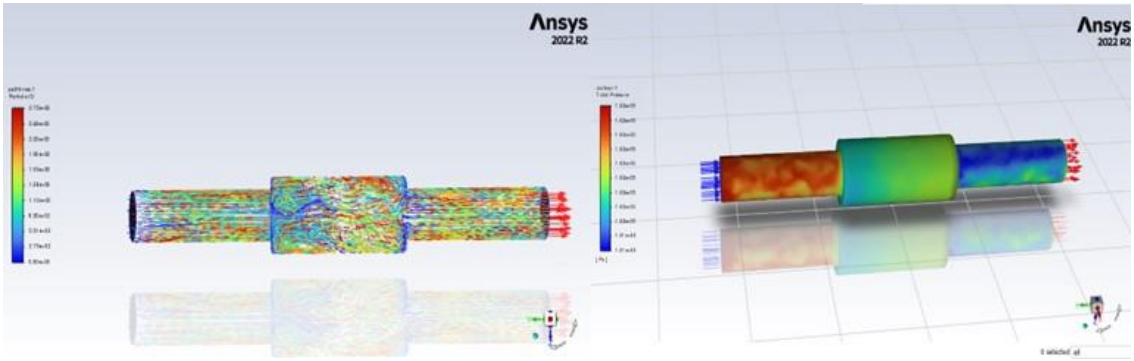


**Figure 189. Flow through an expander-reducer – velocity lines (left) and total pressure (right).**

In addition, CFD simulations were continued using ANSYS software and the full scale COMSOL multi-physics software was procured and installed. The COMSOL software (version 6.1) includes the base version and three additional modules - CAD import module, CFD module and the particle tracing module. Simulations conducted with ANSYS and COMSOL are presented next.

ANSYS 2022 R2 (base version) was used to simulate flow in pipes with fittings including the elbows, reducers and straight sections replicating the change in pipe flow velocities during laminar flow conditions. Flow velocities and stresses on the pipe sections were computed. Previous simulations include individual component analysis, while current simulations include combined pipes resembling part of the flow loop (circuit). The nominal diameter of pipe was chosen to be 2-inch with carbon steel material. The pipe is standard schedule 40 low carbon steel grade. The Velocity Magnitude at the entrance is (1 m/s) with an outer atmospheric pressure of (101,325 Pa) on the surroundings of the pipe. Flow liquid is water and is treated as incompressible. CFD simulations of the pipeline are shown in Figure 190 to Figure 192. Results shown in Figure 190 represent the flow path lines depicting laminar flow conditions. As seen, the flow is uniform with variations along the cross section.

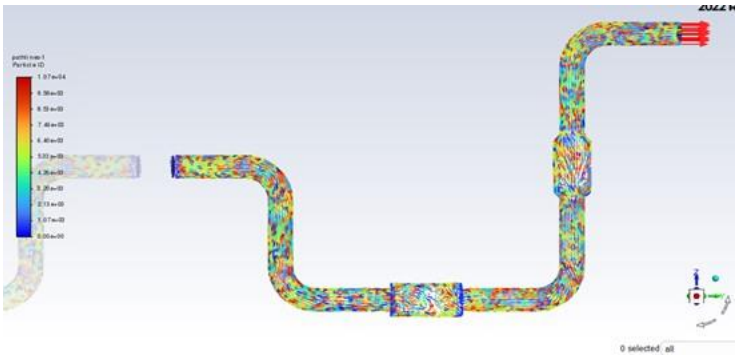

**Figure 190. Pipeline flow results – flow path lines.**

Figure 191 shows the total pressure distribution in the pipe with highest pressure at the inlet side prior to the expander. The surface pressure profile at the first expander varies and after the expander, the pressure increases near the second bend prior to the second expander. Further, it reduces at the expander and finally it is close to the atmospheric pressure at the exit indicating the environmental conditions at the outlet.

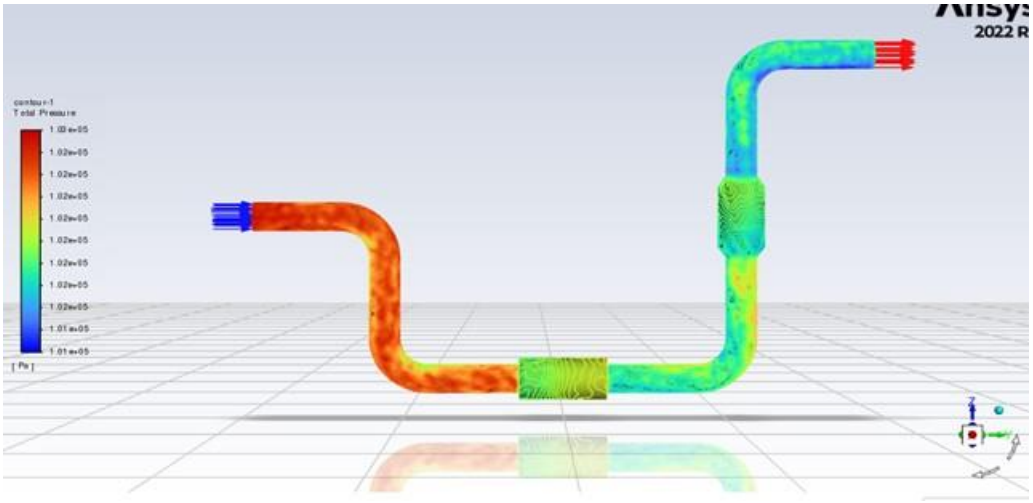

**Figure 191. Pressure distribution due to the flow in the pipeline with bends and expander-reducer sections.**

Figure 192 shows the wall shear stress due to the flow in the pipeline. As indicated in the figure, the wall shear stress is maximum in the bends, particularly at the inner side of the bends. This is due to a lower surface area. Areas closer to the inlet and exit have the highest shear while the reducer-expander sections have the least wall shear. This is due to the peripheral surface area difference between the two sections.

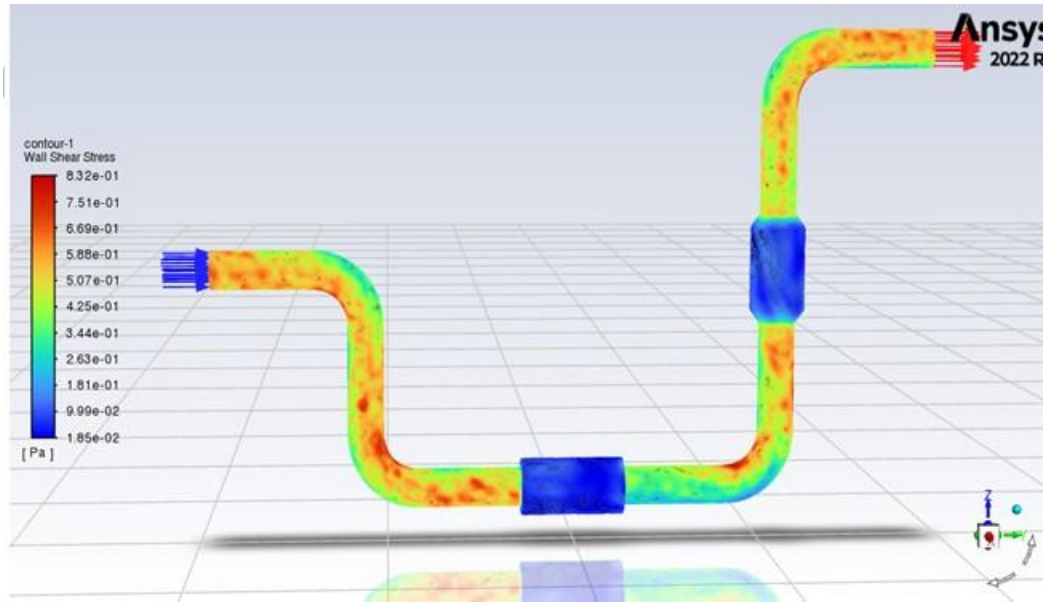


**Figure 192. Wall shear stress distribution in the pipeline with bends and expander-reducer sections.**

Additionally, FIU initiated the process of CFD simulations using the full version of COMSOL Multiphysics software procured. Previously, CFD simulations under laminar conditions were investigated in pipe sections using ANSYS base version. In this period, COMSOL (full version) was obtained, and turbulent flow simulations were hence conducted. A pipe section replicating the 2-inch pipe nipple, with a length of 6 inches, as used in the erosion loop at FIU, was designed in SolidWorks and turbulent flow simulations were conducted using the K-ε CFD model in COMSOL. Fluid flow in the pipe section was investigated with velocity and pressure profiles. The CAD model and finite element mesh of the pipe internal volume are shown in Figure 193.

The pipe material used was steel and an inlet flow velocity was assumed as 1 m/s under turbulent flow conditions. The simulations were conducted with only water. Molar concentrations of chemical solutions and solid particles will be added in the upcoming simulations. Results of the CFD simulations of the pipe section are shown in Figure 194 and Figure 195. The velocity profile and surface pressure are shown in the figures. The velocity is highest at the center and reduces towards the periphery, validating the physics of the pipe flow.

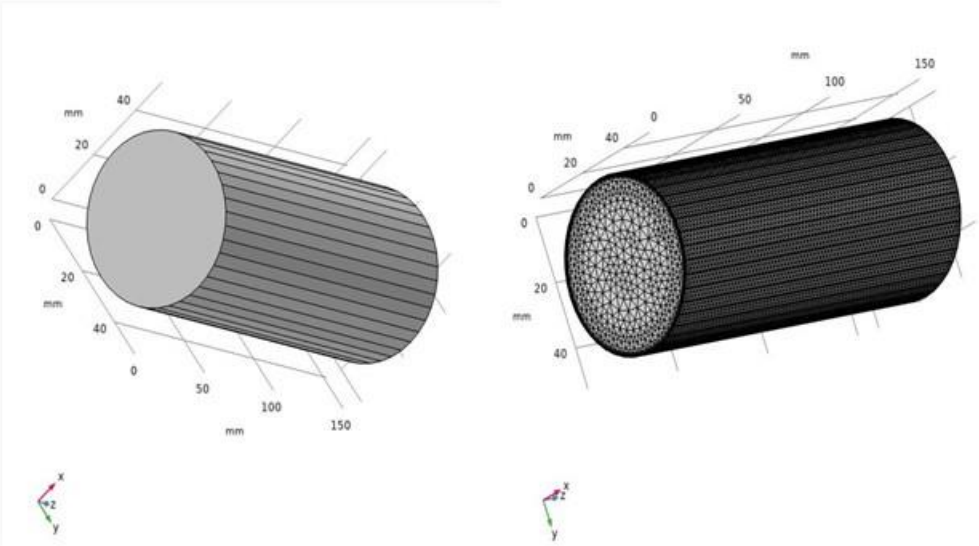


**Figure 193. Pipe section – CAD model (left) and FE mesh (right).**

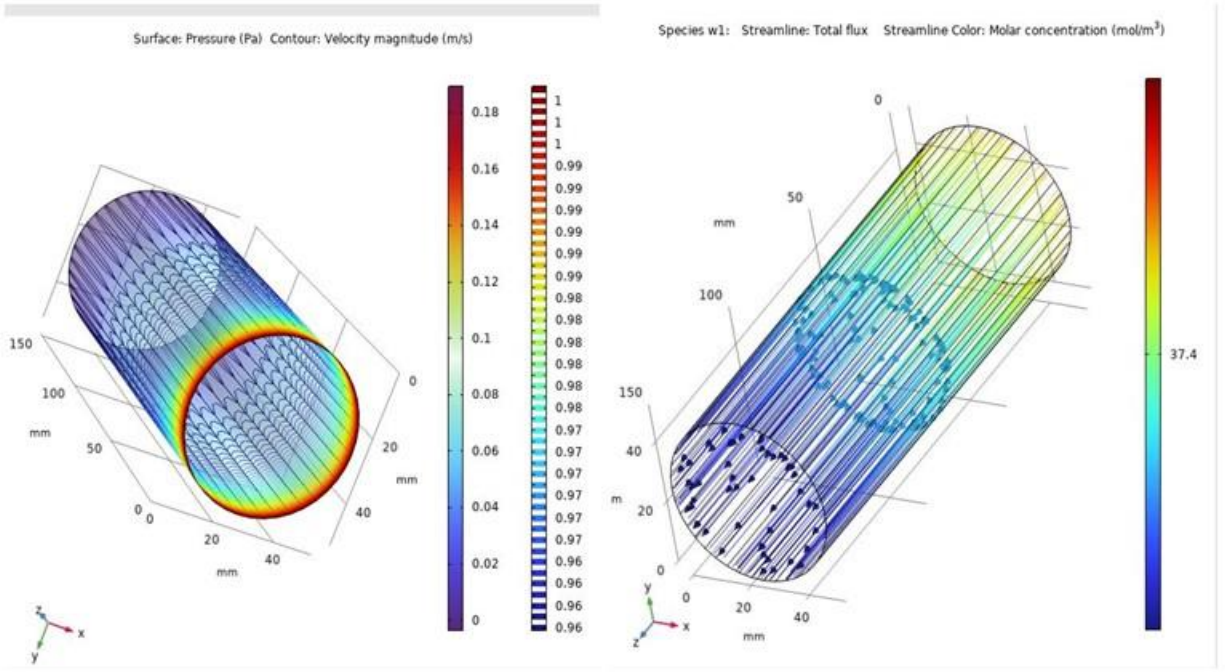


**Figure 194. Surface pressure and velocity distribution (left) and total flux as streamlines (right).**

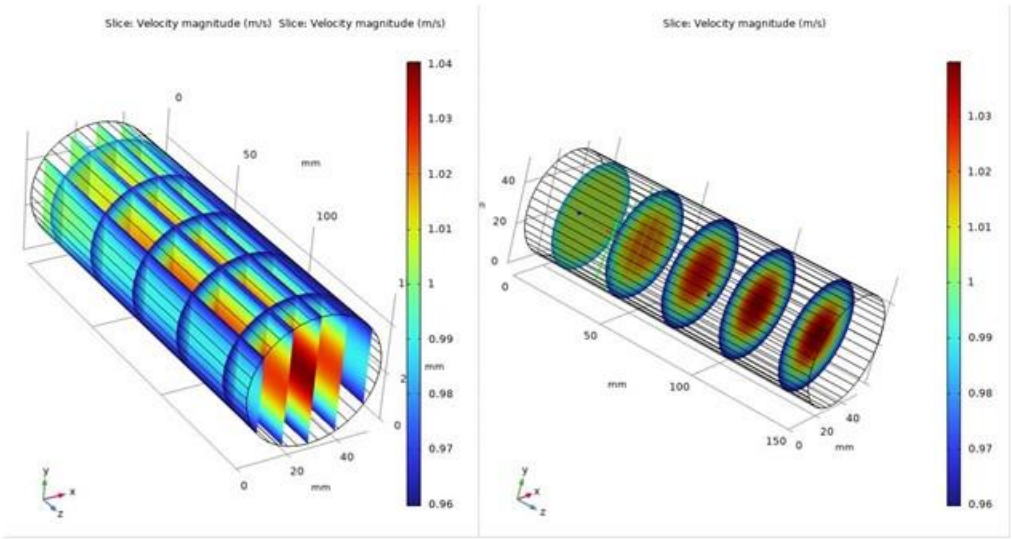


**Figure 195. Velocity slice plots depict distribution along the longitudinal and radial directions.**

## ***Fluid flow simulations within the engineering scale test loop***

Under this subtask, CFD simulations were continued for laminar and turbulent flow conditions in the engineering scale test loop. For this, a CAD rendering of the loop has been developed using SolidWorks software. The finite element mesh for the loop was developed with triangular elements and under coarse conditions to reduce computational expense. The CAD and Finite Element Mesh (FEM) models of the erosion loop are shown in Figure 216.

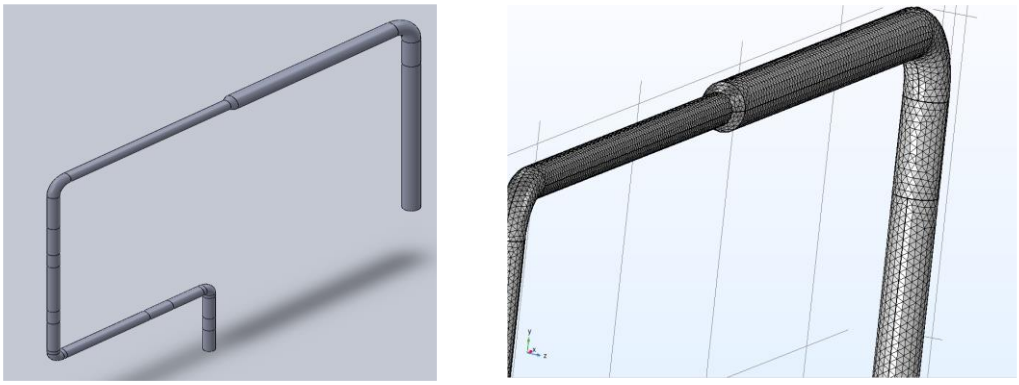

**Figure 196. Erosion loop CAD model (left) and Finite Element Mesh (right).**

Laminar and turbulent flow conditions of the fluid flowing in the loop were evaluated for model validation and feature investigations. The aim is to find "hot spots" or regions in the loop with high flow velocities and pressure conditions that lead to erosion. The health of the loop depends on these critical regions. Sample results with the loop under laminar flow conditions are shown in Figure 197 and Figure 198. The velocity variations in the complete loop are shown in Figure 197. while the detailed sections for surface velocity variation at the junctions are shown in Figure 198.

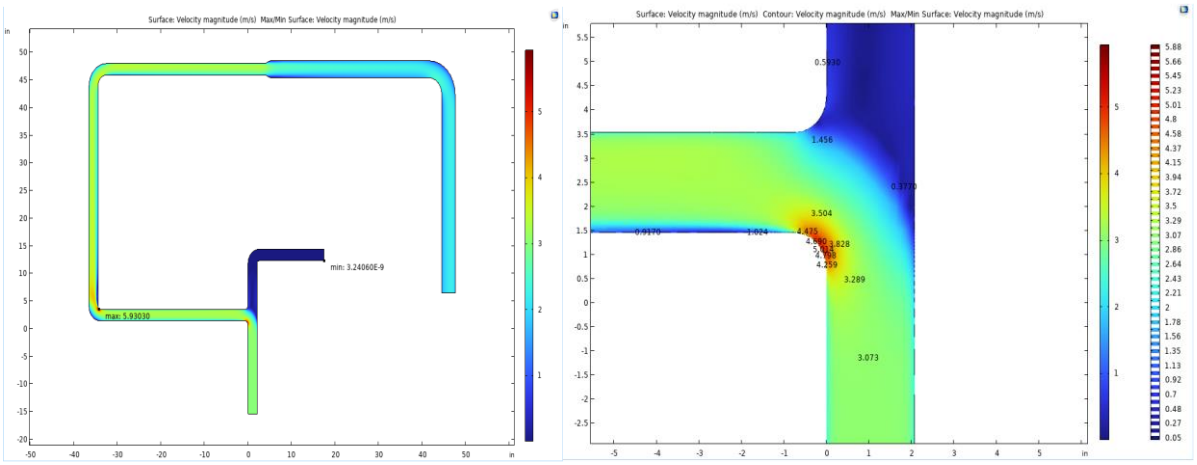


**Figure 197. Erosion loop flow (laminar) with surface velocities (left) and critical section detailed surface velocity (right).**

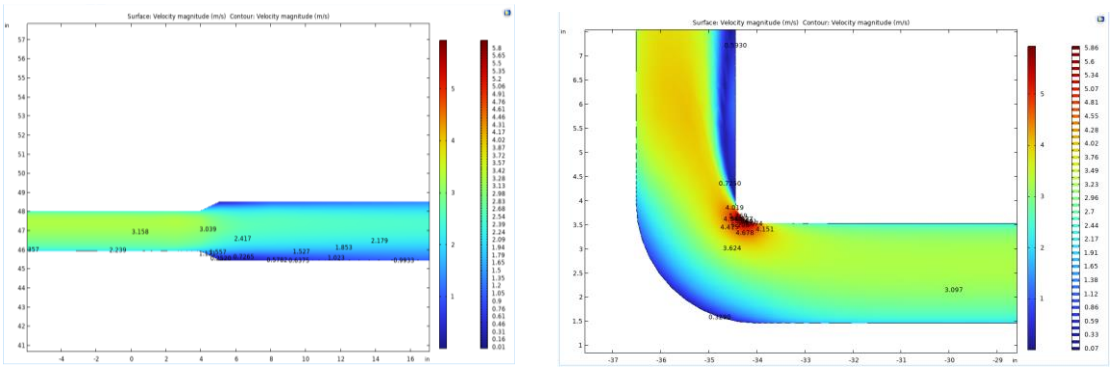


**Figure 198. Surface velocity variation at the reducer (left) and at the second elbow (right).**

Hence, laminar flow conditions for model verification resulted in high velocities at the bends/elbows and the reducer sections. Next, turbulent flow was studied for the same loop. Results for similar FE mesh conditions are shown in Figure 199 and Figure 200. In this case, the pressure variation is also shown in the pipe loop. Currently, results are being analyzed for further model development of particle flows.

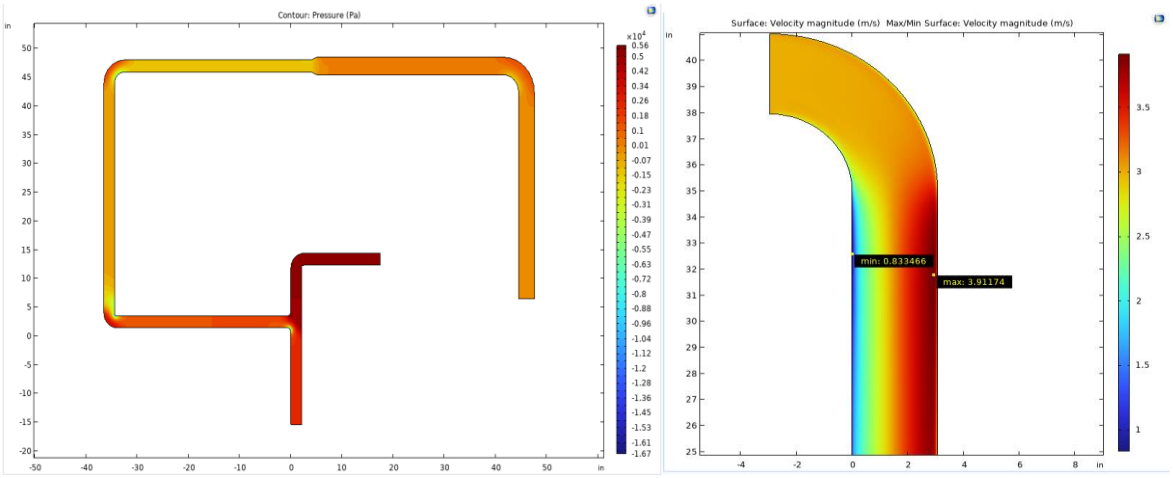


**Figure 199. Pressure variation in the loop (left) and surface velocity variation at the bend (right) under turbulent flow conditions.**

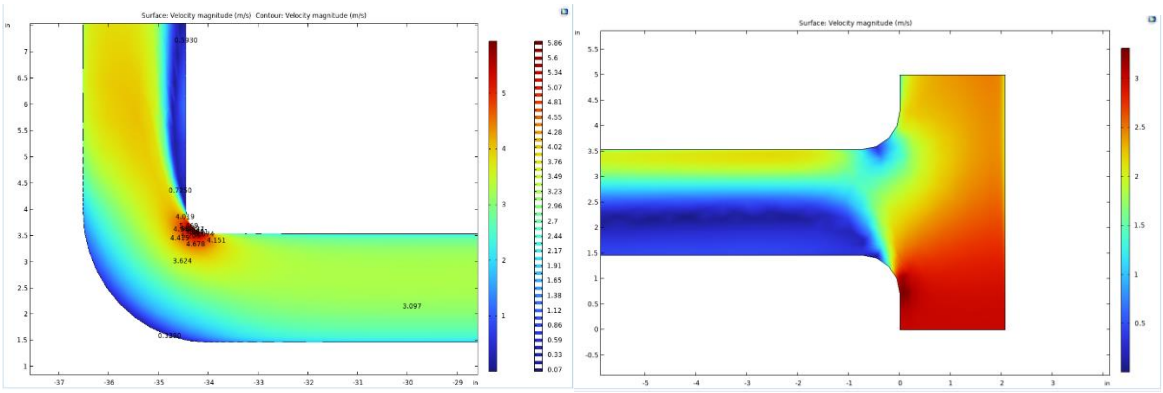


**Figure 200. Surface velocity variation at the bend (left) and at the T-section (right) for the erosion loop.**

## ***Data Analytics - Machine Learning Model Development***

The first iteration of a machine learning algorithm using a modified convolution neural network was developed and corrosion in the coupons was predicted. Methodology, results, conclusions, and next steps are outlined below:

Methodology

Convolutional Neural Networks (CNNs) have been implemented as binary classifiers to classify images as either “corroded” or “normal”. The CNNs are composed of multiple Conv2D layers to extract meaningful/helpful features from the imagery dataset during the training phase. Variations

of network depth [e.g., deeper, shallower] were tested for prediction accuracy and robustness. Some of the networks contained a single Conv2D layer per block (Figure 201) While others contained two Conv2D layers per block (Figure 202). Adding multiple layers in a block increases the receptive field without increasing the number of training parameters as opposed to increasing the kernel size. The dataset is composed of over 600 images labeled as “normal” and 80 images labeled as “corroded”. The distribution of the classes for this dataset is unbalanced since there is a small number of “corroded” samples compared to the baseline. To compensate for this, the training dataset contains 80 “corroded” images and 160 “normal” images. The 160 images were selected at random using a random number generator during the image preprocessing steps to prevent a manual bias from being introduced.

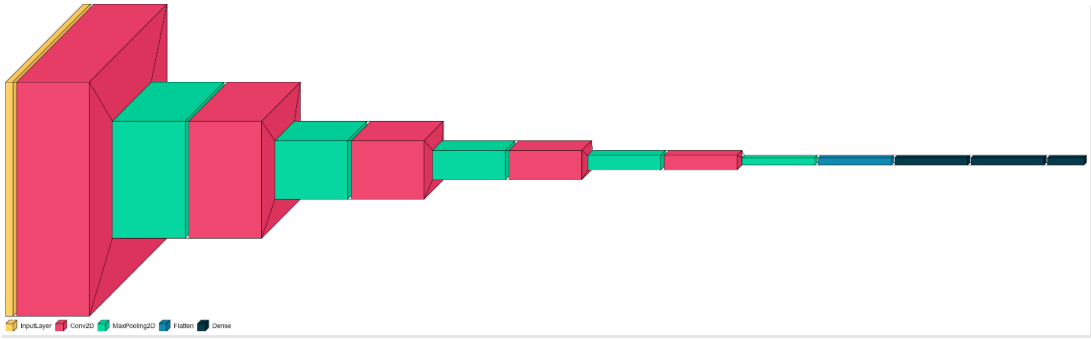


**Figure 201. Convolutional neural network composed of single 2DConv layer per block.**

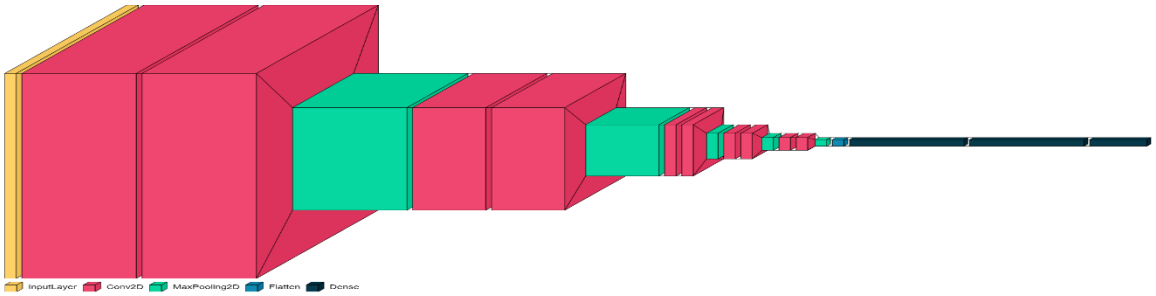


**Figure 202. Convolutional neural network composed of two 2DConv layers per block.**

## Results

The two Conv2D per block CNN architecture performs better on average when compared to the single Conv2D per block CNN. The best model has achieved 94.72% accuracy on the testing imagery dataset.

## Conclusion

The initial ML models developed using CNN provided an accuracy of 94.72%. Further analysis of results revealed that the difference in corroded images obtained from both sides of the coupon affected the model. To improve the training dataset, the image distribution considered in future will contain corroded and normal images from both sides of the coupon. This will force the network to focus on other features and detect corrosion in a more robust manner. Further, data augmentation can be explored to increase the number of samples during training. One option is to

use multiple Convolutional Autoencoders to learn both the distribution of the "corroded" and "normal" classes. Once these networks converge, they can be used to generate new images from the distribution they learned. Additionally, different activation functions and classification heads (i.e., neural network side of the CNN) can be used to optimize the models and increase the accuracy even further.

***Corrosion Detection using Machine Learning and Artificial Intelligence:***

Anomaly detection and classification of the samples as corroded or non-corroded coupons was conducted using the in-house developed Automated Artificial Intelligence and Machine Learning (AAIML) software at FIU. The initial data set included image data of clean and corroded images. Model development is conducted using clean data while the testing and validation included both clean and corroded sample data. For anomaly detection, a Convolution Neural Network (CNN)-based ML algorithm was used with Adams optimized. CNN parameters and other details on the batch size and filters are with kernal size and iterations are provided in Figure 203. For classification, 7 different algorithms were used. Results obtained using the CNN model are shown in Figure 204. The figure shows how the model was able to detect the corrosion in the images provided. As seen in the figure (last column), the model could detect 3 images as normal and the 4th image as an anomaly (meaning corroded). The anomaly score (level of accuracy) with the testing and validation of the models was obtained as 75%, as shown in Figure 205 (left) with outliers as 25%. The accuracy is not significant due to the size of the data set and the quality of the image. The model is currently being improved by providing additional sample data (number and level of corrosion). Histogram of the outliers is shown in Figure 205 (right) indicating similar distribution of higher value for the inliers.

Convolutional Neural Network Parameters ×

| | |
|---|---|
| batch_size | 32 |
| filters | 4 |
| hidden_layer_type | Conv2D |
| kernel_height | 3 |
| kernel_width | 3 |
| layer_activation_function | relu |
| loss | categorical_crossentropy |
| max_epochs | 100 |
| metrics | accuracy |
| num_hidden_layers | 4 |
| optimizer | Adam |
| output_activation_function | softmax |
| padding | same |
| stopped_epoch | 24 |

**Figure 203. Algorithm parameters for anomaly detection.**

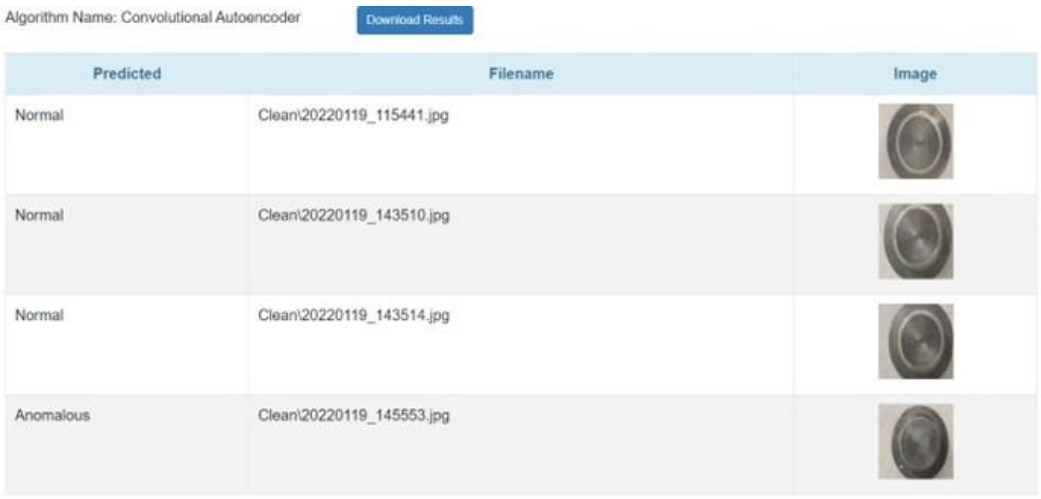


**Figure 204. Anomaly detection of corroded and non-corroded surfaces of the sample coupons.**

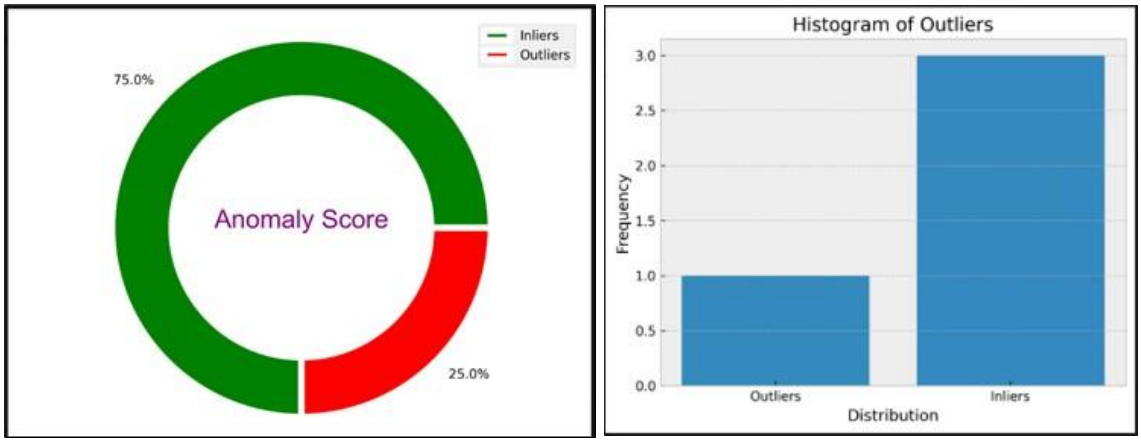


**Figure 205. Anomaly score and histogram of outliers for the corrosion model.**

## ***Journal paper drafting and submission for the data analytics subtask***

Under this subtask, the data obtained from images of the particle erosion testing was used to develop machine learning models. Developed erosion models were used to predict the corrosion in carbon steel material. The research was used to develop a journal paper which was submitted to the Nuclear Engineering Technology journal. A short description of the paper is below:

In the nuclear waste sites, radioactive waste is typically transferred through underground and aboveground pipelines made of carbon steel and stainless-steel material. Structural health monitoring of these lines is of utmost importance due to the hazardous nature of the waste. Decommissioned and excavated buried pipelines are used for structural health investigations and remaining life predictions of the active components. Monitoring of the active pipelines is typically conducted using advanced sensor systems and often periodically with human intervention. One of the alternatives is to use in-situ flow coupons to monitor the condition of the metal pipelines without interrupting the waste transfer process and preventing the excavation of buried lines. The

author's previous work [ref] includes results from experimental testing of flow coupons in custom assembled pipe loops to evaluate the coupon efficacy and erosion-corrosion detection using ultrasonic sensors. Current work develops and implements a novel automated machine learning based framework for detecting corrosion in the flow coupons based on the experimental results of the corrosion images. The framework adapts computational Neural Networks (CNN) architecture with deep transfer learning algorithms to discern between corroded and non-corroded coupons. The maximum accuracy of the proposed image-based method to detect and predict corrosion is found to be 0.95. The results of this study promise insights into the effectiveness of various models for corrosion classification, contributing to the advancement of both corrosion detection methodologies and deep learning practices.

The paper used the machine learning architecture framework shown in Figure 206 (left). Five different CNN model architectures were used to extract the features from the data. These were - VGGNet, ResNet, InceptionNet, EfficientNet, and AlexNet. These architectures are selected for their well-established performance in computer vision tasks. Generic architecture is shown in Figure 206 (right).

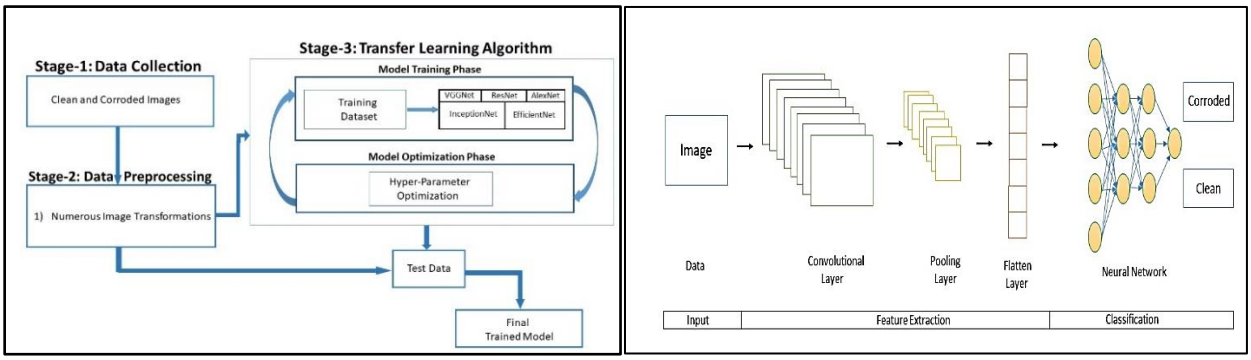


**Figure 206. Machine Learning framework (left) and Convolutional Neural Network (CNN) Architecture for Corrosion Classification.**

## Subtask 19.1.3: Conclusions

Computational Fluid Dynamics (CFD) analysis was conducted to investigate the flow velocities and pressure changes in the pipe sections to identify hot spots (regions prone to high velocities/pressures). The research provides a basis to combine the CFD simulations with experimental results that can potentially be used to develop comprehensive realistic multi-physics-based models for flow in the HLW transfer process. The machine learning models developed using the particle erosion data can be used to predict erosion in pipes based on statistical methods. In future, a comparative study of all simulant mixtures and their simultaneous effect will be investigated. This work will continue further to examine the simultaneous effect of all simulants for more accurate erosion and corrosion prediction in the HLW transfer components, providing baseline data for infrastructure repairs and replacement as needed at several DOE sites.

## Subtask 19.1.3: References

1. https://www.ansys.com/products/fluids/ansys-fluent
2. https://www.comsol.com/cfd-module
3. https://www.comsol.com/particle-tracing-module

4. Szegedy, C., Liu, W., Jia, Y., Sermanet, P., Reed, S., Anguelov, D., Erhan, D., Vanhoucke, V., & Rabinovich, A. (2014, September 17). Going deeper with convolutions. arXiv.org. https://arxiv.org/pdf/1409.4842.pdf
5. Tan, M., & Le, Q. V. (2020, September 11). EfficientNet: Rethinking model scaling for Convolutional Neural Networks. arXiv.org. https://arxiv.org/abs/1905.11946
6. Krizhevsky, A., Sutskever, I., & Hinton, G. E. (2012). ImageNet Classification with Deep Convolutional Neural Networks. NeurIPS Proceedings. https://proceedings.neurips.cc/paper_files/paper/2022/file/9f09f316a3eaf59d9ced5ffaefe97e0f-Paper-Conference.pdf
7. D. P. B. J. L. Kingma, "ADAM: A Method for Stochastic Optimization," in ICLR 2015, 2015
8. Y. An, X. Wang, R. Chu, B. Yue, L. Wu, J. Cui, and Z. Qu, “Event classification for natural gas pipeline safety monitoring based on long short-term memory network and Adam algorithm,” *Structural Health Monitoring*, vol. 19, no. 4, pp. 1151–1159, 2019.
9. K. Janocha and W. M. Czarnecki, “On Loss Functions for Deep Neural Networks in Classification,” *arXiv.org*, 18-Feb-2017. [Online]. Available: https://arxiv.org/abs/1702.05659. [Accessed: 09-Apr-2021].

## Subtask 19.2: Evaluation of Nonmetallic Components in the Waste Transfer System

### Subtask 19.2: Introduction

Nonmetallic materials are utilized in the waste transfer system at the Hanford tank farms; these include the inner hose of the hose-in-hose transfer lines (HIHTLs), Garlock® gaskets and ethylene propylene diene monomer (EPDM) O-rings. These materials are exposed to simultaneous stressors including β and γ radiation, elevated temperatures, caustic supernatant as well as high pressures during normal use. In 2011, the Defense Nuclear Facilities Safety Board recommended to the U.S. Department of Energy (DOE) to conduct post service examination of HIHTLs to improve the existing technical basis for component service life. Suppliers of the nonmetallic components often provide information regarding the effects of some of the stressors, but limited information is available for simultaneous stressor exposure.

An extensive test plan was developed by Sandia National Laboratories to understand the simultaneous effects of the aforementioned stressors [1]; however, this test plan was never executed. Additional studies conducted by Lieberman provide information on HIHTLs at elevated temperature and pressure, but little information is gained regarding the synergistic effects with the caustic supernatant [2]. Florida International University (FIU) has been tasked with supporting this effort by conducting multi stressor testing on typical nonmetallic materials used at the Hanford tank farms. In previous research efforts focused on evaluating the aging behavior of EPDM by exposing samples of HIHTLs as well as EPDM dog-bone shaped specimens to a 25% sodium hydroxide (NaOH) solution at (100°F), operating (130°F) and design temperatures (170°F) for 6 months and 12 months. In addition, HIHTL and the EPDM dog-bone specimens were also exposed to only hot water at 170°F for a duration of one year. After analyzing the data from this phase, it became apparent that the synergistic effects of NaOH with high temperature had a significant effect on the degradation of the specimens. After discussing the findings with the site engineers, it was

decided to conduct additional aging of HIHTL and EPDM dog-bone specimens at various concentrations of NaOH as well as water only at the elevated temperatures. In the previous year's research, four test loops were developed at FIU which allowed for the aging of HIHTL as well as dog-bone specimens utilizing 6.25%, 12.5% and 25% NaOH and water only at 170°F for a duration of one year. After aging, the test specimens had their material properties measured and compared to the baseline (unaged) values. The results showed that the EPDM material specimens' tensile strength and the HIHTL specimens' burst pressure exhibited varying degrees of degradation when exposed to different concentrations of NaOH. Specifically, it was found that the most significant degradation in terms of tensile strength and burst pressure occurred in the samples exposed to the 6.25% NaOH solution. On the other hand, the smallest degradation occurred in the samples exposed to the 25.00% NaOH solution. Additionally, an interesting observation was made regarding a white material coating the inner surface of the HIHTL hoses after aging with different concentrations of NaOH solutions. It was found that the HIHTL aged with only the higher concentrations (12.50% and 25.00%) of NaOH solutions exhibited this white coating, whereas the HIHTL aged with the 6.25% NaOH solution did not show the same phenomenon. It is thought that at higher concentrations, precipitate forms and emerges from the solution of NaOH, subsequently coating the inside of the hoses. Furthermore, it is suggested that once the hoses are coated with the precipitate, the coating may act as a blocking agent. This blocking effect could potentially hinder or limit the further diffusion of NaOH solution into the EPDM, subsequently reducing the extent of degradation.

## Subtask 19.2: Objectives

To obtain a better understanding of what the white material coating the inner surface of the HIHTL hoses is and its effect on the degradation of the hoses, XRD analysis was conducted on the white material. In addition, to determine the level of NaOH ion penetration into the HIHTL material, SEM-EDX analysis was conducted on specimens cut from the aged HIHTLs. To better understand the formation rate of the white material coating on the inside of the HIHTLs, FIU engineers worked with Hanford personnel to develop an experimental test plan that involved aging EPDM material coupons in sodium hydroxide solutions at concentrations of 6.25%, 12.5% and 25% at 170°F.

## Subtask 19.2: Methodology, Results and Discussion

X-Ray Diffraction (XRD) Analysis

The first phase of this year's research involved identifying the composition of the white material coating that was coating the inside of the HIHTLs aged at the higher concentrations (Figure 207).

**Figure 207. Comparison of the inside of unaged and aged HIHTL specimens.**

X-Ray Diffraction (XRD) analysis was conducted on the white crystalline substance from the specimens aged in the 12.5% NaOH solution in order to determine its mineralogy. The XRD analysis was done on a Bruker D2 PHASER X-ray diffractometer equipped with a LYNXEYEXET (1D mode, opening 5° 2θ) detector and a rotating collimator source; Cu Kα radiation, operating at 30 keV. Samples were loaded onto zero diffraction plates (Ø 24.6 mm × 1.0 mm thickness, cavity Ø 10 mm × 0.2 mm depth, MTI Corporation) and scanned from 5° to 90° with a step size of 0.02°, 1s per step. The solid phase identification was conducted via *DIFFRAC.EVA. V5.1 XRD* pattern processing software. Analysis results shown in Figure 208 indicated that the substance is sodium carbonate monohydrate, $Na_2CO_3 \cdot H_2O$.

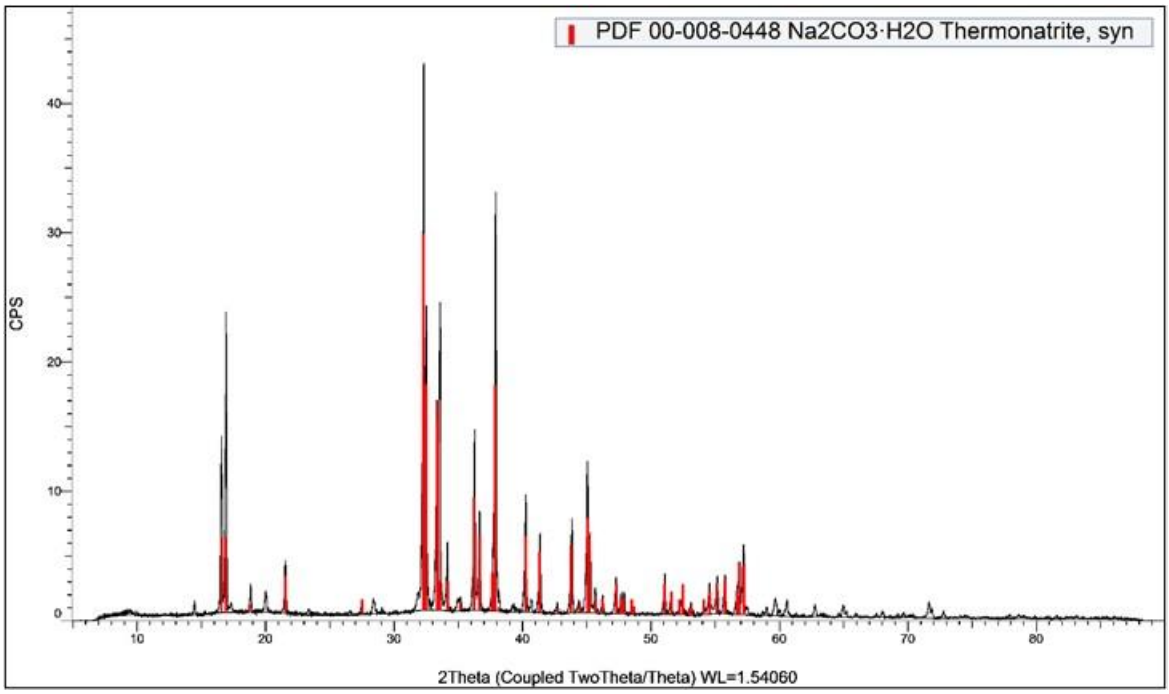


**Figure 208. X-Ray Diffraction (XRD) analysis results from the 12.5% NaOH specimens.**

Even though sodium carbonate monohydrate is water-soluble, it is believed that at the higher NaOH concentrations (12.5% and 25%), it precipitates out of solution and coats the test specimens. It is also believed that once the sodium carbonate monohydrate coats the specimens, it acts like a blocking-agent that prevents additional NaOH solution from penetrating into the EPDM material thus limiting the degradation of the material. XRD analysis was also conducted on the white crystalline substance observed on the dog-bone specimens aged in 25% NaOH solution to determine its mineralogy. As seen in Figure 209, results indicated that the substance is also sodium carbonate monohydrate, $Na_2CO_3 \cdot H_2O$ (Thermonatrite).

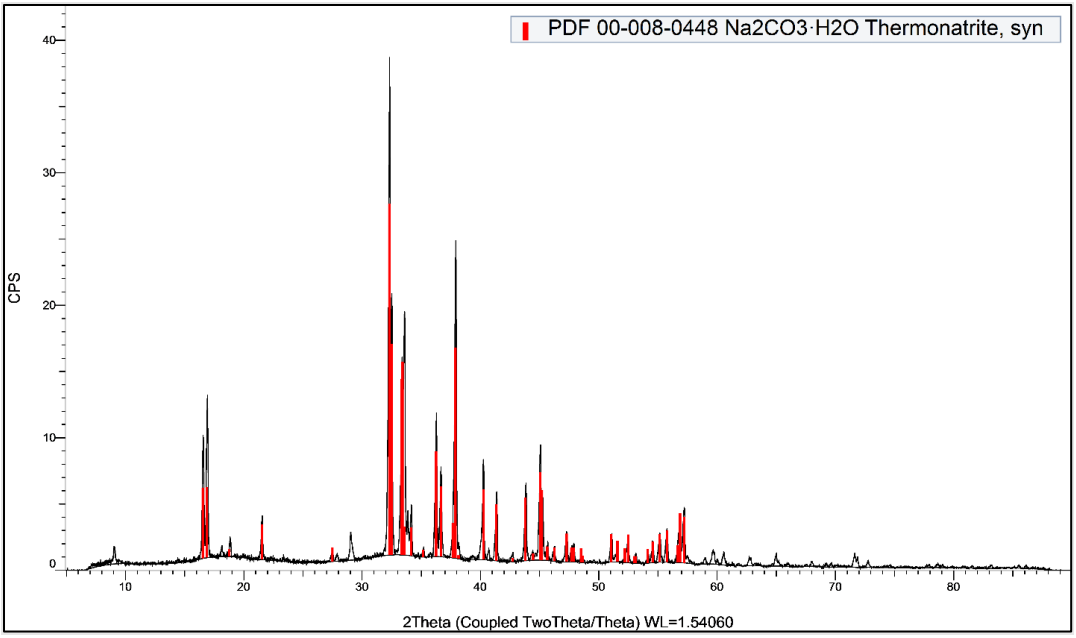


**Figure 209. X-Ray Diffraction (XRD) analysis results from the 25% NaOH specimens.**

## SEM-EDS Analysis

SEM-EDS analysis was conducted on specimens cut from both aged as well as unaged HIHTLs. The purpose of this analysis was to determine how far the sodium hydroxide (NaOH) solution had penetrated the hose specimens during the aging process. These results were then compared to the results from the baseline (unaged) specimens. It is believed that as the NaOH penetrates the wall of the hose, it weakens the wall structure and thus reduces the burst pressure of the hose. When the burst pressures of the baseline hoses were measured, the average burst pressure was 3004 psi. However, when the burst pressures of the hoses aged with 25%, 12.5% and 6.25% NaOH were measured, they had average burst pressures of 2814 psi, 2451 psi, and 2218 psi, respectively. This translated to a decrease of -6.32%, -18.14%, and -26.14% in burst pressure when compared to the baseline value. A JEOL model JSM-F100 Schottky field emission scanning electron microscope was used to conduct the SEM-EDS analysis on the hose specimens. Analysis scans were conducted on the hose specimens starting from the inside wall on the left side in the image towards the first layer of polyester reinforcement weave on the right of the image.

Figure 210 shows the sodium penetration scan results of the baseline hose specimen. As can be seen from the scan result, the baseline (background) sodium counts are low at around 2.

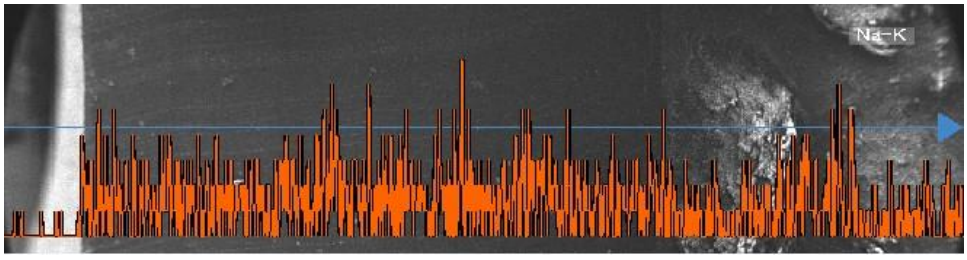

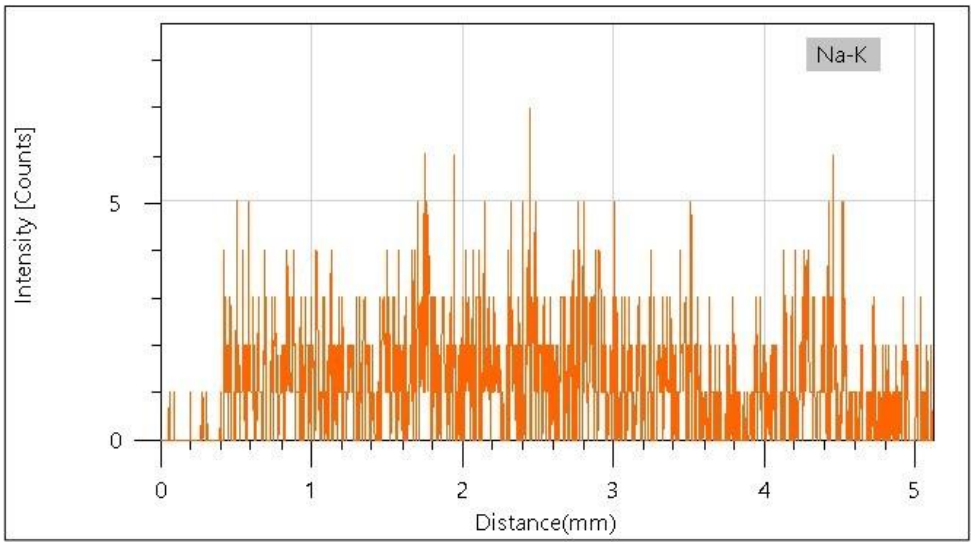


**Figure 210. Baseline hose sodium penetration scan results.**

Figure 211 shows the sodium penetration scan results of the 25% NaOH hose specimen. As can be seen from the scan result, the sodium counts are at an elevated level of around 45 counts and is penetrating 0.3 mm into the hose wall.

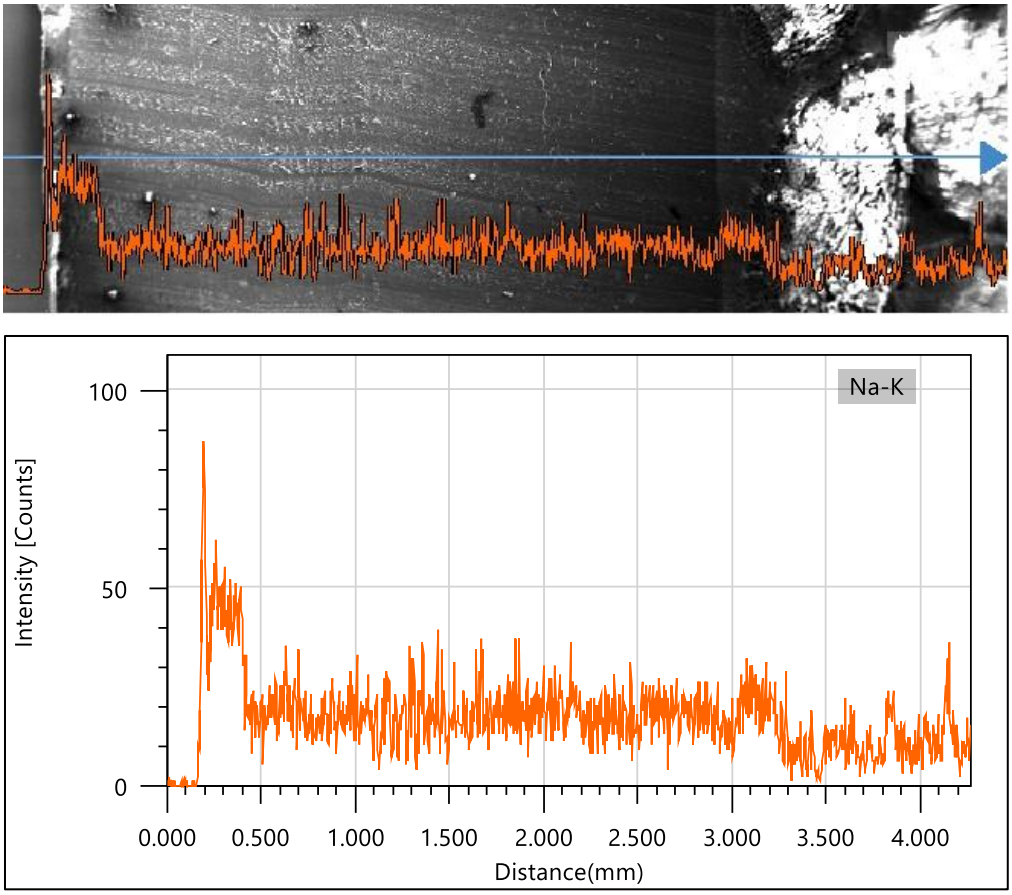


**Figure 211. Scan results of 25% NaOH hose specimen.**

Figure 212 shows the sodium penetration scan results of the 12.5% NaOH hose specimen. As can be seen from the scan result, the sodium counts are at an elevated level of around 150 counts and is penetrating 0.8 mm into the hose wall.

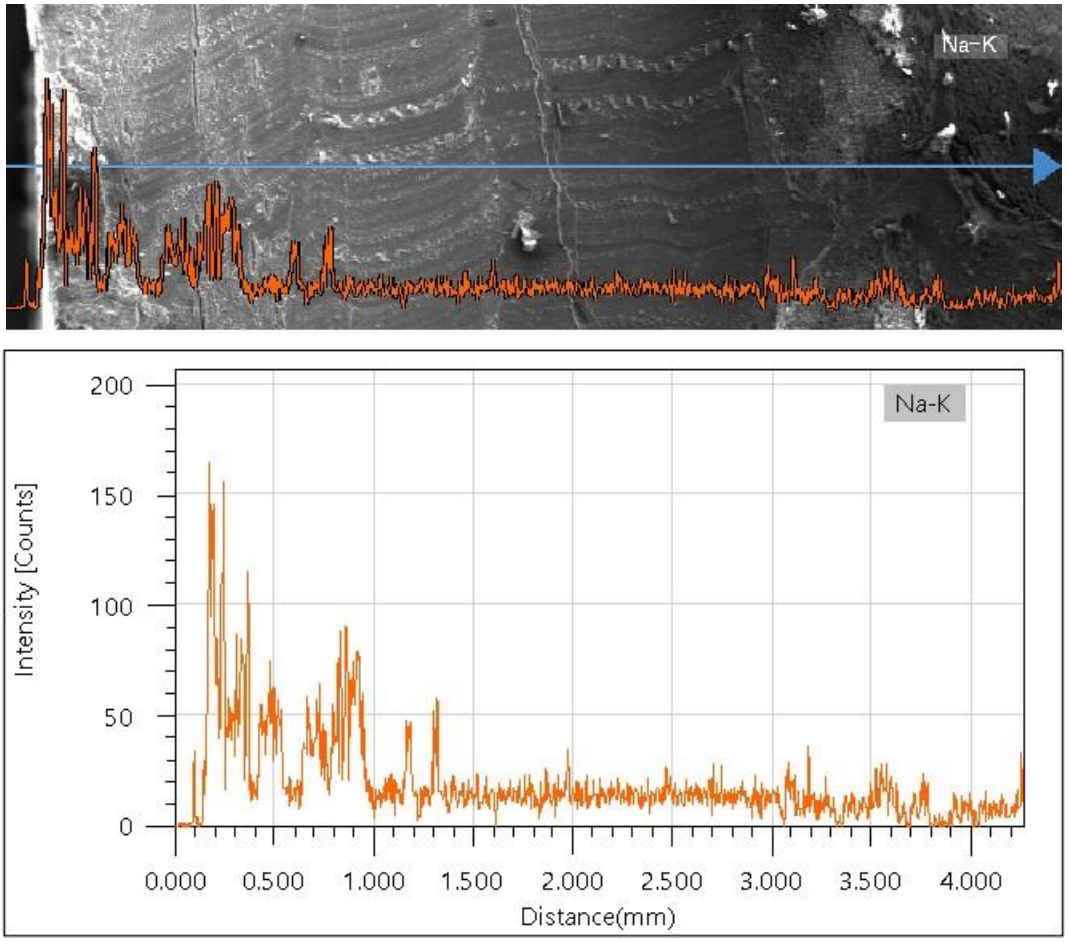


**Figure 212. Scan results of 12.5% NaOH hose specimen.**

Figure 213 shows the sodium penetration scan results of the 6.25% NaOH hose specimen. As can be seen from the scan result, the sodium counts are at an elevated level of around 250 counts and is penetrating 0.9 mm into the hose wall.

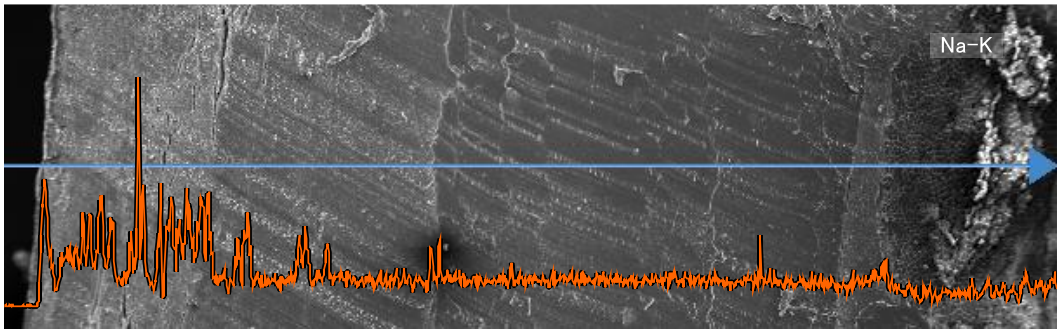

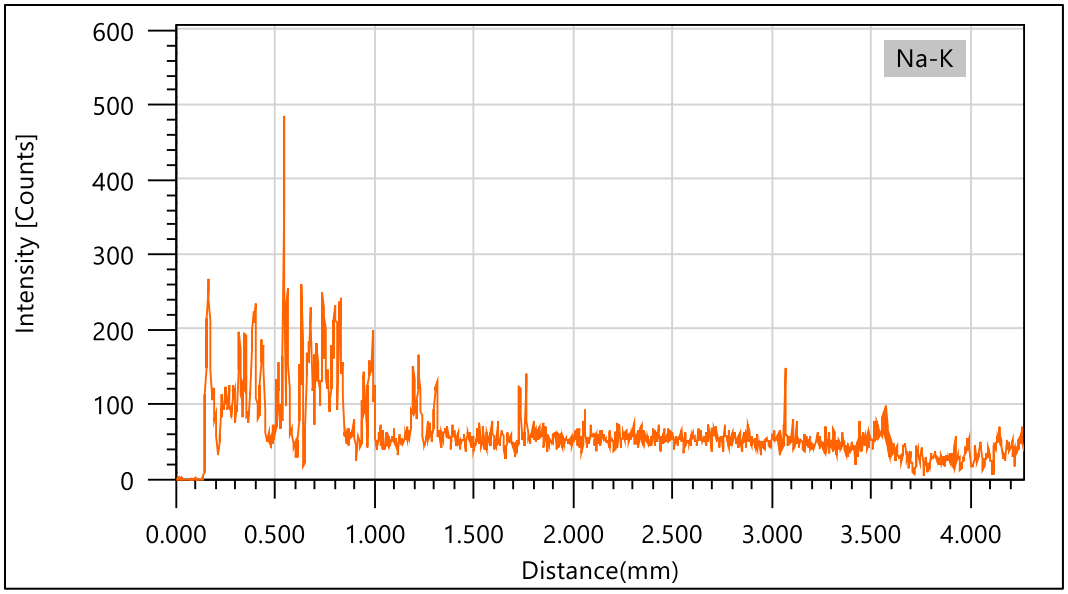


**Figure 213. Scan results of 6.25% NaOH hose specimen.**

After analyzing the results of all the scans, it became apparent that as the concentration of the aging solution (NaOH) increased, the amount of sodium that penetrated the hose material decreased. This is due to the buildup that was observed on the inside of the hose. As previously reported, this material is sodium carbonate and is believed to act as a barrier between the NaOH and the hose material. This is why the hoses aged with the higher concentrations of NaOH had a lower amount of degradation of their burst pressures.

In addition, FIU also conducted SEM-EDS analysis on additional specimens cut from both aged as well as unaged HIHTLs. The purpose of this analysis is to determine how far the sodium hydroxide (NaOH) solution had penetrated the hose specimens during the aging process. These results were then compared to the results from the baseline (unaged) specimens. It is believed that as the NaOH penetrates the wall of the hose, it weakens the wall structure and thus reduces the burst pressure of the hose. Previously a line scan analysis of the specimens was conducted, which provided counts of the sodium atoms detected along a line across the specimen. This time, map scans of the specimens were conducted. The map scans provide a map of the locations of the atoms on the surface of the specimen. A JEOL model JSM-F100 Schottky field emission scanning electron microscope was used to conduct the SEM-EDS analysis on the hose specimens. Analysis scans were conducted on the hose specimens starting from the inside wall on the left side in the image towards the first layer of polyester reinforcement weave on the right of the image.

Figure 214 shows a map of the sodium penetration of the hose specimen aged with a 25% NaOH solution. As can be seen from the scan result, most of the sodium is concentrated at the inside edge of the hose with limited sodium detected in the main part of the hose wall.

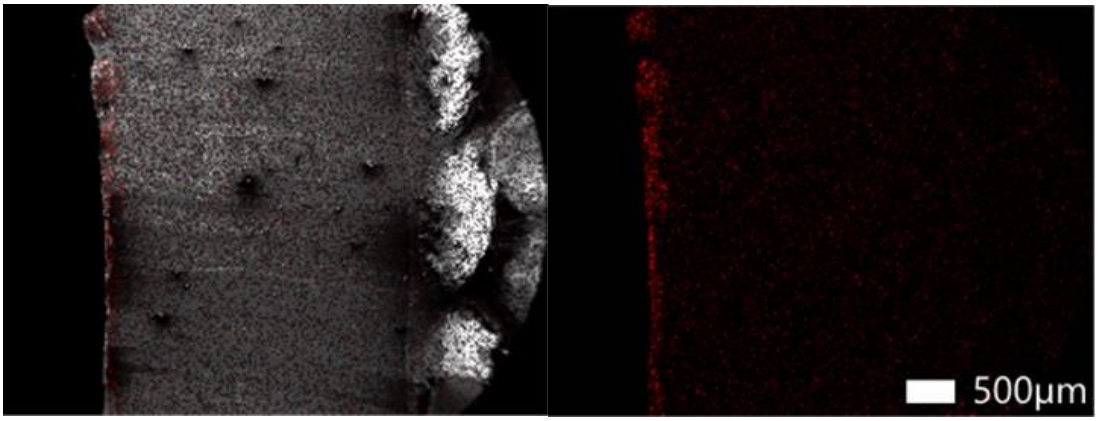


**Figure 214. Map scan results of 25% NaOH hose specimen.**

Figure 215 shows a map of the sodium penetration of the hose specimen aged with a 12.5% NaOH solution. A s can be seen from the scan result, there is more sodium detected that has penetrated further into the hose wall than in the hose aged with the 25% solution.

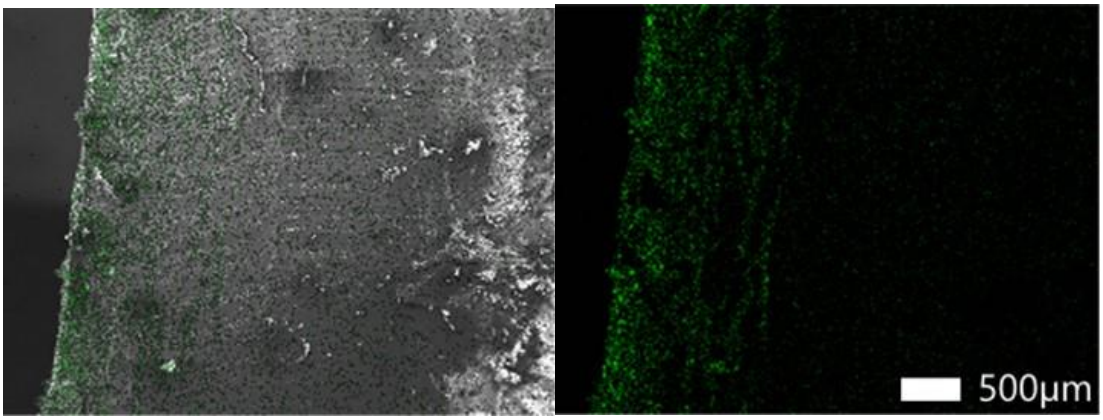


**Figure 215. Map scan results of 12.5% NaOH hose specimen.**

Figure 216 shows a map of the sodium penetration of the hose specimen aged with a 6.25% NaOH solution. As can be seen from the scan result, which is at a lower magnification, a greater quantity of sodium is detected throughout the specimen hose wall than in the hoses aged with 12.5% and 25% solutions.

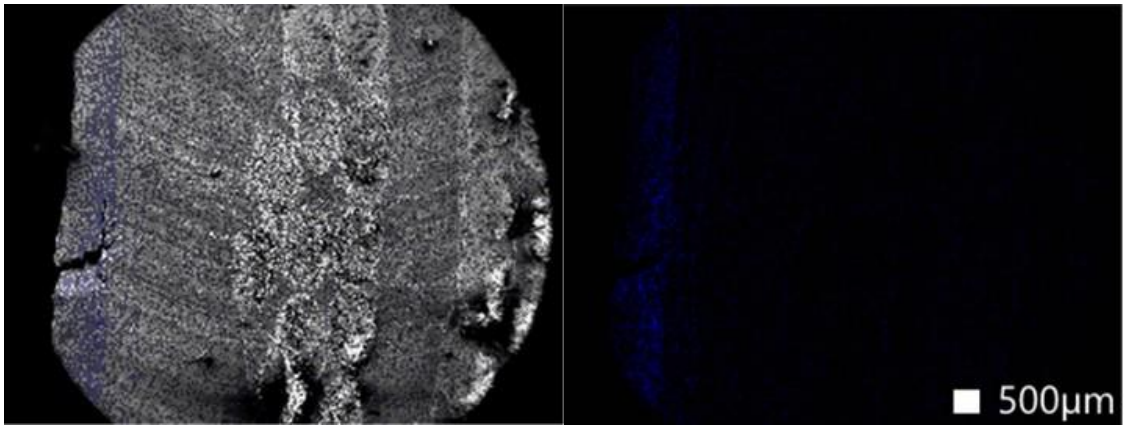


**Figure 216. Scan results of 6.25% NaOH hose specimen.**

When the burst pressures of the baseline hoses were measured, the average burst pressure was 3,004 psi. However, when the burst pressures of the hoses aged with 25%, 12.5% and 6.25% NaOH were measured, they had average burst pressures of 2,814 psi, 2,451 psi, and 2,218 psi, respectively. This translated to a decrease of -6.32%, -18.14%, and -26.14% in burst pressure when compared to the baseline value.

After analyzing the results of all the scans, it became apparent that as the concentration of the aging solution (NaOH) increased, the amount of sodium that penetrated the hose material decreased. This is due to the buildup that was observed on the inside of the hose. As previously reported, this material is sodium carbonate and is believed to act as a barrier between the NaOH and the hose material. This is why the hoses aged with the higher concentrations of NaOH had a lower amount of degradation of their burst pressures. When the burst pressures of the baseline hoses were measured, the average burst pressure was 3004 psi. However, when the burst pressures of the hoses aged with 25%, 12.5% and 6.25% NaOH were measured, they had average burst pressures of 2814 psi, 2451 psi, and 2218 psi, respectively. This translated to a decrease of -6.32%, -18.14%, and -26.14% in burst pressure when compared to the baseline value.

Sodium Carbonate Monohydrate Accumulation Rate Analysis

After determining that sodium carbonate monohydrate acts as a barrier protecting the EPDM material from attack by the NaOH solution, there was interest in determining how long it takes for the sodium carbonate to build enough thickness to protect the EPDM material. FIU engineers worked with Hanford personnel to develop an experimental test plan that involved aging EPDM material coupons in sodium hydroxide solutions at concentrations of 6.25%, 12.5% and 25% at 170°F. The experimental test plan involved aging 1” X 1” X 3/16” EPDM coupons in three stainless steel pans containing sodium hydroxide solutions at concentrations of 6.25%, 12.5% and 25% respectively. The pans were placed in an oven to maintain their temperature at 170°F. Each pan contained nine coupons and one coupon was removed each week for analysis.

A Quincy Lab Analog Oven Model 30 (Figure 217) was used to maintain the specimens and aging solution at a temperature of 170°F.

**Figure 217. Quincy Lab Analog Oven Model 30.**

Stainless steel pans with a capacity of 39 fl. Oz. (Figure 218) were used to contain the specimens along with the aging sodium hydroxide (NaOH) solution.

**Figure 218. Stainless steel pan.**

Stainless steel half-round rods (1/4") (Figure 219) were placed under the EPDM specimens in order to keep the bottom of the specimens elevated above the pan's floor. This allowed the bottom of the EPDM specimen to be exposed to the NaOH solution.

**Figure 219. ¼" stainless steel half-round rod.**

Squares (1" X 1") were cut out of a 3/16" sheet of EPDM rubber (Figure 220). A total of 27 squares were cut to allow for 9 specimens to be aged in one of the three NaOH concentrations of 6.25, 12.5, and 25%.

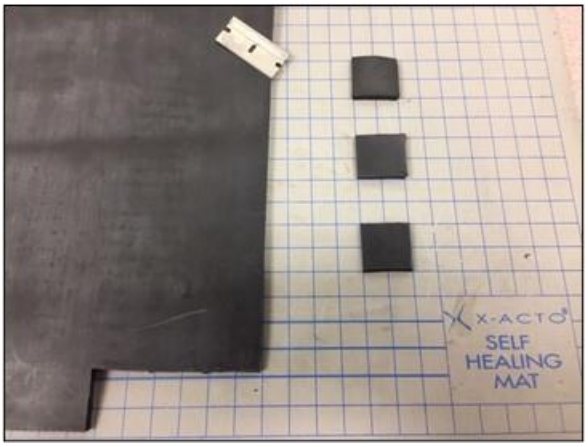


**Figure 220. EPDM squares cut from a 3/16" sheet.**

After all the equipment was acquired and the various solutions of NaOH was prepared, FIU commenced the aging of the EPDM coupons on May 16, 2023. Nine specimens are being aged in

each of the three vessels containing a sodium hydroxide solution at concentrations of 6.25%, 12.50%, and 25.00% v/v respectively. Every week one specimen is removed from each of the aging vessels and allowed to completely dry before being placed into plastic storage bags for future analysis (Figure 221).

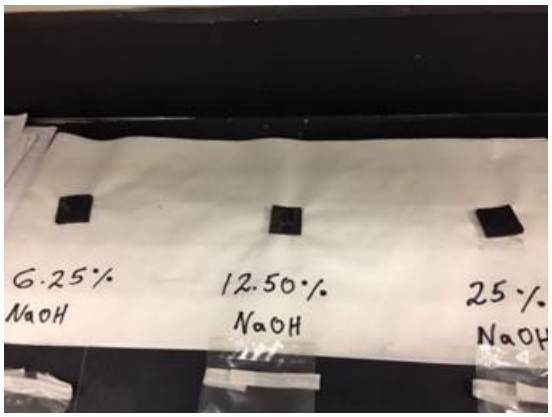


**Figure 221. EPDM specimens after removal from aging vessel.**

Even though the containers are covered while they are maintained at 170°F in the oven, the solution level within each container drops due to the evaporation of the water component of the solution. Three times a week the level in each vessel is checked and brought back to the correct level by adding water. To make sure the level is brought back to the correct level in each vessel, a homemade level gauge (Figure 222) is utilized.

**Figure 222. Solution level gauge.**

The level gauge is placed on top of each vessel and the water is added until the solution level reaches the bottom of the gauge (Figure 223).

**Figure 223. Level gauge being used on a vessel.**

After the 9-week aging period, one specimen was removed every week, SEM-EDX analysis was conducted on the EPDM specimens to determine the level of sodium ion penetration into the EPDM material. The final set of specimens were removed from the aging oven on July 19, 2023. The specimens were then prepared for SEM-EDX analysis to determine sodium penetration into the EPDM material. When SEM-EDX analysis was conducted, the results showed that the number of sodium ion counts detected in both the 1-week and the 9-week coupons were very similar to the baseline (unaged) specimens. This indicated that the 9-week maximum aging period was not enough time to allow the sodium hydroxide to penetrate the EPDM material. The SEM-EDX results are presented below:

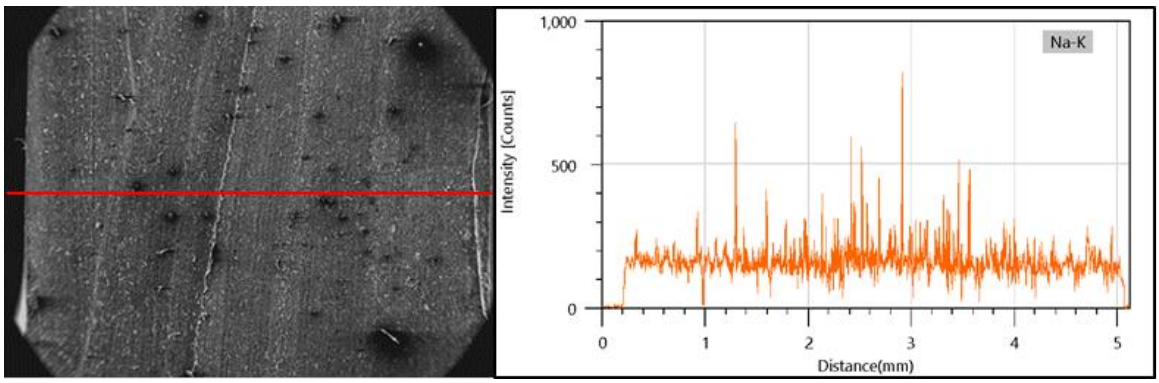


**Figure 224. Baseline (unaged) sodium ion count results.**

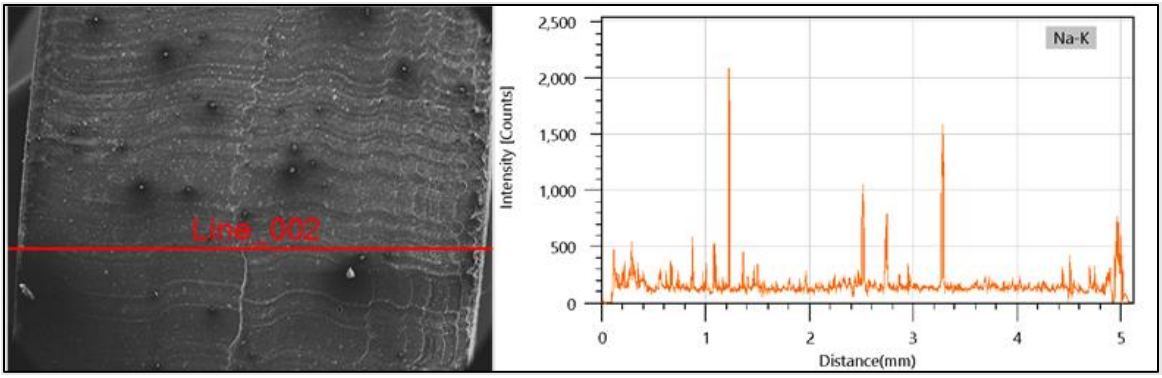


**Figure 225. Sodium ion count results after 1 week of aging in 6.25% NaOH solution.**

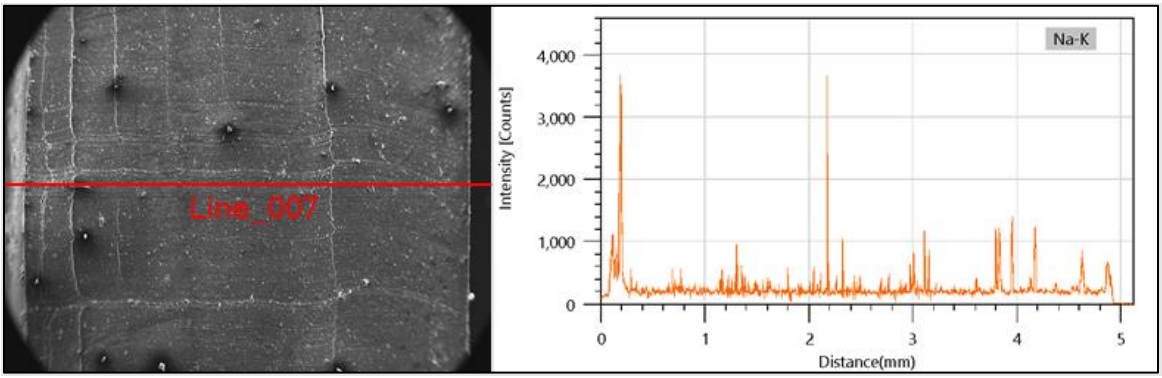


**Figure 226. Sodium ion count results after 1 week of aging in 12.5% NaOH solution.**

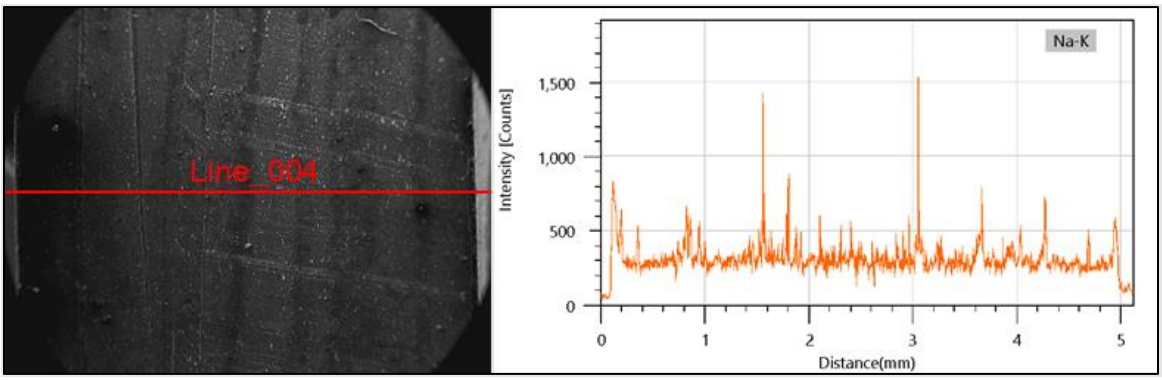


**Figure 227. Sodium ion count results after 1 week of aging in 25% NaOH solution.**

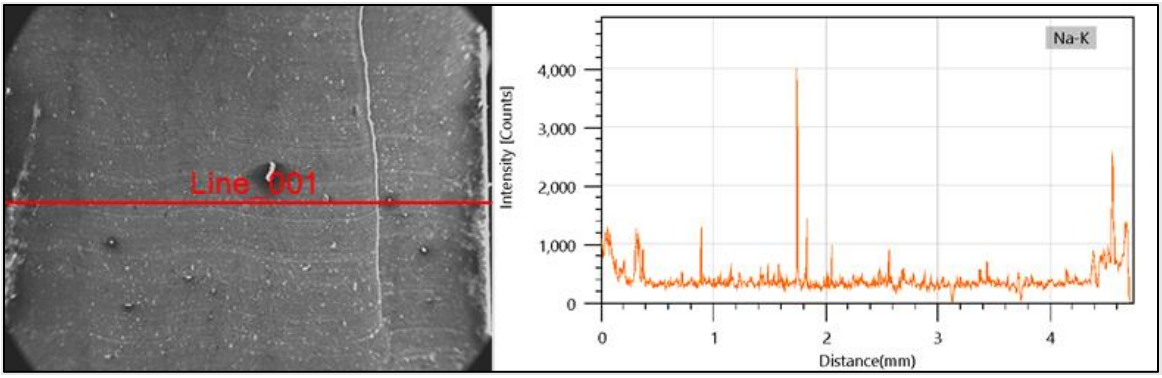


**Figure 228. Sodium ion count results after 9 weeks of aging in 6.25% NaOH solution.**

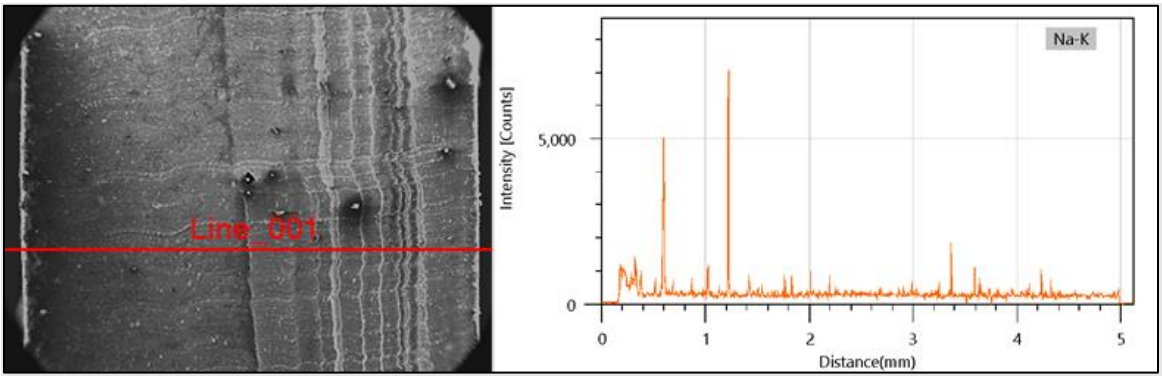


**Figure 229. Sodium ion count results after 9 weeks of aging in 12.5% NaOH solution.**

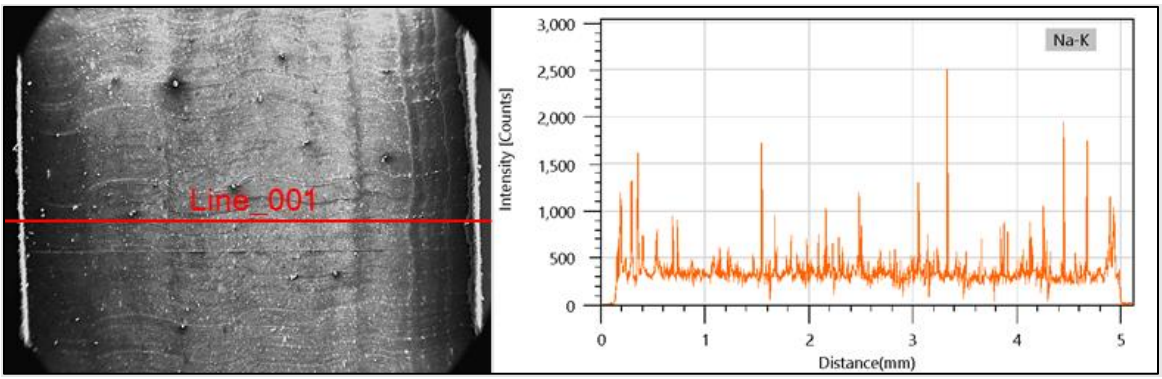


**Figure 230. Sodium ion count results after 9 weeks of aging in 25% NaOH solution.**

As seen in the figures above, there is minimal change between the results of the unaged specimen and the specimens aged for both one and nine weeks in NaOH solutions of 6.25%, 12.50%, and 25.00% respectively. This indicates that the maximum 9-week aging period was not enough to allow the NaOH solution to penetrate the EPDM material. During our previous research where specimens were aged in NaOH solutions for periods of 6-months and 12-months, sodium ions were detected in the EPDM material. That indicated that at these longer aging durations, NaOH solution

did penetrate the EPDM material. These results indicate that at short exposure times EPDM is impenetrable by NaOH solutions.

## Subtask 19.2.2: Conclusions

This year's research concentrated on the effect of sodium ion penetration into the EPDM material of HIHTL on its structural integrity of HIHTLs used in the waste transfer lines at the Hanford Site. Components were aged by exposing them to 77°C sodium hydroxide solutions at concentrations of 6.25, 12.50, and 25.00% (v/v).

The results revealed that the specimens subjected to the lowest NaOH concentration (6.25%) exhibited the greatest decrease in burst pressure. A 6%, 18%, and 26% reduction of the burst pressures was observed for the specimens aged in 25.00%, 12.50%, and 6.25% NaOH solutions respectively, compared to the baseline value. White crystalline deposits were observed on the interior of the dry HIHTL specimens aged with the highest NaOH solutions (25.00% and 12.50%), while no such deposits were found on the specimens exposed to the 6.25% solution. Through analysis, these deposits were identified as Thermonatrite, a mineral form of sodium carbonate ($Na_2CO_3 \cdot H_2O$). The presence of Thermonatrite appears to have acted as a barrier, restricting the further diffusion of NaOH solution into the EPDM material, subsequently reducing the extent of degradation.

SEM-EDX analysis of the aged specimens revealed that the penetration depth of sodium ions was 60% and 70% greater in the specimens aged with 12.50% and 6.25% NaOH solutions, respectively, compared to the specimen exposed to the 25.00% NaOH solution. This indicates that the specimens aged with the lower concentration solutions had the greatest sodium ion penetration and thus the greatest degradation.

## Subtask 19.2.2: References

1. Brush, LH., Ottinnger Farnum, C., Dahl, M., Joslyn, CC., Venetz, TJ. (2013). Test Plan for the Irradiation of Nonmetallic Materials. Albuquerque, New Mexico: Sandia National Laboratories, Albuquerque, NM.

2. P. Lieberman, V. Alfano, A. Onesto, and R. Mendoza, "Banded (BAND-IT) and Swaged Hose-In-Hose Transfer Line (HIHTL) Assembly, Service Life Verification Program," May 2004.

# TASK 20: CORROSION PROTECTION AND CHARACTERIZATION OF EM INFRASTRUCTURE

## Subtask 20.1: Evaluation of Coatings for the H-Canyon Exhaust Tunnel

### Subtask 20.1: Introduction

The H-Canyon is the only remaining chemical processing facility in America capable of reprocessing plutonium, highly-enriched uranium, and other radioactive materials. The H-Canyon Exhaust (HCAEX) Tunnel used to contain and direct the exhaust air flow from the canyon chemical process areas to the sand filter system, where radioactive contamination is removed. After several structural integrity inspections of the HCAEX tunnel, mandated by mission requirements at the Savannah River Site, there is a great concern about the concrete structure degradation. Videos/pictures taken during inspections evidenced significant degradation of the interior concrete walls characterized by surface erosion exposing concrete coarse aggregates, rebars exposed in some tunnel sections and significant amount of concrete loss, all promoted by the aggressive environment inside the tunnel (primarily nitric acid vapors). The application of a protective coating on the degraded tunnel walls can mitigate and prevent further degradation, which constitutes the main goal of the investigation.

This is a multistage investigation including 1) the development and evaluation of aged concrete surfaces similar to the degraded HCAEX tunnel walls, 2) the identification and evaluation of potential coatings applied on the developed aged concrete surfaces, 3) the development and evaluation of a procedure and a robotic platform for the coating application and 4) the application (deployment) of the coating on the tunnel walls through the developed robotic platform.

### Subtask 20.1: Objectives

The objective of this task is to investigate protective coatings that can be used to mitigate and prevent further degradation of concrete walls exposed to the adverse environments in the HCAEX tunnel. Potential coatings will be applied on aged and non-aged concrete surfaces similar to the tunnel degraded walls and further evaluated through accelerated aging tests at the laboratory. A preliminary coating selection was performed based on research findings. FIU initiated communications with various coating companies to identify and prepare a list with the potential coating options for the evaluation stage. Also, a comprehensive test plan for the evaluation of the coating options was prepared. In addition, concrete specimens with raw materials and mix design similar to the tunnel were prepared and will be the substrate of the coatings. A group of concrete samples were aged before coating application. In line with the aforementioned objective, the following subtasks were executed to support the effort:

- Continued the accelerated aging and evaluation of potential coatings through accelerated aging tests. The accelerated aging conditions considered the worst-case scenario during the concrete aging experiments. Several variables of importance in the coating performance were included in the study such as surface preparation, aging conditions of the surface and others.
- Based on the preliminary results of the coating performance in aggressive environments, each of the coatings were ranked. For this ranking, the results of various parameters under

study were considered such as visual inspection, coating failures, thickness loss, impedance, and others.

## Subtask 20.1.1: Evaluation of Coatings through Accelerated Aging Tests

### Subtask 20.1.1: Methodology

Based on lessons learned and results of the concrete aging process, the enhanced aging condition was selected for the accelerated aging of the coatings. The enhanced aging conditions consists of exposing the surface of the specimen to a 0.5M nitric acid solution. Once a week, the surface in contact with the acid solution is exposed to erosion by using a wire brush. This aging procedure combines the chemical and physical effect of the acid solution and the erosion, respectively. Concrete specimens, aged and non-aged and with and without embedded rebar will be used for the bench-scale testing. The abovementioned concrete specimens were the substrate for the evaluation of potential coatings.

Test plan

A factorial design of three variables at two levels was used leading to 8 different experiments. Table 22 below shows the test plan with the experiments for each coating. The single and synergistic effect of the variables were studied. The three variables under study are 1) surface preparation, 2) steel rebar presence and 3) aging of the substrate. Two levels of each variable were studied and represented in the table.

Four potential coatings, from different manufacturers Belzona, Carboline, Sherwin-Williams and Framatome were selected for the study. Two of them, Carboline and Belzona (samples without rebar) completed the aging and evaluation process. Two other coatings, Sherwin-Williams and Belzona (samples with rebar) completed the accelerated aging and evaluation, and the results are presented in this report. The coatings include coating systems or a single coating.

**Table 22. Test Plan for Accelerated Aging of Coatings**

| Test ID | Carboline ID | Belzona ID | S-W ID | **Aged/Non-aged surface** | **Surface Preparation (Yes/No)** | **Steel rebar (Yes/No)** |
|---|---|---|---|---|---|---|
| T1 | CT1-1* | BT1-1* | ST1-1* | Aged | Yes | Yes |
| T2 | CT2-1* | BT2-1* | ST2-1* | Aged | Yes | No |
| T3 | CT3-1* | BT3-1* | ST3-1* | Aged | No | Yes |
| T4 | CT4-1* | BT4-1* | ST4-1* | Aged | No | No |
| T5 | CT5-1* | BT5-1* | ST5-1* | Non-aged | No | Yes |
| T6 | CT6-1* | BT6-1* | ST6-1* | Non-aged | No | No |
| T7 | CT7-1* | BT7-1* | ST7-1* | Non-aged | yes | yes |
| T8 | CT8-1* | BT8-1* | ST8-1* | Non-aged | Yes | No |

ID: identification, *: there are three replicates for each test case and only “No 1” is represented in the table. For example, the replicates for Carboline’s T1 case would be CT1-1, CT1-2 and CT1-3, S-W: Sherwin-William samples.

Specimen preparation

Concrete samples of 4-inch diameter and 2-inch height were used as the substrate to evaluate potential coatings. The concrete samples were prepared in a previous stage of the investigation, using a mix design and raw materials similar to the tunnel. Some of the samples were aged through accelerated aging tests and others were not aged for comparative purposes. After the aging process, aged concrete surfaces with protruded coarse aggregates (uneven), exposed rebar (some cases) and chemical damage were obtained. The developed concrete specimens were used as the substrate of the coatings.

The coating companies prepared the surface of selected concrete samples before the coating application. The type of surface preparation was determined by each coating company and may not be the same. Some samples did not receive surface preparation and served as a reference for comparative purposes. The same analysis was done for the samples with and without rebar.

Table 23 below shows the major characteristics of the coatings. Belzona company proposed two different coatings, Belzona 4311 and Belzona 1381. Both are single coatings. Only one of the two Belzona's coating, Belzona 4311, is under evaluation thus far. The other two companies, Carboline and Sherwin-Williams, proposed coating systems consisting of a resurfacer or repair mortar followed by a coating system (multiple coats). Based on recommendations of Savannah River site engineers, only the coatings without the resurfacer or repair mortar will be evaluated. The surface of the concrete samples was prepared and coated at the manufacturer facilities. Once the applied coatings were cured, samples were sent to FIU laboratories for testing.

Before coating application, some samples received surface preparation, including the group of samples: T1, T2, T7 and T8 (Table 22). For each group, three replicates were prepared. For example, for the T1 group the replicates identification are T1-1, T1-2 and T1-3 (Table 22). The same identification process was done for the rest of the groups. Some of the samples have steel rebar, embedded or exposed, identified as T1, T3, T5 and T7 (Table 22).

**Table 23. Potential Coatings for the Accelerated Aging Tests**

| | Company | Coating | Characteristics |
|---|---|---|---|
| 1 | Belzona | **Belzona 4311**. *Epoxy coating* | - One coat<br>- Chemical resistant coating, up to 20% nitric acid solutions. |
| 2 | | **Belzona 1381**. *Epoxy coating* | - One coat<br>- Erosion and chemical resistant coating, up to 10% nitric acid solutions. |
| | | 1. Repair mortar (optional).<br>**AW Cook Horizontal Pipe Lining Mortar**<br>2. Prime coat (optional). | - Coating system. Multiple coats.<br>- Repair mortar is optional. |

| | | | |
|---|---|---|---|
| 3 | Sherwin-Williams | **Sherwin-Williams Macropoxy 5000 Pre-Prime.** *Epoxy coating*<br><br>3. Finish coat.<br><br>**Sherwin-Williams Envirolastic AR425.**<br><br>*Polyurea coating* | - Abrasion resistant coating (finish coat) |
| 4 | Carboline | *1.* Resurfacer (optional). **Carbocrete 4010.** *Fiber-reinforced repair mortar*<br><br>2. Prime coat. **Dudick Primer 67.**<br><br>*Moisture-tolerant epoxy primer for steel and concrete.*<br><br>**3.** Tie coat primer. **Dudick Primer 27.**<br><br>*Vinyl Ester primer for steel and concrete (required as a tie coat)*<br><br>**4.** Vinyl ester lining. **Dudick Protecto-Coat 700/705.**<br><br>*Flake filled, thermosetting polyester lining* | - Coating system. Multiple coats.<br>- Moisture tolerant primer.<br>- Abrasion resistant coating (finish coat) |

Accelerated aging conditions

The enhanced aging consists of exposing the samples (top coated surface) to a 0.5M nitric acid solution (pH = 0.3) and erosion for the time of the experiment. Once a week, samples were exposed to erosion using a wire brush. Figure 231 shows the schematic of the test setup developed for the exposure of the coated samples to the acid solution. A similar setup was used to age the concrete surfaces. The test setup was placed inside a fume hood to reduce the risk of operator exposure to nitric acid fumes.

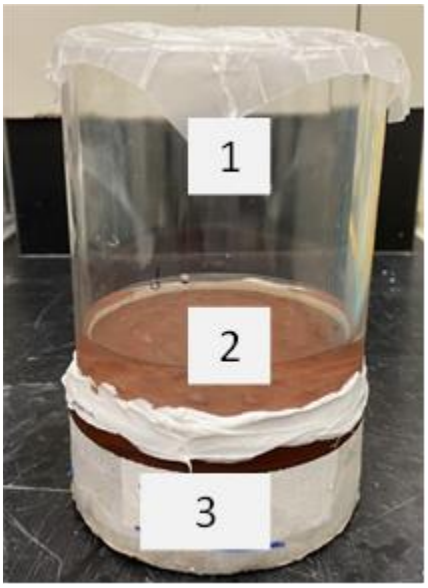


**Figure 231. Test setup for coatings exposure to acid solutions. 1. acrylic tube with acid solution, 2. coating (brown color) covering the top surface of the sample, 3. concrete sample.**

The procedure summarized below was followed for the evaluation of coated surfaces via the accelerated aging conditions.

I. *Take initial data of the samples* - After labelling the samples, visual inspection and images of the coated surface are taken. This allows detection of possible failures on the coatings such as erosion, blistering, cracking, scaling and others. In addition, the initial thickness of the coating is measured. Images of the side and top views are taken.

II. *Measure impedance* - Impedance measurements are carried out with time at the open circuit potential (OCP) condition with 10 mV potential perturbation.

III. *Measure pH* - The acidic test solution in contact with the coated surface is collected for pH measurements. The pH values are recorded over time.

IV. *Measure coating thickness* - Ensure the sample is dry before making measurements. Place drops of water in selected locations. Record all 15 thickness measurements (3 measurements per location, 5 locations on sample) with the Positector 200 Thickness Gage and record the minimum, maximum and average of each sample.

V. *Visual Inspection* - Perform a visual inspection and document the exposed coated surface with photographs (side and top views). This step is repeated at least once a week. Inspect and record the presence of possible coating's failures.

VI. *Erosion* - The specimen is eroded with a small, circular wire brush in a circular motion across the samples' surface for approximately 1 minute.

VII. *Acid replacement* - Add 200 mL of the acid solution with adjusted pH or new in the corresponding acrylic container, exposing the coated concrete sample to the acidic environment.

VIII. Once a week, repeat steps II through VII for each sample.

Measurements

Several durability measurements such as visual inspection, pH changes of the acid solution, coating thickness, coating adhesion, failures identification/evaluation, impedance measurements, as well as surface characterization including x-ray diffraction (XRD), scanning electron microscopy with energy dispersive x-ray (SEM-EDS) and others will be performed for evaluating the potential coatings. Once a week the coating evaluation was conducted. Visual inspection and failure identification of the coated specimens was conducted before, during and after the aging tests. Possible failures that could be observed includes blistering, cracking, scaling and erosion. Images were also taken over time during the visual inspection to facilitate further inspection/evaluation of the failures observed. Other measurements included coating thickness and impedance. Because this is an ongoing investigation, surface characterization is not completed and will not be included in this summary document. Table 24 summarizes the measurements that will be used to evaluate the coating performance.

**Table 24. Measurements to Evaluate Coating Behavior**

| Test | Age | Method |
|---|---|---|
| Visual inspection (failures) | Over time | ASTM D6577 [4] |
| Coating thickness | Over time | Coating Thickness Gauge |
| Water absorption | Over time | Electrochemical |
| Coating protective properties (impedance) | Over time | ASTM D6577 [4], Electrochemical |
| pH change (solution) | Over time | pH measures |
| Adhesion | before/after test | Pull-off test, ASTM D7234 [5], ASTM D4541[6] |
| Surface characterization (SEM-EDS, XRD, IR.) | before/after test | |

Coating thickness measurements were conducted in 5 different locations of the coated surface of each sample, over time, using a Positector 200 Thickness Gage. For each location, at least three measurements were taken. Average values were calculated to get information of the coating's durability.

The evaluation of the failures (blistering, cracking, erosion, etc.) was performed by visual comparison between the samples studied (three replicates) and standard photographs specifically designed for each defect as well as the reference sample (not exposed), conforming to the ASTM D714 [7], ASTM D772[8], and ASTM D661 standards [9].

The pH of the acid solutions was measured with time to control and keep the concentration constant. By using the pH formula, the concentration of the acid solutions, 0.5M, was determined and compared with the original pH value (0.3). The deviation from the original value would indicate coating acid attack. The deviation calculated was used to determine the volume of concentrated acid to be added to keep the concentration of the solution constant.

Impedance measurements were also performed on the coated surfaces providing useful information about the coating protective properties related to durability. The impedance measurements were conducted over time using a PMC-1000 multichannel potentiostat, at the open

circuit potential (OCP) condition with 10 mV potential perturbation. Measurements were performed at a frequency range from 1MHz to 1Hz. A three-electrode arrangement was used using a saturated calomel reference electrode as a reference electrode, a platinum mesh as the counter electrode, and the coated sample as the working electrode.

## Subtask 20.1.1: Results and Discussion

This section includes the results of the two coatings that completed the evaluation this year, Sherwin-Williams and Belzona (samples with rebar). To present the results, the following subsections will be used: 1) Visual inspection and failure analysis, 2) Coating thickness results, 3) Impedance results, etc. Because this is an ongoing experiment, only preliminary results are presented here.

Sherwin-William coating system

The Sherwin-Williams coating system under evaluation is composed of two different coatings: 1) a Macropoxy 5000 epoxy primer and 2) a Envirolastic AR425 polyurea topcoat. Because this is an ongoing investigation, the preliminary evaluation of the coating was done based on visual inspection, failure analysis, coating thickness and impedance measurements results.

*Visual inspection and failure analysis*

Figure 232 shows images of coated specimens before and during accelerated aging conditions. The samples presented here, with (ST1-1, ST7-1) and without (ST3-2, ST5-1) surface preparation, as well as aged (ST1-1, ST3-2) and non-aged (ST5-1, ST7-1) concrete substrates, before coating application, are representative of all test cases (ST1-ST8).

The coated samples show good performance with no major failures after 120 days of accelerated aging. No blistering, cracking, or scaling failures were observed on the coated surfaces except erosion. The erosion of the surface slightly increased with the aging time, leading to the detachment of some coating particles. Also, a color change was observed from day 15 for most of the samples.

The preparation of the substrate greatly determines the durability of the coating. In this study, selected samples received surface preparation (ST1-1, ST7-1) and for comparative purposes another group did not receive preparation (ST3-2, ST5-1). In general, no difference in the coating behavior among samples with and without surface preparation was observed, thus far.

The presence of exposed rebar before coating application, for example sample ST1-1, could eventually lead to coating failures. Peeling or detachment of the coating on top of the rebar was also not observed thus far. Once the steel rebar is oxidized, the corrosion products formed could lead to the coating failure.

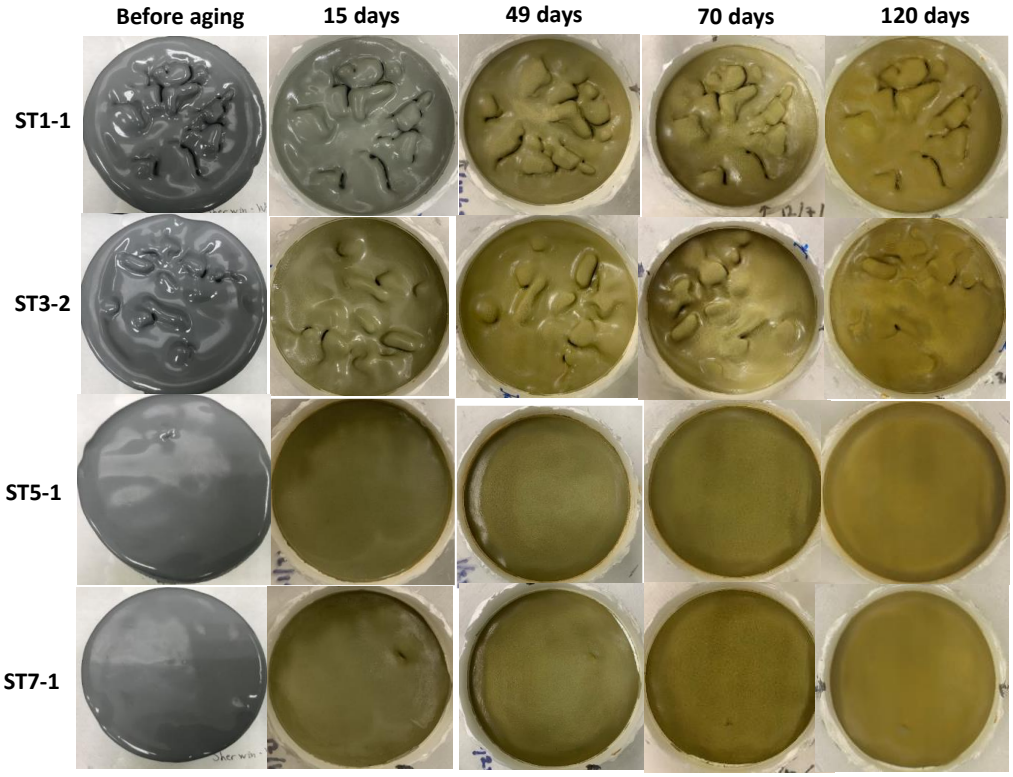


**Figure 232. Images of top view of Sherwin-Williams-coated samples, with (ST1-1, ST7-1) and without (ST3-2, ST5-1) surface preparation, before and during accelerated aging.**

*Coating thickness*

The thickness of the coatings gives quantitative information related to durability. Due to the accelerated aging of the coatings, erosion combined with the acid attack, a deterioration of the coating properties and a decrease in the thickness is expected with the aging time.

The coating composition and number of layers will also determine the deterioration rate. The coating under study is a multilayer system including an epoxy primer and a polyurea finish coat resistant to abrasion. A slower deterioration of the coating system and consequently of the thickness is therefore expected.

Figure 233 shows the evolution of the coating thickness for selected samples of group 1 (ST1 and ST3) and group 2 (ST5 and ST7). All tested samples show a decrease in the thickness no matter the concrete surface conditions (aged and non-aged concrete, with and without surface preparation) before the coating's application. The coating thickness of ST1 and ST3 samples (aged concrete surface) showed no major difference. Coated samples ST5 and ST7 depicted some differences on the thickness values with the greater loss of thickness for coated samples without surface preparation (ST5-1 and ST5-2).

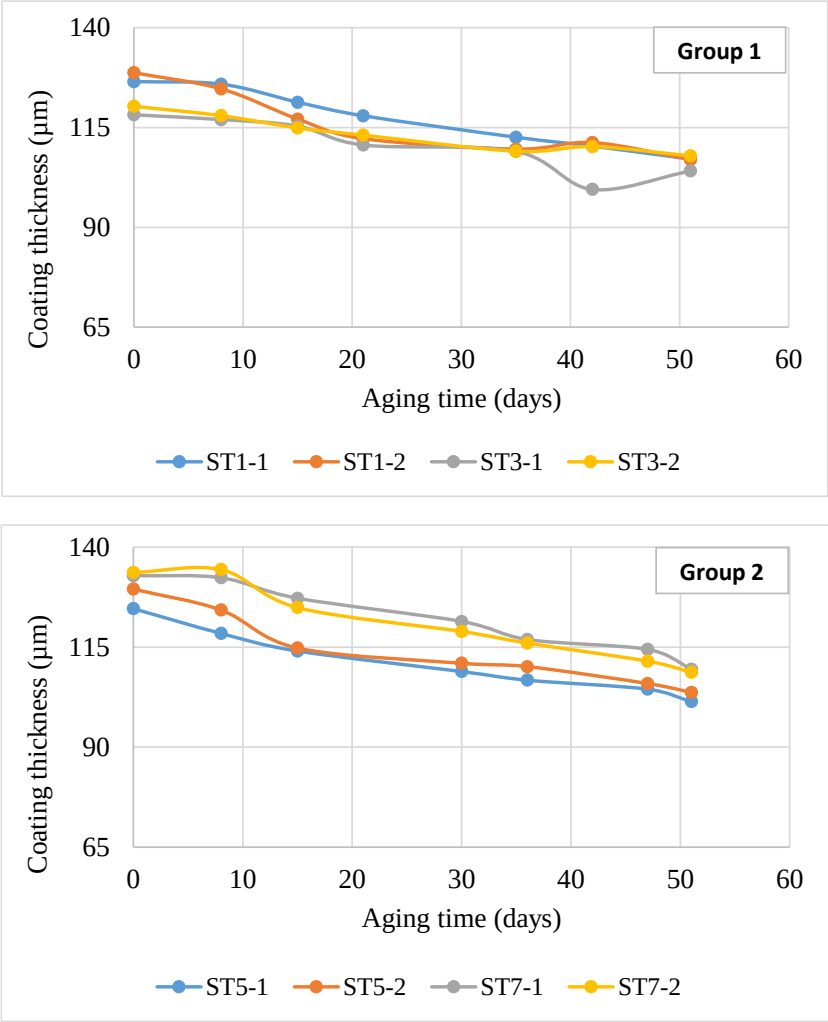


**Figure 233. Average thickness of selected coated samples, with (ST1, ST7) and without (ST3, ST5) surface preparation during accelerated aging. Group 1 (ST1 - ST4) and Group 2 (ST5 - ST8).**

The thickness loss of selected samples (ST1, ST3, ST5 and ST7) was calculated with the initial and final values. As a result, coated samples with aged concrete surfaces (ST1 and ST3) showed the lowest average thickness loss values ranging 10-17%. On the contrary, coated samples with non-aged concrete surfaces showed the greatest thickness loss values between 18-20%. The lowest thickness loss of group 1 samples (ST1, ST3) could be related to the uneven surface with protruded coarse aggregates (aged concrete surface) leading to less contact surface for the erosion. The peaks (protruded aggregate) of the coated surface will have better contact with the wire brush during the erosion than the valleys.

*Impedance results*

Electrochemical impedance spectroscopy (EIS) is a very well-known technique for the study of coatings performance. It allows to measure the coatings resistance to the aggressive environment where it is exposed, that also relates with their barrier properties [10-12]. Baycon, one of the pioneers in coatings evaluation using electrochemical techniques, measured the resistance of three hundred different coating systems with their protectometer and related the values with performance in long-term corrosion tests. As a result, high and constant resistances were typical

of good performance, > $10^8$ –$10^9$ Ω.cm$^2$; rapid decreases to values below $10^6$ Ω.cm$^2$ were typical of poor performance, and anything between these extremes was considered fair [10]. Mayne investigation agrees with previous findings and points that corrosion protective properties of organic coatings have an electrochemical character, as it can be explained by the coating resistance, hindering ions movement between cathodic and anodic areas [11].

Selected coated samples, with (ST1 and ST7) and without (ST3 and ST5) surface preparation and with (ST1 and ST3) and without the aged concrete surface were considered for this summary document. The selected samples are representatives of the eight test cases being studied.

Figure 234 shows the evolution of the impedance modulus of coated samples with an aged concrete surface and with (ST1) and without (ST3) surface preparation at different aging times.

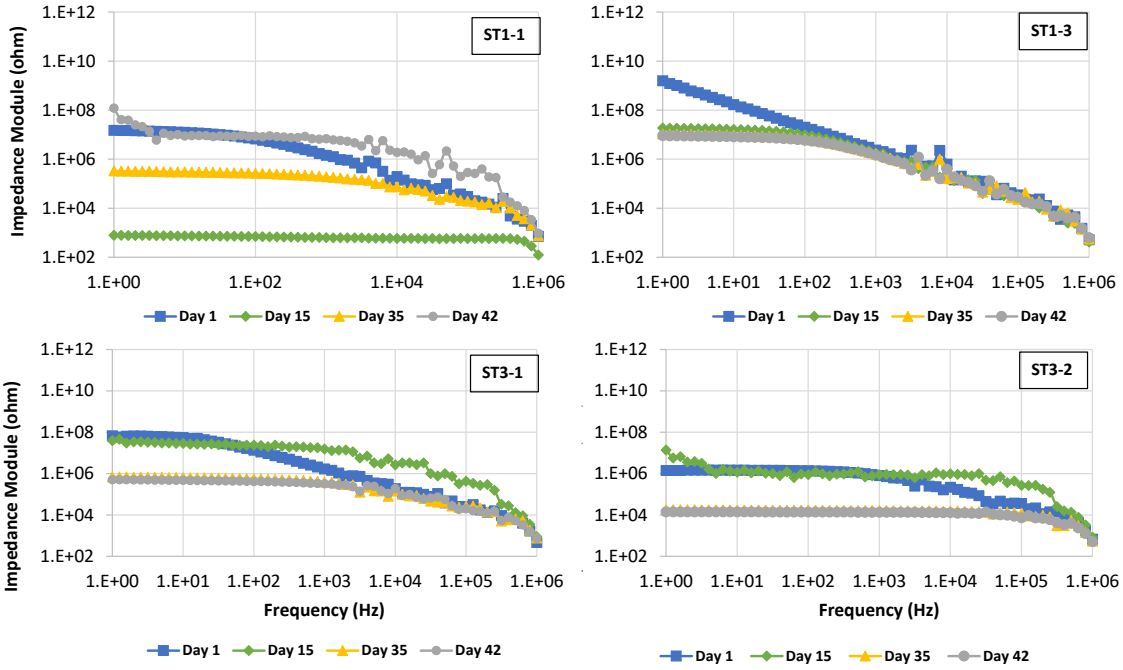


**Figure 234. Bode plot comparison graph for selected coated samples with (ST1) and without (ST3) surface preparation of Group 1.**

As a general trend, the impedance modulus decreases with the aging time up to values ranging $10^4$-$10^7$ Ω.cm$^2$ after 42 days of accelerated aging. The lowest impedance modulus values around $10^4$-$10^6$ Ω.cm$^2$ were observed on those samples (ST3-1 and ST3-2) that did not receive surface preparation before the coating's application. According to Baycon [10], these values are indicative of lower coating resistance and a poor performance against the aging conditions. On the contrary, coated samples with surface preparation showed the greatest values between $10^7$-$10^8$ Ω.cm$^2$, meaning that the coatings performance is fair [10].

Similar analysis was performed on selected coated samples (ST5 and ST7) of Group 2 without the aged concrete surface. Figure 235 shows the impedance modulus of coated samples with (ST7) and without (ST5) surface preparation at different aging times.

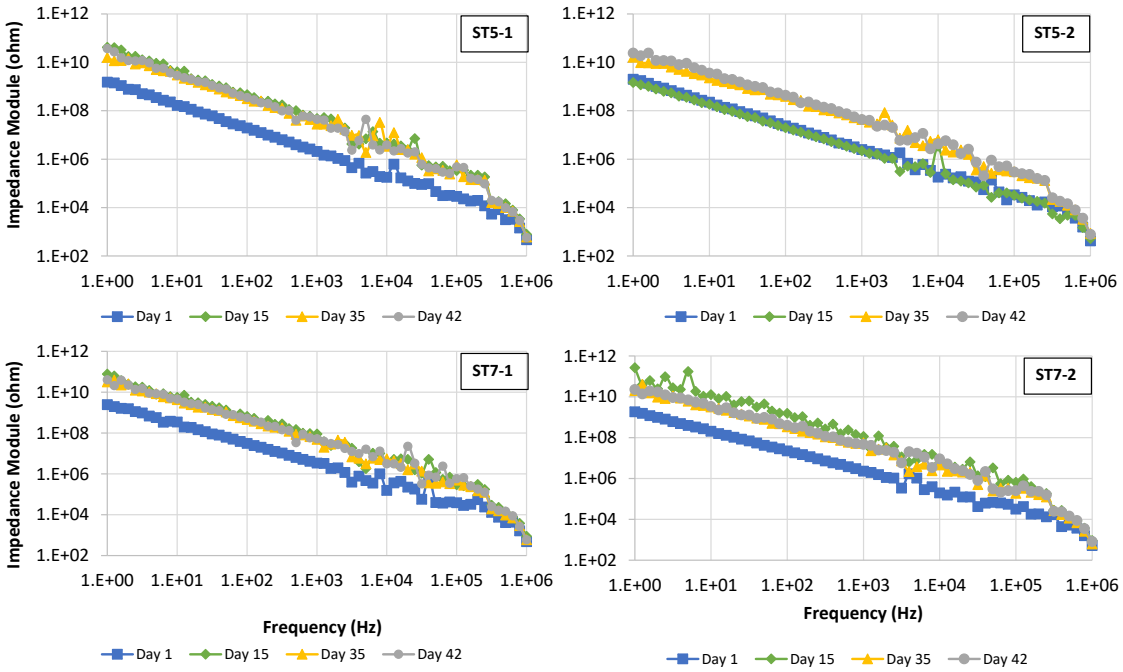


**Figure 235. Bode plot comparison graph for selected coated samples with (ST7) and without (ST5) surface preparation of group 2.**

For this group of samples without the aged concrete surface, it is highlighted how the impedance modulus increase with the aging time for all the coated samples with and without surface preparation. After 42 days of accelerated aging, the impedance modulus for all the samples is around $10^{10}$ $\Omega.cm^2$, indicating a good performance for all the test cases A major difference in the impedance modulus was not observed between samples with and without surface preparation.

In summary, coated samples with the non-aged concrete surface (Group 2) with and without surface preparation showed the best protective properties, with the highest impedance modulus. Coated samples with the aged concrete (Group 1), has an uneven surface with protruded aggregates and exposed rebar (some cases) that is more prone to premature coating failure.

*pH results*

The pH of the nitric acid solution in contact with the coated samples was measured once a week. The idea is to keep constant the pH to 0.3 for the time of the experiment to have a solution with a concentration of 0.5 M.

The pH values of the acid solution of all the coated samples changed with the values between 0.12 and 0.40 during the accelerated aging. The changes in pH are indicative of interaction between the coating and the acid solution. Every week, if necessary, the pH value was adjusted to the desired value (0.3) by adding concentrated acid or diluting the solution. The concrete surface condition, aged and non-aged and with and without surface preparation, was not shown to influence the pH values.

<u>Belzona coatings</u>

The Belzona 4311, a single epoxy coating resistant to chemicals was applied on concrete samples developed at FIU laboratories. Depending on the test case, the rebar is exposed (aged concrete) or

embedded (non-aged concrete) in the coated samples. The same coating was previously evaluated on concrete samples without rebar and this report presents the results on samples with rebar (BT1, BT3, BT5 and BT7). The evaluation of the coating was done based on visual inspection, failure analysis, coating thickness and impedance measurements.

*Visual inspection and failure analysis*

Figure 236 shows images of Belzona-coated specimens before and during accelerated aging conditions. The samples presented here, with (BT1-1, BT7-1) and without (BT3-1, BT5-1) surface preparation, as well as aged (BT1-1, BT3-1) and non-aged (BT5-1, BT7-1) concrete substrates, before coating application, are representative of all test cases (BT1-BT8). In general, no blistering, cracking, or scaling failures were observed on the coated surfaces after 120 days of accelerated aging. However, an increment of the coating's deterioration over time for all tested samples was observed. The deterioration is located on the area where the erosion takes place, and it increases over time. After 14 days of accelerated aging, it is more evident how the color of the coating is lighter due to the loss of material (coating particles) from the aging process. The coating particles detached from the surface were observed in the acidic test solution. In addition, as a general trend, a difference was not observed in the coating behavior among samples with (BT1-1, BT7-1) and without (BT3-1, BT5-1) surface preparation.

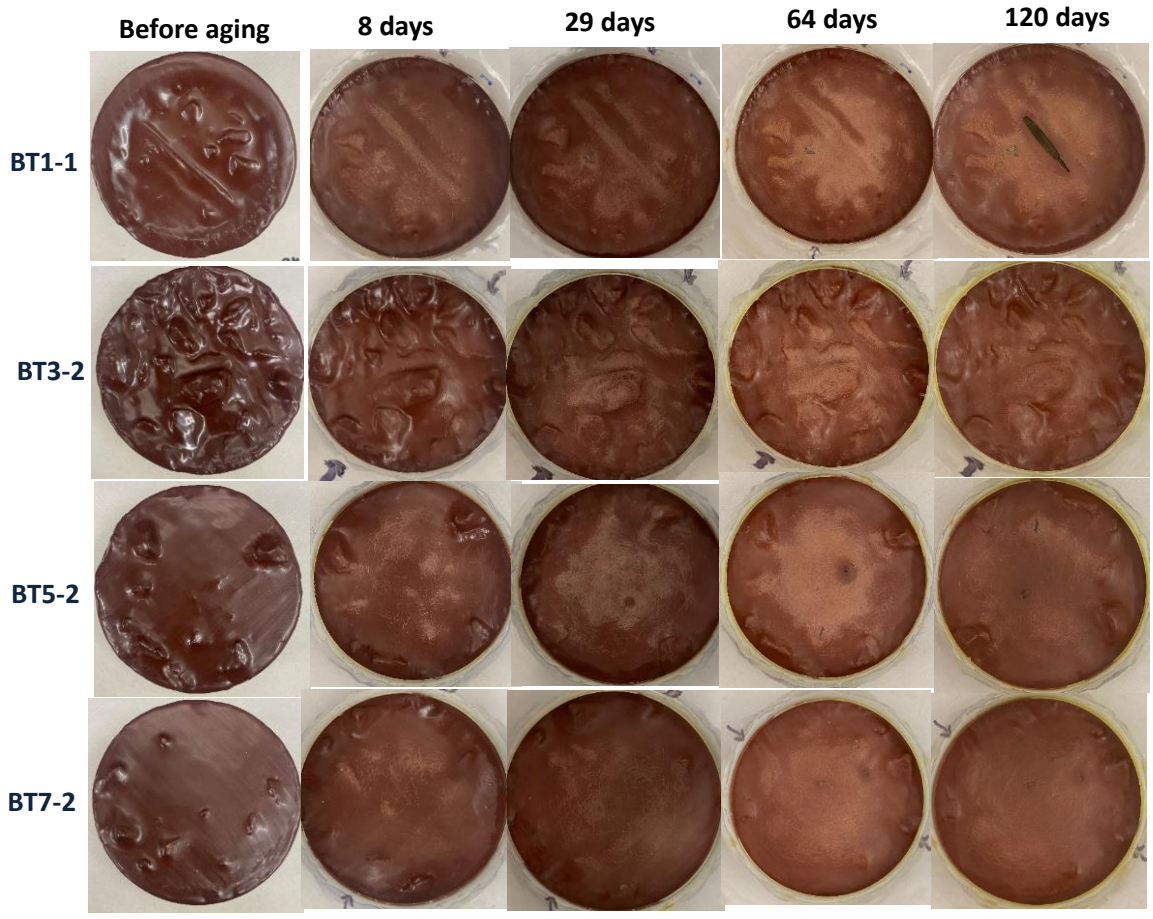


**Figure 236. Comparative images of the top view of Belzona-coated specimens with rebar, with (BT1-1, BT7-1) and without (BT3-1, BT5-1) surface preparation, before and after aging conditions.**

*Coating thickness*

The thickness of the Belzona coatings was monitored over time to get insight about the coatings' durability. Table 25 shows the average thickness and average thickness loss of selected coated samples with (BT1-1) and without (BT3-1) surface preparation. In general, the thickness decreases over time for all test cases. Also, no matter the test case, the thickness of the samples shows a similar trend over time.

**Table 25. Average thickness and average thickness loss of Belzona coating with rebar**

| Sample ID | Average thickness (µm), day 120 | Average thickness loss (%), day 120 |
|---|---|---|
| **BT1** | 63 | 47 |
| **BT3** | 63 | 50 |

The thickness loss of selected coatings was calculated with the initial and final values. As a result, coated samples with and without surface preparation had a thickness loss around 50%, from the initial value, after 120 days of aging.

*Impedance results*

Figure 237 shows the evolution of the impedance modulus of coated samples with an aged concrete surface and with (ST1) and without (ST3) surface preparation at different aging times.

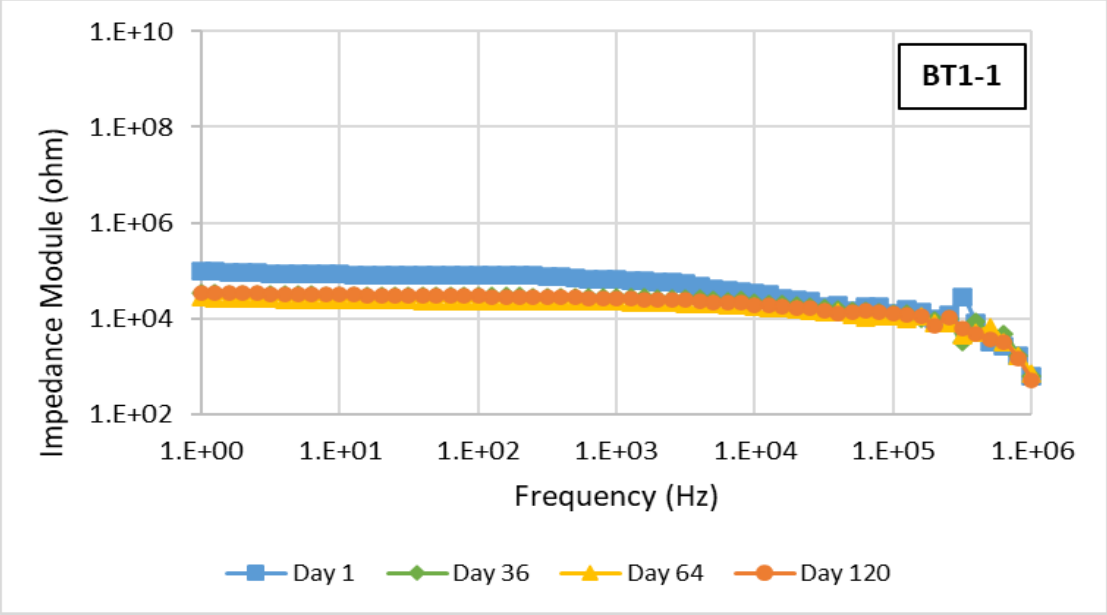

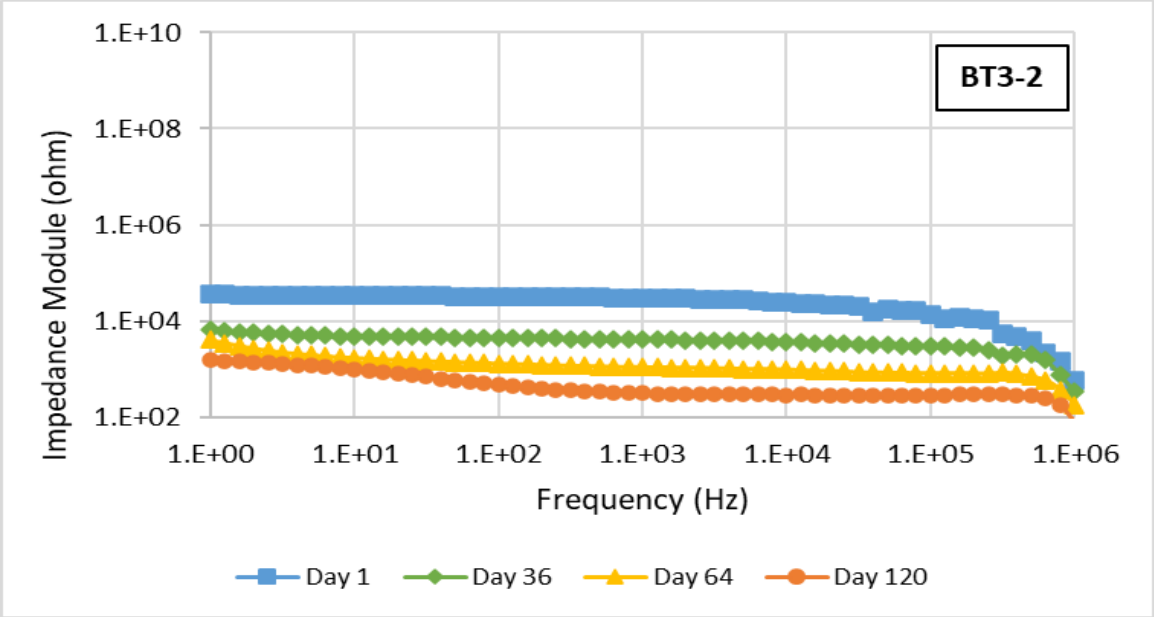


**Figure 237. Bode plot comparison graph for selected coated samples with (BT1) and without (BT3) surface preparation.**

As a general trend, the impedance modulus decreases with the aging time up to values ranging $10^3$-$10^5$ Ω.cm$^2$ after 120 days of accelerated aging. The lowest impedance modulus value around $10^3$ Ω.cm$^2$ was observed on sample BT3-1 that did not receive surface preparation before the coating's application. According to Baycon [10], values below $10^6$ Ω.cm$^2$ were typical of poor performance, which agrees with previous findings.

## Subtask 20.1.1: Conclusions

Visual inspection, failure analysis, thickness and impedance measurements showed slow degradation of the Sherwin-Williams coating system, compared to the Belzona single epoxy coating over time. The degradation of the coatings was characterized by loss of coating particles and color change. The reduction of thickness over time, for all tested coatings, indicated degradation and loss of protective properties, which was greater for the Belzona epoxy single coating. The erosion of the surfaces played a key role in the degradation of the coatings.

## Subtask 20.1.1: References

1. Bob J. Gilliam et al. "Inspection and Assessment of the H-Canyon Ventilation System at the Savannah River Site". Phoenix, Arizona. Waste Management Conference, 2015.
2. Staff Report, Defense nuclear facilities safety board. "H-Canyon exhaust tunnel fragility analysis input and assumptions". 2018.
3. Echeverria, M. et al. "Aging of concrete for the evaluation of repair materials to protect the HCAEX tunnel at Savannah River". Waste Management 2020 Conference, Phoenix, AZ, March 2020. (Best Poster of Track). Paper # 20301
4. ASTM D6577 "Standard Guide for Testing Industrial Protective Coatings". 2019.
5. ASTM D7234-21 "Standard Test Method for Pull-Off Adhesion Strength of Coatings on Concrete Using Portable Pull-Off Adhesion Testers". 2021.

6. ASTM D4541. “Standard Test Method for Pull-Off Strength of Coatings Using Portable Adhesion Testers”. 2017.
7. ASTM D714-02. “Standard Test Method for Evaluating Degree of Blistering of Paints”. 2017.
8. ASTM D772-18. “Standard Test Method for Evaluating Degree of Flaking (Scaling) of Exterior Paints”. 2018.
9. ASTM D661-19. “Standard Test Method for Evaluating Degree of Cracking of Exterior Paints”. 2019.
10. R.C. Bacon, J.J. Smith, F.M. Rugg, Electrolytic resistance in evaluating protective merit of coatings on metals, Ind. Eng. Chem. 40 (1) (1948) 161.
11. J.E.O. Mayne, Current views of how paint films prevent corrosion, J. Soc. 40 (1957) 183.
12. Echeverria M. et al. "Viability of Epoxy Siloxane Coatings for Preventing Steel Corrosion". Progress in Organic Coatings 92 (2016) 29-43.

### Subtask 20.1.2: Establish a Ranking of Coating Candidates from Research Findings

#### Subtask 20.1.2: Methodology

In this investigation, four coating candidates, Carboline, Belzona, Sherwin-Williams and Framatome were selected for the accelerated aging and evaluation. In this ongoing investigation, two coatings, Sherwin-Williams and Belzona, were exposed to accelerated aging conditions thus far and will be considered for this preliminary selection.

The ranking was based on the coating's performance to the accelerated aging conditions, 0.5M nitric acid solution and erosion. Parameters considered for the ranking included preliminary results on 1) visual inspection, 2) coating failures, 3) thickness loss and 4) impedance.

#### Subtask 20.1.2: Results and Discussion

Results of visual inspection, coating thickness and electrochemical measures supported the selection. The Sherwin-Williams coating system showed less thickness loss than Belzona’s single coating. Also, impedance measurements confirmed the greatest drop of the impedance modulus for the Belzona coating thus far, indicative of a reduction in the protective properties.

#### Subtask 20.1.2: Conclusions

Preliminary results suggest that the Sherwin-Williams coating system will offer greater barrier protection and protective properties than the Belzona single coating in aggressive environments with nitric acid and erosion.

## Subtask 20.2: Corrosion Evaluation of Steel Canisters for Hanford Integrated Disposal Facility

### Subtask 20.2: Introduction

A current challenge for DOE and relevant DOE sites is to understand the durability of the steel canisters/containers that will contain low-activity waste (LAW) and secondary waste forms, encapsulated in glass and grout respectively, and that will be placed within the Integrated Disposal

Facility (IDF) at Hanford. Currently, corrosion data of the steel and weld regions of the canisters at Hanford that is exposed to groundwater is limited. In addition, there is limited information on groundwater in contact with waste forms. The primary technical need is to study the corrosion rate of the steel canister's exterior that is exposed to Hanford groundwater and determine how well it shields the waste form that is inside the canister from exposure. Additionally, FIU will investigate how the corrosion rate varies in situations where groundwater has also contacted the waste forms.

### Subtask 20.2: Objectives

The objective of this subtask is to evaluate material (304 SS, 316 SS, carbon steel, mild steel and weld regions) behavior of the canisters in environments similar to IDF conditions and obtain site-specific corrosion data through electrochemical measurements. Obtaining such data can be used to predict the canister's useful life. The following subtask was executed to meet this objective:

- Obtain site-specific corrosion data of the 304 SS and 316 SS canister/container material exposed to simulated IDF conditions by using electrochemical techniques. The corrosion performance of 304 SS and 316 SS canister/container material and the effect of the surface condition will be studied. A solution that simulates Hanford groundwater at the IDF will be used.

## Subtask 20.2.1: Corrosion Behavior of Canister Materials for the Steel Corrosion Study at Hanford - 304 Stainless Steel

### Subtask 20.2.1: Methodology

In this section, information about the test plan, specimen preparation, test setup and electrochemical measurements is presented.

Test Plan

Table 26 shows the test plan developed to get corrosion data of various canister/container materials exposed to simulated Hanford IDF groundwater. Several electrochemical tests and surface characterization tests are listed. The candidates' materials under study are 304SS, 316SS, Hastelloy, 409SS, high carbon steel and ASTM A-569-93 Carbon Steel. Table 27 shows the reason for using each candidate material.

**Table 26. Test Plan**

| Candidate Sample Type | Tests | | | | | | | |
|---|---|---|---|---|---|---|---|---|
| | Potentiodynamic Polarization | | Corrosion Potential 7-28 day | | Polarization Resistance during Ecorr | | Post-corrosion Examination with SEM | |
| | GW A* | GW B* | GW A | GW B | GW A | GW B | GW A | GW B |
| Stainless Steel 304 | | | | | | | | |
| Heat Treated SS 304 | | | | | | | | |
| Welded SS304 | | | | | | | | |
| Welded SS304 - Heat Treat | | | | | | | | |
| ASTM A-569-93 Carbon Steel | | | | | | | | |
| high carbon steel | | | | | | | | |
| Hastelloy | | | | | | | | |
| 316 Stainless Steel | | | | | | | | |
| 409 Stainless Steel | | | | | | | | |

*: GW A and GW B are two representative Hanford groundwater simulants.

**Table 27. Candidate Materials Type for Canister/Container and Reason**

| Candidate Sample Type | Reason |
|---|---|
| Stainless Steel 304 | Glass container base material |
| Heat Treated SS 304 | Base canister material with glass poured within |
| Welded SS304 | Represent canister lid (weak point) |
| Welded SS304 - Heat Treat | Represent canister lid (weak point) after heat cycle |
| ASTM A-569-93 Carbon Steel | B-25 box steel type |
| high carbon steel | Worst case scenario |
| Hastelloy | Best case scenario for a container but expensive |
| 316 Stainless Steel | 55-gallon drum material |
| 409 Stainless Steel | 55-gallon drum material |

Variables of interest in this study are the type of material and the effect of heat treatment and welding on the materials behavior to corrosion. Because this is a multiphase study, in this initial phase, corrosion data for 304SS and 316 SS canister material in a simulated Hanford groundwater solution is obtained.

Specimen preparation

FIU procured 304 SS and 3116 SS square bars and threaded 316 SS rods for the preparation of the specimens. The material under study is the 304 SS and 316 SS. The 304 SS and 316 SS bars were cut to the dimensions of 0.75-inch height, 0.5-inch width and 0.5-inch thickness. The back of the samples was threaded, and a piece of 316 SS rod screwed to it to facilitate the electrical connection between the sample and the cables connected to the rod. Only the bottom squared section of the 304 SS and 316 SS samples were under study, with an area of 1.61 $cm^2$.The specimen was fixed in a cold resin that will allow only one side of the square bar (bottom) to be in contact with the solution. The surface of the sample was cleaned with detergent to remove any grease, oil or dust from the surface. The surface was grinded with 120 grit sandpaper and then, carefully washed with tap water, deionized water and dried. Once the sample was dried, it was stored in a desiccator until the beginning of the electrochemical tests.

Test setup and test solutions

Figure 238 shows the test setup inside a Faraday Cage which is used for the electrochemical measurements. A three-electrode arrangement was used to perform the measurement including a reference electrode (saturated calomel-SCE), a working electrode (the 304 SS sample or the 316 SS sample) and a counter electrode (a platinum mesh). The electrodes were in contact with the test solution and only the bottom surface of the sample (working electrode) was immersed in the solution during the experiment. A PMC-1000 potentiostat was used for the electrochemical measurements, connected to the computer through the VersaStudio software.

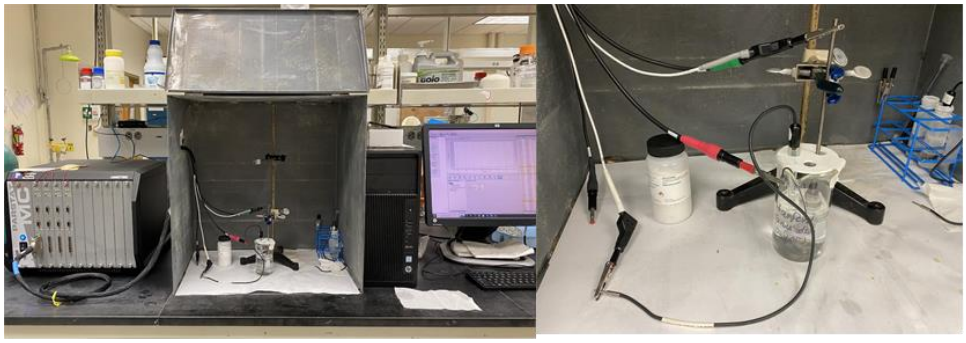

**Figure 238. View of the potentiostat, the Faraday Cage and computer (left image) used for electrochemical measurements. Zoom of the experimental setup (right image).**

The test solution simulates the infiltrating water that would reach the containers/canisters if the IDF surface barrier fails. Hence, the materials being studied will be immersed in this solution for the duration of the experiments. This solution will be identified as GWA or solution 1. For comparative purposes, a similar solution, identified as GWB or solution 2, was prepared only containing the chloride ions of the IDF Hanford groundwater recipe.

Electrochemical measurements

Electrochemical measurements included corrosion potential (Ecorr = OCP), electrochemical impedance spectroscopy (EIS), also known as impedance, and potentiodynamic polarization (PDP) or polarization.

The impedance measurements were conducted over time at the open circuit potential (OCP) condition with 10 mV potential perturbation and at a frequency range from 1MHz to 1 mHz. The

impedance measurements were performed for a week, every 24 hours. The impedance measurements were conducted once the Ecorr was stabilized. For that reason, the Ecorr was measured for an hour or until the value was stable and then, the impedance measurement started. The experimental data was recorded and used to get various graphs such as the Nyquist and Bode plots.

The PDP measurements were conducted following the sequence below:

1. Measure corrosion potential (Ecorr) for 1 hour.
2. Run a PDP scan (single) with the parameters below:
    - Initial potential (V): -200 Vs OCP
    - Scan to 1V vs reference electrode or cut it off at 10 mA/cm$^2$
    - Scan rate (mV/s): 0.1667 mV/s

With the data collected from the PDP measurements, the current–potential graphs, also called polarization curves, can be developed [2]. These curves are very useful to (a) acquire general information on the localized corrosion process, (b) determine critical potential values such as critical pitting potential, critical crevice potential, protection potential, and the corrosion potential, and (c) suggest the composition of the local environment conditions such as pH and chloride content. The corrosion or exchange current can be used to calculate the corrosion rate using Faraday's law [3].

The PDP data was also used to get useful parameters such as the corrosion current (Icorr), the corrosion rate ( R ), the current density (icorr) and others, using the Tafel method. For this method, the material is polarized, typically on the order of ±10mV, relative to its Ecorr, the potential measured when no [net] current is flowing. As the potential of the material (working electrode) is changed, a current will be induced to flow between the working and counter electrodes, and the material's resistance to polarization (Rp) can be found by taking the slope of the potential versus current curve. This is known as a Tafel plot. The Icorr can be determined by the following equation [4].

$$Icorr = \frac{\beta_a \beta_c}{2.3\,(\beta_a+\beta_c)}\left(\frac{n}{I}\right)^{-1} = KRp^{-1} = \frac{K}{Rp} \qquad \text{(Equation 1)}$$

Here, βa and βc are the anodic and cathodic Tafel slopes, respectively, in volts/decade, and n/I is the slope of the polarization curve around the Ecorr, corresponding to the polarization resistance. The term K is called the conversion factor or the Stern-Geary constant, assumed to be 26 mV for active steel and 50 mV for passive steel. When K is already known, the Icorr can be calculated based on the Rp obtained by the linear polarization. Then, if the surface area (anodic steel area), A, being polarized is accurately known, the current density (icorr) can be calculated by the following equation. [5].

$$i_{corr} = \frac{Icorr}{A} \qquad \text{(Equation 2)}$$

The icorr can be also determined by cathodic Tafel extrapolation to corrosion potential. Here, icorr is in A/cm2, EW is the equivalent weight of steel (25.12 g/mol), ρ is the density of the steel (7.94 g/cm3) and F is the Faraday's constant.

## Subtask 20.2.1: Results and Discussion

The electrochemical test results of the 304 SS and 316 SS immersed in the simulated Hanford groundwater solutions, Solution 1 and Solution 2, are presented in two different sections. Each section will include results of 1) impedance, 2) potentiodynamic polarization and 3) surface characterization. Since this is an ongoing experiment, only preliminary results are presented here.

**Electrochemical test results for 304SS in Solutions 1 and 2**

*Impedance (EIS)*

The EIS test is a commonly used method to evaluate the corrosion resistance of stainless steels. Figure 239 shows the Nyquist and Bode plots for the 304 SS samples exposed to the simulated Hanford groundwater Solutions 1 and 2. The Nyquist plots (Figure 239, left) of the 304SS in both solutions display similar semicircular features, with very similar diameters, at the beginning and after 8 days of immersion in the solutions. The trend observed indicates good corrosion resistance of the passive film formed on the surface of the canister material over time. The type of solution used did not show an effect on the material corrosion resistance.

The Bode plots (Figure 239, right) show the impedance modulus of the specimens versus frequency for Solution 1 and Solution 2. The impedance modulus provides information about the corrosion performance or corrosion resistance of the material to the solution. The impedance modulus of the 304SS is very similar at the beginning and at the end of the test, which indicates good corrosion resistance of the stainless steel for the tested conditions. The impedance modulus values were between $10^5$-$10^7$ Ω for all the tested cases.

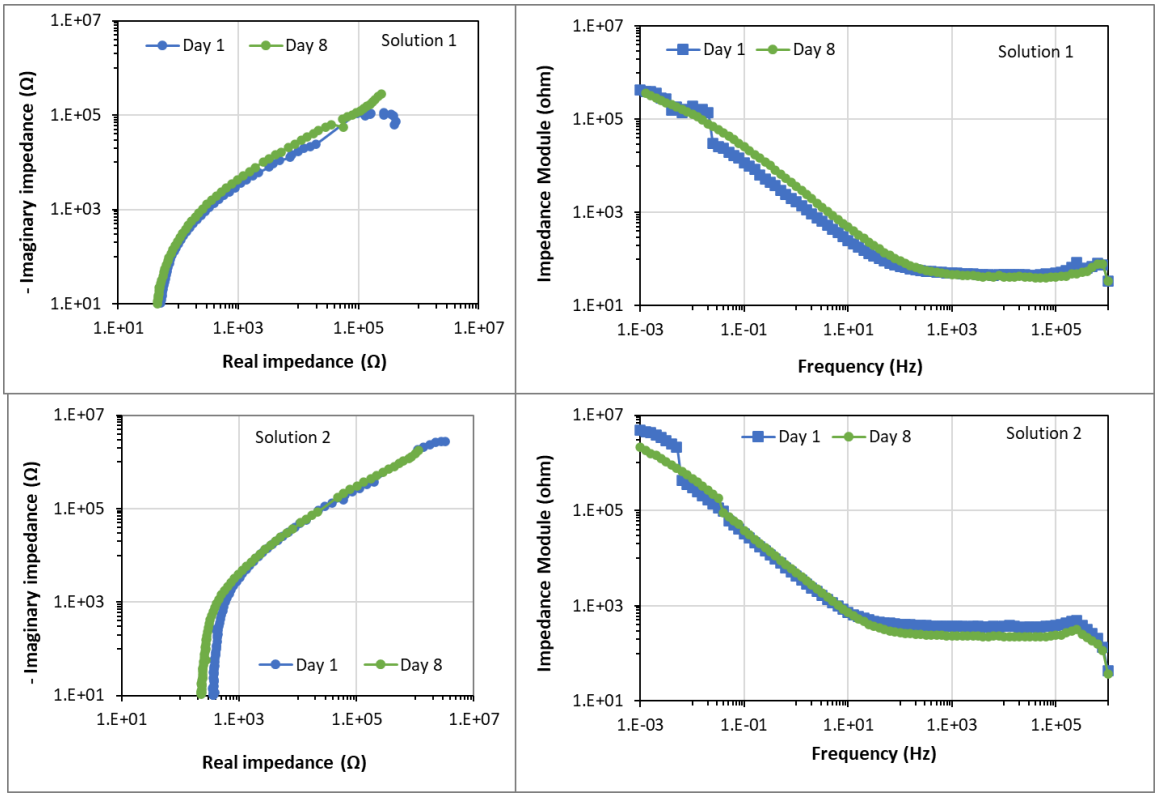


**Figure 239. Nyquist (left) and Bode (right) plots for the 304 stainless steel canister material exposed to Solution 1 and Solution 2 at different immersion times.**

*Potentiodynamic polarization (PDP)*

Figure 240 shows the polarization curve of 304 SS specimen immersed in the simulated Hanford groundwater Solutions 1 and 2. This graph offers insight into the electrochemical performance of the canister material.

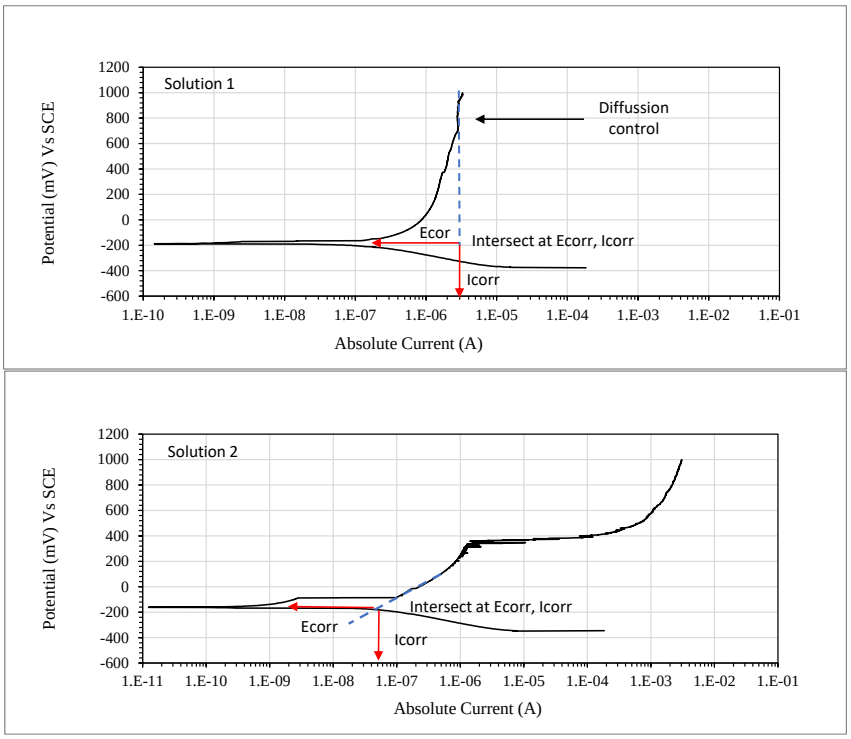


**Figure 240. Potentiodynamic graphs for 304 stainless steel canister material when immersed in simulated Hanford groundwaters, solution 1 (top) and solution 2 (bottom).**

For the 304SS in Solution 1 (Figure 240, top), it is noticeable that the cathodic branch is controlled by electron transfer and the anodic branch by diffusion. Icorr and Ecorr were obtained from the Tafel method, with values 1.8E-5 A and -187.39 mV Vs SCE, respectively. The calculated icorr was 1.12E-5 A/cm$^2$. For the 304SS in Solution 2, (Figure 240, bottom), the anodic domain region shows three different parts. In the first part, the current increases graphically followed by a small quasi-passive region in which current increases slowly due to the formation of small passive film. This passive film breaks at certain critical potential, breakdown potential or Eb = ~ 390 mV at which current returns to increase quickly in the third part of the anodic domain region. This breakdown potential and rupture of the passive film was only observed in the presence of chloride ions (Solution 2). Icorr and Ecorr were also obtained from the Tafel method, with values 6.14E-8 A and -161.63 mV Vs SCE, respectively. The calculated icorr was 3.81E-8 A/cm$^2$.

## Electrochemical test results for 316SS in Solutions 1 and 2

*Impedance (EIS)*

Figure 241 shows the Nyquist and Bode plots for the 316 SS samples exposed to the simulated Hanford groundwater Solutions 1 and 2. For the 316 SS sample immersed in Solution 1, the impedance increased (greater diameter of the semicircular feature) from day 1 to day 8 of immersion. The impedance modulus also increased from ~$10^5$ to $10^7$ Ω in a couple of days. The behavior observed indicates good corrosion resistance of the passive film formed on the surface of the canister material over time. For the 316SS sample immersed in Solution 2, the behavior is slightly different. The Nyquist plot shows semicircular features with the same diameter for day 1 and day 8 of immersion in the solution. The Bode plot also shows similar behavior, with almost the same impedance modulus in the order of $10^7$ Ω. This suggests that the 316 SS offers good corrosion resistance when immersed in Solution 2.

From the previous analysis can be concluded that the 316 SS sample shows better corrosion resistance in Solution 1 than in Solution 2, only with the chloride ions. This could be related to the stability and performance of the passive film in both solutions.

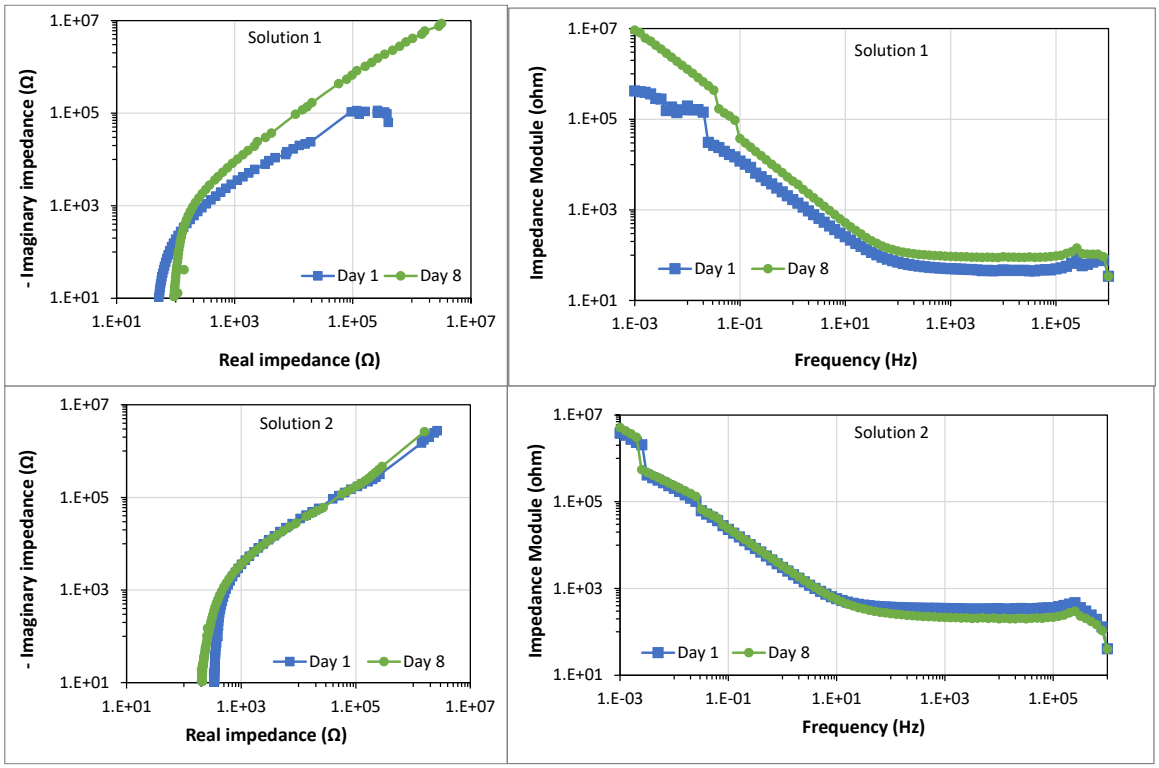


**Figure 241. Nyquist (left) and Bode (right) plots for the 316 stainless steel canister material exposed to Solution 1 and Solution 2 at different immersion times.**

*Potentiodynamic polarization (PDP)*

Figure 242 shows the polarization curve of 316 SS specimens immersed in the simulated Hanford groundwater Solutions 1 and 2. For the 316 SS specimen exposed to Solution 1 (Figure 242, top), the cathodic branch is controlled by electron transfer and the anodic branch shows a slow increase of the current with small current fluctuations or peaks. The slow current increment suggests the formation of the passive film and the small current fluctuations could be related with the formation of some unstable pits that did not broke the passive film. Icorr and Ecorr were obtained from the Tafel method, with values 5.89 E-8 A and -202.46 mV Vs SCE, respectively. The calculated icorr was 3.65 E-8 A/cm$^2$.

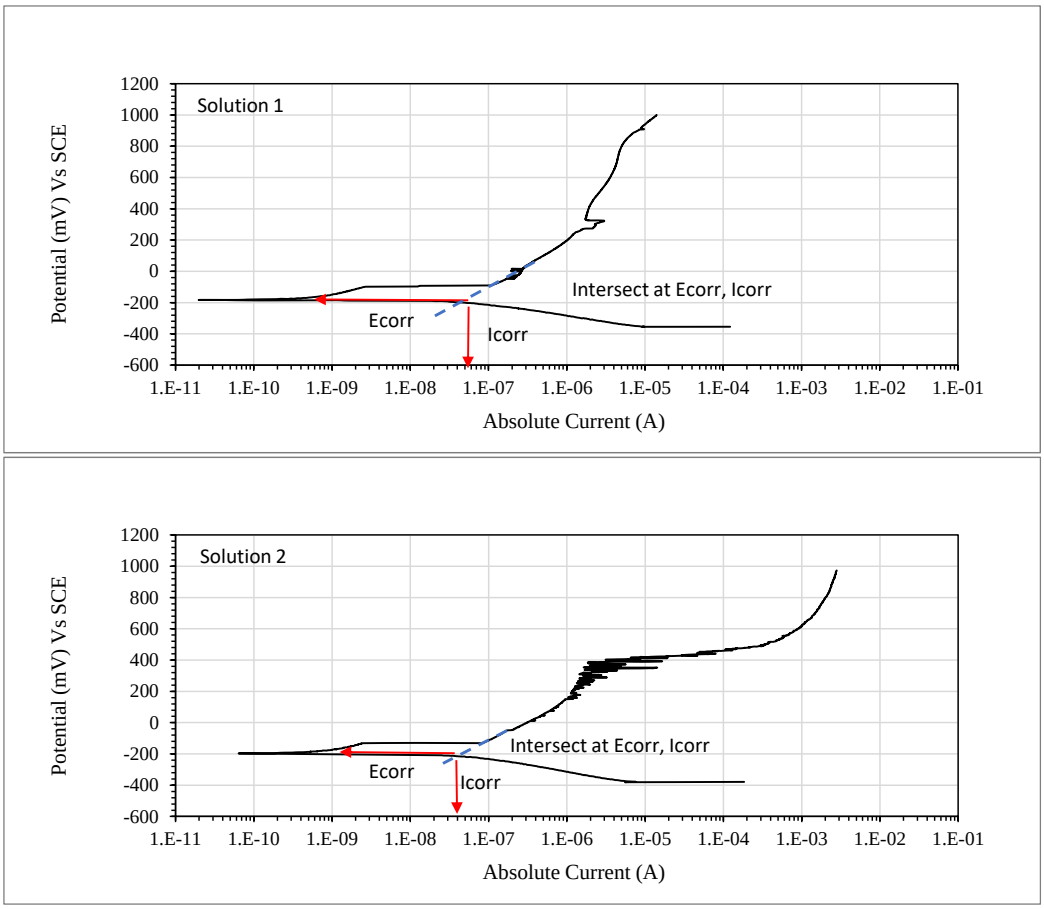


**Figure 242. Potentiodynamic graphs for 316 stainless steel canister material when immersed in simulated Hanford groundwaters, Solution 1 (top) and Solution 2 (bottom).**

On the contrary, when the 316 SS specimen is immersed in Solution 2 (only containing chloride ions), the anodic branch shows three main parts. In the first part, the current increases graphically followed by a small quasi-passive region in which current increases slowly due to the formation of small passive film. This passive film breaks at certain critical potential, breakdown potential or Eb = ~ 400 mV at which current returns to increase quickly in the third part of the anodic domain region. It is clear the effect of chloride ions on the passive film rupture and pitting formation. Similar behavior was observed for the 304 SS sample immersed in Solution 2. Icorr and Ecorr were also obtained from the Tafel method, with values 3.49E-8 A and -211.93 mV Vs SCE, respectively. The calculated icorr was 2.16E-8 A/cm$^2$.

## Surface characterization of the 304SS and 316SS samples

Because this is an ongoing investigation, only the preliminary results of the characterization are presented here. It is expected to characterize the surface of the samples using various techniques including optical microscopy, scanning electron microscopy (SEM-EDS) and X-ray diffraction (XRD).

The surface of the 304SS and 316SS samples were characterized using the optical microscopy technique. The intention was to identify the possible presence of pitting corrosion and study the morphology and dimensions of the pits. Images of the samples after the polarization test (PDP)

were taken at different magnifications. For comparative purposes, images of the samples before the test (reference sample) were also taken.

Figure 243 shows images of the 304 SS before (reference sample) and after the test. No pittings were observed on the images of the reference sample, only the lines formed due to the surface preparation with the 120-grit sandpaper. On the contrary, images of the sample after the test at 5X magnification show some round pittings formed on the tested surface. The same image was then 10X magnified and pittings were better visualized. The pitting lengths were 26.15 µm and 38.50 µm. These findings agree with the potentiodynamic results in the groundwater environment with chloride ions (Solution 2).

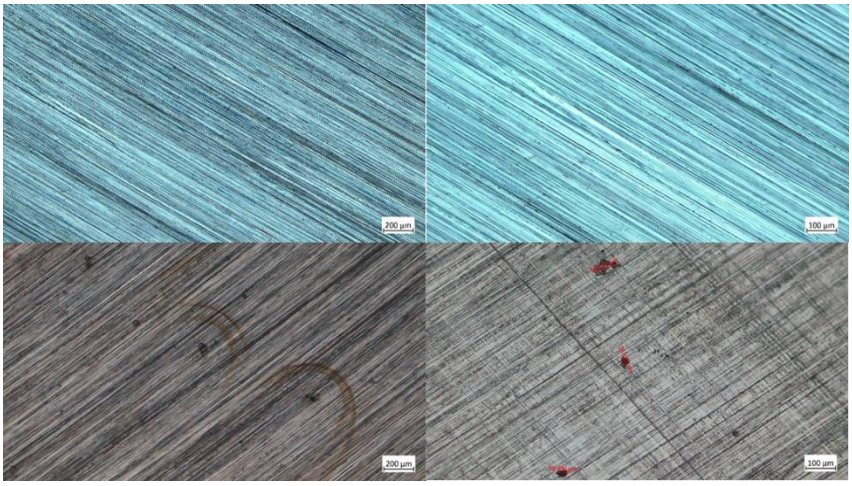

**Figure 243. Images of the 304 stainless steels before (reference) and after the potentiodynamic test in Solution 2 at different magnifications. Top images for the reference sample and bottom images for the sample after test.**

Figure 244 shows images of the 316 SS before (reference sample) and after the potentiodynamic test at different magnifications. No pittings were observed on the images of the reference sample, only the lines formed due to the surface preparation with the 120-grit sandpaper. After the potentiodynamic test, the sample was dried and stored in a dessicator until the images were taken.

On the contrary, images of the 316SS after the test at 5X magnification, shows some round pitting formed on the tested surface. The same image was then 10X magnified and shows two of the previous pitting. The pitting length were 31.53 µm and 36.53 µm. These findings agree with the potentiodynamic results in groundwater environment with chloride ions (Solution 2).

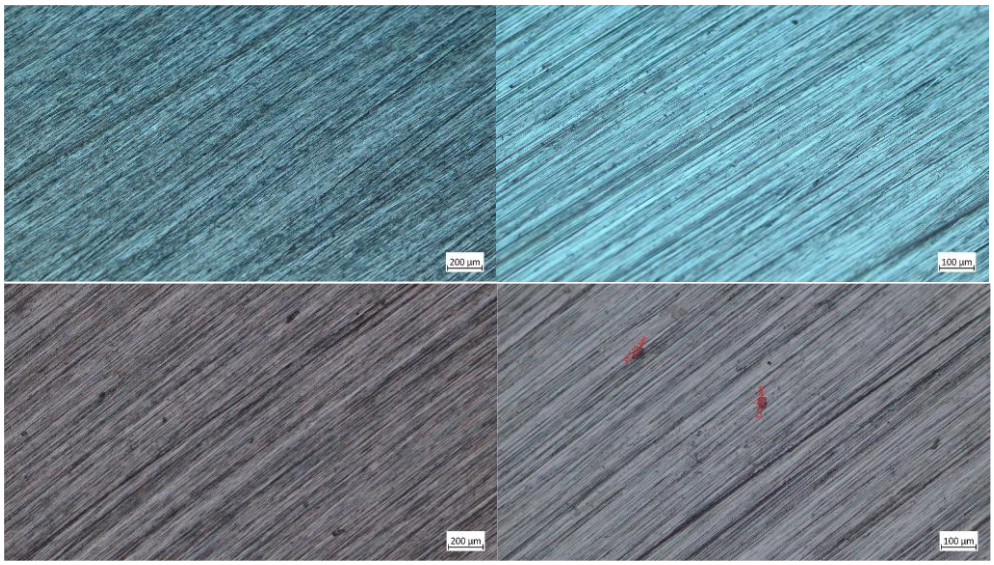


**Figure 244. Images of the 316 stainless steel before (reference) and after the potentiodynamic test in Solution 2 at different magnifications. Top images for the reference sample and bottom images for the sample after test.**

## Subtask 20.2.1: Conclusions

Electrochemical measurements included impedance and potentiodynamic polarizations allowing useful corrosion data of the canister materials to be acquired. The polarization graphs for both samples, in the presence of Solution 2 and only with chloride ions, showed that the anodic branches were controlled by passive film formation followed by rupture of the passive film due to pitting formation or some current instability. The morphology of the surfaces, before and after the tests, were evaluated by means of the optical microscopy technique and various pittings were identified and measured.

## Subtask 20.2.1: References

1. Serne R.J. et al. “Extended leach testing of simulated LAW cast stone monoliths”. Pacific Northwest National Laboratory. RPT-SWCS-010, Rev. A. June 2016.
2. Marcus, F. and Mansfeld, F. “Analytical methods in corrosion science and engineering”. Taylor and Francis group. 2005.
3. Kruger, J. and Hardman, V. Kay. “Current understanding of pitting and crevice corrosion and its application to test methods for determining the susceptibility to such corrosion of nuclear waste metallic containers”. Center for Materials Science. Washington, D.C. 20234. 1982.
4. Hiromoto S. “Corrosion of metallic biomaterials” in Metals for Biomedical Devices, 2010, Book chapter.
5. R.A. Buchanan, E.E. Stansbury, in Handbook of Environmental degradation of materials, 2012.

# CONFERENCE PARTICIPATION, PUBLICATIONS, AWARDS & ACADEMIC MILESTONES

**Oral and Poster presentations (presenter is underlined)**

M. Echeverria Boan, N. Espinal, L. Lagos, D. McDaniel, "Evaluation of Coatings for the Protection of the HCAEX tunnel Concrete Walls at Savannah River – 23103", Proceedings of the Waste Management Symposia 2023, Phoenix, AZ, February 26 - March 2, 2023.

**WM Student Posters**

Nicholas Espinal - Assessing Surface Preparation Effect on the Protective Properties of a Multilayer Coating System for Application in DOE Sites Infrastructures (22485)

**Awards**

N. Espinal (DOE Fellow), M. Echeverria, L. Lagos and D. McDaniel. "Assessing Surface Preparation Effect on the Protective Properties of a Multilayer Coating System for Application in DOE Sites Infrastructures". (Poster). Waste Management 2023 Conference, Phoenix, AZ, March 2023. (Roy G. Post Scholarship Winner)

# ACKNOWLEDGEMENTS

Funding for this research was provided by U.S. DOE Cooperative Agreement #DE-EM0005213. FIU's Applied Research Center would like to acknowledge the commitment of DOE-EM to this Chemical Process Alternatives for Radioactive Waste project and to all the research being conducted as part of the Cooperative Agreement. The partnership between DOE EM and FIU has resulted in the development and training of outstanding minority STEM students that will benefit this country as a whole.

# APPENDIX

The following documents are available at the DOE Research website for the Cooperative Agreement between the U.S. Department of Energy Office of Environmental Management and the Applied Research Center at Florida International University:
https://doeresearch.fiu.edu/SitePages/Welcome.aspx

FIU Year 3 Annual Research Review Presentations:

1. FIU Research Review - Project 1
2. FIU Research Review - Project 2
3. FIU Research Review - Project 3 - D&D IT ML
4. FIU Research Review - Project 4 & 5
5. FIU Research Review - Project 4 - DOE Fellow Aris Duani Rojas
6. FIU Research Review - Project 4 - DOE Fellow Aubrey Litzinger
7. FIU Research Review - Project 4 - DOE Fellow Brendon Cintas
8. FIU Research Review - Project 4 - DOE Fellow Bryan Torres
9. FIU Research Review - Project 4 - DOE Fellow Carolina Trummer
10. FIU Research Review - Project 4 - DOE Fellow Joel Adams
11. FIU Research Review - Project 4 - DOE Fellow Josue Estrada
12. FIU Research Review - Project 5 - DOE Fellow Shawn Cameron
13. FIU Research Review - Wrap Up - Project 1
14. FIU Research Review - Wrap Up - Project 2
15. FIU Research Review - Wrap Up - Project 3 – D&D IT ML
16. FIU Research Review - Wrap Up - Project 4
17. FIU Research Review - Wrap Up - Project 5